Development of a spectral dependent electrical & thermal model for High Concentrating Photovoltaic (HCPV) receivers

Marios Theristis

Submitted for the degree of Doctor of Philosophy

Heriot-Watt University
School of Engineering & Physical Sciences
Institute of Mechanical, Process and Energy Engineering
September 2016

Abstract

High concentrating photovoltaic (HCPV) systems employ III-V multijunction (MJ) solar cells. Such solar cells are monolithically connected in-series and therefore present a strong dependence on the solar spectrum variations. In addition, the concentrated solar flux contributes to the heat generation within the solar cells and, in combination with the current mismatch between the subcells, can force the device to operate in elevated temperatures. It is important therefore, to investigate the influence of the atmospheric parameters on the electrical performance of HCPV and also to quantify the cooling requirements based on the spectrum changes.

In this thesis, a spectral dependent electrical model has been developed to calculate the electrical characteristics and quantify the heat power of a multijunction solar cell. A three-dimensional finite element analysis is also used to predict the solar cell's operating temperature and cooling requirements for a range of ambient temperatures. The combination of these models improves the prediction accuracy of the electrical and thermal behaviour of triple-junction solar cells. The convective heat transfer coefficient between the back-plate and ambient air is quantified based on input spectra. A theoretical investigation is performed to analyse the influence of air mass (*AM),* aerosol optical depth (*AOD*) and precipitable water (*PW*) on the performance of each subcell and whole. It has been shown that the *AM* and *AOD* have a negative impact on the spectral and electrical performance of 3J solar cells while the *PW* has a positive effect, although, to a lesser degree. In order to get a more realistic assessment and also to investigate the effect of heat transfer coefficient on the annual energy yield, the methodology is applied to four US locations using data from a typical meteorological year (TMY3). The integrated modelling procedure is validated experimentally using field measurements from Albuquerque, NM. The importance of the effect of atmospheric parameters on the solar spectrum and hence the performance of HCPV systems is highlighted in this work. The outdoor characterisation provides with useful insight of the influence of spectrum on the performance of a HCPV monomodule and the current CSOC and CSTC ratings are evaluated based on different spectral filtering criteria.

In loving memory of my grandmother, Maria Ioannou...

Acknowledgements

First and foremost, I would like to express my deepest gratitude and appreciation to my supervisor, Dr. Tadhg S. O'Donovan. His advice, patience, honesty and support have been tremendous during my PhD pursuit. I would like to thank him for his constant encouragement, his inspiring enthusiasm for research and for allowing me to grow as a researcher. I would also like to thank Dr. Tapas K. Mallick for his co-supervision during the first year of my PhD and Dr. Ioannis A. Papazoglou who, although my research is outside his expertise, is always supportive, encouraging and interested in my career development.

I would like to thank my friends and colleagues that I have met in Edinburgh: Leonardo Micheli with whom we kept the collaboration running and, more importantly, our friendship, despite his move to the University of Exeter; Yiorgos Arnaoutakis, Panos Alevras, Yiorgos Demetriou, Ityona Amber, Daniel Rylatt for the (mostly) non-research related conversations over a pint of beer!

Special thanks to the team at CSE Fraunhofer in Albuquerque, New Mexico: Cameron Stark, Mark Hill and Pooja Kapadia; thank you for everything you have taught me and for your patience helping me run my experiments. I would also like to thank the team at CFV Solar: Jim Crimmins, Larry Pratt, Michael Yamasaki, Nick Riedel; for the short collaboration we had giving me the opportunity to work on one of their projects that helped me learn about standard procedures and other field problems. Many thanks to Kathleen Connors and Erica Moss of CFV who also made me feel very welcome while in Albuquerque. The team from Suncore US and, in particular, Mike Sumner and Dr. James Foresi; thank you for generously lending the HCPV monomodules used for the experiments. The discussions and correspondence with Mike Sumner on topics related to outdoor CPV characterisation have been invaluable and I thank him very much for sharing his knowledge and experience with me. The final stop of my PhD journey was the University of Jaén, Spain and I would like to thank Dr. Eduardo F. Fernández and Dr. Florencia Almonacid for giving me the opportunity to work with them and also for being so welcoming.

I am grateful for the financial support I have received from EPSRC and ETP for the PhD studentship, CSE Fraunhofer for the research fellowship, the Royal Society of

Edinburgh for the J. M. Lessells scholarship, the Supergen Supersolar and Nielson for the conference travel funds. The University of Jaén is also acknowledged for funding my 3-month research visit. Most importantly, the free and public education provided by the Republics of Cyprus and Greece is gratefully acknowledged; without that I could never afford higher education.

I would like to thank all my friends in Cyprus for their unconditional love and support and for being so welcoming every time I was back on the island; for making me feel like I was not away even for a single day, although it has been 10 years on and off.

I am deeply thankful to my family: my father Takis, brother Yiannos, sister-in-law Lena and my beautiful nephew Christophoros and niece Andrea Theoni who just arrived into this world in March 2016. Without my family's love and support, this thesis would never have been written. All my work is modestly dedicated to the memory of my grandmother, Maria, whose role in my life and education remains immense despite her lack of literacy.

Marios Theristis

ACADEMIC REGISTRY
Research Thesis Submission

Name:	Marios Theristis		
School/PGI:	School of Engineering and Physical Sciences/Institute of Mechanical, Process and Energy Engineering		
Version: *(i.e. First, Resubmission, Final)*	Final	Degree Sought (Award **and** Subject area)	PhD in Photovoltaic Engineering

Declaration

In accordance with the appropriate regulations I hereby submit my thesis and I declare that:

1) the thesis embodies the results of my own work and has been composed by myself
2) where appropriate, I have made acknowledgement of the work of others and have made reference to work carried out in collaboration with other persons
3) the thesis is the correct version of the thesis for submission and is the same version as any electronic versions submitted*.
4) my thesis for the award referred to, deposited in the Heriot-Watt University Library, should be made available for loan or photocopying and be available via the Institutional Repository, subject to such conditions as the Librarian may require
5) I understand that as a student of the University I am required to abide by the Regulations of the University and to conform to its discipline.

* *Please note that it is the responsibility of the candidate to ensure that the correct version of the thesis is submitted.*

Signature of Candidate:		Date:	

Submission

Submitted By *(name in capitals):*	
Signature of Individual Submitting:	
Date Submitted:	

For Completion in the Student Service Centre (SSC)

Received in the SSC by *(name in capitals):*			
Method of Submission (Handed in to SSC; posted through internal/external mail):			
*E-thesis Submitted (**mandatory for final theses**)*			
Signature:		Date:	

Table of contents

List of tables

List of figures

Glossary

Nomenclature

Symbol	Definition	Unit
A	area	m^2
AM	air mass	
AOD	aerosol optical depth	
APE	average photon energy	eV
$ARMSE$	absolute root mean square error	
c	speed of light in vacuum	m/s
C_p	heat capacity	J/(kg·K)
CR	concentration ratio	
DNI	direct normal irradiance	W/m^2
EQE	external quantum efficiency	
E	energy	eV
E_{yield}	energy yield	kWh/kWp
FF	fill factor	
GNI	global normal irradiance	W/m^2
h	Planck's constant	J·s
h_{conv}	convective heat transfer coefficient	$W/(m^2 \cdot K)$
I	current	A
J	current density	A/m^2
k	thermal conductivity	W/(m·K)
k_B	Boltzmann constant	eV/K
K_c	R_s intensity coefficient	
$LCOE$	levelised cost of energy	
MAE	mean absolute error	
MBE	mean bias error	
$MTTF$	mean time to failure	
$NRMSE$	normalised root mean square error	
N	number of datapoints	
n	diode ideality factor	
p	local pressure	mbar

P	power	W
$P_{el,norm}$	normalised electrical power	
PW	precipitable water	cm
q	elementary charge	C
q_{heat}	heat power	W
$q_{heat,norm}$	normalised heat power	
q''	heat flux rate	W/m^2
q'''_{heat}	heat generation	W/m^3
R	resistance	Ω
R_{th}	thermal resistance	K/W
RH	relative humidity	%
RMS	root mean square	
s	number of cycle iterations	
SF	spectral factor	
SMR	spectral matching (or mismatch) ratio	
SR	spectral response	A/W
T	temperature	°C
t	thickness	mm
T_{SOG}	transmittance of SoG	
UF	useful fraction	
V	voltage	V
WS	wind speed	m/s
X	ratio of top to middle J_{sc}	
Z	spectral index	
z	zenith angle	°

Greek letters

α	material dependent constant	eV/K
a_{Isc}	short-circuit current temperature coeff.	A/°C
β	material dependent constant	K
β_{Voc}	open-circuit voltage temperature coeff.	V/°C
γ	constant related to saturation current	
δ	efficiency temperature coefficient	%/°C
ΔT	temperature difference	°C
ε	emissivity	
η	efficiency	
κ	constant related to saturation current	$A/(cm^2 \cdot K^4)$
λ	wavelength	nm
ρ	density	kg/m^3
σ	Stefan-Boltzmann constant	$W/(m^2 \cdot K^4)$
Φ	photon flux density	# of photons/m·s

Subscripts

amb	ambient
avg	average
cell	solar cell
CM	current mismatch
cond	conduction
conv	convection
eff	effective
g	bang-gap
geo	geometric
HS	heat sink
i	number of subcell/layer
irr	irradiance
in	incident
meas	measured
mod	module
mp	maximum power
norm	normalised
oc	open-circuit
opt	optical
ph	photon
rad	radiation
ref	reference
s	series
SC	short-circuit
sh	shunt
S0	R_s at low intensity
$S\infty$	R_s at high flux
0	dark saturation
1	top subcell
2	middle subcell
3	bottom subcell

Abbreviations

ANN - Artificial Neural Network

ASTM - American Society for Testing and Materials

BPI - Black Photon Instruments

CCA - Concentrator Cell Assembly

CPV - Concentrating Photovoltaic

CPVT - Concentrating Photovoltaic Thermal

CSE - Center for Sustainable Energy Systems

CSP - Concentrated Solar Power

CSTC - Concentrator Standard Test Conditions

CSOC - Concentrator Standard Operating Conditions

DBC - Direct Bonded Copper

DC - Direct Current

DEM - Double Exponential Model

ECT - Equivalent Cell Temperature

EM - Electrical Model

FEA - Finite Element Analysis

FETM - Finite Element Thermal Model

GMRES - Generalized Minimal RESidual method

HCPV - High Concentrating Photovoltaic

IEC - International Electrotechnical Commission

IR - Infrared

ISFOC - Instituto de Sistemas Fotovoltaicos de Concentración

LCPV - Low Concentrating Photovoltaic

MCPV - Medium Concentrating Photovoltaic

MJ - Multijunction

MPP - Maximum Power Point

NREL - National Renewable Energy Laboratory

PV - Photovoltaic

RA - Receiver Assembly

REN21 - Renewable Energy Policy Network for the 21st Century

SEM - Single Exponential Model

SMARTS2 - Simple Model of the Atmospheric Radiative Transfer of Sunshine, v. 2

SoG - Silicon-on-glass

TC - Thermocouple

TIM - Thermal Interface Material

TMY - Typical Meteorological Year

TTM - Thermal Transient Measurements

UV - Ultraviolet

Vis - Visible

1D - One-Dimensional

1J - Single-junction

2J - Two-junction

3D - Three-Dimensional

3J - Triple-junction

4J - Four-junction

List of materials

Ag - Silver

Al - Aluminium

AlN - Aluminium Nitride

Al_2O_3 - Aluminium Oxide

Cu - Copper

GaAs - Gallium Arsenide

GaInAs - Gallium Indium Arsenide

GaInP - Gallium Indium Phosphide

Ge - Germanium

Si - Silicon

Sn - Tin

List of physical constants

Boltzmann constant	$k \approx 1.381 \times 10^{-23}$ $m^2 \cdot kg \cdot s^{-2} \cdot K^{-1}$ (or J/K)
Electron charge	$q \approx 1.602 \times 10^{-19}$ C (or A·s)
Plack's constant	$h \approx 6.626 \times 10^{-34}$ $m^2 \cdot kg/s$ (or J·s)
Speed of light in vacuum	$c \approx 2.998 \times 10^{8}$ m/s
Stefan-Boltzmann constant	$\sigma \approx 5.670 \times 10^{-8}$ $W/(m^2 \cdot K^4)$

List of publications

Journal publications

1) **M. Theristis**, and T. S. O’Donovan, "Electrical-thermal analysis of III-V triple-junction solar cells under variable spectra and ambient temperatures", *Solar Energy*, vol. 118, 2015, pp. 533-546
2) **M. Theristis**, E. F. Fernández, C. Stark, and T. S. O'Donovan, "A Theoretical Analysis of the Impact of Atmospheric Parameters on the Spectral, Electrical and Thermal Performance of a Concentrating III-V Triple-Junction Solar Cell", *Energy Conversion and Management*, vol. 117, 2016, pp. 218-227 .
3) **M. Theristis** *et al.*, "Numerical modelling and experimental validation of a HCPV monomodule taking into account the spectral and thermal aspects", (in preparation).
4) **M. Theristis** *et al.*, "Outdoor spectral and electrical performance evaluation of a HCPV monomodule", (in preparation).

Peer reviewed conference publications

1) **M. Theristis**, N. Sarmah, T. K. Mallick, and T. S. O'Donovan, "Design and Numerical Analysis of Enhanced Cooling Techniques for a High Concentration Photovoltaic (HCPV) System," in *27th European Photovoltaic Solar Energy Conference and Exhibition (EU PVSEC)*, Frankfurt, Germany, 2012, pp. 260-265.
2) **M. Theristis**, G. E. Arnaoutakis, N. Sarmah, T. K. Mallick, and T. S. O'Donovan, "Solar Spectrum Dependent Thermal Model for HCPV Systems," in *13th UK Heat Transfer Conference (UKHTC)*, London, UK, 2013, pp. 124/1 - 124/8.
3) **M. Theristis**, M. E. Arnaoutakis, N. Sarmah, T. K. Mallick, and T. S. O'Donovan, "3D Thermal Numerical Analysis of a Densely Packed Concentrating Photovoltaic Receiver," in *4th International Conference on Advances in Energy Research (ICAER)*, Mumbai, India, 2013, pp. 1655 - 1661.
4) **M. Theristis**, and T. S. O'Donovan, "An integrated thermal electrical model for single cell photovoltaic receivers under concentration", in *15th International Heat Transfer Conference (IHTC)*, Kyoto, Japan, 2014.

Peer reviewed conference publications (continued)

5) **M. Theristis**, and T. S. O'Donovan, "Determination of the cooling requirements for single cell photovoltaic receivers under variable atmospheric parameters", in *42nd IEEE Photovoltaic Specialist Conference (PVSC),* New Orleans, LA, USA, 2015.
6) **M. Theristis**, E. F. Fernández, J. P. Ferrer-Rodríguez, C. Stark, and T. S. O'Donovan, "Energy Yield Assessment of a High Concentration Photovoltaic Receiver Based on Simulated Spectra from Typical Meteorological Year Datasets", in *12th International Conference on Concentrator Photovoltaic Systems (CPV-12)*, Freiburg, Germany, 2016.

Other publications

1) **M. Theristis**, G. C. Bakos, and I. A. Papazoglou, "Development of a reliability model for the estimation of the Loss of Load Probability and O&M cost for an off-grid PV system," in *27th European Photovoltaic Solar Energy Conference and Exhibition (EU PVSEC),* Frankfurt, Germany, 2012, pp. 4245 - 4248.
2) **M. Theristis**, and I. A. Papazoglou, "Markovian Reliability Analysis of Standalone Photovoltaic Systems Incorporating Repairs", *IEEE Journal of Photovoltaics*, vol. 4, no. 1, pp. 414-422, 2014.
3) A. Phinikarides, G. Arnaoutakis, **M. Theristis**, G. Kocher, "Comparison of a stand-alone PV system with a stand-alone hybrid (PV/Wind) system on a building in Cyprus", in *29th European Photovoltaic Solar Energy Conference and Exhibition (EU PVSEC),* Amsterdam, Netherlands, 2014, pp. 3833-3836.
4) C. Stark, and **M. Theristis**, "The impact of atmospheric parameters on the spectral performance of multiple photovoltaic technologies", in *42nd IEEE Photovoltaic Specialist Conference (PVSC)*, New Orleans, LA, USA, 2015.
5) **M. Theristis**, Eduardo F. Fernández, Florencia Almonacid, and Pedro Pérez-Higueras, "Spectral corrections based on air mass, aerosol optical depth and precipitable water for CPV performance modelling," *IEEE Journal of Photovoltaics* (in press).

Seminar and conference presentations

1) **M. Theristis**, T.K. Mallick, and T.S. O'Donovan, "Numerical Investigation of Heat Transfer within a High Concentration Photovoltaic (HCPV) System," in *EUROTHERM Seminar No. 98, Concentrating Solar Energy Systems*, Vienna University of Technology, 4th-5th July 2013.
2) **M. Theristis**, N. Sarmah, T.K. Mallick, and T.S. O'Donovan, "Development of an integrated thermal – electrical model for multijunction solar cells under concentration," in *Advances in Concentrator Photovoltaics*, Imperial College London, 5th February 2014.
3) **M. Theristis**, C. Stark, and T. S. O'Donovan, "III-V multijunction cell temperature prediction under concentration and realistic atmospheric conditions", in *14th UK Heat Transfer Conference (UKHTC)*, Edinburgh, UK, 7th-8th September 2015.
4) **M. Theristis**, "Integrated modelling of concentrating photovoltaic devices; the importance of considering the solar spectrum," MSc in Renewable Energy for University of Jaén (Máster en Energías Renovables por la Universidad de Jaén), Spain, 11th April 2016 (Invited talk).

Chapter 1: Introduction

1.1. Renewables and solar energy

Energy supply and the environment are fundamental and pressing issues for society. The need to reduce society's dependence on fossil fuels is vital to mitigate the effects of global warming and related economic pressures. Therefore, there is an urgent need to develop alternative ways of producing energy with high reliability, efficiency and low carbon emissions. In contrast to carbon-based energy, solar power is considered to be an infinite source of energy and to have minimal impact on our environment.

Solar power has therefore attracted much research attention, including developments in the field of photovoltaic systems, in the last few decades. The Earth's surface receives an average of approximately 1.2×10^{17} W of solar power [1] while the hourly energy from the sun reaching the Earth is almost the same as the amount of worldwide energy demand for one year. Therefore, the fast evolution of photovoltaic (PV) systems during the last two decades resulted in the installation of numerous systems all over the world.

According to the Renewable Energy Policy Network for the 21st Century, REN21 [2], the global installed capacity of solar PV increased sharply between 2004 and 2014 with an average increase of about 31.6% per year. Since 2010, there has been an average increase in installed capacity of about 34.3 GW/year with a new record in 2014 of about 39 GW. The global installed capacity is about 177 GW (Figure 1). Moreover, the period between 2010 and 2014 accounts for 87% of all solar PV capacity.

In terms of investment in solar energy during 2014, REN21 [2] reported 87 billion USD for developed countries and 63 billion USD for developing countries which is 25% higher than the investments of 2013. The amounts invested in solar energy in 2014 are the highest compared to any other renewable energy technology (Figure 2). Wind energy follows with 41 billion USD in developed countries and 58 billion USD in developing countries.

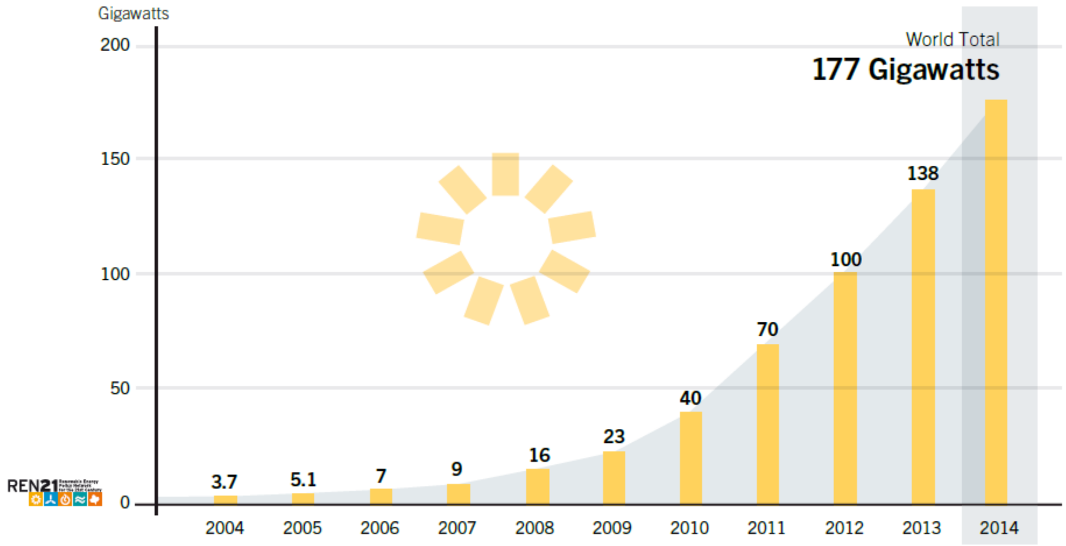

Figure 1: **Solar PV total world capacity between 2004-2014 [2].**

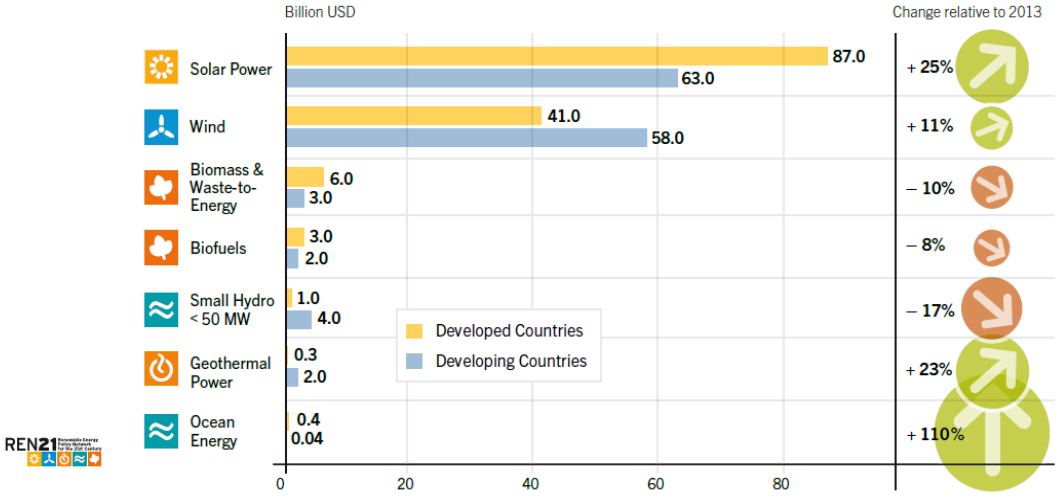

Figure 2: **Global new investment in renewable energy by technology for developed and developing countries, 2014 [2].**

The above mentioned statistics highlight the importance of solar energy in the worldwide energy mix. Further cost reduction of photovoltaic systems is therefore vital for their commercial success and the corresponding reduction in carbon dioxide emissions. This can be achieved either by increasing the efficiency of the solar cell or/and by using concentrating systems.

Concentrating or concentrator photovoltaics (CPV) use optical components that focus the direct sunlight by reflection or refraction onto a smaller area usually made of high-efficiency III-V multijunction (MJ) solar cells. Such solar cells overcome the thermodynamic Shockley-Queisser limit of single junction solar cells [3] and even though their market share is small and relatively young, there is still a great interest in the technology due to the higher efficiencies especially at sites with high annual direct normal irradiation [2]. In addition, CPV can achieve greater energy density and thus less semiconductor material is required [4]. This technology however, must overcome the technical and economic challenges to achieve success in the energy market [4, 5].

1.2. Multijunction solar cells

In an attempt to increase electrical conversion efficiencies, researchers have been focusing on techniques to absorb a larger range of the solar spectrum [6]. Silicon (Si) solar cells, which is the most popular solar cell material, can typically operate between 400 nm to 1100 nm (for an energy band-gap, $E_g \approx 1.1$ eV) and therefore can only convert a maximum of 30% [7] of the solar energy. De Vos [8] calculated the theoretical maximum efficiencies of tandem solar cells and found that a two-junction (2J) solar cell can convert 42%, a triple-junction (3J) solar cell 49% and a four-junction (4J) solar cell can convert 53% of the incident sunlight under 1 sun (i.e. no concentration). In addition, De Vos [8] also calculated the theoretical maximum efficiencies under a concentration ratio (CR) of 45,900× and found that for single-junction solar cells the conversion efficiency was 40%, for 2J was 55%, 3J was 63% and 4J was 68%.

The explanation of how the solar energy is converted into electricity and heat in MJ solar cells is described here: Consider a 3J solar cell in a tandem (or stacked) configuration as illustrated in Figure 3 with energy band-gaps $E_{g,1}$ (for top subcell), $E_{g,2}$ (for middle subcell) and $E_{g,3}$ (for bottom subcell). Incident photons with energies E_{ph} greater than $E_{g,1}$ will be absorbed by the top subcell while incident photons with energies lower than $E_{g,1}$ will not be absorbed and therefore will be "seen" as transparent and pass to the middle subcell. The photons with energies $E_{g,1} > E_{ph} > E_{g,2}$ will be absorbed by the middle subcell and finally $E_{g,2} > E_{ph} > E_{g,3}$ will be absorbed by the bottom subcell. The photons that will not be absorbed by the 3J solar cell will be converted to heat.

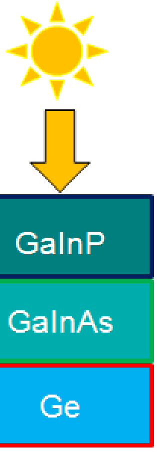

Figure 3: **III-V 3J solar cell configuration.**

The utilisation of multiple subcells with different energy band-gaps in a stacked configuration, results in a cumulative effect and subsequently the increased overall efficiency. Such solar cells are used for both space and terrestrial applications [9]. The state of the art 3J solar cell in the market consists of GaInP (gallium indium phosphide), GaInAs (gallium indium arsenide) and Ge (germanium) [10] and the efficiencies range from 37% to 42% [11]. According to the National Renewable Energy Laboratory (NREL) [12] 3J cells have reported a conversion efficiency of 44.4% at 302× (Figure 4). The record for solar cell efficiency was achieved by a 4J solar cell at 46% (Figure 4) and 508 suns [13]. The monolithically (i.e. series connection with two terminal outputs) connected 3J solar cells are considered in this thesis.

The portion of the solar spectrum (AM1.5) that can be absorbed by a Si solar cell and a III-V 3J solar cell is shown in Figure 5. It is obvious that the 3J solar cell can absorb a wider range of the spectrum, thus offering much higher efficiency than the silicon cells. Furthermore, 3J solar cells can offer higher reliability with a lifetime (or Mean Time To Failure, *MTTF*) of more than 34 years (100,000 hours, assuming 8 hours/day operation) [14, 15] while silicon cells offer a *MTTF* of 25 years with a failure rate of 0.04 per year [16]. However, the reliability prediction still needs further investigation as this technology is still immature in the field. Therefore, long-term reliability is also a key for the technology's market success [4].

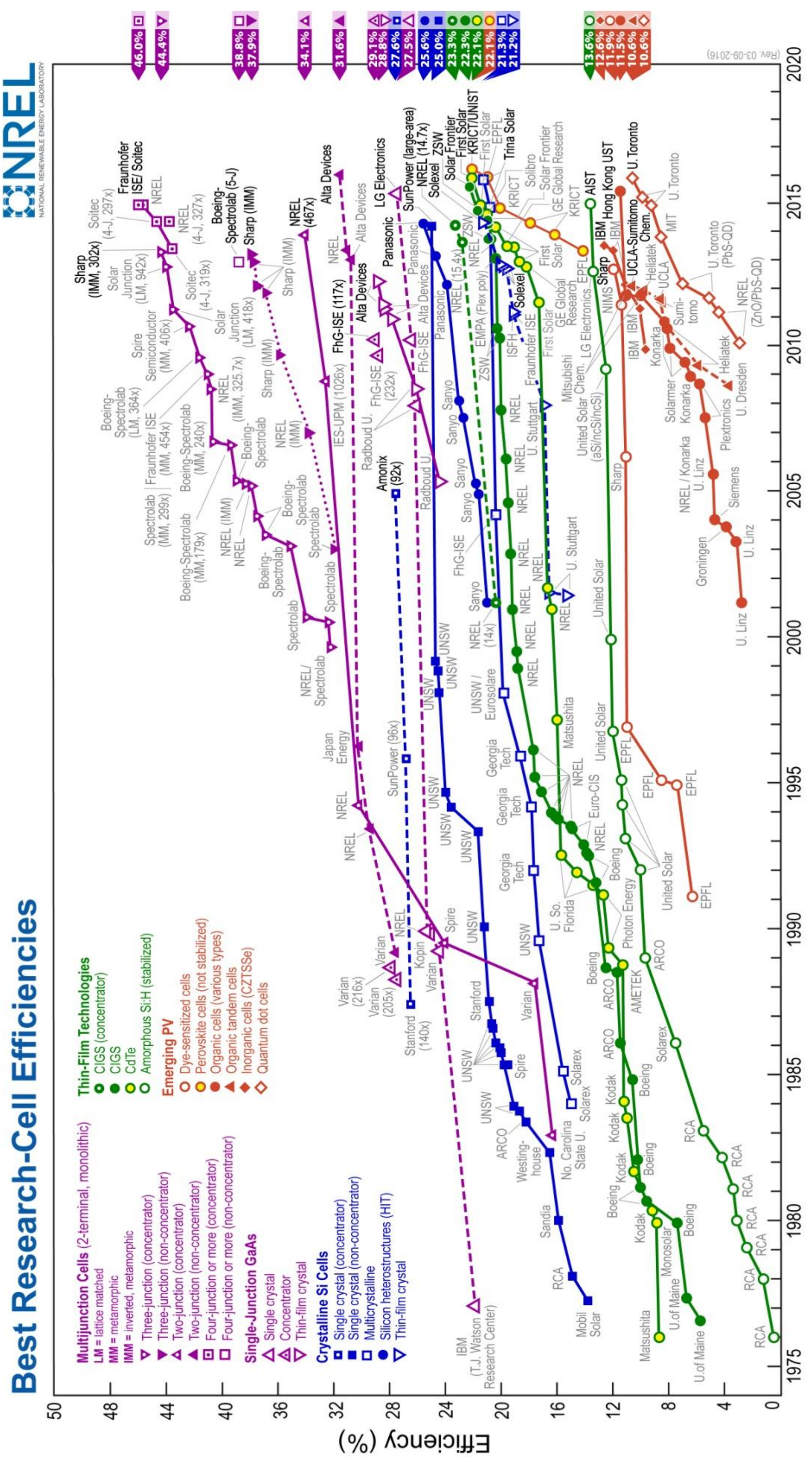

Figure 4: Best research PV cell efficiencies reported up to date (03/05/2016) [12].

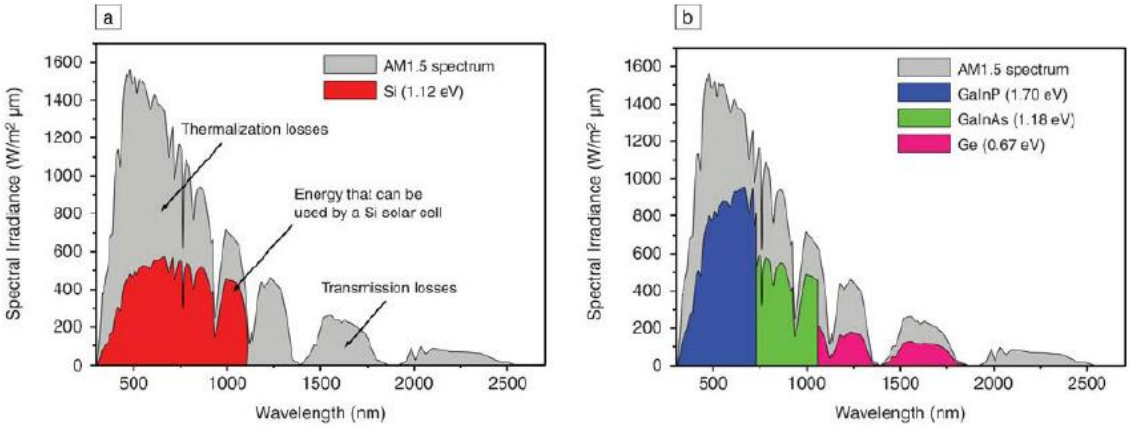

Figure 5: **The portion of solar spectrum that can theoretically be absorbed by: (a) Si solar cells; (b) GaInP/GaInAs/Ge solar cells [17]. The AM1.5 is also shown in the background as a reference.**

1.3. Solar concentrators

Solar concentrators collect the direct component of sunlight (direct normal irradiance, *DNI*) and concentrate it on a smaller area (i.e. a receiver) to directly produce electricity (in CPV systems), or heat (in Concentrated Solar Power, CSP systems) which in turn is used to drive a heat engine for electricity generation [18].

CPV systems were first introduced in the 1970s with Sandia National Laboratories developing the first system [19]. A complete overview of the history of CPV was presented by Swanson [20] where he concluded that this technology has the potential of achieving a levelised cost of energy (*LCOE*) at the range of 0.07 to 0.15 USD/kWh.

The CPV systems are categorised according to their receiver design, the way the sunlight is concentrated and their concentration level. A concentrator can be a Fresnel lens [21-23], a dish using mirrors or any other high reflective material [24, 25], a parabolic trough [26, 27], a compound parabola [28-30], a ring array [31] or luminescent [32, 33] to name a few. The concentration level of a CPV system is usually referred to as the geometric *CR* (i.e. CR_{geo}) which describes the number of times the direct sunlight is concentrated on the receiver and it is defined as the ratio of the concentrator area ($A_{concentrator}$) to the solar cell's active area (A_{cell}):

$$CR_{geo} = \frac{A_{concentrator}}{A_{cell}} . \tag{1}$$

The CR_{geo} is expressed in suns, where 1 sun = 1×. Other definitions regarding the *CR* are the optical and intensity *CR* [34]; the optical *CR* includes the optical losses when multiplied by the optical efficiency (i.e. $CR_{opt} = CR \cdot \eta_{opt}$) while the intensity *CR* is given in kW/m^2. This thesis will use the CR_{geo} and refer to it as *CR*.

Depending on their concentration level CPV systems are usually categorised in the following three groups [35]:

- Low Concentrating PV (LCPV) where the *CR* is between 1 and 40 suns (1-40×)
- Medium Concentrating PV (MCPV) where the *CR* is between 40 and 300 suns (40-300×)
- High Concentrating PV (HCPV) where the *CR* is between 300 and 2000 suns (300-2000×)

According to Pérez-Higueras *et al.* [35], the HCPV systems present merits against the LCPV and MCPV systems such as the higher potential to reduce the costs, the higher interest from investors and the greater installed power capacity. However, as a result of the high concentrated heat flux, the temperature at the receiver might be up to 1400°C [36-39] (see Figure 6). The increasing temperatures decrease the electrical conversion efficiency of the solar cell and also run some risks regarding their long-term stability [5]. Therefore, an appropriate heat exchanger (passive or active) must be incorporated during the module design.

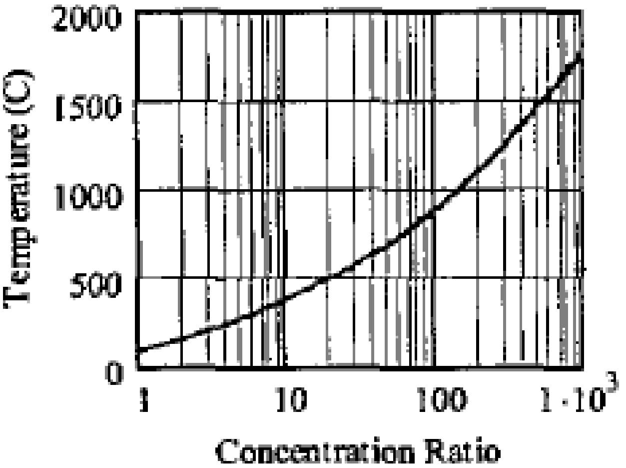

Figure 6: **Temperature variations under concentrated illumination. Note that for concentration of 500× the temperature could reach 1400°C [37].**

CPV systems can be also grouped into the following categories depending on the receiver's design [40]:

- single cell geometry where the direct sunlight is focused onto each cell separately (Figure 7); i.e. each cell having its own concentrator

- densely packed geometry where the direct sunlight is focused on a larger-point focus receiver which consists of a number of solar cells that are electrically and mechanically connected (Figure 8)
- a linear receiver where a parabolic trough or a Fresnel lens is used to focus the solar light onto a row of cells (Figure 9)

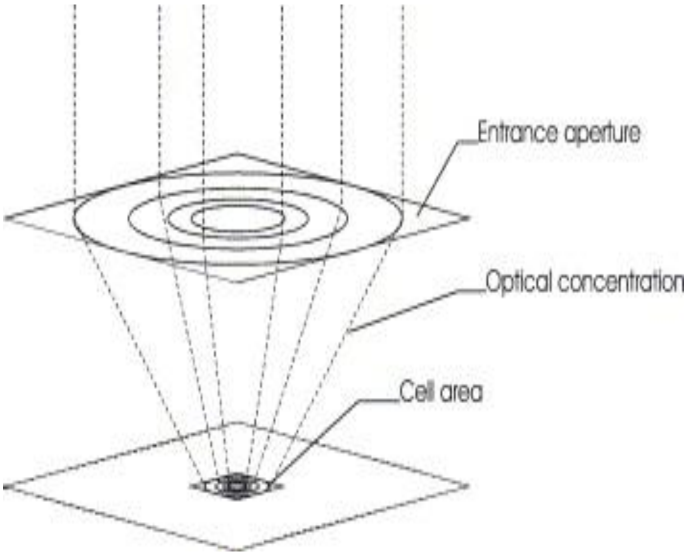

Figure 7: **Single cell concentrator were the solar radiation is focused onto the cell [40].**

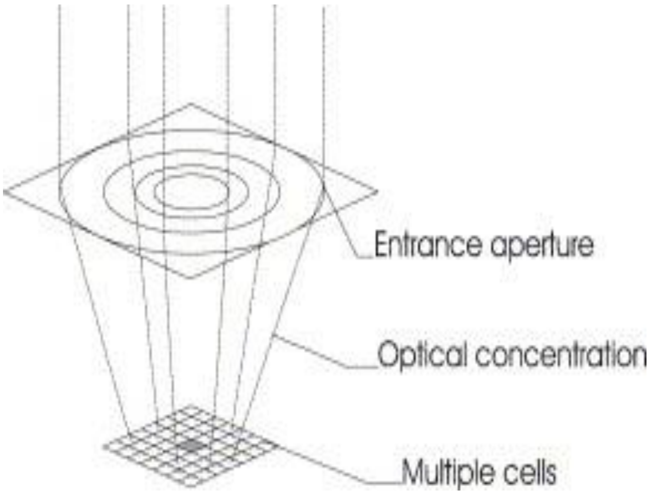

Figure 8: **Densely packed cells where the sunlight is focus onto an array of cells [40].**

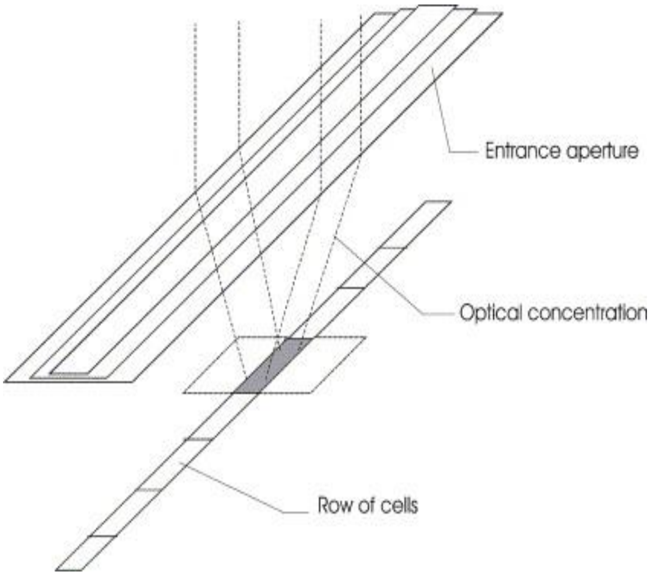

Figure 9: **Linear receiver where Fresnel lenses are used to focus the solar radiation onto a row of cells [40].**

To date, the record module efficiency belongs to Soitec at 38.9% [11, 41]. Soitec's record HCPV module is a single cell geometry using 36 Fresnel lenses with an aperture area of 812 cm^2 and also incorporates the record 4J solar cell mentioned earlier. According to the same press release by Soitec [41], the record efficiency was measured both indoors and outdoors. Recently [42], an efficiency of 43.4% was demonstrated by Fraunhofer ISE for a CPV subunit device at 340 suns.

1.4. Solar irradiance

When the performance of a solar energy system is evaluated, it is important to know the incident irradiance [43, 44]. The solar irradiance before entering the Earth's atmosphere is referred to as the extraterrestrial irradiance. As the solar irradiance passes through the atmosphere it is modified by scattering and absorption [45] (also referred to as extinction or attenuation [46]). While conventional PV technologies (or flat plate collectors) require the total amount of incident solar irradiance per unit area (i.e. global solar irradiance), concentrating systems, such as CPV and CSP, require knowledge of the *DNI*; the solar irradiance that passes directly through the atmosphere and impinges on a plane normal to the sun [47]. The global solar irradiance consists of the diffuse irradiance (irradiance after scattering in the atmosphere) and direct however, concentrating systems can only use the direct component due to the use of concentrating optics (Figure 10).

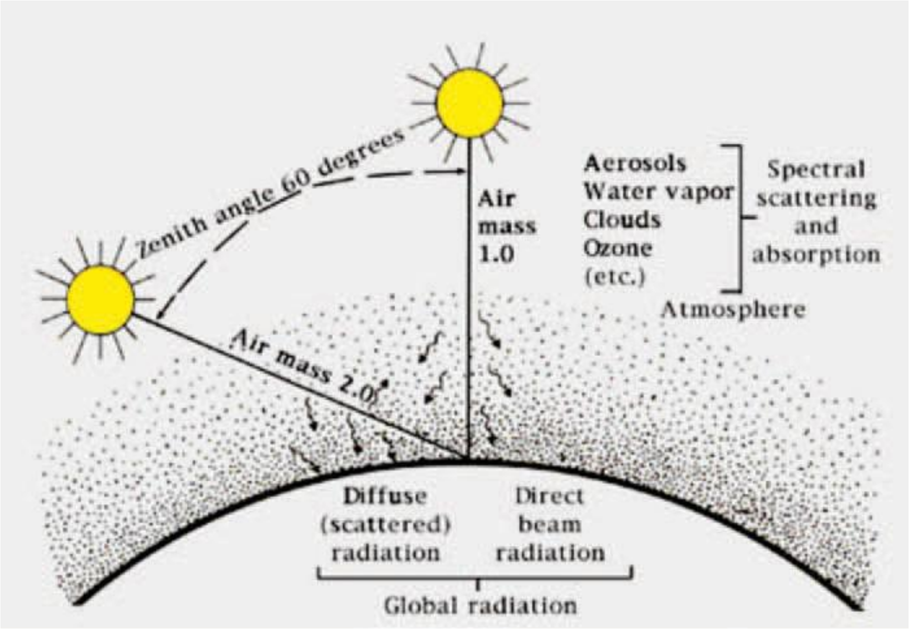

Figure 10: Schematic illustrating the change of air mass, the spectral scattering and absorption through the atmosphere (due to aerosols, water vapour, clouds etc.). The global irradiance is the sum of the diffused (scattered) irradiance and the direct irradiance. CPV systems can only use the *DNI* because of the concentrating optics. Figure courtesy of Sengupta *et al.* [48].

The spectral and broadband (i.e. integrated over all wavelengths) solar irradiance in Earth's surface is affected by a number of factors such as the changes in air mass (*AM*) and atmospheric effects. The *AM* is defined as the "path length through the atmosphere relative to the zenith (overhead position) [49]" and is given by [50]:

$$AM = \frac{1}{\cos(z)} \tag{2}$$

where z is the zenith angle and is defined as the angle between the sun's position and the zenith. The calculation in equation (2) assumes that the atmosphere is flat and therefore, if the curvature of Earth is included the equation is [51]:

$$AM = \frac{1}{\cos(z) + 0.50572(96.07995 - z)^{-1.6364}} \tag{3}$$

which is referred as the relative *AM* and is applicable for pressure at sea level. For pressures above sea level, the equation is corrected by multiplying equation (3) by $p/1013.25$, where p is the local pressure in mbar; this is referred to as the absolute *AM* [52].

The performance of MJ solar cells and therefore of CPV systems that employ such cells, is highly influenced by the changes in the spectral distribution of the incident *DNI*; this is due to the tandem configuration of subcells with different energy band-gaps and also due to the in-series connection that limits the current output to the minimum current of the subcells. In addition to *AM*, the atmospheric parameters that predominantly affect the spectral distribution of *DNI* and hence the performance of CPV systems are the aerosols (aerosol optical depth, *AOD*) and the water vapour (or precipitable water, *PW*) [53-56]. According to Chan *et al.* [54], other atmospheric components (or gases such as the ozone), have a relatively minor effect on the CPV performance and can therefore be neglected.

The *AOD* represents the amount of aerosols (small particles) in the atmosphere and it has a strong impact on the spectral irradiance. High values of *AOD* indicate a relatively hazy atmosphere while low values of *AOD* indicate a relatively clear atmosphere. It is wavelength dependent and is represented by the Ångström power law [57-59]:

$$\tau_{a\lambda} = \beta\lambda^{-\alpha} \tag{4}$$

where $\tau_{a\lambda}$ is the *AOD*, α is the Ångström exponent and relates to the particle size of aerosols, β is the *AOD* at 1000 nm (also called the turbidity coefficient [60]) and λ is the wavelength (in microns). Ångström exponent values, $\alpha \leq 1$ indicate relatively large particles (e.g. dust, sea salt) while values $\alpha \geq 2$ indicate relatively small (or finer) particles such as urban pollution [60]. Moreover, the Ångström exponent has no effect on the spectral irradiance for $\lambda > 1000$ nm [45].

The *PW* represents the total amount of water in a column in the zenith direction; i.e. "if the water vapour in a vertical column of 1 cm^2 base area was condensed, *PW* would be the height (cm) of that column [46]". The *PW* at a specific location can vary significantly during the year, depending on the season [52]. Low values of *PW* indicate a relatively dry atmosphere while high values of *PW* indicate a relatively wet or humid atmosphere.

1.5. Scope & thesis outline

HCPV systems present a significant complexity (as compared to flat-plate PV technologies) in terms of energy modelling and prediction of their actual operation in the field [61, 62]. This is mainly due to the use of optics, trackers, heat exchangers and MJ solar cells that, combined with the optics, also add a strong spectrum dependence. Although accurate electrical models exist in literature (will be thoroughly discussed in Chapter 2), the need of an integrated model that incorporates the spectral dependence along with the electrical and thermal behaviour of CPV systems remains unsolved. The better understanding of the HCPV system's behaviour would also gain more trust from the investors [4]. Moreover, the accurate quantification of the cooling requirements of such systems, can contribute to the optimum material usage and more compact design. Therefore, in this thesis, an attempt is made to fill the gaps in the direction of an integrated model that combines three models: a spectral, an electrical and a three-dimensional (3D) finite element analysis (FEA) thermal model.

The thesis is structured as follows: in Chapter 2 an extensive literature review is performed, analysing the thermal and electrical models for CPV, passive cooling systems and methods to predict the cell temperature. In addition, the various spectral indices and models are also presented. Finally, the rating procedures for CPV are introduced, although they are still in the draft stage.

Chapter 3 continues with the methodology of the numerical models and how the integration between them is achieved. The three models are described separately and the mathematical equations are given for the electrical and 3D FEA thermal models. The experimental setup and equipments used at the solar test site of the Center for Sustainable Energy Systems (CSE), Fraunhofer USA, Albuquerque, New Mexico are also presented.

The first investigation of the influence of the incident spectral irradiance on the electrical and thermal performance of 3J solar cells is presented in Chapter 4. The *AM* and ambient temperatures are varied and the heat transfer coefficient (h_{conv}) between the back-plate and ambient air is quantified. Recommendations on heat sinking requirements for a concentrator cell assembly (CCA) are given in order to operate safely below 90°C.

The experimental validation is presented in Chapter 5. The 3D thermal model of a Suncore monomodule is described and the models are validated separately (spectral, thermal, electrical) and also as an integrated model.

Chapter 6 expands on the model of Chapter 4 and incorporates the effect of *AOD* and *PW*. Firstly, the impact of *AM*, *AOD* and *PW* on the spectral and electrical performance is investigated. Then, the cooling requirements under worst-case conditions (i.e. a "hot and dry" climate) are quantified and in order to get a more realistic evaluation, case studies using data from typical meteorological years are performed to determine the spectral and electrical performance and also to quantify the optimum h_{conv} at each location.

The outdoor testing at the CSE Fraunhofer's facilities in Albuquerque, NM are presented in Chapter 7. The Suncore monomodule is characterised electrically in terms of the spectral variations. This chapter ends with Concentrator Standard Operating Conditions (CSOC) and Concentrator Standard Test Conditions (CSTC) estimations using different scenarios and filtering criteria. The CSTC is also compared to indoor measurements performed by a private company.

Finally, in Chapter 8, conclusions are drawn from the procedures followed in this thesis and suggestions for future work are given.

Chapter 2: Models and methods reported in literature

This chapter describes the state-of-the-art models and methods that are reported in literature, for the spectral and electrical characterisation and also for the solar cell temperature prediction. Thermal management models and passive cooling devices are also reviewed and finally the CPV power rating procedures are described in the last section.

2.1. Spectral indices

As discussed in Chapter 1, the solar spectrum varies with changes in *AM*, *PW*, *AOD*, clouds etc. In order to characterise the variation of the solar spectrum, some spectral indices have been introduced. In this brief analysis, indices that have been used by the PV community will be discussed.

The Average Photon Energy (*APE*) was first introduced by Jardine *et al*. [63] and Williams *et al*. [64] and it was adapted to many CPV-related studies [65-70]; it can basically qualitatively describe the content of the incident spectral irradiance compared to the reference spectrum AM1.5 [71]. *APE* (eV) therefore, is defined as the ratio of measured spectral irradiance divided by the integral of the photon flux density [68]:

$$APE = \frac{\int E_{irr}(\lambda)\, d\lambda}{q \cdot \int \Phi(\lambda)\, d\lambda} \tag{5}$$

where q is the elementary charge, E_{irr} is the spectral irradiance and Φ is the direct photon flux density. *APE* can only characterise the solar spectrum and is a device-independent parameter [72].

Unlike *APE*, the Useful Fraction (*UF*) [73] is a device-dependent index and is defined as the ratio of the broadband irradiance within the proportion of spectrum to which the device corresponds to the total broadband irradiance:

$$UF = \frac{\int_{\lambda}^{\lambda_{Eg}} E_{irr}(\lambda)\, d\lambda}{\int_{0}^{\infty} E_{irr}(\lambda)\, d\lambda} \tag{6}$$

where $\int_{\lambda}^{\lambda_{Eg}} E_{irr}(\lambda)\,d\lambda$ is the incident irradiance within the spectral range of the PV device.

Another important spectral index is the spectral factor (*SF*) [74, 75] which is basically a normalisation of the short-circuit current density (J_{sc}). This index allows the quantification of the spectral performance (spectral gains or losses) of a particular device as compared to the reference spectrum AM1.5. In the case of multijunction solar cells, the *SF* of each subcell is given by [53]:

$$SF_i = \frac{\int DNI(\lambda)\cdot\eta_{opt}(\lambda)\cdot SR_i(\lambda)\,d\lambda}{\int DNI(\lambda)\,d\lambda}\cdot\frac{\int DNI_{ref}(\lambda)\,d\lambda}{\int DNI_{ref}(\lambda)\cdot\eta_{opt}(\lambda)\cdot SR_i(\lambda)\,d\lambda} = \frac{J_{sc}^{i}}{DNI}\cdot\frac{DNI_{ref}}{J_{sc,ref}^{i}} \qquad \textbf{(7)}$$

while the *SF* of the whole device, due to the in-series connection, is given by:

$$SF = \frac{\min\left(\int DNI(\lambda)\cdot\eta_{opt}(\lambda)\cdot SR_i(\lambda)\,d\lambda\right)}{\int DNI(\lambda)\,d\lambda}\cdot\frac{\int DNI_{ref}(\lambda)\,d\lambda}{\min\left(\int DNI_{ref}(\lambda)\cdot\eta_{opt}(\lambda)\cdot SR_i(\lambda)\,d\lambda\right)} \Rightarrow$$

$$SF = \frac{\min\left(J_{sc}^{i}\right)}{DNI}\cdot\frac{DNI_{ref}}{\min\left(J_{sc,ref}^{i}\right)} \qquad \textbf{(8)}$$

where $SR(\lambda)$ is the spectral response (i.e. the ratio of current generation to the incident power). The subscript, "ref", denotes the reference conditions and "i" the corresponding subcell (1 = top, 2 = middle, 3 = bottom). *SF* values above 1 indicate spectral gains, below 1 indicate spectral losses and equal to 1 the same spectral conditions as the reference (i.e. AM1.5D). The output current of a 3J solar cell is restricted to the minimum current of the three subcells because of the in-series connection. An alternative and also important index is the spectral matching ratio (*SMR*) [76-78]. *SMR* between two subcells is defined as the ratio of the measured short-circuit current density of one subcell at a specific spectrum to the short-circuit current density at reference conditions divided by the same ratio of the other subcell. In the case of 3J solar cells, *SMR1* of top to middle subcell is described as [77-79]:

$$SMR1 = \frac{\dfrac{\int DNI(\lambda)\cdot\eta_{opt}(\lambda)\cdot SR_{top}(\lambda)\,d\lambda}{\int DNI_{ref}(\lambda)\cdot\eta_{opt}(\lambda)\cdot SR_{top}(\lambda)\,d\lambda}}{\dfrac{\int DNI(\lambda)\cdot\eta_{opt}(\lambda)\cdot SR_{middle}(\lambda)\,d\lambda}{\int DNI_{ref}(\lambda)\cdot\eta_{opt}(\lambda)\cdot SR_{middle}(\lambda)\,d\lambda}} = \frac{\dfrac{J_{sc}^{top}}{J_{sc,ref}^{top}}}{\dfrac{J_{sc}^{mid}}{J_{sc,ref}^{mid}}} \qquad \textbf{(9)}$$

where *SMR1* > 1 when the incident spectrum is blue-rich and *SMR1* < 1 when the incident spectrum is red-rich. The *SMR1* = 1 when the incident spectrum matches the reference conditions. In a similar manner, the *SMR2* of middle to bottom subcell becomes:

$$SMR2 = \frac{\dfrac{\int DNI(\lambda)\cdot\eta_{opt}(\lambda)\cdot SR_{mid}(\lambda)\,d\lambda}{\int DNI_{ref}(\lambda)\cdot\eta_{opt}(\lambda)\cdot SR_{mid}(\lambda)\,d\lambda}}{\dfrac{\int DNI(\lambda)\cdot\eta_{opt}(\lambda)\cdot SR_{bot}(\lambda)\,d\lambda}{\int DNI_{ref}(\lambda)\cdot\eta_{opt}(\lambda)\cdot SR_{bot}(\lambda)\,d\lambda}} = \frac{\dfrac{J_{sc}^{mid}}{J_{sc,ref}^{mid}}}{\dfrac{J_{sc}^{bot}}{J_{sc,ref}^{bot}}} \tag{10}$$

Contrarily to the *SMR1*, *SMR2* (i.e. middle to bottom) is not described quantitatively in literature, but in general terms, the higher the *SMR2*, the higher the *PW* is (i.e. wetter atmosphere) [80].

Both of these spectral indices (*SF* and *SMR*) have been widely used in the PV community [80-83]. It is worth mentioning that because the 3J solar cells are monolothically connected (i.e. no access to individual subcell), the SF_i and *SMR* indices can be either evaluated by using component cells (also called isotypes) or by modelling the short-circuit current at each subcell, assuming that the required data are available (i.e. spectrum, *SR* etc). Component cells have the same composition as 3J III-V solar cells but with only one active p-n junction [84] and can therefore allow the characterisation at the subcell level.

Another spectral index that quantifies the spectral conditions is the *Z* index. This index was first introduced by Meusel *et al*. [85] and it is also calculated by component isotypes; a value $Z > 0$ represents a blue-rich spectrum while a $Z < 0$ represents a red-rich spectrum [86]. The full procedure is described by Meusel *et al*. [85] and Peharz *et al*. [86]. It is remarkable that although this index is proven to be robust, it has not been widely used in the CPV industry; this might be due to the higher complexity compared to the other indices presented in this section.

2.2. Electrical models for CPV

Electrical modelling is the most important task when a power generation system is evaluated in terms of the performance. In this section, the electrical performance models of CPV cells and modules that are reported in literature are reviewed; other methods using 3D distributed models are not presented. Such models are complex to develop, they usually require knowledge of the cell's structure and are not widely used at the engineering level [87]; however they can be used for the optimisation of the cell structure (e.g. metal grid), calculation of the various solar cell's resistances [88] to name a few.

Rodrigo *et al.* [87], described the HCPV cell models based on the equivalent circuit of the multijunction cell. Two models were first described, the Single Exponential Model (SEM) and the Double Exponential Model (DEM); these models differ only on the number of diodes, one diode for the first one and two diodes for the latter (Figure 11).

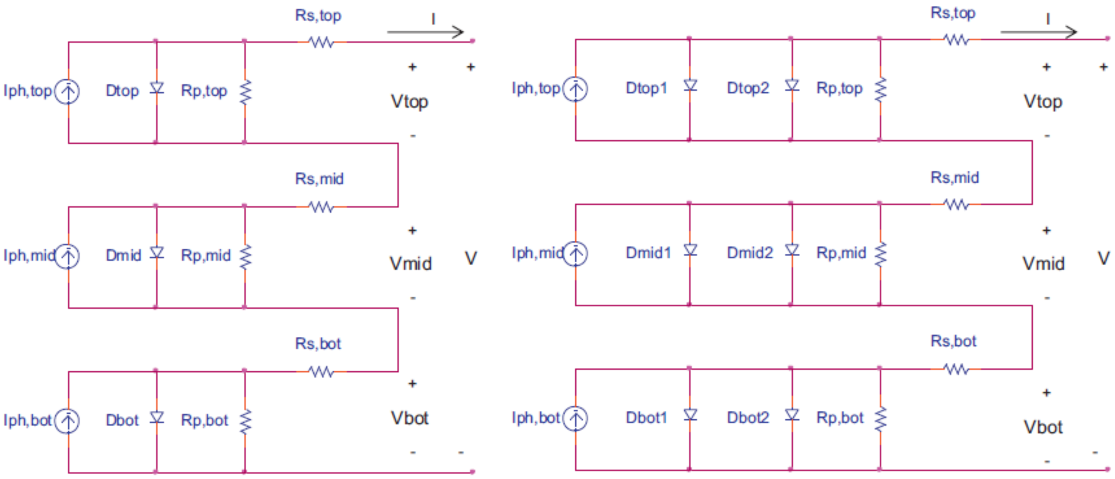

Figure 11: Equivalent circuit model for 3J solar cells for SEM (left) and DEM (right) [87].

The voltage and current output of the DEM can be calculated from:

$$V = \sum_{i=1}^{3} V_i \tag{11}$$

$$I_i = I_{sc,i} - I_{01,i}\left(e^{\frac{q\cdot(V_i+I\cdot R_{S,i})}{n_{1,i}\cdot k_B\cdot T_{cell}}}-1\right) - I_{02,i}\left(e^{\frac{q\cdot(V_i+I\cdot R_{S,i})}{n_{2,i}\cdot k_B\cdot T_{cell}}}-1\right) - \frac{\left(V_i+I\cdot R_{S,i}\right)}{R_{sh,i}} \tag{12}$$

where I_0 are the dark saturation currents, V is the voltage, I is the current, R_s is the series resistance, R_{sh} is the shunt (or parallel, i.e. R_p) resistance, n are the diode ideality factors, k_B is the Boltzmann constant and I_{SC} (or I_{ph}) is the short-circuit current.

In the SEM, the second part of equation (12) disappears and the *I*-*V* equation becomes:

$$I_i = I_{sc,i} - I_{0,i}\left(e^{\frac{q\cdot(V_i+I\cdot R_{S,i})}{n_i\cdot k_B\cdot T_{cell}}}-1\right) - \frac{\left(V_i+I\cdot R_{S,i}\right)}{R_{sh,i}} \tag{13}$$

The SEM is characterised by 5 parameters while the DEM by 7 parameters. Due to the fact that the subcells of a multijunction solar cell are monolithically connected and hence have only two electrical connections, the measurement of each subcell's parameters is difficult. These parameters are also affected by the operating conditions such as concentration and cell temperature. Various methods exist in literature that can be used to extract the parameters by using different assumptions [89-92].

Kinsey *et al.* [93, 94] used a simple diode model (by neglecting R_s and R_{sh} in equation (13)) to simulate the performance of 3J solar cells as a function of cell temperature, concentration ratio and spectrum. The spectrum dependence is incorporated by the calculation of the short-circuit current density (J_{sc}) at each subcell; therefore knowledge of the external quantum efficiency (EQE) of each subcell is required. EQE is defined as the ratio of the number of carriers collected by the cell to the number of incident photons. The short-circuit current density distribution for each subcell as a function of temperature is calculated using equation:

$$J_{sc,i}(T_{cell}) = \int_{\lambda_{i,\min}}^{\lambda_{i,\max}} \frac{q \cdot \lambda \cdot EQE_i(\lambda, T_{cell}) \cdot \eta_{opt}(\lambda) \cdot CR \cdot DNI(\lambda)}{h \cdot c} \cdot d\lambda, \tag{14}$$

where $\lambda_{i,min}$ and $\lambda_{i,max}$ correspond to the wavelength range of each subcell; λ is the wavelength of incidents photons, η_{opt} is the optical efficiency, h is Planck's constant and c is the speed of light in a vacuum.

Due to the in-series connection, the whole cell's short-circuit current density output is given by the minimum short-circuit current density of the three subcells, i.e.:

$$J_{sc} = \min(J_{sc,1}, J_{sc,2}, J_{sc,3}) \tag{15}$$

Therefore, the maximum power (P_{mp}) can be calculated by the product of J_{sc}, cell's area (A_{cell}), V_{oc} and fill factor (FF):

$$P_{mp} = J_{sc} \cdot A_{cell} \cdot V_{oc} \cdot FF \tag{16}$$

These parameters will be explained in Chapter 3.

While in the Kinsey *et al.* [93, 94] model, input spectra are required (either by spectroradiometer measurements or simulated using the Simple Model of the Atmospheric Radiative Transfer of Sunshine, SMARTS), Dominguez *et al.* [76] proposed a model that uses component cells instead. The model that Dominguez *et al.* [76] proposed, is translational for irradiance, spectrum and temperature and it does not require any *EQE* measurements. The authors reported average root mean square (RMS) errors between 0.53% to 0.85%, for a *CR* range from 100 to 700 suns and cell temperature between 25°C and 75°C.

Fernández *et al*. [95, 96] presented a simplified procedure based on a two subcells (top, middle) equivalent solar cell model to predict the maximum power of triple-junction solar cells. The bottom subcell (germanium) was considered to be only a voltage source since, due to the excess current under all conditions, it never contributes to the current output; the top and middle subcells contribute to it. Therefore, the *I*-*V* equation is given by:

$$V = \frac{n \cdot k_B \cdot T_{cell}}{q}\left[\ln\left(\frac{I_{sc,1} - I}{I_{0,1}}\right) + \ln\left(\frac{I_{sc,2} - I}{I_{0,2}}\right)\right] - I \cdot R_s \tag{17}$$

The equation is then corrected to take the R_{sh} into consideration. For simplification purposes, the series resistance, shunt resistance and diode's ideality factor are used for the whole device rather than individually for each subcell; these are then used to fit the model. Despite the model's simplicity to implement, it requires an indoor setup for *EQE* measurements at different temperatures, isotype solar cells and also a multi-source solar simulator to vary the spectrum.

The "Photovoltaic Array Performance Model" was developed by King *et al.* [97] (usually referred to as Sandia model) in order to fit the industrial needs. This model does not require any complicated experimental setup to obtain any of the parameters, but it is mainly based on outdoor measurements; a publicly available database was also created, that contains the necessary parameters for commercially available modules. Although it has been mainly used by the flat-PV industry, it proved to be versatile and accurate enough for CPV also. Therefore in this analysis we will refer to *DNI* rather than global irradiance. This model introduces a spectrum correction based on *AM*; *AOD* and *PW* also affect the spectrum but to a lesser extent. Therefore, this model does not require any measurements of the spectral irradiance, but instead, it uses a 4th order polynomial equation to account for the spectrum variation as a function of *AM*:

$$f(AM) = a_1 AM^4 + a_2 AM^3 + a_3 AM^2 + a_4 AM + offset \tag{18}$$

Then the "effective irradiance" (i.e. the irradiance that a PV cell corresponds to) is calculated by the following equation:

$$DNI_{eff} = \frac{DNI \cdot f(AM)}{DNI_{ref}} \tag{19}$$

Once the irradiance and ambient data are available, the *I-V* curve is calculated based on five points (see Figure 12); I_{sc}, open-circuit voltage (V_{oc}), maximum power point (at maximum power current, I_{mp}), I_x at $V_{oc}/2$ and I_{xx} at $(V_{oc}+V_{mp})/2$ where V_{mp} is the maximum power voltage. The following equations are used to calculate the I_{sc} and V_{oc} [87]:

$$I_{sc} = DNI_{eff} \cdot \left(I_{sc,ref} + \alpha_{I_{SC}} \cdot \left(T_{cell} - T_{cell,ref}\right)\right) \tag{20}$$

$$V_{oc} = V_{oc,ref} + \frac{n \cdot k \cdot T_{cell}}{q} \cdot \ln\left(DNI_{eff}\right) + \beta_{V_{OC}} \cdot \left(T_{cell} - T_{cell,ref}\right) \tag{21}$$

where α_{Isc} and β_{Voc} are the temperature coefficients of short-circuit current and open-circuit voltage respectively. The rest of the parameters in the *I-V* curve are easily obtainable using regression analysis.

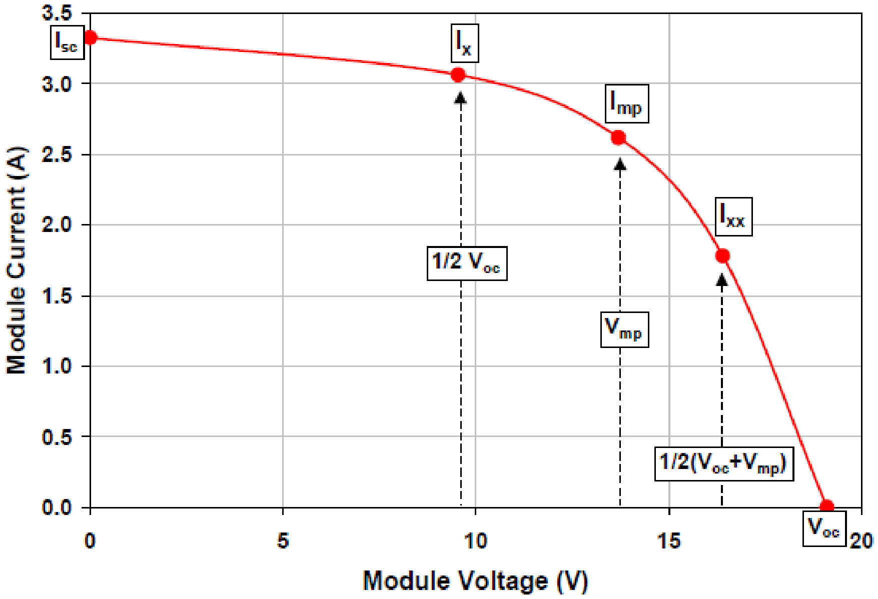

Figure 12: Illustration of how the Sandia "Photovoltaic Array Performance Model" calculates an *I-V* curve [97].

The Syracuse model developed by Ekins-Daukes *et al.* [98] was used by Chan *et al.* [55, 99] to calculate the performance of a CPV module in Japan. The model was extended to include *AOD* and *PW*; the latter was calculated by the relative humidity and ambient temperature (T_{amb}). The atmospheric parameters were then imported to the SMARTS2 (will be discussed also later) [100] to calculate the *DNI*. A function is incorporated to calculate the *EQE* at varying temperature. The model accounts for non-uniformities on the solar cell's surface. It was concluded that the modelling procedure can predict the energy yield of a CPV system within 2%. The Syracuse model simulates the operation of a solar cell using fundamental physics and therefore, a detailed knowledge of the composition and structure of the HCPV cells is required. In addition, outdoor measurements are required to obtain some of the parameters.

An integrated modelling approach has been introduced by Steiner *et al.* [101, 102] named YieldOpt. This model, combines the SMARTS2 [100] to simulate the input spectral irradiance, a ray tracing along with a FEA model to calculate the spectral optical efficiency as a function of temperature [103, 104] and a SPICE network model to calculate the *I-V* characteristics [105]. A function to calculate the *EQE* at any temperature is also included. YieldOpt also takes into account the alignment of the tracker and module. The P_{mp} prediction is then corrected to compensate for other losses that occur in the field; such as the losses due to inhomogeneous irradiance on the solar cell's surface. Steiner *et al.* [101, 102] reported very low normalised root mean square errors (*NRMSE*, between 2.6% and 3.9%). The disadvantage however of this integrated modelling approach is the requirement of a large set of outdoor equipment, the lack of information regarding the coupling of ray tracing with the FEA model and also the heat transfer within the module is not considered.

Artificial Neural Network (ANN) models have been also reported in literature for the estimation of maximum power of HCPV systems. The model by Rivera *et al.* [106] takes into account the *DNI*, T_{amb}, wind speed (*WS*) and spectrum. The spectral variations are characterised by the *APE* index and the coefficients of the ANN were taken from outdoor measurements. Almonacid *et al.* [107] used a feed-forward neural network trained with the Levenberg-Marquardt back-propagation algorithm and their model considered the spectral influences by taking into account the *AM* and *PW* and therefore there is no requirement for a spectroradiometer. In addition, the *DNI*, T_{amb} and *WS* are taken into account; similarly to Rivera *et al.* [106], the coefficients of the ANN were also taken from outdoor measurements. The main disadvantage of ANN models is the difficulty to adapt in the industry level. A low *RMSE* value of 3.29% was reported by Almonacid *et al.* [107].

A maximum power prediction model has been proposed by García-Domingo *et al.* [81] taking into account the *DNI*, T_{amb}, *WS* and the spectrum based on the *SMR1* index. The model calculated the normalised short-circuit current (or spectral factor *SF* as mentioned earlier) and the normalised maximum power. The *SF* was calculated based on 2nd order polynomial equations as a function of *SMR1* and a T_{amb} range; 5°C - 20°C, 20°C - 30°C and 30°C - 45°C. From the *SF* the normalised maximum power ($P_{mp,norm}$) was calculated and then the equation for the P_{mp} was given as:

$$P_{mp} = P_{mp,norm} \cdot DNI \cdot P_{mp,ref} \Big/ DNI_{ref} \tag{22}$$

The model was validated against outdoor measurements offering a relatively good agreement with a maximum *RMSE* of 5.27%.

A simplified model that accounts for the atmospheric parameters was introduced by Fernández *et al.* [108], extending from [109] which only included an *AM* correction. The *DNI*, *AM*, *AOD* and solar cell temperature (T_{cell}) were used as inputs to the new model. The T_{cell} in turn, is given as a function of T_{amb}, *DNI* and *WS* (discussed later). The maximum power of a HCPV module is given as:

$$\begin{aligned} P_{mp} = {} & \frac{P_{mp,ref}}{DNI_{ref}} \cdot DNI \cdot \left[1-\zeta \cdot \left(T_{cell}-T_{cell,ref}\right)\right] \cdot \left[1-\varepsilon \cdot \left(AM-AM_{U}\right)\right] \\ & \cdot \left[1-\varphi \cdot \left(AOD_{550}-AOD_{550,U}\right)\right] \end{aligned} \tag{23}$$

where ζ is the temperature coefficient of maximum power, ε is the *AM* coefficient of maximum power, φ is the *AOD* coefficient of maximum power, and AM_U, $AOD_{550,U}$ are defined as the umbral *AM* and *AOD* at 550 nm respectively. The umbral parameters are dependent on the module design [110]. An *RMSE* value of 2.67% was reported which is a very good agreement compared to the 3.53% and 4.96% *RMSE* of the models that take into consideration the *DNI*, T_{cell}, *AM* and *DNI*, T_{cell} respectively.

A comparison of the CPV electrical models reviewed in this section is presented in Tables 1 and 2; it is extended from a comparison table published by Rodrigo *et al.* [87].

Models	Equivalent circuit	Kinsey	Domínguez	Fernández (2013)	Sandia
Required inputs					
Concentration ratio	√	√	√	√	√
Cell temperature	√	√	√	√	√
Incident spectrum	√	√			
Subcells photocurrents	√*	√	√	√	
Air Mass	√*				√
Aerosol Optical Depth	√*				
Precipitable Water	√*				
Material parameters					
Optical efficiency dependent on temperature					
EQE dependent on temperature					
Advantages					
Provides the whole I-V curve	√		√	√	
Spectral effects quantified with high accuracy	√	√	√	√	
Explicit equations		√	√	√	√
Algorithms for extracting the model parameters are easy to implement		√		√	√
It does not require knowing in detail the incident spectrum			√	√	√
It does not require indoor characterisation of the solar cell					√

Table 1: Comparison of CPV electrical models; table extended from data published by Rodrigo *et al.* [87].

* If equation (14) and spectral data are used for the short-circuit current calculation.

Models (continues from Table 1**)**	Syracuse	YieldOpt	García-Domingo	Fernández (2015)	Almonacid
Required inputs					
Concentration ratio	√	√	√	√	√
Cell temperature	√	√		√	√
Incident spectrum	√	√	√		
Subcells photocurrents	√	√			
Air Mass	√	√		√	√
Aerosol Optical Depth	√	√		√	
Precipitable Water	√	√			√
Material parameters	√				
Optical efficiency dependent on temperature		√			
EQE dependent on temperature	√	√			
Advantages					
Provides the whole I-V curve	√	√			
Spectral effects quantified with high accuracy	√	√		√	
Explicit equations			√	√	
Algorithms for extracting the model parameters are easy to implement			√	√	
It does not require knowing in detail the incident spectrum			√	√	√
It does not require indoor characterisation of the solar cell	√		√	√	√

Table 2: Comparison of CPV electrical models; table extended from data published by Rodrigo *et al.* [87] (continues from Table 1).

2.3. Solar cell temperature prediction methods

3J solar cells exhibit a negative performance with increasing operating temperature due to the linear decrease in V_{oc} and FF [111]. Therefore, knowing the solar cell's operating temperature is important for the performance evaluation of HCPV systems [112]. The direct measurement of the solar cell's temperature in HCPV systems however, is difficult due to the concentrated irradiance and the geometry of such systems. Hence, indirect methods have to be applied in order to estimate the solar cell's temperature.

Rodrigo *et al.* [113] who presented a comprehensive review of the existing methods for the solar cell's temperature calculation, categorised the methods based on measurements of the:

1) Electrical parameters
2) Heat sink temperature
3) Atmospheric parameters.

The IEC 60904-5 [114] contains a method to determine the equivalent cell temperature (ECT) based on measurements of the electrical parameters:

$$T_{cell} = \frac{V_{oc} - V_{oc,ref} + \beta_{Voc,ref} \cdot T_{cell,ref}}{N_s \cdot \left(\frac{n \cdot k_B}{q} \right) \cdot \ln \left(\frac{DNI}{DNI_{ref}} \right) + \beta_{Voc,ref}} \tag{24}$$

where N_s is the number of cells connected in series inside the module. King *et al.* [97] however, reported on a modified equation where the use of a pyrheliometer is avoided:

$$T_{cell} = \frac{V_{oc} - V_{oc,ref} + \beta_{Voc,ref} \cdot T_{cell,ref}}{N_s \cdot \left(\frac{n \cdot k_B}{q} \right) \cdot \ln \left(\frac{I_{sc}}{I_{sc,ref}} \right) + \beta_{Voc,ref}} \tag{25}$$

This equation is known as the V_{oc}-I_{sc} method and is also included in the procedure for translation of outdoor *I-V* measurements to CSTC introduced by Muller *et al.* [115]. Ju *et al.* [116] later introduced an improvement of the V_{oc}-I_{sc} method by introducing a correction for β_{Voc} with concentration:

$$\beta_{Voc}(CR) = \beta_{Voc,ref} + \frac{n \cdot k_B}{q} \cdot \ln\left(CR\right) \tag{26}$$

So if *CR* is determined from King *et al.* [97] as:

$$CR = \frac{I_{sc}}{I_{sc,ref} + \alpha_{Isc,ref} \cdot \left(T_{cell} - T_{cell,ref}\right)} \tag{27}$$

then the improved V_{oc}-I_{sc} method by Ju *et al.* [116] becomes:

$$T_{cell} = \frac{\left(V_{oc} - V_{oc,ref} - \frac{n \cdot k_B \cdot T_{cell,ref}}{q} \cdot \ln(CR) \right)}{\left(\beta_{Voc,ref} + \frac{n \cdot k_B}{q} \cdot \ln(CR) \right)} + T_{cell,ref} \tag{28}$$

Peharz *et al.* [117] also proposed a method to calculate the T_{cell} based on indoor experiments using infrared light to heat up the modules:

$$T_{cell} = \frac{V_{oc} - \alpha_1 \cdot \ln(I_{sc}) - \alpha_2}{\alpha_3 \cdot \ln(I_{sc}) + \alpha_4} \quad \textbf{(29)}$$

where the coefficients α_1 to α_4 can be derived by regression analysis. However, in order to obtain the coefficients, the module has to be characterised indoors using a solar simulator varying the intensity and a heat source to vary the cell temperature; this is not a straightforward procedure.

A method that uses easily obtainable parameters was proposed by Fernández *et al.* [112]. First, a linear regression equation was proposed to calculate the V_{oc} as a function of DNI and T_{cell} and by solving for T_{cell} then:

$$T_{cell} = \frac{V_{oc} - \alpha_1 \cdot DNI - offset}{\alpha_2} \quad \textbf{(30)}$$

This method is simple and exhibits a high accuracy, especially at high temperatures with a mean relative error of 0.45%.

Only a few solar cell operating temperature prediction methods have been reported in literature based on measurements of heat sink temperature; this is mainly due to the external factors that can affect the measurement, i.e. the wind speed and direction, the solar tracker position, the positioning of the temperature sensor, etc. The methods proposed by King *et al.* [97] and Instituto de Sistemas Fotovoltaicos de Concentración (ISFOC) [118] assume one-dimensional (1D) heat transfer through the materials that constitute the receivers/modules. The former is given as:

$$T_{cell} = T_{HS} + \frac{DNI}{DNI_{ref}} \Delta T \quad \textbf{(31)}$$

where T_{HS} is the measured heat sink temperature and ΔT is the temperature difference between the solar cell and the heat sink at DNI_{ref} = 1000 W/m^2. The T_{HS} in this case is the temperature of a flat back-plate surface/heat sink and not a finned heat sink. In the ISFOC [118] method, the operating cell temperature is calculated by:

$$\begin{gathered} \rho = \frac{T_{cell} - T_{HS}}{DNI} \Rightarrow \\ \Rightarrow T_{cell} = T_{HS} + \rho \cdot DNI \end{gathered} \quad \textbf{(32)}$$

where [113]:

$$\rho = \eta_{opt} \cdot CR \cdot R_{th} \quad \textbf{(33)}$$

and [113]:

$$R_{th} = \sum_i \frac{t_i}{k_i} \tag{34}$$

where t_i and k_i is the thickness and thermal conductivity of each i layer (behind the solar cell) respectively. Therefore, the knowledge of each layer's material and dimensions are required for this method. Although these methods exhibited good accuracy, the disadvantage is that they cannot be applied to modules with a finned heat sink since they assume 1D thermal heat conduction.

The method proposed by Muller *et al.* [119] is based on thermal transient measurements (TTM) where the module is initially covered/shuttered and when uncovered the transients of V_{oc} are measured and therefore the operating cell temperature is measured by:

$$T_{cell}(t) = T_{HS,0} + \frac{\left(V_{oc,\max} - V_{oc}(t)\right)}{\beta_{Voc}} \tag{35}$$

where $T_{HS,0}$ is the heat sink temperature when the module is covered. An example is illustrated in Figure 13 after uncovering the module. The dashed lines are calculated by equation (35). The disadvantage of the TTM method is that the measurements have to be very fast and that it has to be applied to each CPV module technology independently. In addition, Muller *et al.* [115] suggest to repeat the experiment multiple times in order to reduce the uncertainty when temperature coefficients are evaluated.

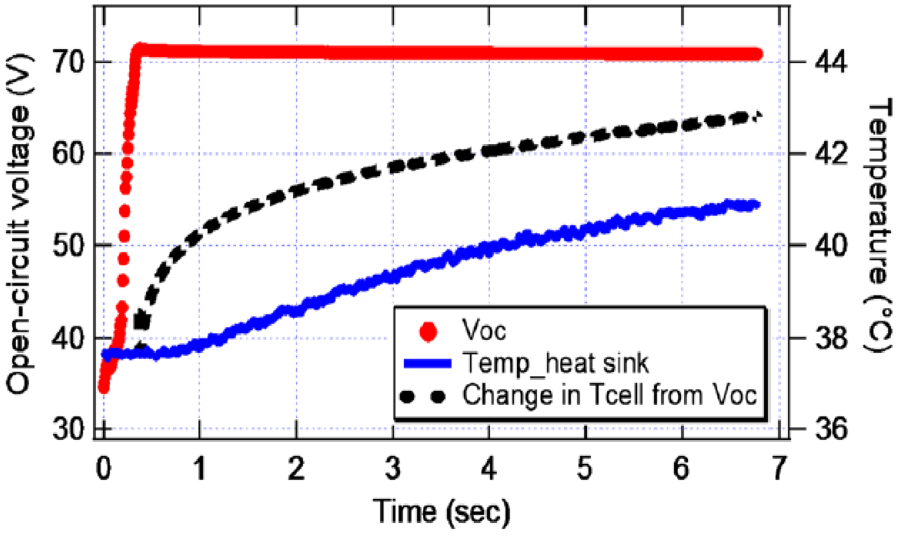

Figure 13: Thermal transient method (TTM) data measured by Muller *et al.* [115, 119].

Although the aforementioned methods for the solar cell's operating temperature calculation require some electrical or temperature measurements, the methods based on atmospheric parameters can estimate the T_{cell} using only available meteorological data. Almonacid *et al.* [120] presented a simple formula to calculate the solar cell temperature as a function of T_{amb}, *DNI* and *WS* i.e.:

$$T_{cell} = T_{amb} + \alpha_1 \cdot DNI + \alpha_2 \cdot WS \tag{36}$$

where the coefficients α_1 and α_2 are calculated based on regression analysis with outdoor data. The method showed an overestimation at low solar cell temperatures, an underestimation at medium T_{cell} and the best agreement at high temperatures. When the relative error was compared against the *DNI*, it was found that the average error for $DNI < 400\ \text{W/m}^2$ was 4.8% and for $DNI > 400\ \text{W/m}^2$ the average error was -0.17%. Hornung *et al.* [121] on the other hand used the same parameters and assumed that the T_{cell} or T_{lens} is proportional to *DNI* with an exponential influence on *WS*:

$$T_{cell} = T_{amb} + m \cdot \left(e^{\left(-\frac{WS}{2 \cdot WS_0}\right)} + c \right) \cdot DNI \tag{37}$$

where *m*, WS_0, *c* are calculated for cell and lens separately through regression analysis.

Fernández *et al.* [122] presented an ANN method to estimate the cell temperature using atmospheric parameters and compared with IEC 60904-5 [114], ISFOC [118] and linear [120] methods presented earlier in this section. The ANN used the Levenberg-Markquard algorithm and the T_{cell} was calculated as a function of T_{amb}, *DNI* and *WS* like the other methods. The comparative analysis showed that all methods performed well with the ISFOC method offering the highest accuracy (*RMSE* = 1.7°C). The *RMSE* values for IEC 60904-5, linear and ANN were found to be 2°C, 4.3°C and 3.24°C respectively. Rodrigo *et al.* [113] and Fernández *et al.* [122] concluded that the methods based on measurements on heat sink and/or electrical parameters provide higher accuracy compared to the methods based on the atmospheric parameters.

The only validated method available in literature that estimates the T_{cell} at maximum power point is presented by Fernández *et al.* [123]. This method is based on measurements on heat-sink and the electrical characteristics:

$$T_{cell@P_{mp}} = T_{HS} + R_{th} \cdot \left(DNI \cdot CR \cdot \eta_{opt} - \frac{P_{mp}}{N \cdot A_{cell}} \right) \tag{38}$$

where *R* is the thermal resistance between solar cell and the back surface of the module and *N* is the number of solar cells in the module. This method allows the T_{cell} estimation under actual conditions where the electrical energy is harvested. Fernández *et al*. [123] reported that the ΔT_{cell} between open-circuit and maximum power point conditions can be up to 21°C. The accuracy of the method was validated with a very good agreement of $RMSE$ = 0.96°C.

2.4. Passive thermal management in CPV

Due to the concentrated heat fluxes that occur in CPV receivers, it is crucial to investigate the thermal management and cooling mechanisms that will allow safe operating temperatures. Various comprehensive investigations have been performed on the cooling and thermal management of CPV receivers [124-126]; according to Royne *et al*. [40], who presented an extensive overview on different cooling techniques, passive cooling can be sufficient for single cell geometries for solar flux up to 1000× assuming that there is a large area available below the cell for a heat sink. For densely packed cells configuration and for concentrations greater than 150×, active cooling with a thermal resistance less than 10^{-4} $(m^2 \cdot K)/W$ is required [40]. The main difference between passive and active cooling is that passive does not require any electrical or mechanical power as an input and that the heat exchange (or cooling) is achieved mainly through natural convection. Because the vast majority of the commercial HCPV systems use passive cooling (e.g. Suncore [127] and Semprius [128]), this overview will not include any active cooling techniques [129-136].

A good representation of how the solar flux is converted in electrical and thermal power was presented by García *et al*. [137] in Figure 14. DNI of 1000 W/m^2 is incident on a Fresnel lens surface of 0.0432 m^2 (43.2 W). With an optical efficiency of 80%, 34.56 W are transmitted and focus on the secondary optical element with an optical efficiency of 92%. Therefore, 31.8 W solar power is available; assuming an electrical conversion efficiency (η_{cell}) of 38%, 12.08 W are transformed into direct current (DC) electrical power and the remaining 62% is transformed into heat with 19.72 W of power. A similar way to calculate the heat power is by:

$$P_{heat} = DNI \cdot CR \cdot \eta_{opt1} \cdot \eta_{opt2} \cdot A_{cell} \cdot (1 - \eta_{cell}) \tag{39}$$

where assuming CR = 432× and A_{cell} = 1 cm^2 gives the same result.

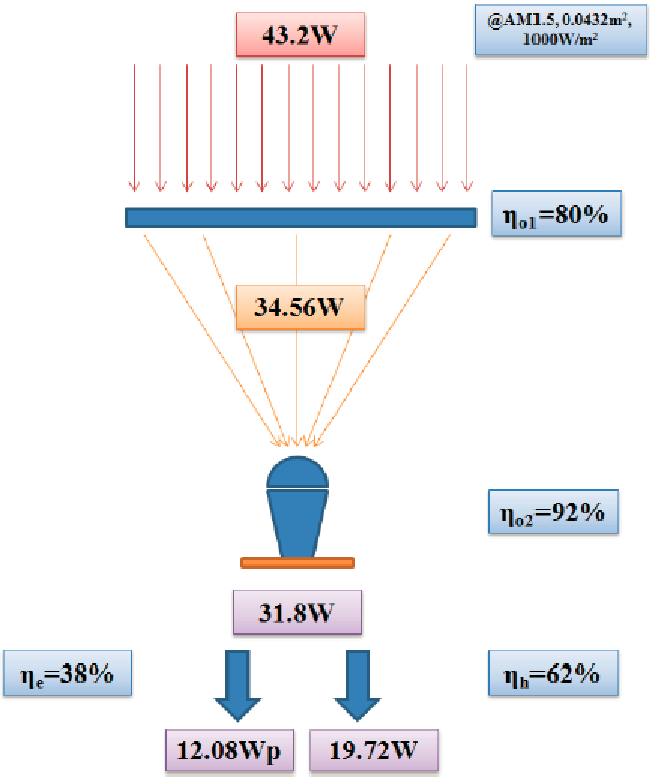

Figure 14: Representative example of how solar flux converts to electrical and thermal power in a CPV system [137].

A straightforward approach of reducing the cell temperature is by spreading the heat. Araki *et al.* [37] used a Fresnel lens to focus the direct sunlight onto a solar cell's surface by a factor of 500×. The solar cell was placed on a printed epoxy and copper sheet and then onto a 3 mm thick normal grade aluminium plate to spread and dissipate the heat (Figure 15). The outdoor experiments showed a cell temperature increase with a ΔT of only 18°C between ambient and cell temperature. A good thermal contact between the cell and the heat spreader (i.e. low thermal resistance) is critical to keep the solar cell's temperature as low as possible.

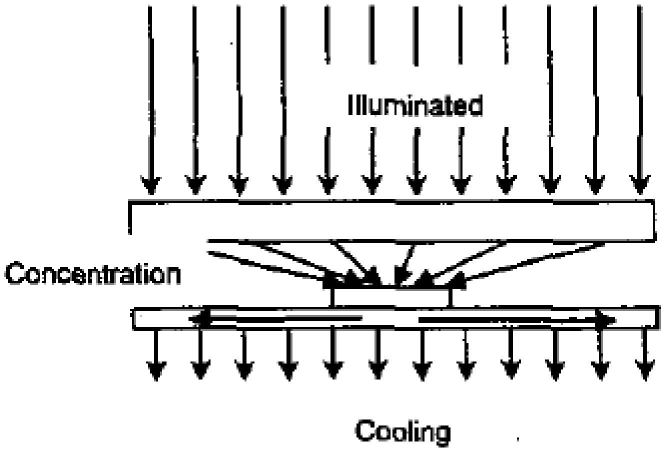

Figure 15: Passive cooling by means of heat spreading presented by Araki *et al.* [37].

Minano *et al.* [138] used gallium arsenide (GaAs) solar cells under a *CR* = 1000× placed on an aluminium truncated cone heat sink and a plate with the same area as the concentrator's entry aperture (Figure 16). The conduction through the dielectric material was not considered and a convective heat transfer coefficient of 5 W/(m^2·K) was assumed in all free surfaces. Minano *et al.* [138] pointed out the importance of using small size solar cells in order to achieve lower heat generation and hence temperatures.

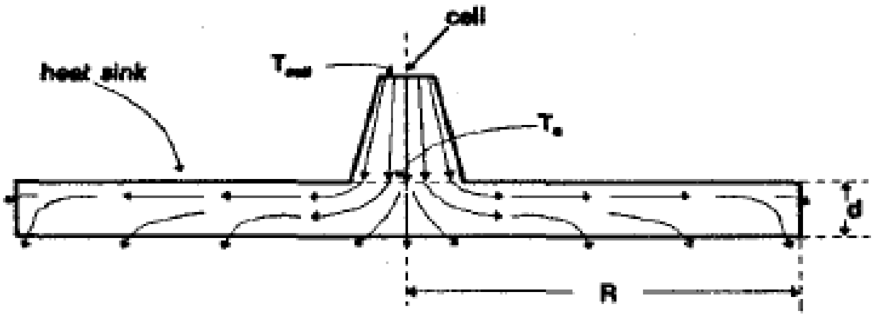

Figure 16: **An aluminium truncated cone bonded on an aluminium plate with the same area as the entry aperture [138].**

Kuo *et al.* [36] developed a plug-and-play solar engine that consisted of a solar cell coupled to a finned heat exchanger by a micro heat pipe (see Figure 17). A thermal resistance of 1.5°C/W was reported and the 3J solar cell temperature was maintained below 57°C under 800 suns (T_{amb} = 25°C). The authors highlighted the advantage of this design being able to change a faulty receiver instead of the whole module in a similar way of changing a light bulb.

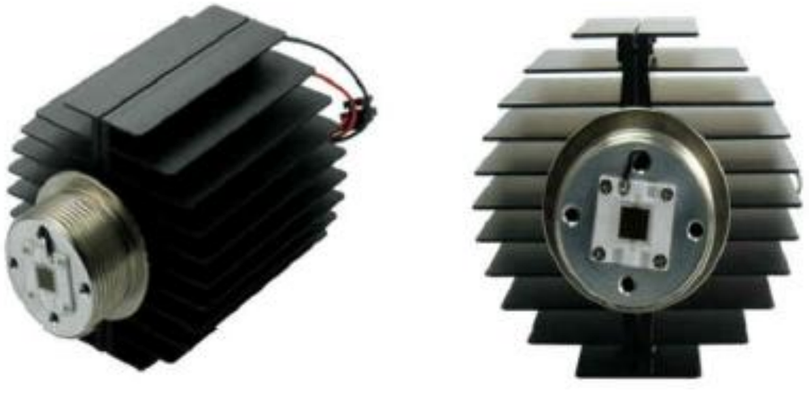

Figure 17: **The NeoPac 10W Solar Engine [36].**

Chou *et al.* [139] modelled the thermal management of a HCPV using FEA in ANSYS. Using an aluminium plate as a heat sink, Chou *et al.* [139] calculated a maximum solar cell temperature of 69.02°C and a maximum plate temperature of 66.89°C for a thermal resistance of 4.67°C/W, ambient temperature of 34°C, wind velocity of 4.2 m/s under an optical concentration ratio of 380× (i.e. after optical losses). A constant solar cell conversion efficiency was calculated at 36.5%. Due to the complexity in directly measuring the cell temperature, the temperature of the aluminium plate was compared with the outdoor measurements. A good agreement was reported with a maximum and minimum ΔT of 6.07°C and 0.07°C respectively.

A thermal model for single concentrator solar cells was designed and tested by Min *et al.* [38]. A black coated aluminium plate was used as a heat sink which was 700 times larger than the 3J solar cell's size (3 x 3 mm^2) in order to maintain the temperature below 40°C and achieve a high conversion efficiency; the concentration ratio was 400×. The ΔT between simulated and measured cell temperature was 3°C. Similarly to Chou *et al.* [139], a constant conversion efficiency was assumed (30%).

Jaus *et al.* [140] established a heat transfer model that was used to predict the thermal behaviour of a FLATCON®-type CPV module; this was used to improve the reliability, performance and geometric design (in terms of material usage). The FEA model of the CPV system concentrated solar radiation using a Fresnel lens and was passively cooled. Due to the symmetry in geometry and also to save computation time, "only the 1/4 or even 1/8" of the geometry was used for the modelling. A Gaussian inhomogeneous irradiance distribution on the solar cell's surface was also taken into consideration. The meshing was performed according to the geometric dimensions of each component of the module. The results were given as a function of the edge length of the heat sink and the cell temperature varied from circa 86°C to 97°C. Temperature differences of around 8°C were also observed inside the module.

The applicability of light weight silicon micro-finned heat sinks for CPV systems was investigated by Micheli *et al.* [141]. A Cassegrain-based system (see Figure 18) was used for a CR = 500×; such designs do not limit the heat sink's size [141]. A 3J solar cell with an active area of 3 x 3 mm^2 was used for the simulations; therefore the generated heat was 2.20 W at maximum power point conditions (DNI = 1000 W/m^2, T_{amb} = 25°C, cell efficiency 42.5%) and 3.83 W at open-circuit conditions (cell efficiency at 0%, i.e. no electrical power harvested). A 5 x 5 cm^2 silicon wafer was selected and the most effective fin geometry was determined based on experimental measurements. A maximum temperature of 78.8°C was predicted for a flat silicon wafer and 70.4°C for a silicon finned surface. The mass-specific power ratio (i.e. ratio of electrical power output to weight) was used to compare the design with other CPV modules equipped with heat sinks. It was found that the mass-specific power ratio was enhanced from around 60 W/kg to more than 300 W/kg. This application could potentially reduce the weight of CPV modules and hence the load on the solar tracker, improving the tracking accuracy and therefore the electrical power output.

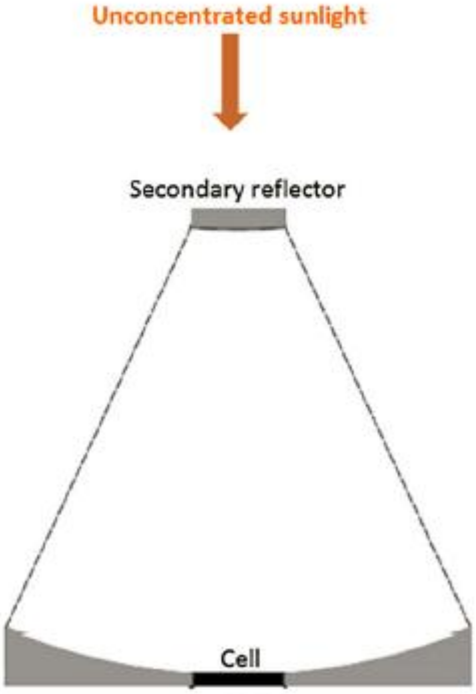

Figure 18: CPV system based on Cassegrain mirror optics [141].

2.5. CPV power rating procedures

The rating procedures of PV devices and modules are very important for the comparison of the technologies [142]. HCPV modules can be either rated indoors and outdoors (by translating outdoor *I-V* measurements to CSTC [115]) under Concentrator Standard Test Conditions (CSTC, i.e. AM1.5D, DNI = 1000 W/m^2 and T_{cell} = 25°C) or outdoors under Concentrator Standard Operating Conditions (CSOC, i.e. AM1.5D, DNI = 900 W/m^2, T_{amb} = 20°C and wind speed WS = 2 m/s).

The CSOC and CSTC are evaluated according to the IEC 62670-01 [143] (Concentrator Photovoltaic (CPV) Performance Testing - Standard Conditions) and IEC 62670-3 [144] (Concentrator Photovoltaic (CPV) Performance Testing - Performance

Measurements and Power Rating) [145] that is still in the draft stage [115]. CSOC and CSTC must be consistent with the AM1.5D spectral irradiance described in IEC 60904-3 [146]. The CSOC can be evaluated using the multiple regression equation of power from ASTM E2527-09 [147] as a function of *DNI*, T_{amb} and *WS*. The CSTC power rating can be determined indoors using a solar simulator or outdoors by the translation of outdoor measurements according to the method described by Muller *et al.* [115].

The ASTM E2527-09 [147] uses a simple equation to calculate the P_{CSOC}:

$$P_{CSOC} = DNI \cdot \left(\alpha_1 + \alpha_2 \cdot DNI + \alpha_3 \cdot T_{amb} + \alpha_4 \cdot WS\right) \tag{40}$$

where the coefficients α_1 το α_4 are calculated using regression analysis on outdoor measurements. As can be seen, the spectral dependence is not taken into consideration in ASTM E2527-09.

On the other hand, the P_{CSOC} equation suggested by Steiner *et al.* [145] using the "averaging method" is described by:

$$P_{CSOC} = \frac{\left(\sum_i P_i \cdot \frac{900}{DNI_i}\right)}{N} \tag{41}$$

where *P* is the measured power and *N* is the number of measurements. The "translation method" suggested by the same authors is the same as equation (41), with the *DNI* being multiplied (i.e. corrected) by the *SMR2*, so that the effect of *PW* is considered:

$$P_{CSOC} = \frac{\left(\sum_i P_i \cdot \frac{900}{DNI_i \cdot SMR2}\right)}{N} \tag{42}$$

Peharz *et al.* [117] introduced two multi-linear regression equations for HCPV modules that he also used for rating purposes as a function of *DNI* and spectrum using the spectral index *Z*:

$$P_{mp} = c_{DNI} \cdot DNI + c_{Z2} \cdot Z + c_T \cdot T_{cell} + offset \tag{43}$$

$$P_{mp} = c_{DNI} \cdot DNI + c_{Z2} \cdot Z^2 + c_z \cdot Z + c_T \cdot T_{cell} + offset \tag{44}$$

The reason for the second regression equation is because one of the modules that Peharz *et al.* [117] tested had a maximum efficiency at $Z = -0.015$. The calculations were based on two conditions:

1) $DNI = 850$ W/m^2, $Z = 0$, $T_{cell} = 25$°C

2) $DNI = 850$ W/m^2, $Z = 0$, $T_{cel} = 60$°C

Lastly, Steiner *et al.* [145] also reported on a multi-linear regression method based on the following mathematical equations published in [102] where the P_{CSOC} is estimated by:

$$P_{CSOC}\left(DNI,Z,T_{amb}\right)=I_{sc}\left(DNI,Z,T_{amb}\right)\cdot V_{oc}\left(DNI,Z,T_{amb}\right)\cdot FF\left(DNI,Z,T_{amb}\right) \tag{45}$$

where the spectral index Z is:

$$Z=1-\frac{2}{1+SMR} \tag{46}$$

The last method however, is considered to be relatively too complex to be adapted by the industry. It is preferable to use more simplified methods using stricter filtering criteria.

For the CSTC method described by Muller *et al.* [115], i.e. by the translation of outdoor *I-V* measurements, it is necessary to know the operating T_{cell} in order to correct to standard test conditions. Therefore the I_{sc}-V_{oc} method is used. A relative factor has been proposed for voltage correction [115]:

$$f_{V_{OC}}=1-\frac{n\cdot k\cdot T_{cell}}{q\cdot V_{oc,meas}}\ln\left(\frac{DNI}{1000}\right) \tag{47}$$

This relative factor is then used for the efficiency calculation under CSTC [115]:

$$\eta_{\mathrm{mod},CSTC}=f_{V_{oc}}\cdot\left(\eta_{\mathrm{mod},meas}-\delta\cdot\left(T_{cell}-T_{cell,ref}\right)\right) \tag{48}$$

where δ is the efficiency temperature coefficient. Therefore, the P_{CSTC} can be then calculated by:

$$P_{CSTC}=DNI_{ref}\cdot A_{\mathrm{mod}}\cdot CR\cdot\eta_{CSTC,avg}\Big/100 \tag{49}$$

where the $DNI_{ref} = 1000$ W/m^2 at CSTC.

2.6. Summary

This chapter presented a detailed literature review on the subjects that are concerning this thesis. Firstly, the spectral indices that can characterise either the spectral irradiance or the effect of it on a PV device are described and then the electrical models reported in literature for CPV systems are presented. The cell temperature measurement of CPV systems is not trivial and therefore, all the indirect methods for the estimation of the solar cell temperature are analysed. The thermal management in CPV and some cooling techniques follow this review chapter and finally, the CPV power ratings for CSTC and CSOC are described.

Based on the literature review, the present work has been undertaken for the development of an integrated modelling procedure that accounts for the spectral, electrical and thermal performance of CPV systems. The influence of the atmospheric parameters on the CPV performance is also evaluated. The procedure is validated experimentally using a HCPV monomodule in a test site in Albuquerque, NM. The influence of spectral variation is also evaluated outdoors in terms of the monomodule's chatacterisation but also for its power rating.

Chapter 3: Materials and methods

This chapter begins with the description of the mathematical equations of the numerical models used in Chapters 4 to 6. These models investigate the impact of the atmospheric parameters on the spectral, electrical and thermal performance of a III-V 3J solar cell. The Simple Model of the Atmospheric Radiative Transfer of Sunshine (SMARTS2) is also described. In addition, a description of the integrated modelling is given. Finally, the experimental setup and equipments used to carry out the work presented in Chapters 5 and 7 are also presented.

This chapter includes material from the following publications [148-150]:
M. Theristis, and T. S. O’Donovan, "Electrical-thermal analysis of III-V triple-junction solar cells under variable spectra and ambient temperatures", *Solar Energy*, vol. 118, 2015, pp. 533-546
M. Theristis, and T. S. O'Donovan, "An integrated thermal electrical model for single cell photovoltaic receivers under concentration", in *15th International Heat Transfer Conference*, Kyoto, Japan, 2014.
M. Theristis, N. Sarmah, T. K. Mallick, and T. S. O'Donovan, "Design and Numerical Analysis of Enhanced Cooling Techniques for a High Concentration Photovoltaic (HCPV) System," in *27th European Photovoltaic Solar Energy Conference and Exhibition*, Frankfurt, Germany, 2012, pp. 260-265.

3.1. Simple Model of the Atmospheric Radiative Transfer of Sunshine (SMARTS2)

In order to investigate the spectral performance of a MJ solar cell based on measured data, a relatively expensive spectroradiometer is required. Besides the high cost, spectroradiometers also present a typical 5-10% uncertainty [151]. A cost effective way to accurately evaluate the spectral performance is by generating solar spectra using the SMARTS2 [100]. This robust and free model was developed by Dr. Christian Gueymard for the NREL and it is able to predict the spectral irradiance under clear-sky conditions based on atmospheric inputs. In addition, SMARTS2 was used to generate the reference spectra AM1.5 (American Society for Testing and Materials, ASTM G173-03 [152]) seen in Figure 19. The integration of the spectral irradiance at global air mass 1.5 (AM1.5G) and direct air mass 1.5 (AM1.5D) results in 1000 W/m^2 and 900 W/m^2 respectively. The AM1.5G is used for flat-plate PV systems while AM1.5D is used for CPV applications. AM1.5D includes the circumsolar component also [153] (aureole around the solar disk). The specified atmospheric conditions for the generation of AM1.5 spectra are given in Table 3. SMARTS2 uses the *AOD* at 500 nm as an input and the *AOD* at other wavelengths is calculated internally by the model. Therefore, the *AOD* values in this thesis, are specified at 500 nm.

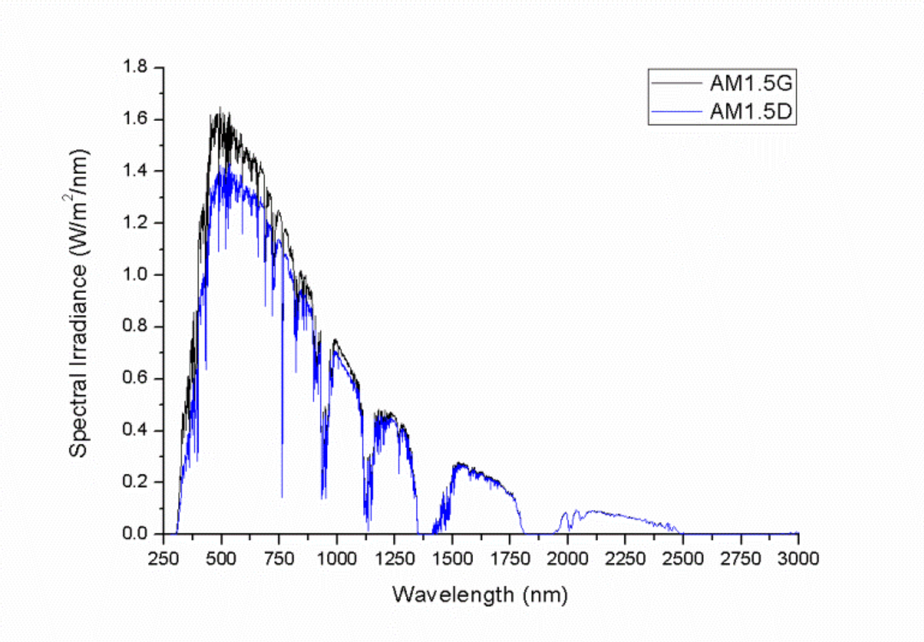

Figure 19: **Standard AM1.5 ASTM G173-03 solar spectra for terrestrial applications.**

Specified atmospheric parameters	Value
AM	1.5
AOD at 500 nm	0.084
PW	1.42 cm

Table 3: **Specified atmospheric parameters used for the generation of the AM1.5 ASTM G173-03 spectra.**

3.2. Electrical Model (EM)

A single-diode model was used to model the electrical characteristics of a 3J solar cell in Matlab® [154]. According to Segev *et al.* [89], the one-diode equivalent circuit model is adequate to describe a 3J solar cell in practical applications. Each junction of the solar cell can be represented by an equivalent circuit model and therefore, by connecting the three junctions in series, the one diode equivalent circuit model for a 3J solar cell can be obtained (Figure 20). This model differs from the two diodes in the number of diodes that describe the saturation current. In the single-diode model, the diode represents recombination in both the depletion and quasi-neutral regions [89].

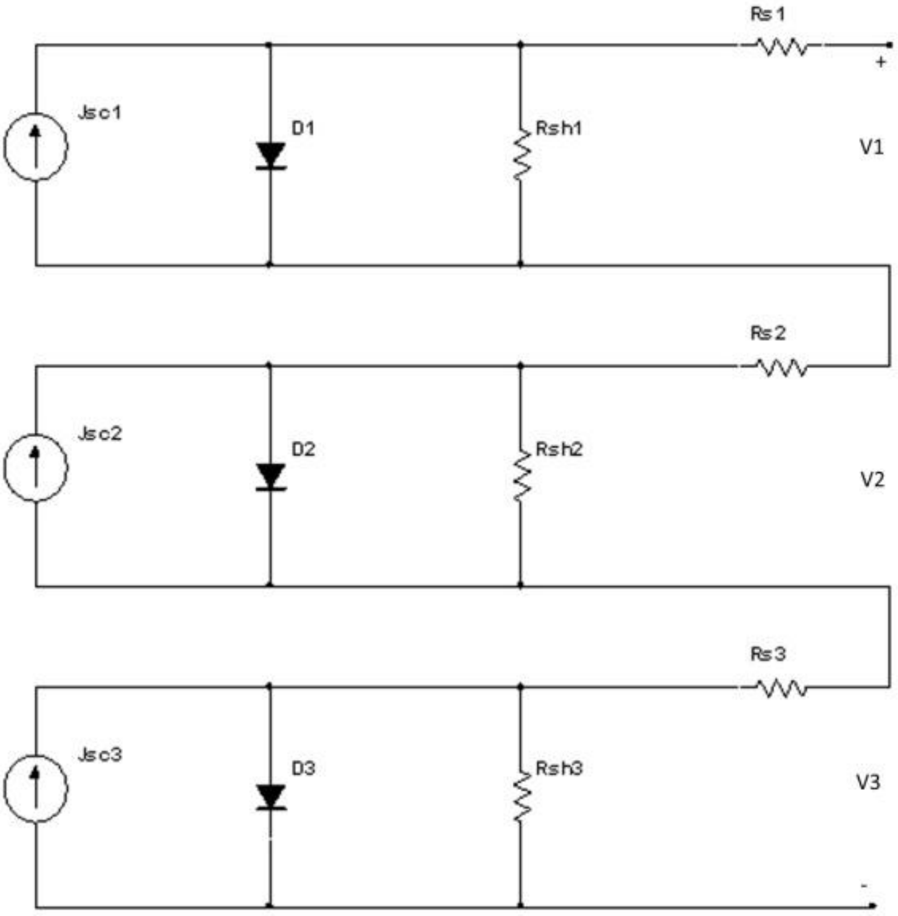

Figure 20: **One-diode equivalent circuit 3J cell model [89].**

If the shunt resistances ($R_{sh,i}$) are sufficiently large to be neglected in equation (13), the current density-voltage (*J*-*V*) relationship is given by

$$J_i(V) = J_{0,i}(T_{cell}) \cdot \left(e^{\frac{q(V_i - J_i \cdot A_{cell} \cdot R_s)}{n_i \cdot k_B \cdot T_{cell}}} - 1 \right) - J_{SC,i}(T_{cell}), \tag{50}$$

The dark saturation current density is strongly affected by temperature and is described as:

$$J_{0,i}(T_{cell}) = k_i \cdot T_{cell}^{(3+\gamma_i/2)} e^{(-E_{g,i}(T_{cell})/n_i \cdot k_B \cdot T_{cell})}, \tag{51}$$

where k and γ are constants. The E_g decreases with increasing temperature and is given by the Varshni relation [155]:

$$E_{g,i}(T_{cell}) = E_{g,i}(0) - \frac{\alpha_i T_{cell}{}^2}{T_{cell} + \beta_i}, \tag{52}$$

where $E_{g,i}(0)$ is the energy band-gap of subcell i at 0 K and α, β are material dependent constants.

Solving equation (50) for $J_i = 0$, the open-circuit voltage for each subcell is obtained by:

$$V_{oc,i} = \frac{n_i \cdot k_B \cdot T_{cell}}{q} \ln\left(\frac{J_{sc,i}(T_{cell})}{J_{0,i}(T_{cell})} + 1 \right) \tag{53}$$

The voltage in each junction can be also calculated by rearranging equation (50):

$$V_i = \frac{n_i \cdot k_B \cdot T_{cell}}{q} \ln\left(\frac{J_{SC,i}(T_{cell}) - J_i}{J_{0,i}(T_{cell})} + 1 \right) - J_i \cdot A_{cell} \cdot R_{s,i} \tag{54}$$

The total voltage output is the sum of the voltage in each junction, therefore:

$$V = \sum_{i=1}^{3} V_i,$$
$$V = \frac{k_B \cdot T_{cell}}{q} \left[\sum_{i=1}^{3} n_i \ln\left(\frac{J_{SC,i}(T_{cell}) - J}{J_{0,i}(T_{cell})} + 1 \right) \right] - J \cdot A_{cell} \cdot R_s \tag{55}$$

The *FF* describes the "squareness" of an *I-V* curve and is defined as the ratio of P_{mp} to the product of the I_{sc} and V_{oc}:

$$FF = \frac{I_{mp} \cdot V_{mp}}{I_{sc} \cdot V_{oc}} = \frac{P_{mp}}{I_{sc} \cdot V_{oc}} \tag{56}$$

The solar cell's efficiency is defined as the ratio of the maximum power output of the cell to the *DNI* which is incident on the cell:

$$\eta_{cell} = \frac{P_{out}}{P_{in}} = \frac{P_{mp}}{\int_{280}^{4000} CR_{geo} \cdot A_{cell} \cdot \lambda \cdot DNI(\lambda) \cdot \eta_{opt}(\lambda) \cdot d\lambda} \tag{57}$$

Therefore, the heat power produced on the cell is

$$q_{heat} = P_{in} \cdot (1 - \eta_{cell}) \tag{58}$$

3.3. Finite Element Thermal Model (FETM)

A 3J solar cell receiver is evaluated using FEA in COMSOL Multiphysics® [156], a commercially available software. COMSOL Multiphysics offers the possibility to combine different engineering or physical problems in the same model while being able to choose different solvers in order to achieve better accuracy. Another advantage is that it gives the option to import data from Matlab.

A Finite Element Thermal Model (FETM) has been developed to predict the thermal behaviour of 3J solar cells. Firstly, a three-dimensional environment and the heat transfer module (in solids) were selected for a stationary study. The 3D geometry of the device under study was then produced in the graphics window (main window of COMSOL). Once the materials were defined, the boundary conditions, heat source and other assumptions were introduced in the physical model; these are analysed in the following chapters. A screenshot of the COMSOL Multiphysics environment is illustrated in Figure 21.

The MJ solar cell is attached to a Direct Bonded Copper (DBC) substrate for heat dissipation and electrical insulation. The heat is transferred by conduction between the solid layers of the receiver. Some heat is lost to the environment, due to natural convection and surface to ambient radiation from all free surfaces.

In the case of a passively or actively cooled receiver, the heat is transferred by conduction between the solid layers of the receiver and the steady state equation is given by the Fourier’s law of heat conduction:

$$q''_{cond} = -k\nabla T \tag{59}$$

where q'' is the heat flux rate (W/m^2), k the heat conductivity and ∇ is the three-dimensional operand. The solar flux that is transformed to heat must be dissipated from the bottom substrate or cooling system to the environment or harnessed for use in another application. The heat which is dissipated either by natural or forced convection is described by:

$$q''_{n/f,conv} = h_{n/f} \cdot \Delta T \tag{60}$$

where h is the heat transfer coefficient (natural or forced) and ΔT the temperature difference between the cell and the ambient air or ultimate heat sink. The heat, which is lost to the environment, due to natural convection occurs on every surface that faces the ambient. COMSOL Multiphysics contains the correlations for each surface orientation (vertical, horizontal or inclined); these can be found in Incropera and DeWitt [157]. In this work, it is assumed that *h* represents the overall heat transfer coefficient usually described as *U*-value. However, it will only include the thermal resistance from the thermal interface material (TIM between the DBC and heat sink) and the "imaginary" heat sink itself, i.e.:

$$U = \frac{1}{R_{th,TIM} + R_{th,HS}} \tag{61}$$

unless otherwise stated. *U*-value will be referred to as h_{conv} during the modelling analyses in the following chapters.

The heat loss due to radiation is given by:

$$q''_{rad} = \varepsilon \cdot \sigma \cdot (\mathrm{T}^4 - T_{amb}^4) \tag{62}$$

where ε is the material’s emissivity and σ the Stefan-Boltzmann constant. The heat transfer in solids is defined by the following heat equation to simulate the thermal behaviour:

$$q'''_{heat} = \rho \cdot C_p \frac{\partial T}{\partial t} - \nabla \cdot (k \nabla T), \tag{63}$$

where ρ is the density, C_p is the heat capacity and t is time. The term $\rho \cdot C_p \, \partial T / \partial t$ disappears in steady state problems and q'''_{heat} is the heat source (W/m^3) which is calculated from the electrical model divided by the solar cell's volume. Therefore, in Cartesian coordinates, the steady-state heat equation becomes:

$$q'''_{heat} = -k \cdot \left(\frac{\partial^2 T}{\partial x^2} + \frac{\partial^2 T}{\partial y^2} + \frac{\partial^2 T}{\partial z^2} \right), \tag{64}$$

where from its solution the temperature distribution can be obtained [157].

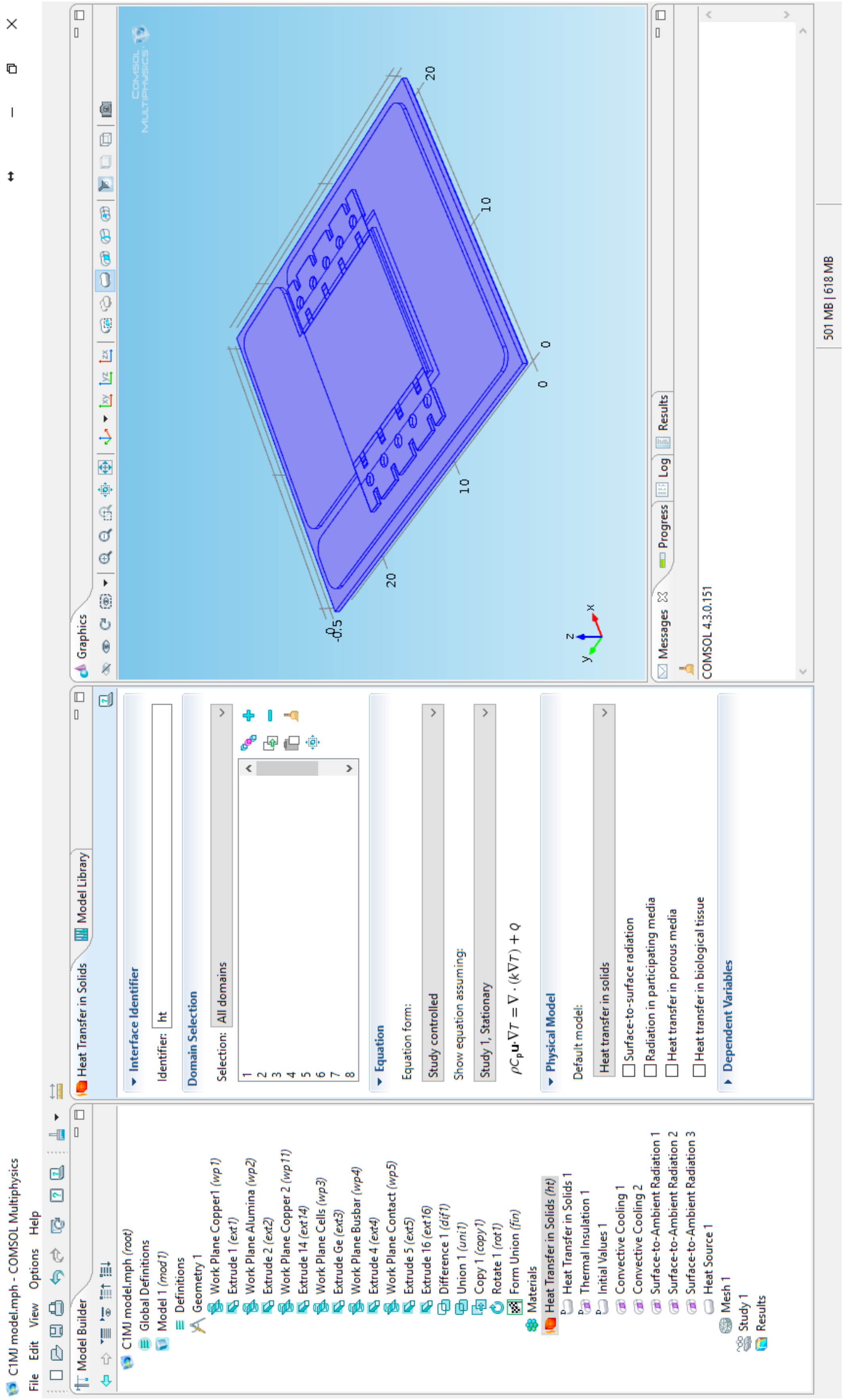

- C1MJ model.mph *(root)*
  - Global Definitions
  - Model 1 *(mod1)*
    - Definitions
    - Geometry 1
      - Work Plane Copper1 *(wp1)*
      - Extrude 1 *(ext1)*
      - Work Plane Alumina *(wp2)*
      - Extrude 2 *(ext2)*
      - Work Plane Copper 2 *(wp11)*
      - Extrude 14 *(ext14)*
      - Work Plane Cells *(wp3)*
      - Extrude Ge *(ext3)*
      - Work Plane Busbar *(wp4)*
      - Extrude 4 *(ext4)*
      - Work Plane Contact *(wp5)*
      - Extrude 5 *(ext5)*
      - Extrude 16 *(ext16)*
      - Difference 1 *(dif1)*
      - Union 1 *(uni1)*
      - Copy 1 *(copy1)*
      - Rotate 1 *(rot1)*
      - Form Union *(fin)*
    - Materials
    - Heat Transfer in Solids *(ht)*
      - Heat Transfer in Solids 1
      - Thermal Insulation 1
      - Initial Values 1
      - Convective Cooling 1
      - Convective Cooling 2
      - Surface-to-Ambient Radiation 1
      - Surface-to-Ambient Radiation 2
      - Surface-to-Ambient Radiation 3
      - Heat Source 1
    - Mesh 1
  - Study 1
  - Results

Interface Identifier

Identifier: ht

Domain Selection

Selection: All domains

1
2
3
4
5
6
7
8

Equation

Equation form:

Study controlled

Show equation assuming:

Study 1, Stationary

$\rho C_p \mathbf{u} \cdot \nabla T = \nabla \cdot (k \nabla T) + Q$

Physical Model

Default model:

Heat transfer in solids

☐ Surface-to-surface radiation
☐ Radiation in participating media
☐ Heat transfer in porous media
☐ Heat transfer in biological tissue

Dependent Variables

COMSOL 4.3.0.151

501 MB | 618 MB

Figure 21: Screenshot from the COMSOL Multiphysics environment showing the thermal model built for the C1MJ CCA from Spectrolab (will be analysed in Chapter 4).

3.4. Integrated modelling

The models described above are integrated based on the process flow diagram in Figure 22. The SMARTS2 generates the spectral *DNI* based on *AM*, *AOD* and *PW* inputs. The EM runs the single-diode model in Matlab® for an initial T_{cell} of 25°C and the q_{heat} is then introduced in the 3D FETM in COMSOL Multiphysics. The 3D FETM is simulated for a given T_{amb} and h_{conv} and calculates the integrated volumetric solar cell temperature. The "new" solar cell temperature is then imported back to the EM model which, in turn, calculates a "new" q_{heat}. The procedure is repeated until a steady state between models is achieved; i.e. when $|T_{cell}(s)-T_{cell}(s+1)| \leq 0.002\text{K}$, where s is the number of cycle iterations. It is important to highlight, that in the case of natural convection, the heat transfer coefficient is dependent on ΔT and heat flux, therefore is not constant. However, a constant typical h_{conv} is assumed in the following chapters.

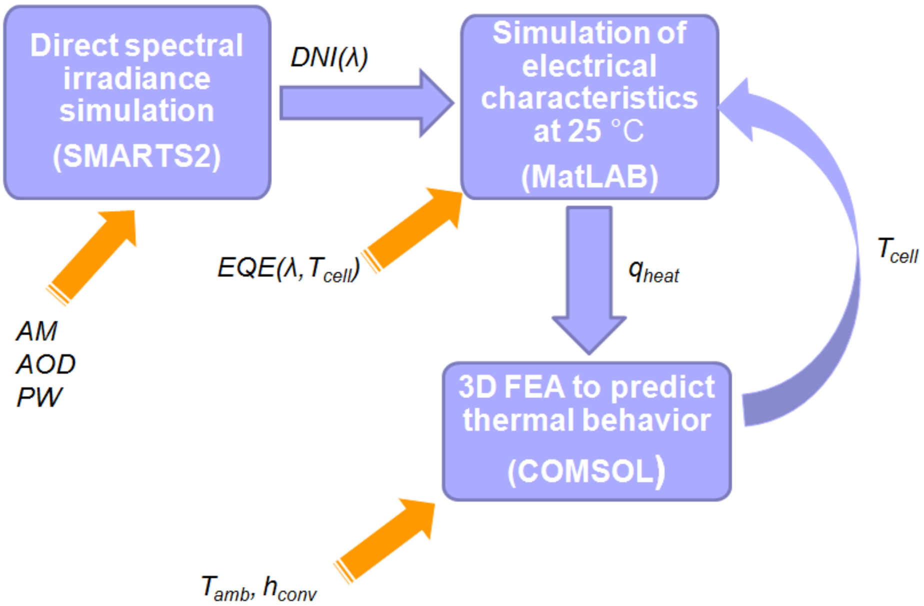

Figure 22: Process flow diagram of integrated model.

To ensure that the integrated modelling procedure converges irrespective of the initial conditions, the $T_{cell}(0)$ was varied and the volumetric solar cell temperature was calculated. Figure 23 shows the convergence for $T_{cell}(0) = 25°\text{C}$ and $T_{cell}(0) = 35°\text{C}$; both initial conditions results to the same T_{cell}. Similarly, in Figure 24 the initial conditions of $T_{cell}(0) = 25°\text{C}$ and $T_{cell}(0) = 120°\text{C}$ give the same T_{cell} estimation. Therefore, it can be concluded that the process converges irrespective of the initial conditions, i.e. the $T_{cell}(0)$.

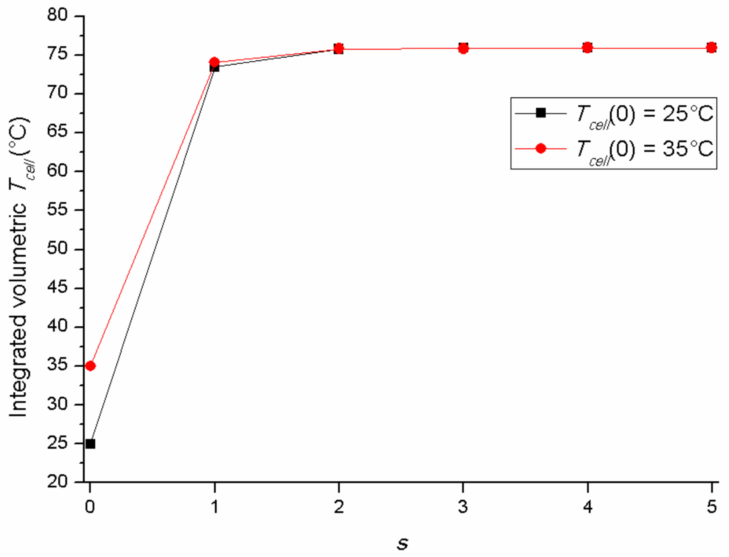

Figure 23: Integrated volumetric solar cell temperature for different initial conditions: $T_{cell}(0)$ = 25°C and $T_{cell}(0)$ = 35°C. The results correspond to AM1D, T_{amb} = 25°C and h_{conv} = 1200 W/(m^2·K).

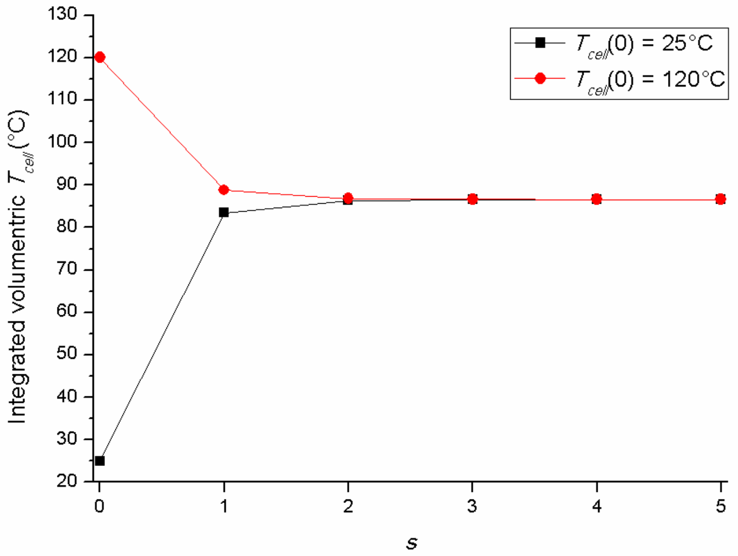

Figure 24: Integrated volumetric solar cell temperature for different initial conditions: $T_{cell}(0)$ = 25°C and $T_{cell}(0)$ = 120°C. The results correspond to AM1D, T_{amb} = 35°C and h_{conv} = 1200 W/(m^2·K).

3.5. Experimental setup

Experiments were conducted at the Fraunhofer CSE [158] and CFV [159] solar test site in Albuquerque, New Mexico (latitude 34.996°N, longitude 106.621°W, altitude 1632 m). A CPV monomodule manufactured by Suncore [127] for research purposes was used for the outdoor testing and experiments.

The monomodule is a DDM-1090× receiver assembly (RA) and consists of a silicon-on-glass (SoG) Fresnel lens and an Emcore 10 × 10 mm 3J solar cell bonded to a DBC substrate, i.e. a receiver. The typical electrical characteristics of the Emcore CTJ PV cell are given in Table 4. The transmittance of the SoG Fresnel lens and *EQE* of the 3J solar cell are shown in Figures 25 and 26 respectively. The monomodule has an acceptance angle of approximately ±0.7°.

Parameter	**Value**
η_{cell} (%)	39.6
I_{SC} (A)	6.48
I_{mp} (A)	6.34
V_{OC} (V)	3.19
V_{mp} (V)	2.76

Table 4: Typical electrical characteristics of the Emcore CTJ PV cell at 50 W/cm^2 and 25°C [160].

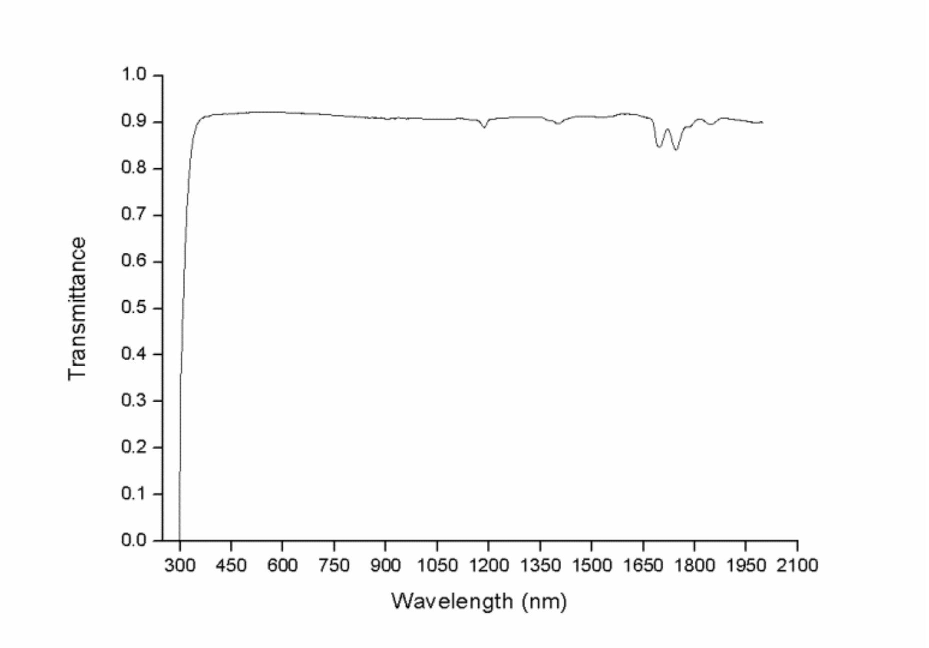

Figure 25: **Spectral optical transmittance of SoG Fresnel lens.**

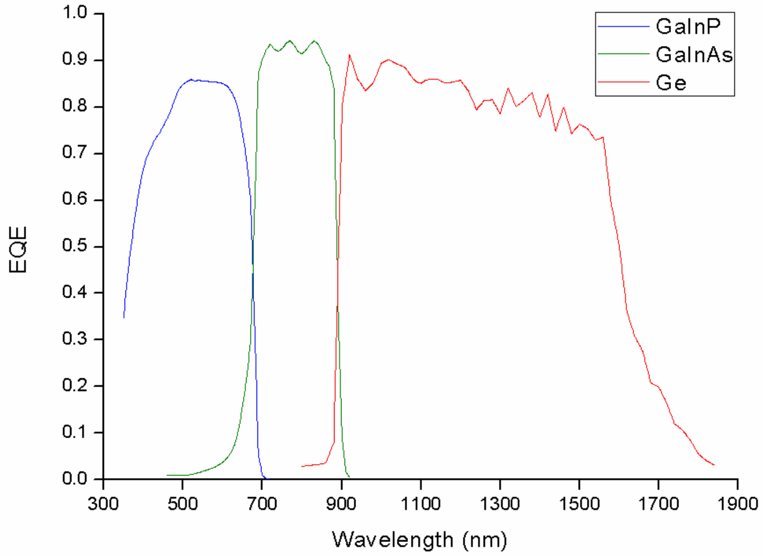

Figure 26: ***EQE* of each subcell of the 3J solar cell.**

The receiver is bonded to an aluminium radially finned heat sink. Positive and negative lead wires are attached to the assembly as a means of making external electrical contact to the single cell in the assembly. The assembly includes a bypass diode for routing current around the cell when the assembly is light starved relative to other RAs in a series connected string of RAs. Ceramic sun shields in the assembly protect heat sensitive parts from exposure to concentrated sunlight. Silicone sealant waterproofs the assembly. The large fins on the heat sink passively cool the RA. Five T-type thermocouples (TC) are integrated in the assembly to measure the temperature of selected materials or parts near the solar cell (sealant, diode, encapsulant, wire insulation and wire to box connector). Photographs of the assembly before and after mounting the optical component are shown in Figures 27 and 28 respectively.

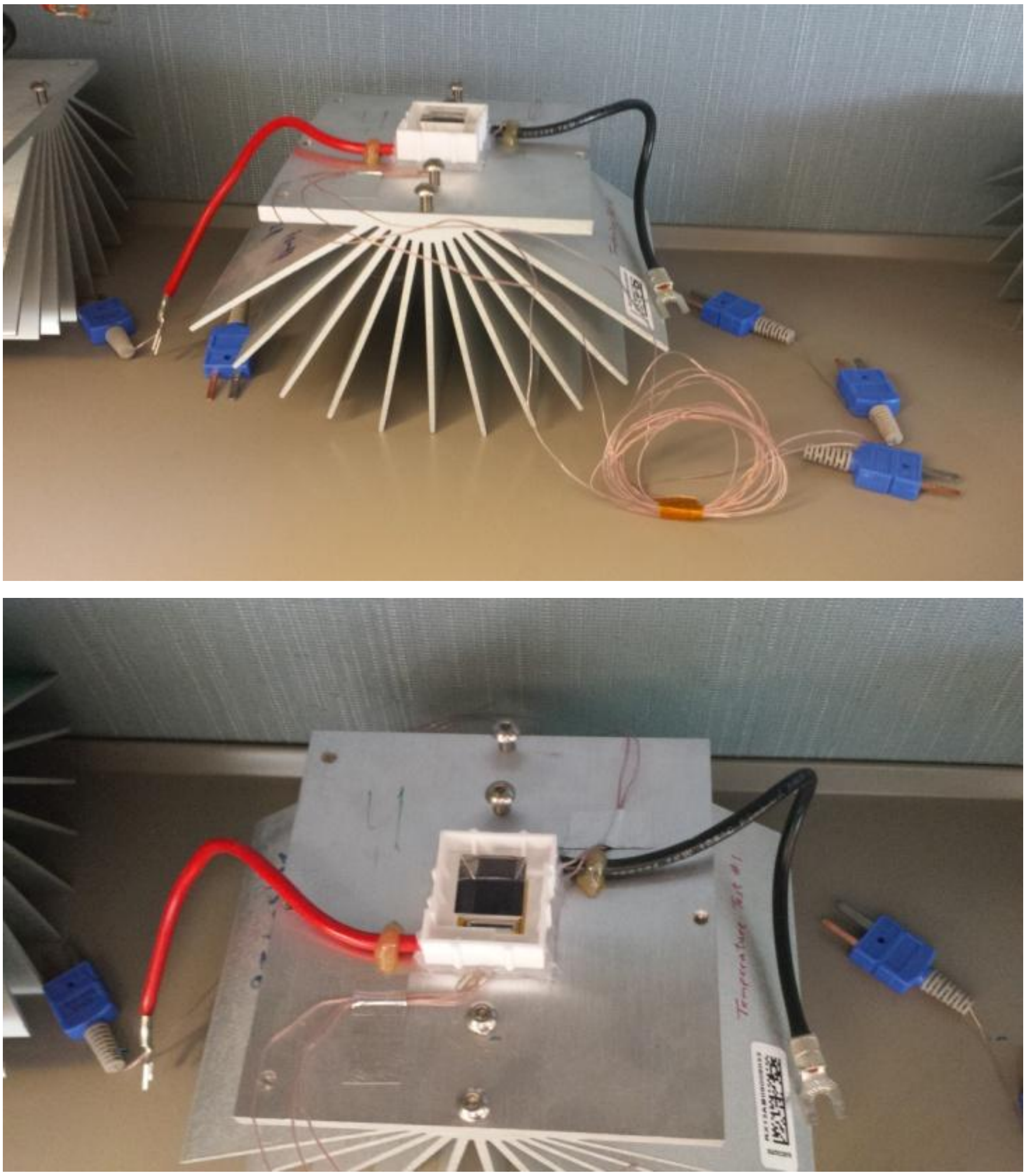

Figure 27: **A CPV receiver using a 3J solar cell bonded to a DBC and an aluminium heat sink.**

Figure 28: **Front (top Figure) and rear (bottom Figure) photographs of two DDM-1090× receiver assemblies (RAs or monomodules) mounted on a high-accuracy solar tracker in Albuquerque, NM.**

The CPV monomodule was mounted on a high-accuracy (within 0.3°) two-axis solar tracker. A Vaisala weather transmitter WXT520 [161] monitored the meteorological conditions of the location (Figure 29); wind speed and direction, relative humidity, barometric pressure, liquid precipitation (rainfall and hail) and ambient temperature. The Vaisala's WXT520 technical data can be found in Table 5 [162].

Figure 29: The Vaisala weather transmitter WXT520.

Instrument	Parameter	Range	Resolution	Accuracy
Anemometer	WS	0 to 60 m/s	0.1 m/s	±3% at 10 m/s
Thermometer	T_{amb}	-52°C to 60°C	0.1°C	±0.3°C at 20°C ±0.7°C at 60°C
Barometer	$p_{barometric}$	600 to 1100 hPa	0.1 hPa	±0.5 hPa at 0°C to 30°C ±1 hPa at -52°C to 60°C
Hygrometer	RH	0 to 100%RH	0.1%RH	±3%RH at 0 to 90%RH ±5%RH at 90 to 100%RH

Table 5: Technical data of Vaisala WXT520 weather transmitter [162].

The solar radiation, tracking and spectral sensors are shown in Figure 30; a sNIP Eppley [163] and a CHP1 Kipp & Zonen [164] pyrheliometer measure the *DNI*, a Black Photon Instruments (BPI) tracking accuracy sensor [165] measures the tracker's accuracy with high precision and speed, BPI isotype sensors [166] measure the spectral composition of solar irradiance, a sun finder sensor keeps the tracker facing the sun, an additional tracking accuracy sensor and a CMP6 Kipp & Zonen pyranometer [167] measure the global normal irradiance, *GNI*. The specifications of the equipment used can be found in Tables 6 to 9 [163-167].

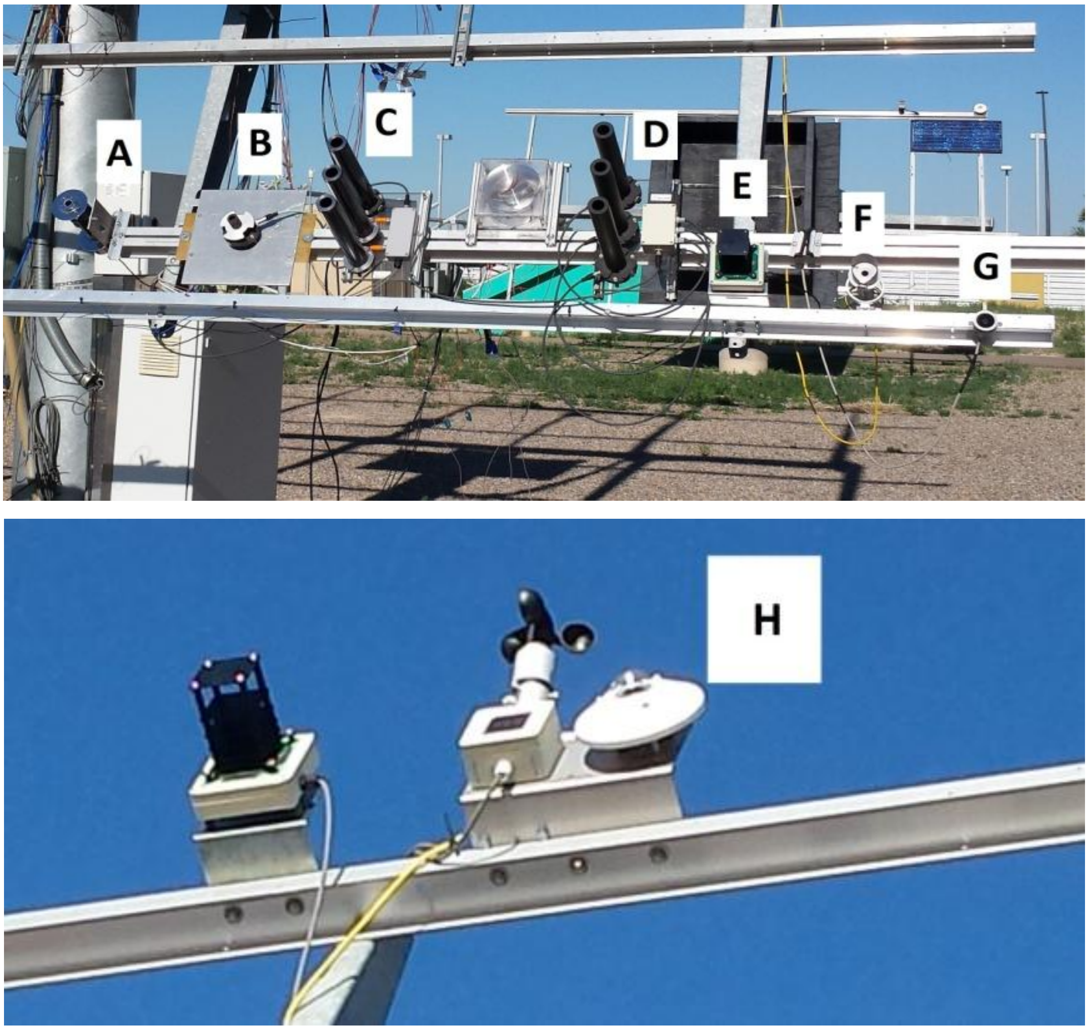

Figure 30: **Solar irradiance, tracking and spectral sensors: a) sNIP Eppley pyrheliometer, b) BPI tracking accuracy sensor, c) and d) BPI isotype sensors, e) sun finder sensor, f) CHP1 Kipp & Zonen pyrheliometer, g) tracking accuracy sensor, h) CMP6 Kipp & Zonen pyranometer.**

Specifications	**CHP1 Kipp & Zonen**	**sNIP Eppley**
Classification	First Class	Secondary Standard/ High Quality
Spectral range	200 to 4000 nm	250 to 3000 nm
Sensitivity	7 to 14 μV/W/m^2	Approx. 8 μV/W/m^2
Non-stability	< 0.5%	0.5%
Non-linearity	< 0.2%	0.2%
Temperature response	< 0.5%	0.5%
Output	10 to 20 mV for 1400 W/m^2	0 to 10 mV
Response time	< 5 s	5 s
Zero offset	< 1 W/m^2	1 W/m^2
Field of view	5±0.2°	5°
Daily uncertainty	< 1%	Approx. 1%

Table 6: Technical data of CHP1 Kipp & Zonen and sNIP Eppley pyrheliometers [163, 164].

Specifications	CMP6 Kipp & Zonen
Classification	First Class
Spectral range	285 to 2800 nm
Sensitivity	5 to 20 μV/W/m^2
Impedance	20 to 200 Ω
Output	0 to 30 mV (0 to 1500 W/m^2)
Maximum Irradiance	2000 W/m^2
Response time (63%) Response time (95%)	< 6 s < 18 s
Zero offsets: thermal radiation (at 200 W/m^2) temperature change (5 K/h)	 < 12 W/m^2 < 4 W/m^2
Non-stability	< 1%
Non-linearity	< 1%
Directional response	< 20 W/m^2
Spectral selectivity (350 to 1500 nm)	< 3%
Temperature response	< 4%
Tilt response	< 1%
Field of view	180°
Accuracy of bubble level	< 0.1°
Operational temperature range	-40°C to 80°C

Table 7: Technical data of CMP6 Kipp & Zonen pyranometer [167].

Specifications	BPI-TA1
Measurement range	±1.2°
Measurement speed	Up to 1 kHz
Resolution	0.0005°
Linearity	±1.8% between 5°C to 45°C ±3% between -20°C to 60°C
Accuracy	±2.4% between 5°C to 45°C ±4.5% between -20°C to 60°C
Output	-10 to 10 V

Table 8: Technical data of BPI-TA1 tracking accuracy sensor [165].

BPI-IT1 Specifications			
	Top	Middle	Bottom
Composition	$Ga_{0.5}In_{0.5}P$	$Ga_{0.99}In_{0.01}As$	Ge
Spectral range	375-700 nm	700-900 nm	900-1750 nm
Operating range	-20°C to 65°C		
Slope angle	±2.5°		
Opening angle	±2.75°		
Stop angle	±3°		
Resistor shunts	50 Ω	50 Ω	10 Ω
Resistors accuracy	±0.1%		
Spectrum	AM1.5D ASTM G173 at 1000 W/m^2		

Table 9: Technical data of BPI-IT1 isotype sensors [166].

The *I-V* characteristic of the monomodule is traced by a Daystar DS-1000 *I-V* curve tracer [168] (Figure 31). This portable I-V curve tracer was designed for field use. A laptop is connected to the DS-1000 by a USB and is used to control the *I-V* curve tracer using the IVPC software [169] for Windows. The *I-V* tracer uses a capacitive load to vary the resistance across the monomodule's terminals in order to measure the output current and voltage and to calculate the electrical characteristics such as the open-circuit voltage, short-circuit current, maximum power, voltage at maximum power, current at maximum power and fill factor. The errors associated to the DS-1000 measurements are given in Table 10.

Figure 31: Daystar DS-1000 *I-V* curve tracer connected to a laptop.

Specifications	Daystar DS-1000		
Parameter (range)	**Error @ 25°C**	**Error 0-50°C**	**Resolution**
Voltage (10 V)	±4 mV (±0.01%)	±7 mV (±0.15%)	300 μV
Current (100 A)	±50 mA (±0.05%)	50 mA (±0.1%)	3 mA

Table 10: Typical absolute errors (typical percentage errors) of Daystar DS-1000 [168].

Bachour [170] concluded that sunphotometer measurements at the ground level can reduce the uncertainty of the modelled *DNI* data. Hence, the atmospheric parameters were measured using a Solar Light Microtops II sunphotometer [171] (Figure 32); a five channel hand-held instrument which measures the *AOD* at 440 nm, 500 nm, 675 nm, 870 nm and 936 nm. The *PW* is also determined by the measurements at 870 nm and 936 nm. The specifications are given in Table 11.

Figure 32: Solar Light Microtops II sunphotometer positioned towards the sun.

Specifications	Solar Light Microtops II
Resolution	0.01 W/cm^2 on 305 nm Channel
Dynamic range	> 300000
Viewing angle	2.5°
Precision	1-2%
Non Linearity	Max. 0.002% FS
Operating environment	0 to 50°C, no precipitation

Table 11: Specifications of Solar Light Microtops II sunphotometer [171].

The *I*-*V* measurements were logged on the laptop every one minute and then transferred to the SQL database while the weather, irradiance and spectral measurements were directly recorded in the database every one minute using a Campbell Scientific CR1000 datalogger [172] (see specifications in Table 12). The sunphotometer was only used under clear-sky conditions (i.e. no visible clouds) to measure the *AOD* and *PW*; these data were then transferred to the database and SMARTS2 was used to simulate the spectral irradiance at every timestamp. The reference time is winter period UTC/GMT.

It should be noted that the modules and measuring equipment were cleaned at least once a week or after rain. The monomodule's alignment was also checked periodically. In addition, all measuring equipment were within the calibration period.

Specifications	**Campbell Scientific CR1000**
Maximum scan rate	100 Hz
Analog inputs	16 single-ended or 8 differential
Pulse counters	2
Switched excitation channels	3 voltage
Digital Ports	8 I/O or 4 RS-232 COM
Communications/Data Storage Ports	1 CS I/O, 1 RS-232, 1 parallel peripheral
Switched 12 Volt	1
Input voltage range	±5 Vdc
Analog voltage accuracy	±(0.06% of reading + offset), 0 to 40°C
Analog resolution	0.33 μV
A/D bits	13
Power requirements	9.6 to 16 Vdc
Standard temperature range	-25 to 50°C
SRAM for CPU usage and final storage	4 MB

Table 12: Campbell Scientific CR1000 datalogger specifications [172].

Chapter 4: Electrical and thermal analysis of a concentrating III-V triple-junction solar cell as a function of air mass and ambient temperature

The influence of the incident spectral irradiance on the electrical and thermal behaviour of triple-junction solar cells has been investigated. A spectral dependent electrical model has been developed to calculate the electric characteristics and quantify the heat power of a multijunction solar cell. A three-dimensional finite element analysis is also used to predict the solar cell's operating temperature and cooling requirements for a range of ambient temperatures. The combination of these models improves the prediction accuracy of the electrical and thermal behaviour of triple-junction solar cells (quantification follows in the analysis). The heat transfer coefficient between the back-plate and ambient air was found to be the significant parameter in achieving high electrical efficiency. These data are important for the electrical and thermal optimisation of concentrating photovoltaic systems under real conditions. The objective of this chapter is to quantify the temperature and cooling requirements of multijunction solar cells under variable solar spectra and ambient temperatures. It is shown that single cell configurations with a solar cell area of 1 cm^2 can be cooled passively for concentration ratios of up to 500× with a heat sink thermal resistance below 1.63 K/W, however for high ambient temperatures (greater than 40°C), a thermal resistance less than 1.4 K/W is required to keep the solar cell operating within safe operating conditions.

This chapter has been published in [148]:
M. Theristis and T. S. O’Donovan, "Electrical-thermal analysis of III–V triple-junction solar cells under variable spectra and ambient temperatures," *Solar Energy*, vol. 118, pp. 533-546, 2015.

4.1. Introduction

As mentioned in Chapter 1, MJ solar cells are made of III-V compound semiconductors and are used in space and terrestrial applications [173]. Currently the state-of-the-art solar cell on the market is the lattice matched 3J solar cell made of GaInP/GaInAs/Ge subcells [10, 174]. These subcells, are monolithically connected in series in a specific way to absorb a larger proportion of the solar spectrum (compared to single-junction solar cells) and thus, to achieve higher conversion efficiencies. To date, the highest recorded efficiency for a 3J solar cell is 44.4% and 46% for 4J [12]. Such solar cells can be economically viable if sunlight is concentrated by a factor greater than 300× [93, 175, 176].

High concentration results in high heat flux on the solar cell's surface and a rapid increase in the cell's temperature. High temperatures reduce the electrical conversion efficiency because of the temperature dependence of the V_{oc} and V_{mp} [177]. It has been shown that under 500× concentration and without any cooling arrangements, the solar cell can exceed 1000°C [36-39, 176, 178]. This emphasises the need for appropriate cooling technology to decrease the temperature to within safe operation limits and to avoid suboptimal performance and risk of system failure.

The recommended operating temperature varies for different manufacturers; Spectrolab Inc. suggests a maximum operating cell temperature of 100°C [179], Azurspace GmbH suggests 110°C for their latest products 3C42A [180], 3C44A [181] and 150°C for the old product 3C40A [182] while Sharp data are given for up to 120°C [89]. Reliability analysis on 3J solar cells has shown that, at operating conditions of 820× and 80°C, the warranty time was 113 years; at 100°C however, the warranty time was reduced to 7 years [183]. It is also worth noting that, in high temperatures (over 120°C, 1×), the voltage output of the low energy band-gap germanium subcell decreases to almost zero [10, 184]. Therefore, to avoid long term degradation problems and also the risk of destroying the connections (melting), the CCA should not operate in excess of 100°C.

MJ solar cells are usually characterised under standard conditions, although in the field, the atmospheric conditions can vary significantly [185]. Due to the fact that the subcells of the 3J solar cell are monolithically connected and also because of their sensitivity to the spectral variations and intensity of sunlight, the prediction of the electrical and thermal behaviour is still challenging [101]. There also exists a limitation relating to the in-series connection of such solar cells; a mismatch in the current produced by each subcell will limit the overall output to the lower value which will result in greater heat production within the cell. Therefore, by applying a simple *DNI* value as an input in thermal models may give inaccurate results. It is important therefore, to develop smart algorithms, models or methods to realistically determine the electrical performance of the cell to accurately determine the thermal characteristics, temperature and cooling requirements of the system.

CPV thermal numerical models and experimental designs have been thoroughly discussed in literature using passive [23, 36, 37, 139, 186] and active [25, 129, 133, 187] cooling techniques. According to Royne *et al.* [40], who presented an extensive review on different cooling techniques, passive cooling can be sufficient for single cell geometries and solar flux up to 1000 suns where a "large area" is available below the cell for a heat sink. For densely packed cells and *CR* higher than 150 suns, active cooling is necessary [40]. It was also concluded that the R_{th} of the cooling system must be less than 10^{-4} ($m^2 \cdot K/W$) for concentration levels above 150×. However, the spectral effects on temperature and hence, the electrical efficiency are not included in the aforementioned thermal models.

In addition, the prediction of solar cell's temperature is very important for the electrical characterization of CPV modules. Rodrigo *et al.* [110, 113] reviewed various methods for the calculation of the cell temperature in HCPV modules. The methods have been described in Chapter 2 and were categorised based on the: heat sink temperature, electrical parameters, atmospheric parameters. The first two categories are based on direct measurements of CPV modules in indoor or outdoor experimental setups and present the highest degree of accuracy (*RMSE* between 1.7K - 2.5K). Most of the methods reviewed by Rodrigo *et al.* [113] calculate the cell temperature at open-circuit conditions. Methods that predict the cell temperature at maximum power point (MPP) operation offer a more realistic approach since they include the electrical energy generation of the solar cells (i.e. real operating conditions); Yandt *et al.* [188] described a method of predicting the cell temperature at MPP based on electrical parameters and Fernández *et al.* [123] based on heat sink temperature with absolute *RMSE* 0.55K - 1.44K. Fernández *et al.* [122] also proposed an artificial neural network model to estimate the cell temperature based on atmospheric parameters and an open-circuit voltage model based on electrical parameters [112] offering good accuracy (*RMSE* 3.2K and 2.5K respectively [113]). The main disadvantage of the aforementioned methods is that an experimental setup is required to obtain the parameters used for the cell temperature calculation.

Despite the fact that several electrical models and experimental procedures for MJ solar cells have been described thoroughly in literature [76, 87, 89, 90, 93-95, 109, 189] which included the spectrum and irradiance dependence, the challenge to develop an integrated thermal-electrical model which predicts the cell temperature and includes the cooling needs is still unsolved. As described in Chapter 3, the current methodology combines three models; the solar spectral irradiance is generated by the NREL SMARTS2 [49, 100, 153], the EM uses a single-diode model to simulate the electrical characteristics and heat power of a 3J solar cell at MPP and the FETM that uses the heat power as an input from the electrical model in order to predict the temperature and the cooling requirements as a function of ambient temperature.

4.2. Methodology

The models described in Chapter 3 are simulated iteratively based on the flowchart in Figure 33. The solar spectrum is generated using the SMARTS2. Clear-sky days are assumed and the z, and hence the AM is considered to be the only variant that affects the direct spectral irradiance.

The simulations are conducted in steady state. The EM runs for a given CR, an initial T_{cell} of 25°C, $1 \leq AM \leq 15$ and the heat power is then introduced in the 3D FETM in COMSOL Multiphysics. Solar spectra ranging from AM1.5D to AM15D have been chosen as a rigorous test for this integrated model. They are not location specific; they are used to demonstrate the applicability of the model to a wide range of solar geometries. For $25°\text{C} \leq T_{amb} \leq 45°\text{C}$ and $1200\ \text{W/(m}^2\cdot\text{K)} \leq h_{conv} \leq 1600\ \text{W/(m}^2\cdot\text{K)}$ at the back surface of the CCA, the cell's temperature is predicted from the thermal model and is then imported to the electrical model. The procedure is repeated until the solution converges (see also Chapter 3).

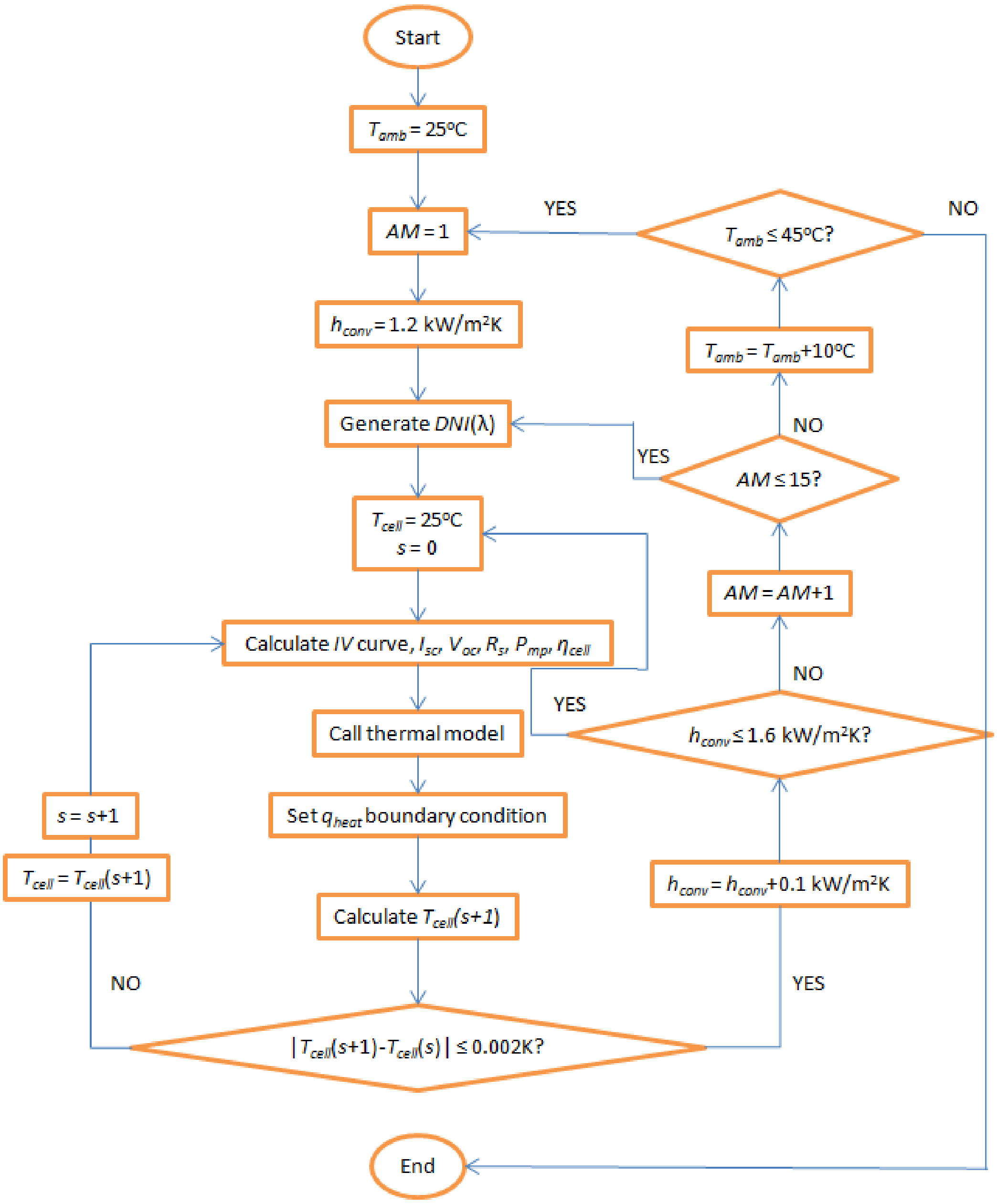

Figure 33: Flowchart of simulation algorithm.

Table 13 summarises the variable input parameters used for the simulation program, the range of each parameter, the model from which they are generated and the model that uses them as an input. The maximum convective heat transfer coefficient considered in this study is 1600 W/(m²K), as this has been shown by Mudawar [190] to be the maximum achievable under passive cooling conditions. Lower convective heat transfer coefficients than 1200 W/(m²K) are not reported as they were found to be insufficient to maintain the cell temperature below 100°C.

Variable input parameter	**Range**	**Generated from**	**Used in**
AM	1 - 15	SMARTS2	EM
h_{conv}	1.2 - 1.6 kW/(m^2·K)		FETM
q_{heat}		EM	FETM
T_{cell}		FETM	EM
T_{amb}	25°C - 45°C		FETM

Table 13: Model variables, ranges and where are generated from and used in.

4.3. Results & discussion

This section describes an application of the aforementioned methodology using the C1MJ CCA from Spectrolab. Literature based data from Kinsey and Edmondson [94] and Segev *et al.* [89] are used in the EM. The *CR* discussed in this section is assumed to be 500× unless otherwise stated.

4.3.1. SMARTS2

The generated direct spectral irradiance from SMARTS2 is shown in Figure 34. For the sake of clarity some air mass values are not illustrated. The integration of the spectral irradiance at a specific air mass gives the irradiance intensity; the values are shown in Figure 35 as a function of *z*. Other parameters were kept constant at the reference conditions of the standard ASTM G173-03 [191] (*PW* = 1.42 cm, rural aerosol model, turbidity value 0.084 specified as *AOD* at 500 nm). Figure 36 shows the percentage of ultraviolet (UV, 280-400 nm), visible (Vis, 400-780 nm) and infrared (IR, > 780 nm) light as a function of air mass. It can be seen that for $AM \geq 3$ the IR wavelengths have the highest proportion while the UV component is zero for $AM > 7$.

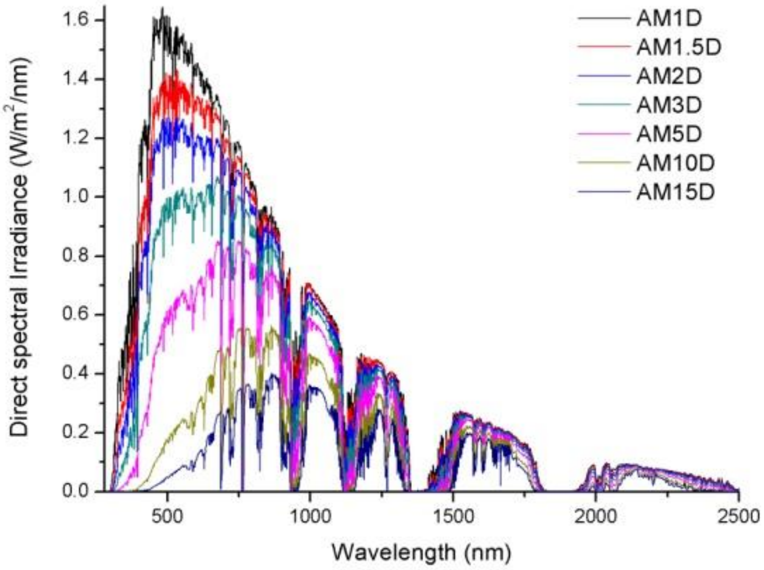

Figure 34: Direct spectral irradiance generated by SMARTS2 for AM1D to AM15D. Some air mass values are not illustrated for clarity purposes.

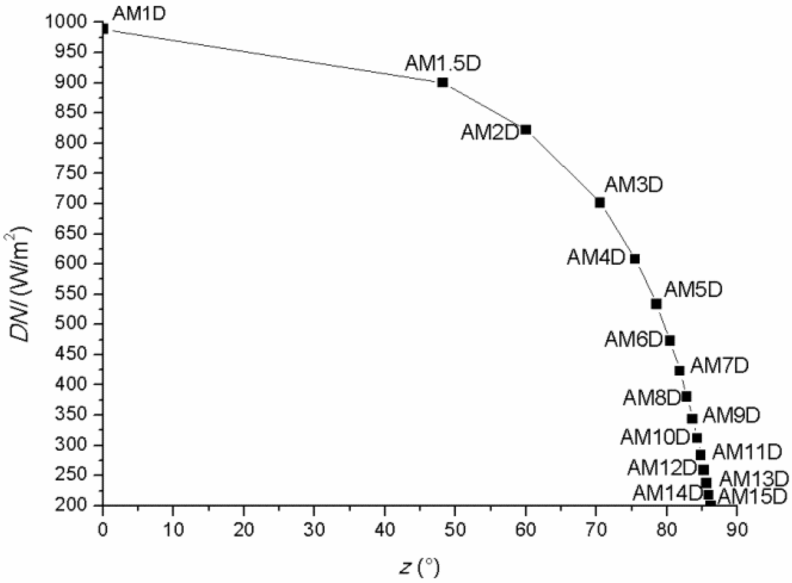

Figure 35: Direct intensity versus zenith angle and air mass. Intensity values are calculated by integrating the solar spectral irradiance.

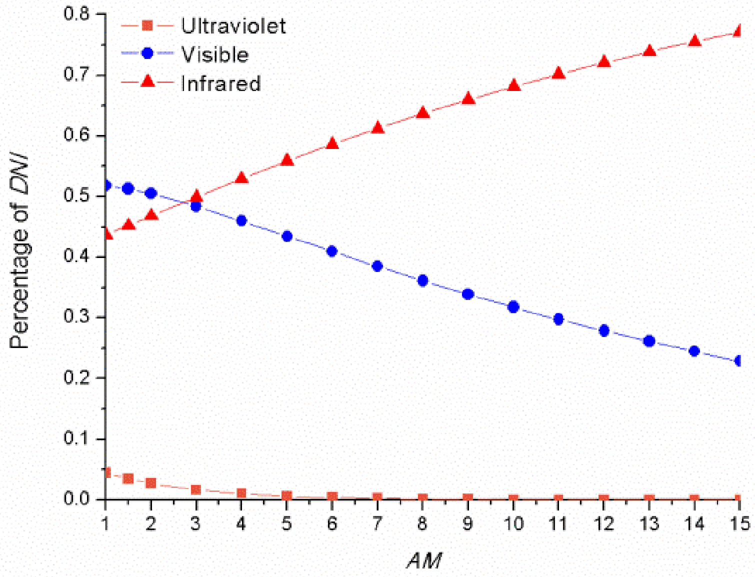

Figure 36: Ultraviolet, visible and infrared light percentage of direct normal irradiance as a function of air mass.

4.3.2. Electrical model (EM)

The *EQE* of the Spectrolab C1MJ 3J solar cell, as characterised by Kinsey and Edmondson [94] for a temperature range between 25°C and 75°C, was used for this application. The bottom subcell was measured using a C1MJ subcell isotype.

The input parameters used for the electrical model are listed in Table 14. The cell area was taken as $A_{cell} = 1$ cm^2 and the optical efficiency was assumed to be $\eta_{opt} = 0.8$. The series resistance as a function of the incident power was calculated according to [192]:

$$R_s = \frac{R_{S0}}{CR^{K_c}} + R_{s\infty}, \tag{65}$$

where $R_{S0} = 11$ mΩ is the series resistance at low intensity, $R_{s\infty} = 40$ Ω is the series resistance at high flux and $K_c = 1.75$ is a series resistance intensity coefficient. Table 15 shows the fitting parameters for the C1MJ single-diode model which were adopted directly from Segev *et al.* [89].

Subcell	**α (eV/K)**	**β (K)**	**E_g at 0 K (eV)**
1	4.72×10^{-4}	269	1.86
2	5.39×10^{-4}	204.7	1.495
3	4.77×10^{-4}	235	0.756

Table 14: Inputs of electrical model.

Subcell	**κ (A/(cm^2·K^4))**	**γ**	**n**
1	1.833×10^{-8}	1.81	1.89
2	2.195×10^{-7}	1.86	1.59
3	1.9187×10^{-5}	1.44	1.43

Table 15: Fitting parameters for C1MJ single-diode model adopted directly from Segev *et al.* [89].

4.3.2.1. Short-circuit current density

From equation (14), the J_{sc} distribution for each subcell can be calculated. As mentioned earlier (see Chapter 3), higher T_{cell} decreases each subcell's band-gap causing the *EQE* to shift towards the longer wavelengths and therefore the J_{sc} follows the same behaviour ($J_{sc,3}$ is plotted separate to $J_{sc,1}$ and $J_{sc,2}$ for clarity; see Figures 37 and 38). Figures 39 and 40 show the effect of *AM*; higher air mass values show a significant drop in the short wavelength region (see also Figures 34 and 36) and therefore the effect on higher band-gap subcells is higher than the low band-gap (germanium) subcell. This will be the case especially for $J_{sc,1}$ which decreases rapidly for $AM > 2$ acting as the current limiting subcell. Also considering that in the winter period, the *AM* will always be greater or equal to 2 at middle to high latitudes, the subcells will never be current matched [56]. This has an impact on the electrical performance of the cell since the excess current will be transformed directly to heat. Moreover, by comparing Figures 34 and 36 with Figures 37 to 40, it is apparent that the germanium subcell will never limit the current output.

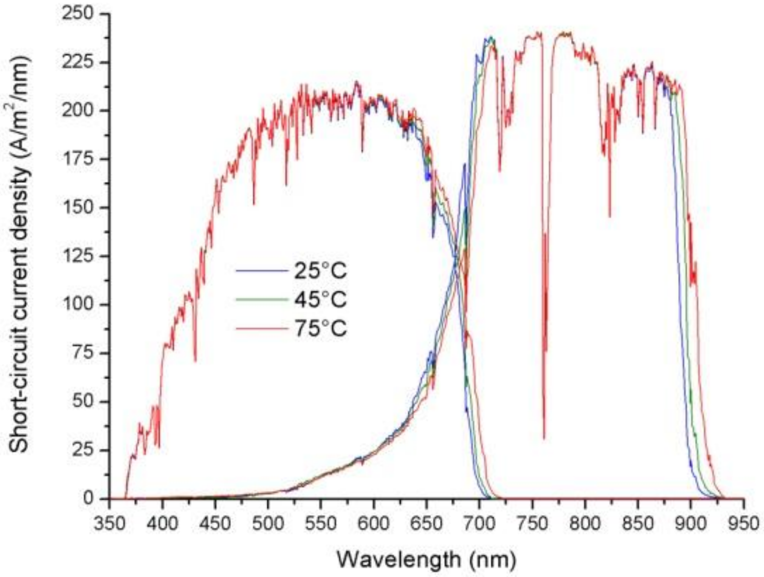

Figure 37: Short-circuit current density distribution of top and middle subcell under 500× and AM1.5D as a function of temperature (the J_{sc} at 65°C is not illustrated because of the proximity of *EQE* data to the 75°C [94]).

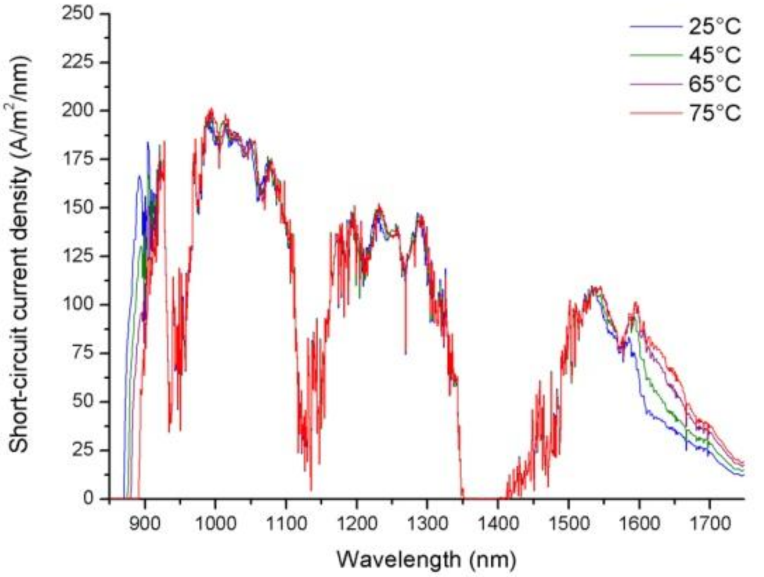

Figure 38: Short-circuit current density distribution of bottom subcell under 500× and AM1.5D as a function of temperature.

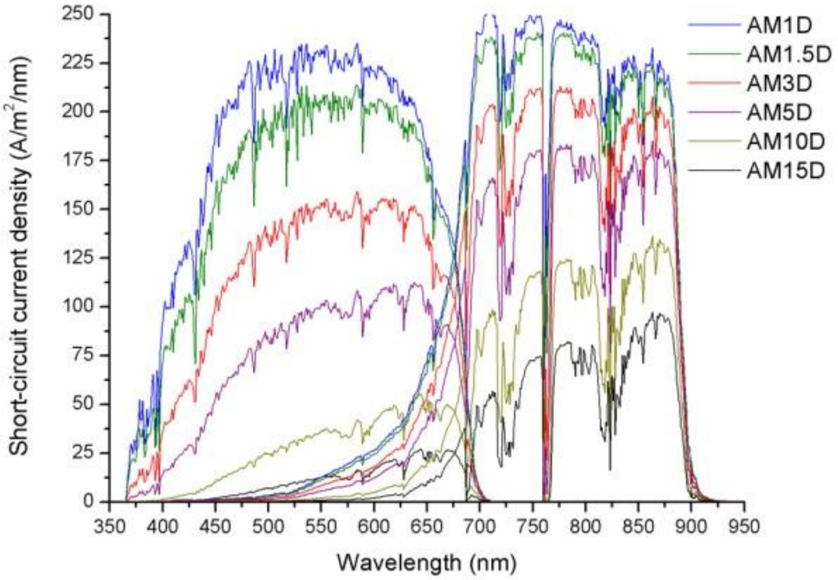

Figure 39: Effect of *AM* on short-circuit current density distribution of top and middle subcell under 500× and T_{cell} = 25°C.

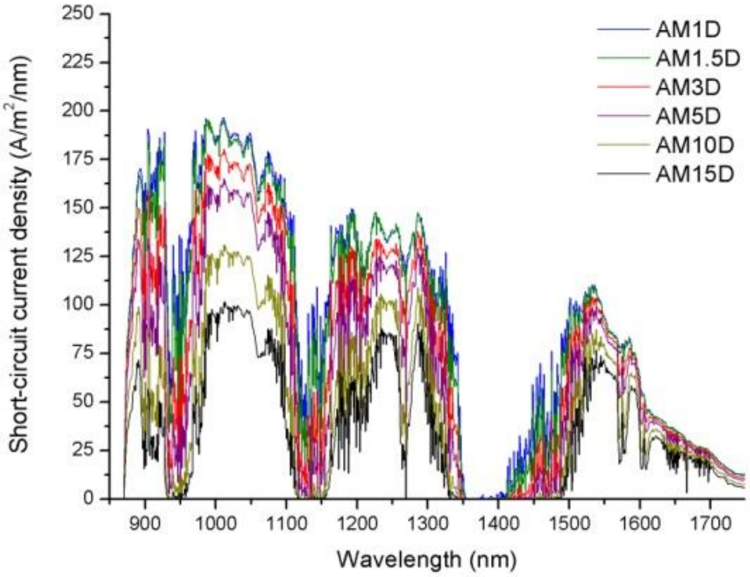

Figure 40: Effect of *AM* on short-circuit current density distribution of bottom subcell under 500× and T_{cell} = 25°C.

4.3.2.2. Total open-circuit voltage

The V_{oc} dependence on temperature under variable *AM* is plotted in Figure 41. Increasing temperatures result in an increase in the J_0 which, in turn, decreases the V_{oc} (see also equations (51), (52) and (53)). The relative temperature coefficient range is between -0.16%/K for AM1D to -0.18%/K for AM15D. This shows that there is only a weak dependency of *AM* change on the V_{oc} temperature coefficient. By increasing the *AM*, the V_{oc} decreases by 0.48%/AM at 25°C, 0.56%/AM at 45°C, 0.61%/AM at 65°C and 0.63%/AM at 75°C. This reduction is due to the J_{sc} decrease.

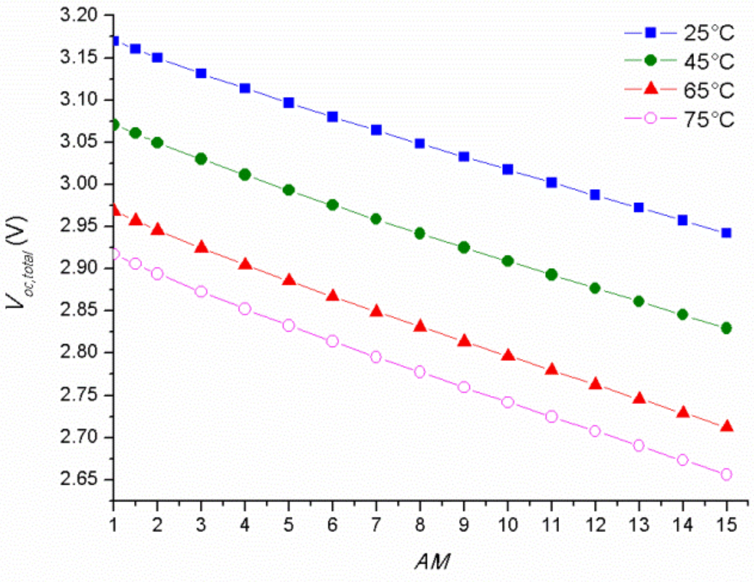

Figure 41: C1MJ total open-circuit voltage at *CR* = 500× under variable air mass and cell temperature.

4.3.2.3. Efficiency

Since the bottom subcell will never limit the current (as explained in section 4.3.2.1.) the ratio of the top to the middle subcell's short-circuit current density ($X = J_{sc,1}/J_{sc,2}$) is used for comparison. Figure 42 shows that the maximum efficiency at any temperature is achieved when the top and middle subcells are current matched. Also the middle subcell is the current limiting cell only for air mass values lower than AM1.5D while for all other air mass values the current limiting subcell is the top subcell. X is shown only for 25°C for clarity purposes because it is very close to the short-circuit current ratio at higher temperatures (X at 75°C is 0.58% higher for AM1D and 3% for AM15D).

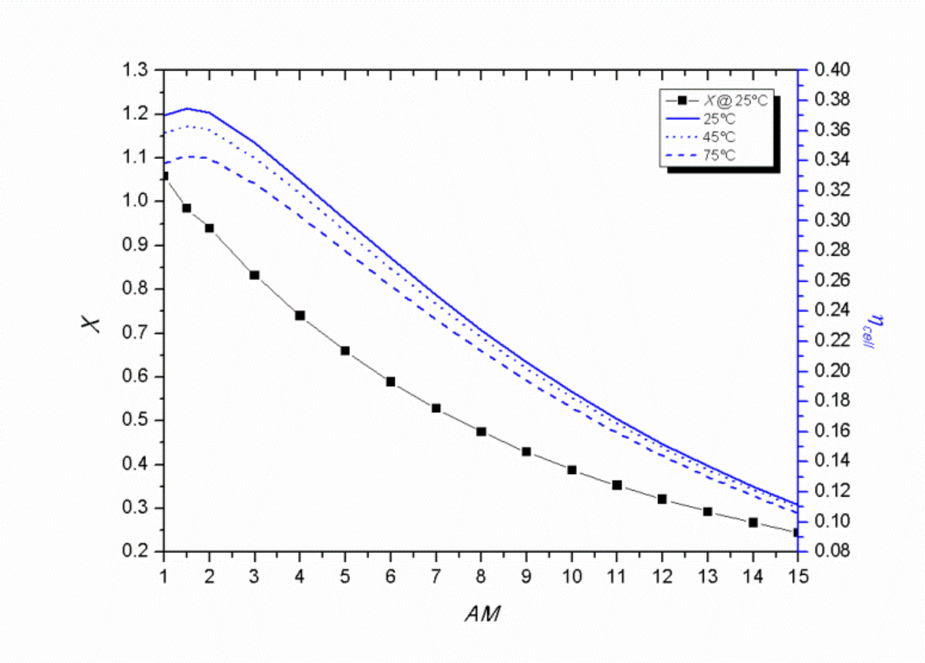

Figure 42: Ratio of top to middle subcell's short-circuit current density, *X* at 25°C (left black axis) and cell's efficiency (right blue axis) at *CR* = 500× over a range of air mass values and cell temperatures.

4.3.2.4. Heat power

The analysis of the triple-junction solar cell's electrical output is important to quantify the heat power which is produced and needs to be dissipated by the cooling mechanism. In order to calculate the heat power over a range of air mass values and temperatures, equation (58) is used. The maximum heat power is found to be 25.5 W at AM1D and 75°C (Figure 43). Inset graph in Figure 43 shows the air mass values of interest for the thermal model; thermal issues are not significant for $AM > 2$, since any cooling mechanism which is designed to dissipate the heat at $AM \leq 2$, will be adequate for any range of higher air mass values.

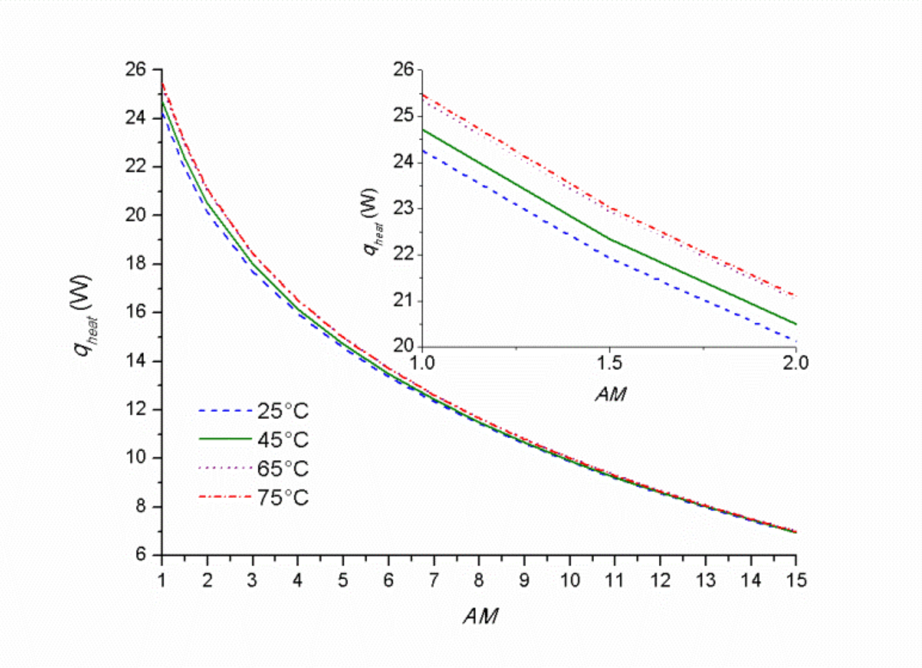

Figure 43: Heat power at *CR* = 500× over a range of cell temperatures and air mass values; inset graph shows the air mass values of interest for the thermal model.

4.3.2.5. Current mismatch effect on heat power

The maximum heat power produced on the cell due to current mismatch is quantified using equation (66) [193] and is shown graphically in Figure 44. The minimum heat power due to current mismatch is found when the top and middle subcells generate the same current (i.e. under AM1.5D), however the increasing operating temperature shows a reduction of 13% which is due to the reduction of the E_g which in turn reduces the V_{oc}. For *AM* > 2 the heat increases sharply because a subcell limits the current until *AM* > 7 where the heat power is reduced mainly due to the decrease in the spectral irradiance intensity.

$$q_{heat,CM} \leq \sum_{1}^{3} \left| I_{sc,i} - I_{total} \right| \cdot V_{OC,i} \tag{66}$$

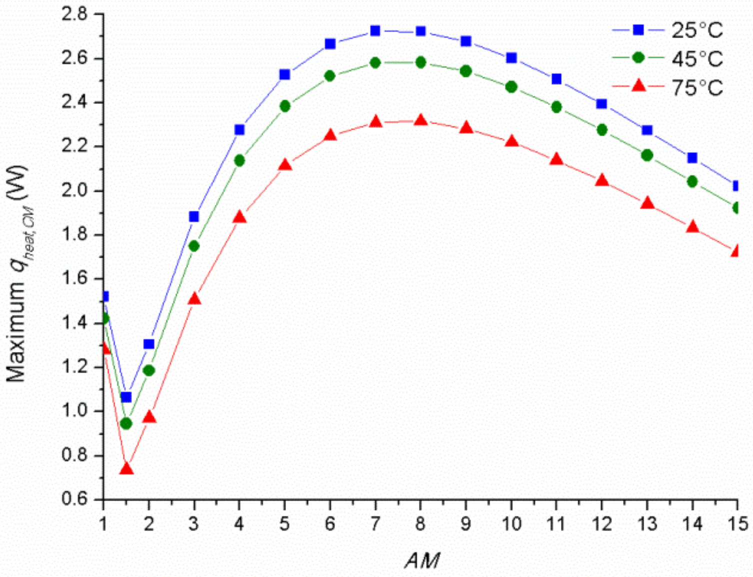

Figure 44: Maximum heat power produced on the solar cell due to current mismatch for a range of air mass values and operating temperatures at *CR* = 500×.

4.3.2.6. Validation of electrical model

For validation purposes, the electrical model used the same inputs as Kinsey and Edmondson [94] (CR = 555×, η_{opt} = 1) and was then simulated to compare the calculated electrical efficiency with measured data from Kinsey and Edmondson [94]. The C1MJ short-circuit current density values were adopted directly from Kinsey and Edmondson [94] for the four measured temperatures. The absolute root mean square error ($ARMSE$) of efficiency was calculated as:

$$ARMSE = \sqrt{\frac{\sum_{i=1}^{N}\left(\eta_{cell,meas}(T_{cell}) - \eta_{cell,calc}(T_{cell})\right)^2}{N}} \quad \textbf{(67)}$$

where $\eta_{cell,meas}$ is the measured electrical efficiency at T_{cell} from Kinsey and Edmondson [94] and $\eta_{cell,calc}$ is the calculated electrical efficiency from the model. These are shown graphically in Figure 45 for $ARMSE$ = 0.0025.

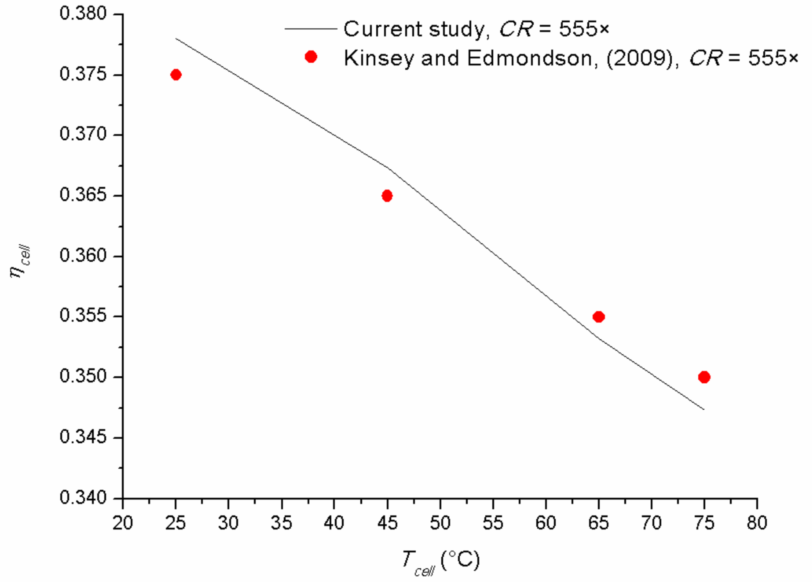

Figure 45: C1MJ calculated efficiency at 25°C, 45°C, 65°C and 75°C for AM1.5D, *CR* = 555×, η_{opt} = 1 and comparison with published data [94].

4.3.3. Thermal model (FETM)

The calculated heat power from the electrical model was used as an input to the thermal model. The geometry, thermal boundary conditions and assumptions of the C1MJ model are shown in Figure 46 and Table 16. The 3J solar cell is modelled as one entity (germanium cell) because the top and middle subcells are much thinner than the bottom and therefore they would not affect the thermal model; this is confirmed by Chou *et al.* [139]. The solar cell is attached on a DBC substrate which is made of copper (Cu)/aluminium oxide (Al_2O_3)/copper. The electrical connections are made of silver (Ag). The cell is connected to a 12A Schottky diode which, for simplicity is not modelled. The CCA (solar cell, DBC, connections) is modelled for this application in order to be more generally applicable and not specific to one particular module where all the bespoke design of packaging materials would need to be introduced. The thermophysical properties and dimensions are listed in Tables 17 and 18 respectively.

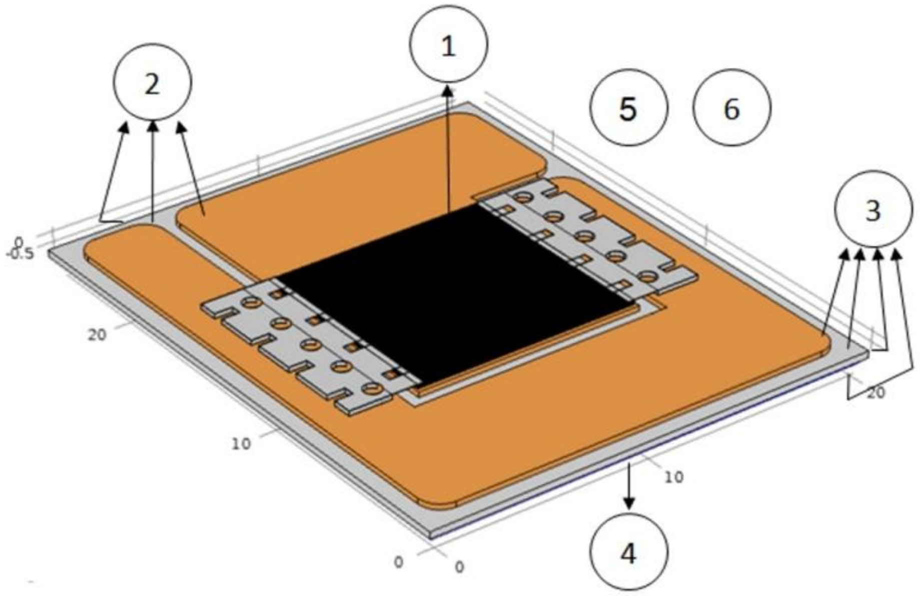

Figure 46: Geometry, thermal boundary conditions and assumptions of 3D C1MJ thermal model.

No	Region	Boundary Condition/Assumption
1	C1MJ solar cell surface	Heat source as found from EM equation (58)
2	All free surfaces on top and sides	Natural convection
3	All free surfaces	Surface to ambient radiation
4	Back plate surface	Variable h_{conv} (Table 13)
5	Ambient	Variable ambient temperature (Table 13)
6	All surfaces	Assume initial temperature (= 25°C)

Table 16: Thermal boundary conditions and assumptions.

Material	k (W/(m·K))	C_p (J/(kg·K))	ρ (kg/m^3)	ε
Ge	60	320	5323	0.9
Cu	400	385	8700	0.05
Al_2O_3	30	900	3900	0.75
Ag	430	235	10490	0.03

Table 17: Materials' thermophysical properties.

Layer	Thickness (mm)	Length (mm)	Width (mm)
C1MJ solar cell	0.19	10	10
Cu	0.25	24	19.5
Al_2O_3	0.32	25.5	21
Cu	0.25	25	20.5
Busbar	0.006	10	0.305
Contacts	0.025	10	3.5

Table 18: Assembly's dimensions.

The simulation ran using the Generalized Minimal RESidual method (GMRES) which is an iterative solver. The CCA configuration was meshed using the physics controlled mesh sequence as part of COMSOL. A mesh independency analysis was conducted by progressively increasing the number of elements until the temperature change was minimised; this was found to be at approximately 400,000 elements. Due to significantly lower computational time and relatively small error of 0.03% in maximum temperature, a fine mesh setting with 237,288 elements over a 435 mm^3 mesh volume was used.

The 3J C1MJ solar cell is modelled as a heat source. All the free areas at the top release heat to the environment through external natural convection and surface radiation. The back-plate's surface (copper) releases heat to the environment through surface to ambient radiation and also convection where the convective heat transfer coefficient is varied; the air temperature is also varied. For reliability purposes, all the cases up to a cell temperature of 100°C are examined, as the cell can degrade if operated at higher temperatures for a prolonged time [183].

As described in section 4.2 and the flowchart in Figure 33, the integrated model runs iteratively for an initial temperature of $T_{cell}(s)$ = 25°C; the electrical model calculates the heat power at 25°C and the thermal model runs until it converges. The calculated $T_{cell}(s+1)$ from the thermal model is then imported back to the electrical model to calculate the heat power at $T_{cell}(s+1)$. The iterations are continued until a difference lower or equal to 0.002K is achieved (i.e. convergence). Figure 47 shows the integrated volumetric solar cell's temperature after 6 iterations for convective heat transfer coefficients ranging from 1200 $W/(m^2 \cdot K)$ to 1600 $W/(m^2 \cdot K)$ and a constant T_{amb} = 35°C. The solution is shown to converge in all cases after the 3^{rd} iteration.

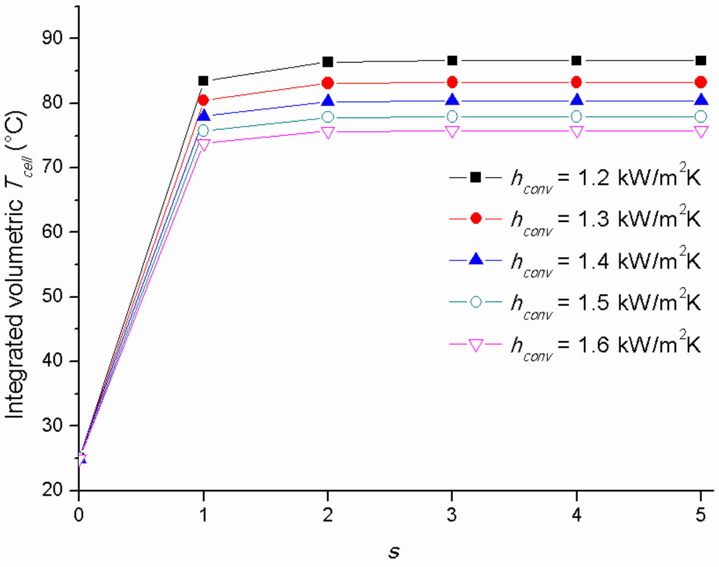

Figure 47: Integrated volumetric solar cell temperature as a function of the cycle iteration, ambient temperature T_{amb} = 35°C and AM1D.

Figure 48 shows the temperature distribution across the C1MJ solar cell for AM1D, h_{conv} = 1600 W/(m^2·K) (i.e. R_{th}=1/(h_{conv}·A) = 1.22 K/W, area of 5.13 × 10^{-4} m^2) and T_{amb} = 45°C. A maximum temperature of 90.33°C is observed at the centre of the cell while the temperatures of the top layer of the DBC board, which is not illuminated, range from 70°C at the edges to 80°C near the cell. The integrated volumetric temperature of the solar cell is 86.82°C.

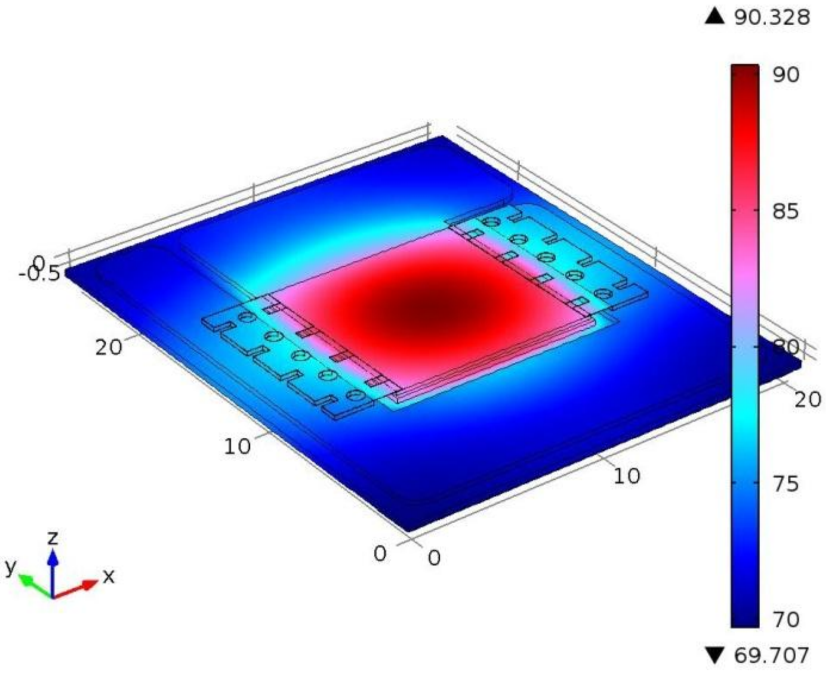

Figure 48: Temperature distribution (°C) across the C1MJ CCA for h_{conv} = 1.6 kW/(m^2·K) and T_{amb} = 45°C.

In Figure 49, the solar cell’s temperature is estimated for 1200 W/(m^2·K) $\leq h_{conv} \leq$ 1600 W/(m^2·K) and 25°C $\leq T_{amb} \leq$ 45°C. Each point on the graph represents 5 simulations/iterations as shown in Figure 47. As expected, ambient air temperature has a strong influence on the cell’s temperature, with approximately degree directly proportion increase in temperature with air temperature. At AM1D, where the integrated direct spectral intensity is 988.8 W/m^2 and for an ambient temperature of 45°C, the C1MJ CCA can be cooled sufficiently by a convective heat transfer coefficient, $h_{conv} >$ 1200 W/(m^2·K) if a maximum operation temperature at 100°C is assumed. However, if the maximum temperature is set at 90°C, then h_{conv} should be higher than 1400 W/(m^2·K). For the same spectral conditions and ambient temperature of 35°C, a heat transfer coefficient, $h_{conv} >$ 1200 W/(m^2·K) can adequately cool the solar cell's temperature well below 90°C.

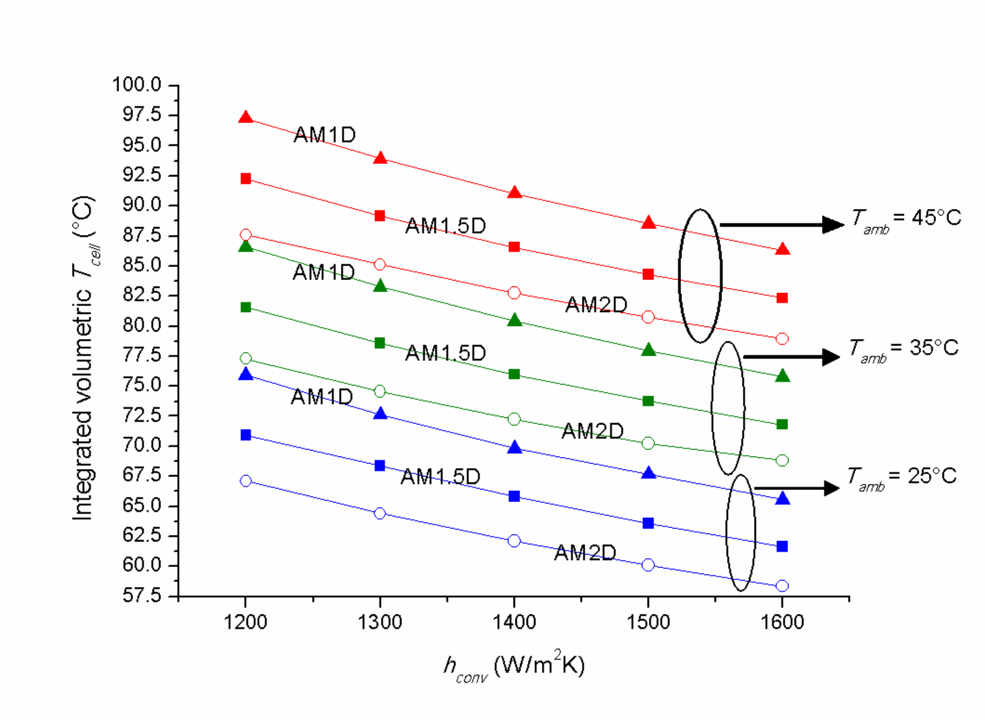

Figure 49: Integrated volumetric solar cell temperature as a function of convective heat transfer coefficient, air mass (triangle AM1D, square AM1.5D, circle AM2D) and ambient temperature (blue 25°C, green 35°C, red 45°C).

At AM1.5D conditions and ambient air temperature of 35°C, the maximum solar cell temperature is 81.93°C for a surface convective heat transfer coefficient of 1200 W/(m^2·K) and as low as 72.12°C for h_{conv} = 1600 W/(m^2·K). However, under extreme conditions (T_{amb} = 45°C), the maximum temperature is 92.59°C for h_{conv} = 1200 W/(m^2·K) and 82.64°C for h_{conv} = 1600 W/(m^2·K). At higher values of air mass, a higher thermal resistance is acceptable and therefore, only up to AM2D are presented. It is also shown that $R_{th} \leq 1.4$ K/W ($h_{conv} > 1400$ W/(m^2·K)) can be sufficient to maintain the cell below a safe operating limit without risking any long term degradation of the system. For locations with ambient temperatures lower than 40°C, a higher heat sink thermal resistance may be acceptable.

4.4. Summary, conclusions and future work

An integrated solar spectrum dependent electrical-thermal model was described for 3J solar cells under concentration followed by an application for the C1MJ CCA. It was shown that, since the solar spectrum is transient during the day, the AM1.5D does not offer representative results of the realistic operation of the solar cell in the field. Instead, designing the cooling or heat sinking requirements at $AM < 1.5$ is preferable because the 3J solar cell is not current matched and also because the heat is higher, due to higher solar radiation intensity.

This model examines the thermal behaviour of 3J solar cells under variable air mass, ambient temperature and thus electrical characteristics. It can therefore accurately quantify the thermal power which needs to be dissipated, including the excess thermal output due to current mismatch.

It was found that a CPV single cell configurations of 1 cm^2 area, can be adequately cooled passively with a heat sink thermal resistance below 1.63 K/W while for locations with extreme ambient conditions, a thermal resistance less than 1.4 K/W is needed to keep the CCA operating under 90°C.

This chapter investigated the thermal behaviour of a solar cell assembly; however the concentrator optics were not modelled in terms of their spectral transmittance or reflectivity as a function of temperature. Increasing temperatures on refractive optics will result in a change in the refractive index of the lens due to thermal expansion; this can lead to an increase in the focal length and therefore change the overall system power generation [121]. Also, the non-uniformity of the irradiance on the surface of the solar cell was not been considered in this work; Jaus *et al.* [140] considered the inhomogeneous intensity of the sun by dividing the solar cell area into different regions. Jaus *et al.* [140] did not consider the spectral dependent irradiance, which is considered here. If the spectral optical efficiency as a function of temperature and the inhomogeneity of spectral irradiance are incorporated in the model [194], the accuracy of the model is likely to be increased further.

Chapter 5: Experimental validation of modelling procedure

The experimental validation of the numerical models presented earlier is the subject of this chapter. An outdoor characterisation has been performed in Albuquerque, NM for a Suncore HCPV monomodule. Firstly, the spectral changes have been monitored under clear-sky conditions using a sunphotometer that measured the *AOD* and *PW*. These values were then imported in SMARTS2 to generate the spectrum. The spectrum was used as an input in the EM to simulate the electrical characteristics. A three-dimensional thermal model has been developed in COMSOL Multiphysics to predict the thermal behaviour of the monomodule. The temperatures in places near the cell were compared to measurements. The procedure validates each model independently and also as an integrated model according to the process flow diagram presented in Chapter 3.

5.1. Description of numerical model for DDM-1090× monomodule

The system under study is the DDM-1090× monomodule. As mentioned in Chapter 3, the *DNI* is concentrated by a SoG Fresnel lens. A secondary optic is used to homogenise the solar flux on the solar cell surface. The solar cell is attached on a DBC substrate but instead of Al_2O_3, it uses an AlN (aluminium nitride) which offers greater thermal conductivity (see Tables 17 and Table 20). A Schottky bypass diode 15 A is also incorporated to provide protection (from hot spots) to the cell. The CCA is attached to a radially finned aluminium alloy (Al-6063; will be referred to as Al) heat sink by a thermal interface material (TIM). The total area of the heat sink is 0.192 m^2 and consists of 11 fins. Sylgard-184 encapsulates the assembly. A 3D FETM model has been developed to predict the instantaneous thermal behaviour of the monomodule. For simplicity, the contacts, terminals and packaging materials are not modelled. The Schottky diode is modelled as a silicon entity with a plastic packaging. The Sn-Ag-Cu (tin, silver, copper alloy) solder paste (between the solar cell and DBC board) and the TIM (between the DBC board and heat sink) are modelled as thin thermally resistive layers (0.125 mm thickness, $k = 78$ W/(m·K) and 0.05 mm thickness, $k = 2.83$ W/(m·K) respectively) [110, 195]. The geometry, thermal boundary conditions and assumptions are illustrated in Figure 50 and explained in Table 19. The thermophysical properties of the materials that have not been used in the numerical models earlier are given in Table 20. Table 21 shows the dimensions of each domain.

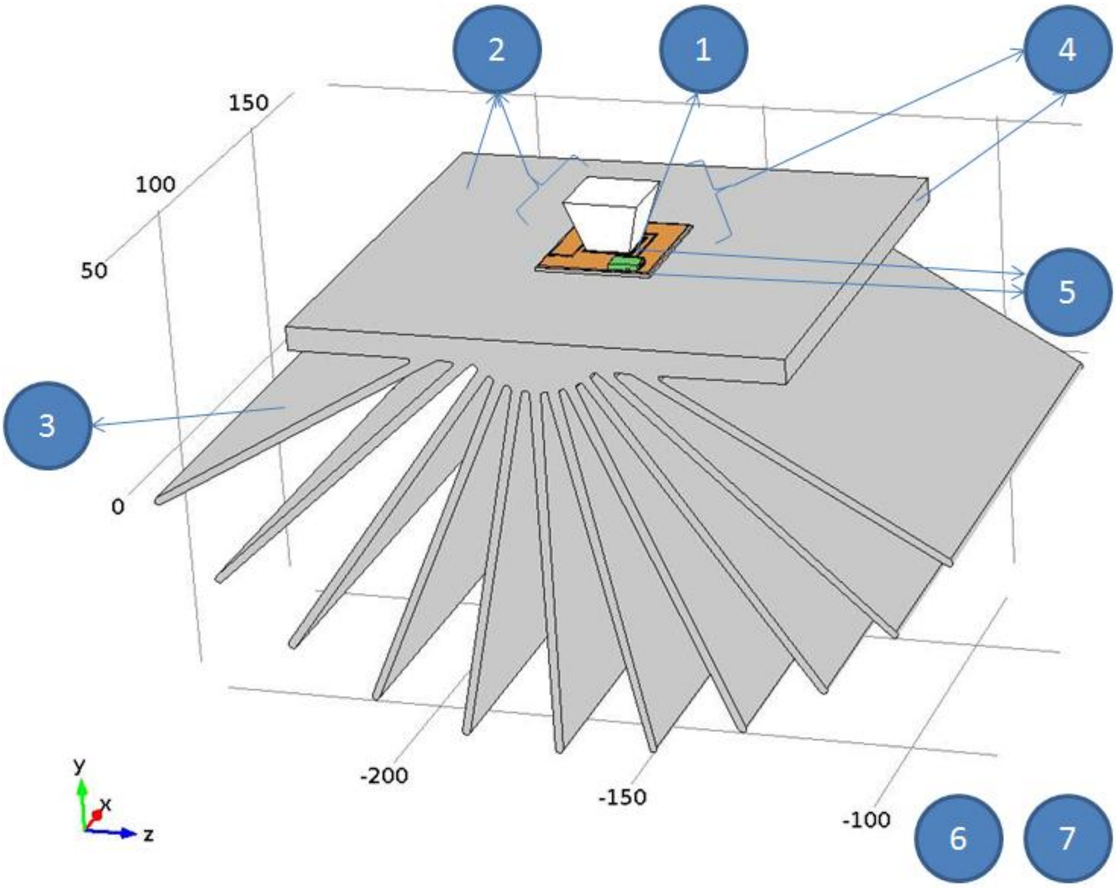

Figure 50: Geometry, thermal boundary conditions and assumptions of DDM-1090× monomodule thermal model.

No	Region	Boundary Condition/Assumption
1	Emcore solar cell surface	Heat source at open-circuit conditions
2	All free surfaces inside	Natural convection, h_{in}
3	Extended heat sink facing ambient	Mixed convection (natural & wind), h_{HS}
4	All free surfaces	Surface radiation
5	Below DBC and solar cell	Thin thermally resistive layers
6	Ambient	Ambient temperature
7	All surfaces	Assume initial temperature (= 25°C)

Table 19: Thermal boundary conditions and assumptions of HCPV monomodule.

Material	k (W/(m·K))	C_p (J/(kg·K))	ρ (kg/m^3)
AlN	180	740	3300
Si	130	700	2329
Al	200	900	2700

Table 20: Materials' thermophysical properties; materials used earlier can be found in Table 17.

Domain	Layer	Thickness (mm)	Length (mm)	Width (mm)
Solar cell	Ge	0.185	10	10
DBC substrate	Cu	0.3	27.3	22.8
	AlN	0.635	28.3	23.8
	Cu	0.3	27.3	22.8
Diode	Si	1.2	6.15	4.75
Heat sink	Al base	5	101.6	101.6
	Al fins	~2.6[a]	65 - 75.8	101.6

[a] measured at the round edge of the fin and therefore it is an approximate value.

Table 21: Dimensions of monomodule's domains.

The solar cell is modelled as a heat source. The heat is transferred through the solid layers via conduction. All free areas inside the monomodule packaging release heat through natural convection (h_{in}) and surface radiation. The finned heat sink is exposed to the ambient and releases heat to the environment through natural and forced (caused by wind) convection (h_{HS}) and surface to ambient radiation. The ambient temperature is given and the initial temperature of all surfaces is assumed to be 25°C; the convergence is independent of initial temperature; this is discussed and verified in Chapter 3.

The GMRES solver was also used for this model, similarly to the model presented in Chapter 4. A physics-controlled mesh setting was initially tested but due to the much greater size of heat sink as compared to the CCA, the configuration was meshed using the user-controlled mesh sequence. Therefore, a non-uniform mesh was applied. A mesh independency analysis was conducted by progressively increasing the number of elements until the temperature change was minimised. From Figures 51 and 52 it can be seen that for a number of elements higher than about 800,000 (i.e. mesh sequence number 8 in Figure 52) the temperature difference between the finest mesh setting and the investigated one was near zero. Therefore, an extremely fine mesh was applied on the CCA and a fine mesh on the heat sink. This resulted to 875,664 elements over a 226,500 mm^3 mesh volume. The maximum temperature difference between the selected mesh and other finer mesh settings was 0.01%.

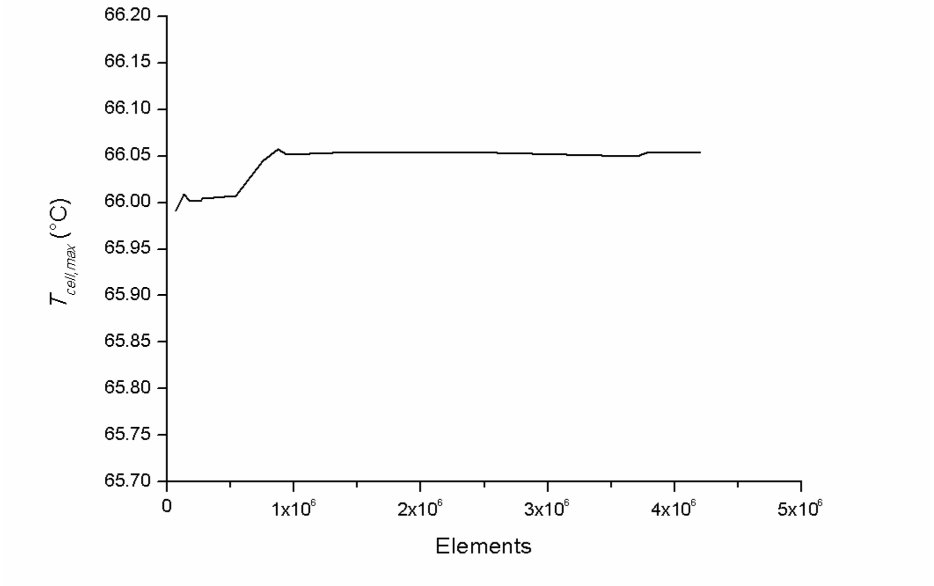

Figure 51: Variation of maximum cell temperature as a function of the number of mesh elements.

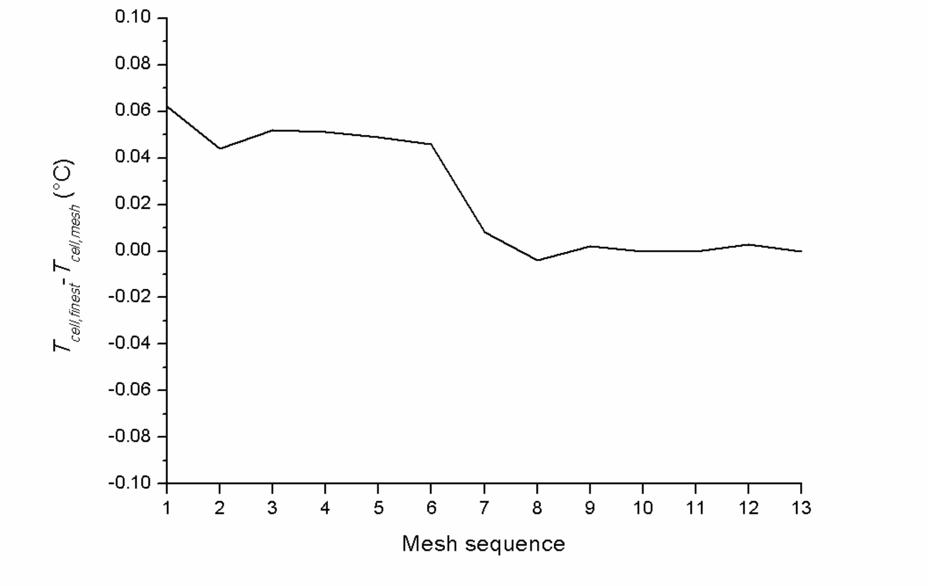

Figure 52: Temperature difference of finest mesh setting and others. After the 8th sequence the difference drops to almost zero.

5.2. Experimental validation

The measurement of solar cell temperature in concentrating systems is not a trivial procedure; the thermocouple cannot be placed in the path of the concentrated beam because the measured temperature would be much higher than the real cell temperature. Therefore, indirect methods must be applied [115, 188] as mentioned earlier in Chapter

2. A TC is usually placed at the back surface of the module, however the temperature difference between the solar cell and back surface can be large; it can also be higher than 10°C across the solar cell's surface itself [196].

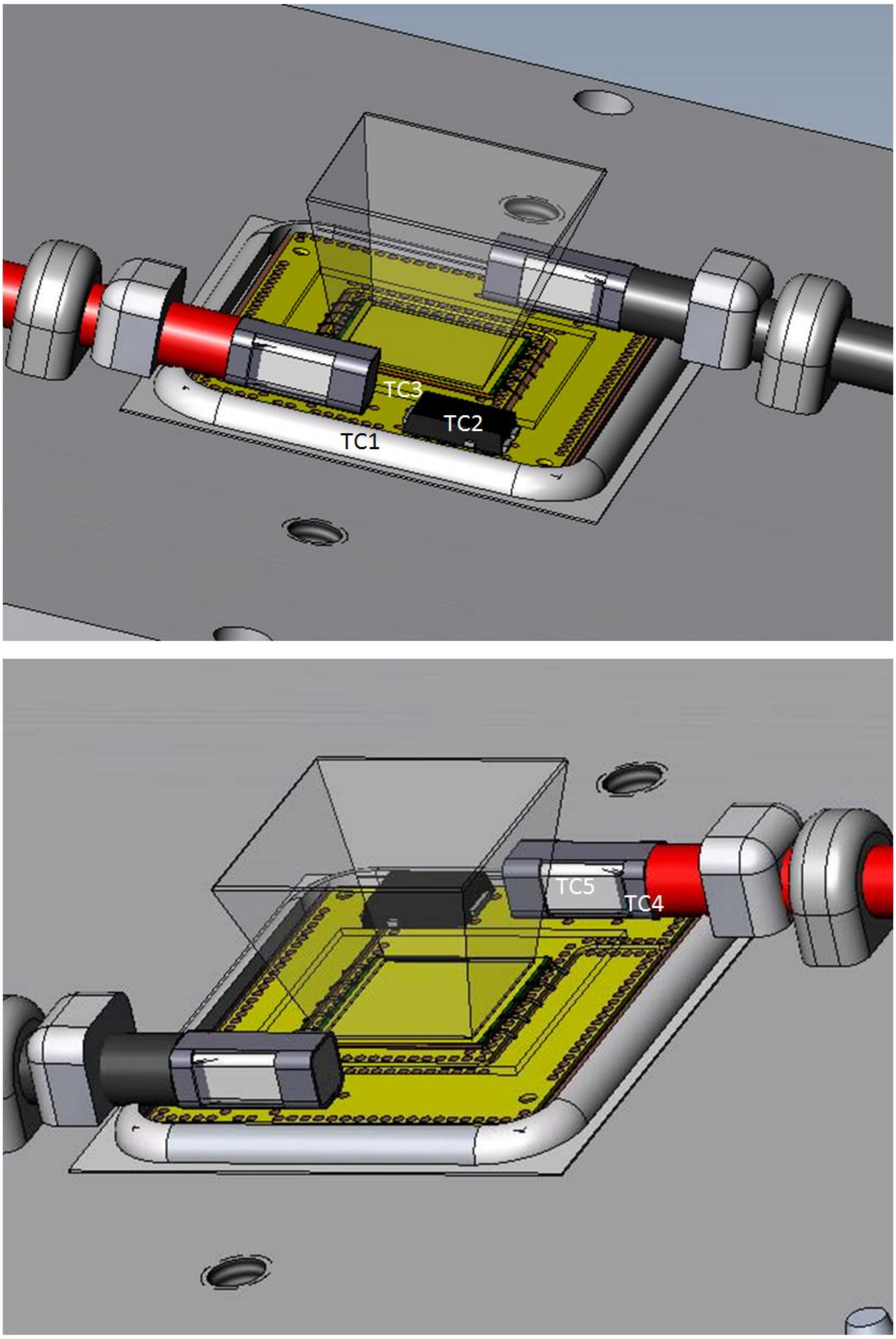

Figure 53: Thermocouple placements on the monomodule's receiver: TC1 in SS-109 sealant, TC2 on diode package, TC3 in sylgard-184, TC4 near wire insulation, TC5 on metal contact (Figure courtesy of M. Sumner, Suncore US).

In this monomodule, Suncore embedded five T-type thermocouples (TC1 - TC5) as close to the solar cell as possible (see Figure 53). In addition, a thermocouple (TC6) has been also placed in the centre of the heat sink's base (i.e. "the root" [110]). The calibrated thermocouples offer an accuracy of ±1°C.

5.2.1. Validation of spectral modelling

The prediction accuracy of *DNI* is the most important parameter when a performance of a HCPV system is assessed. As described earlier, sunphotometer measurements were taken manually during clear-sky days. The solar spectrum was then generated using SMARTS2. In order to gain confidence in the simulated spectra, a comparison between measured and modelled broadband *DNI* has been conducted.

The relative *AM* calculation and sunphotometer measurements (*AOD*, *PW*) from 25/06/2015 to 21/08/2015 in Albuquerque, NM are shown in Figures 54, 55 and 56 respectively.

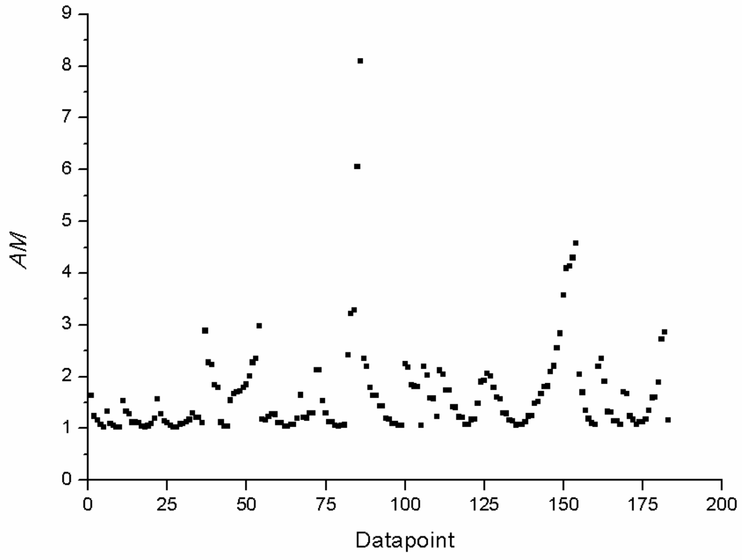

Figure 54: Relative *AM* values for period between 25/06/2015 to 21/08/2015 in Albuquerque, NM.

Due to the season (summer period in a northern hemisphere site), the majority of relative *AM* values (79.2%, or 145 out of 183 datapoints) in Figure 54 are between *AM* = 1 to *AM* = 2. In Figure 55, the *AOD* values range from 0.05 to 0.27 while for the

PW in Figure 56, the range is between 0.83 cm and 2.17 cm. A summary of maximum, minimum and average values is given in Table 22.

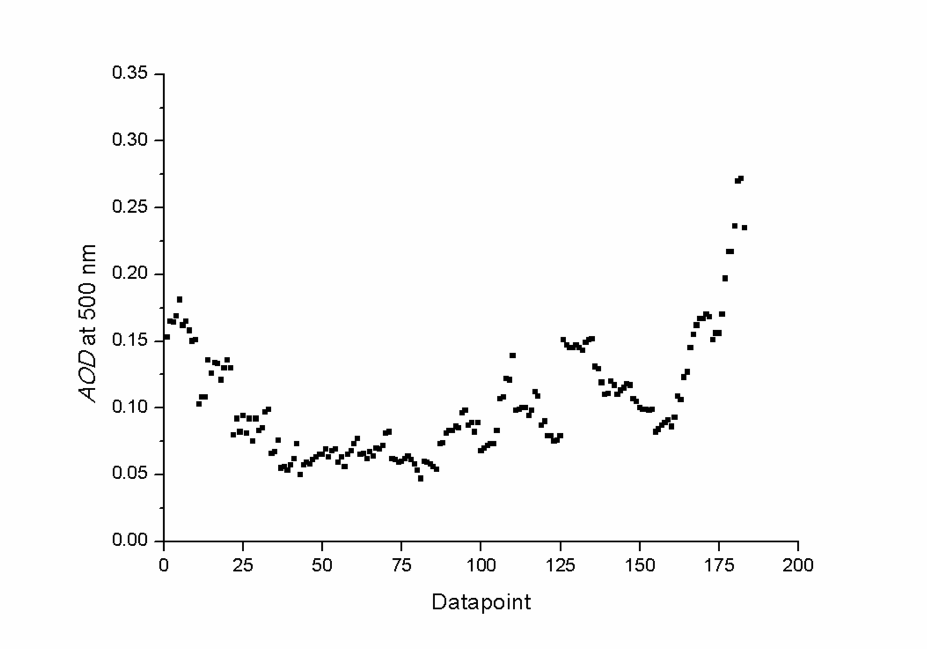

Figure 55: ***AOD*** **at 500 nm for period between 25/06/2015 to 21/08/2015 in Albuquerque, NM.**

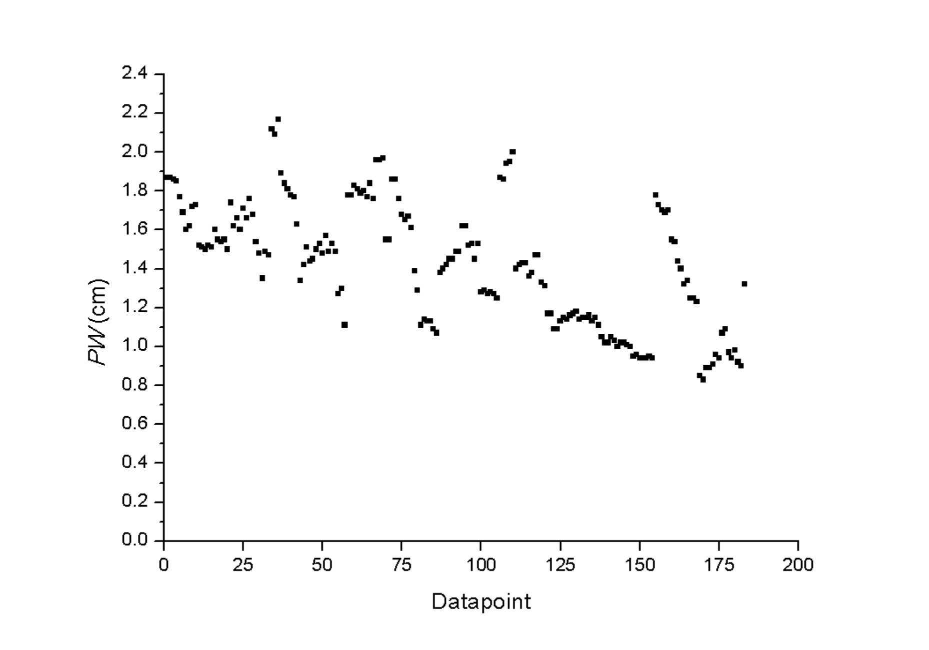

Figure 56: ***PW*** **values for period between 25/06/2015 to 21/08/2015 in Albuquerque, NM.**

Parameter	Maximum	Minimum	Average	ASTM G173-03
AM	8.09 (1.93)	1.02 (1.02)	1.63 (1.31)	1.5
AOD	0.27 (0.24)	0.05 (0.05)	0.10 (0.11)	0.084
PW (cm)	2.17 (2.17)	0.83 (0.83)	1.43 (1.45)	1.42

Table 22: Unfiltered maximum, minimum and average values of *AM*, *AOD*, *PW* and in parenthesis the values after filtering for *AM* < 2. The ASTM G173-03 values are also given as a reference.

The simulated *DNI* values are compared to pyrheliometer measurements. Pyrheliometers do not measure the spectral distribution but the broadband *DNI* hence, the simulated broadband *DNI* is obtained by the trapezoidal integral of the spectral *DNI* modelled by SMARTS2. In order to quantify the accuracy of the simulated *DNI* the following statistical parameters have been used:

The *ARMSE* [197, 198]:

$$ARMSE = \sqrt{\frac{1}{N} \cdot \sum_{i}^{N} (\Delta DNI_i)^2} \tag{68}$$

The normalised root mean square error (*NRMSE*) [81]:

$$NRMSE = \frac{ARMSE}{\frac{1}{N} \sum_{i}^{N} DNI_{measured,i}} \cdot 100 \tag{69}$$

The mean bias error (*MBE*) [62, 99]:

$$MBE = \frac{100}{N} \cdot \sum_{i}^{N} \frac{\Delta DNI_i}{DNI_{measured,i}} \tag{70}$$

The mean absolute error (*MAE*) [197, 199]:

$$MAE = \frac{1}{N} \sum_{i}^{N} \left| \Delta DNI_i \right| \tag{71}$$

where

$$\Delta DNI = DNI_{\mathrm{mod}elled} - DNI_{measured} \tag{72}$$

and N is the number of datapoints (or predictions).

A comparison over 183 datapoints is illustrated in Figure 57. It can be seen that there is a relatively good accuracy between modelled and measured data; $NRMSE$ = 5.75%, $ARMSE$ = 50.61 W/m^2, MAE = 30.51 W/m^2 and MBE = -1.85%. Taking a careful look at the comparison in Figures 57 and 58, it can be seen that the highest residuals occur for low values of irradiance; this issue is consistent with studies by Chan [99] and

Gueymard [200]. Moreover, high residuals have also been noticed during the early morning and late afternoon hours, where the *AM* was relatively higher.

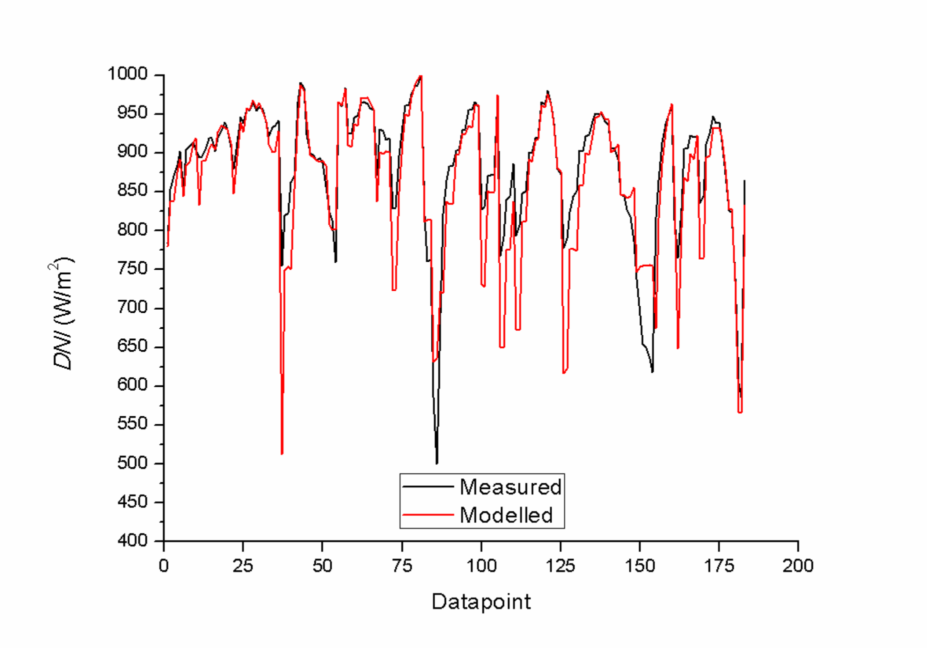

Figure 57: Comparison of measured *DNI* with modelled broadband *DNI* for period between 25/06/2015 to 21/08/2015 in Albuquerque, NM.

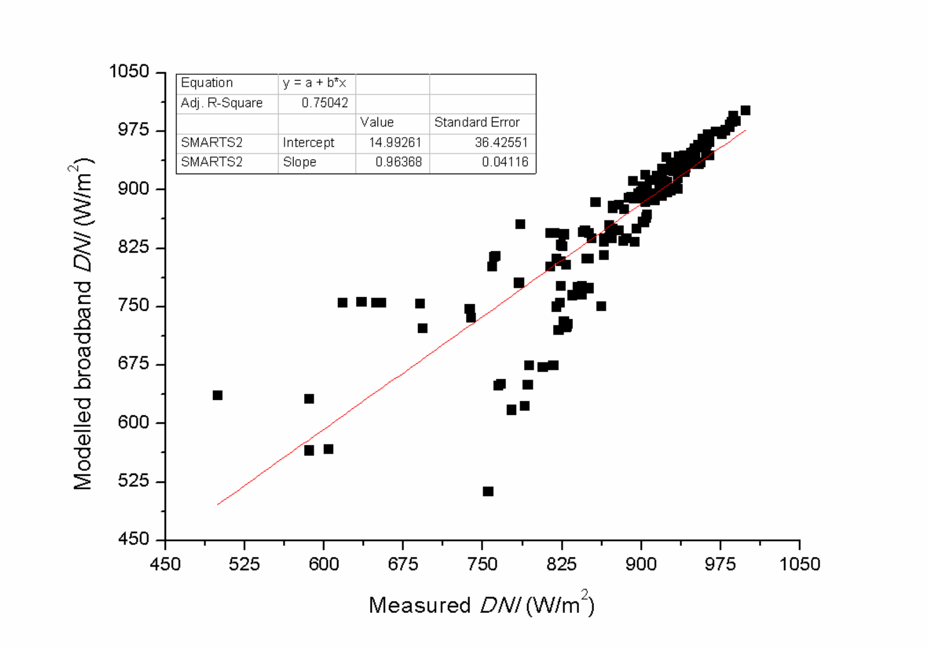

Equation	y = a + b*x		
Adj. R-Square	0.75042		
		Value	Standard Error
SMARTS2	Intercept	14.99261	36.42551
SMARTS2	Slope	0.96368	0.04116

Figure 58: : Linear regression analysis of modelled broadband *DNI* versus the measured *DNI*.

Since the main parameter affecting the *DNI* under clear-sky conditions is the *AM*, a filter has been applied for $AM < 2$. The filtering criterion reduced the datapoints to 145 and the comparison is shown in Figure 59. The $AM < 2$ filter has significantly improved the accuracy of the SMARTS2 generated *DNI* showing *NRMSE* = 2.80%, *ARMSE* = 25.64 W/m^2, *MAE* = 16.75 W/m^2 and *MBE* = -1.62%. In addition, the regression analysis is illustrated Figure 60.

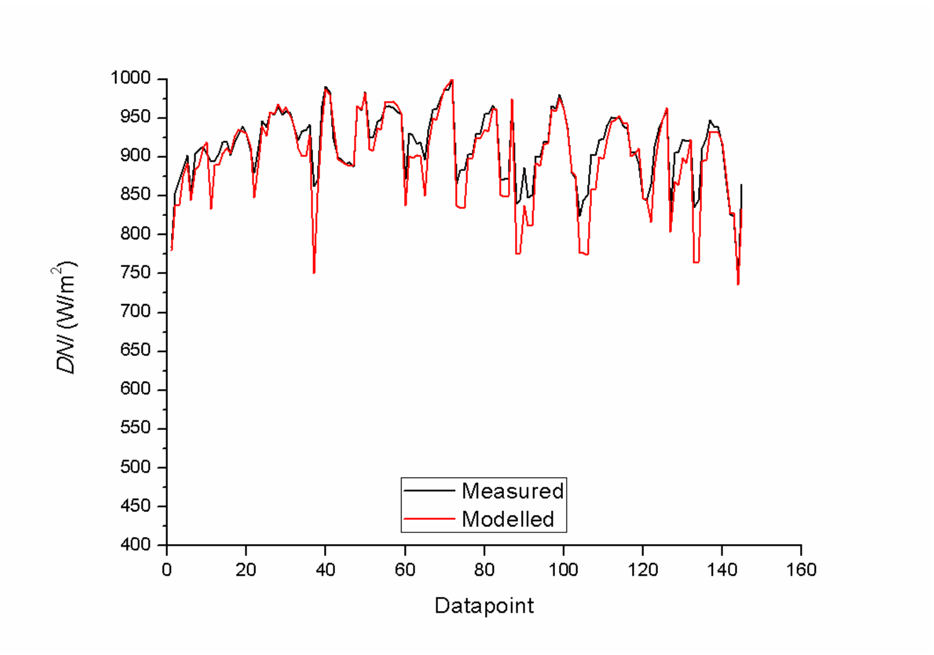

Figure 59: Comparison of measured *DNI* with modelled broadband *DNI* after the *AM* < 2 filter for period between 25/06/2015 to 21/08/2015 in Albuquerque, NM.

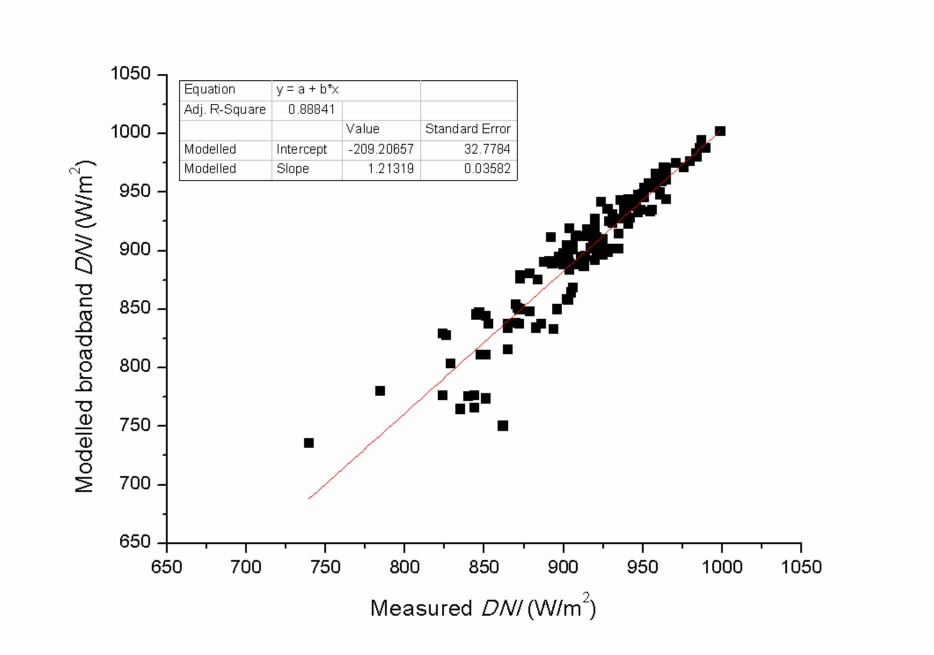

Figure 60: Linear regression analysis of the modelled broadband *DNI* versus the measured *DNI* after the *AM* < 2 filter.

A summary of the errors for both comparisons is shown in Table 23. The *MBE* in both cases is negative and shows that the modelled *DNI* underestimates the measured. The *NRMSE* is 5.75% when no filter is applied and as explained above, the higher residuals were due to the higher *AM* during the early morning and late afternoon hours; when the *AM* < 2 filter was applied the *NRMSE* dropped to 2.8%. The *ARMSE* and *MAE* of both methods are well below 100 W/m^2 which according to the results of the *DNI* validation of Chan *et al.* [54] are reasonable.

Method	***NRMSE* (%)**	***ARMSE* (W/m^2)**	***MAE* (W/m^2)**	***MBE* (%)**
No filter	5.75	50.61	30.51	-1.85
Filtered	2.80	25.64	16.75	-1.62

Table 23: A summary of errors for both methods comparing the modelled against the measured *DNI*.

5.2.2. Validation of thermal modelling

Before validating the electrical model, it is important to validate the thermal behaviour of the monomodule in terms of temperature prediction on certain parts of the receiver. In order to achieve this in a relatively low computational time, a parametric study has been performed in COMSOL Multiphysics by varying one parameter at a time for the following ranges:

- 45 W $\leq q_{heat} \leq$ 80 W, step 5 W
- 10°C $\leq T_{amb} \leq$ 40°C, step 10°C
- 10 W/(m^2·K) $\leq h_{HS} \leq$ 24 W/(m^2·K), step 2 W/(m^2·K)

Since the *I-V* measurements were taken at open-circuit conditions (i.e. no electrical energy was harvested), the q_{heat} was calculated by:

$$q_{heat,oc} = \int_{280}^{4000} \lambda \cdot DNI(\lambda) \cdot CR_{geo} \cdot T_{SoG}(\lambda) \cdot \eta_{opt,2} \cdot A_{cell} \cdot d\lambda \tag{73}$$

where $T_{SoG}(\lambda)$ is the spectral transmittance of the SoG Fresnel lens and $\eta_{opt,2}$ is the optical efficiency of the secondary optic (homogeniser). In instances where spectral data were not available, the broadband *DNI* value was used instead and a T_{SoG} = 0.91.

The solution time of the simulations of the parametric study was 6 hours, 42 minutes and 7 seconds. Regression analysis has been performed to quantify the temperatures on the solar cell (volumetric), diode (average on top surface) and heat sink (average on central fin; i.e. as close to the "root" as possible) as a function of the parameters described in the bullet points of this section (i.e. q_{heat}, T_{amb}, h_{HS}). The other TC readings were not compared since they were not modelled for simplicity. The equations are given below ((74) to (76)) and the intercepts, coefficients and R^2 values are shown in Table 24.

$$T_{cell} = \alpha_{cell} + \beta_{cell} \cdot q_{heat} + \gamma_{cell} \cdot T_{amb} + \delta_{cell} \cdot h_{HS} \tag{74}$$

$$T_{diode} = \alpha_{diode} + \beta_{diode} \cdot q_{heat} + \gamma_{diode} \cdot T_{amb} + \delta_{diode} \cdot h_{HS} \tag{75}$$

$$T_{HS} = \alpha_{HS} + \beta_{HS} \cdot q_{heat} + \gamma_{HS} \cdot T_{amb} + \delta_{HS} \cdot h_{HS} \tag{76}$$

Coefficient	**Solar cell**	**Diode**	**Heat Sink**
α (°C)	22.317	22.108	22.409
β (°C/W)	0.654	0.437	0.385
γ	0.995	0.993	0.995
δ (°C/(W·m^{-2}K^{-1}))	-1.305	-1.284	-1.308
R^2	0.986	0.984	0.983

Table 24: Intercepts and coefficients of linear regression performed for the calculation of solar cell, diode and heat sink temperatures.

For the temperatures comparison, the "clearest" day during the measurements period has been selected (13th of August 2015). The following filters have been applied to the measured data:

- 5 minute DNI deviation < 2%
- tracking error < 0.3°
- $WS < 5$ m/s.

No clear-sky filter was required. The convective heat transfer between the heat sink and ambient air is also affected by the wind speed and direction. Constant values of h_{HS} exhibited a large error due to the variable forced convection caused by the wind. In order to take this into account the h_{HS} has been optimised to fit the measured data [201, 202]. Therefore, assuming that the natural and forced convective heat transfer coefficient was $h_{HS} = 15 + 1.5 \cdot WS$ and the natural convective heat transfer coefficient inside the module $h_{in} = 5$ W/(m^2·K), the comparison of the measured against the simulated T_{diode} is shown in Figure 61; the solar cell temperature prediction is also shown with an average ΔT between the simulated cell and diode temperatures of about 15.5°C. The highest residuals between simulated and measured diode temperatures occur around noon, although the DNI, T_{amb}, WS are relatively constant (less than 1% change). This can be attributed to the wind direction and the tracker position that have not been taken into account in the analysis. Nevertheless, the errors of the T_{diode}

prediction are *NRMSE* = 4.6%, *ARMSE* = 2.85°C, *MAE* = 2.18°C and *MBE* = 0.56%; these values are considered acceptable, because such systems typically operate at temperatures between 50°C to 80°C [203].

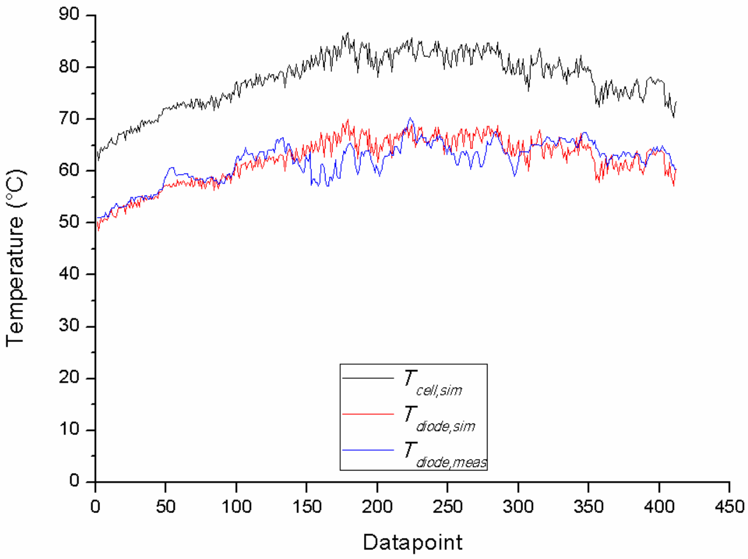

Figure 61: T_{cell} prediction and comparison of measured with simulated T_{diode} on the 13th of August 2015 in Albuquerque, NM. Simulated T_{cell} is also illustrated as a reference.

In addition, the comparison of the measured against the simulated heat sink temperature is shown in Figure 62 for *NRMSE* = 5.68%, *ARMSE* = 3.27°C, *MAE* = 2.67°C and *MBE* = 1.75%. The higher error, compared to the T_{diode}, was expected because the TC was attached manually in the "root" of the heat sink. Equation (76) estimates the average temperature between the central located fins (assuming that it is directly below the solar cell) and therefore the higher errors were caused due to the inaccurate placement of the TC on the heat sink. The average ΔT of simulated T_{cell} and measured T_{HS} was found to be approximately 20°C.

Parameter	Value
$I_{sc,ref}$ (A)	11.54
$V_{oc,ref}$ (V)	3.15
β (V/°C)	-4.5E-3
n	5
$T_{cell,ref}$ (°C)	25

Table 25: Input parameters for the T_{cell} calculation using the V_{oc}-I_{sc} method.

The predicted volumetric cell temperature has been compared with the V_{oc}-I_{sc} method described earlier in Chapter 2 (equation (25)). The input parameters of the equation and

CSTC values of the monomodule are given in Table 25. A very good agreement between the two methods is shown in Figure 63 for *NRMSE* = 3.03%, *ARMSE* = 2.36°C, *MAE* = 1.94°C and *MBE* = -0.03%.

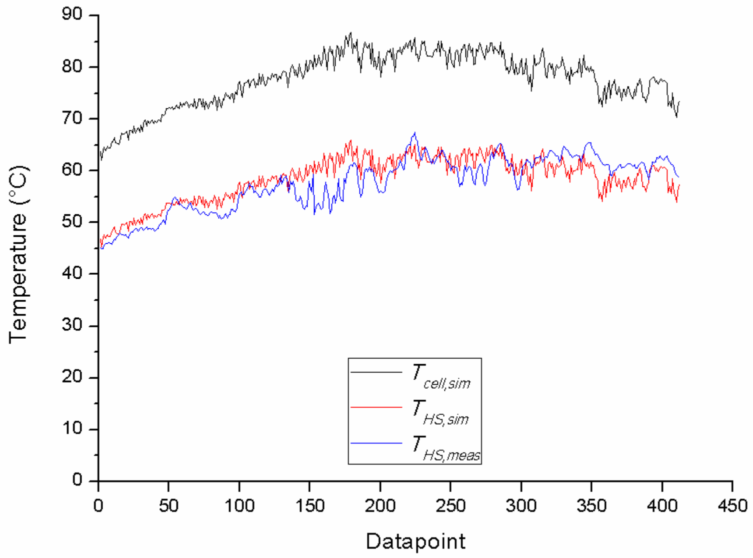

Figure 62: T_{cell} prediction and comparison of measured with simulated T_{HS} on the 13th of August 2015 in Albuquerque, NM. Simulated T_{cell} is also illustrated as a reference.

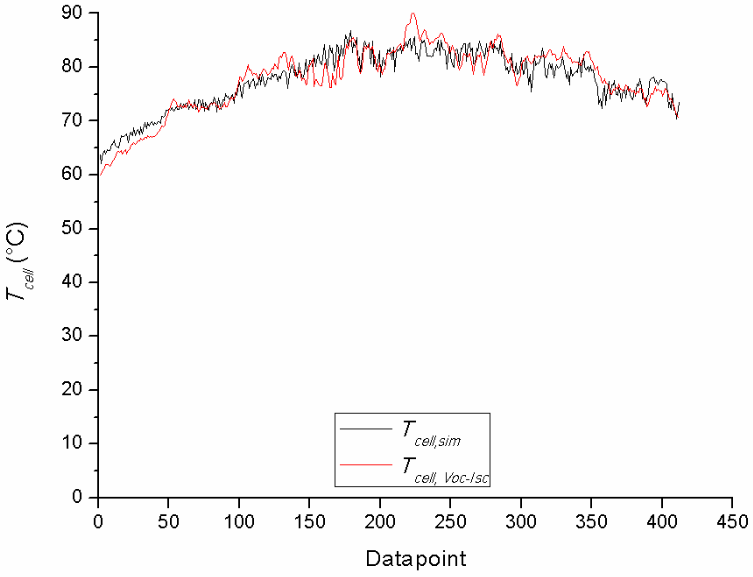

Figure 63: Comparison of simulated T_{cell} against the V_{oc}-I_{sc} method of calculating T_{cell} on the 13th of August 2015 in Albuquerque, NM

The average global R_{th} of the monomodule was found to be 0.28 K/W and the effect of *WS* is shown in Figure 64. It can be seen that the increasing wind speed reduces the R_{th} however; there is evident noise in the data mainly caused by the wind direction. Further analysis is required to quantify the impact of wind direction with respect to the module's (or tracker's) position. A preliminary analysis has been presented by Castro *et al.* [204] and it was concluded that northern winds improve the convective cooling of the modules (compared to the western winds of same speed).

It has to be noted that the coefficients used for the temperatures estimation depend on the specific monomodule's geometry, characteristics and materials. The coefficients will vary in other type of systems and should be fitted with experimental data and simulations.

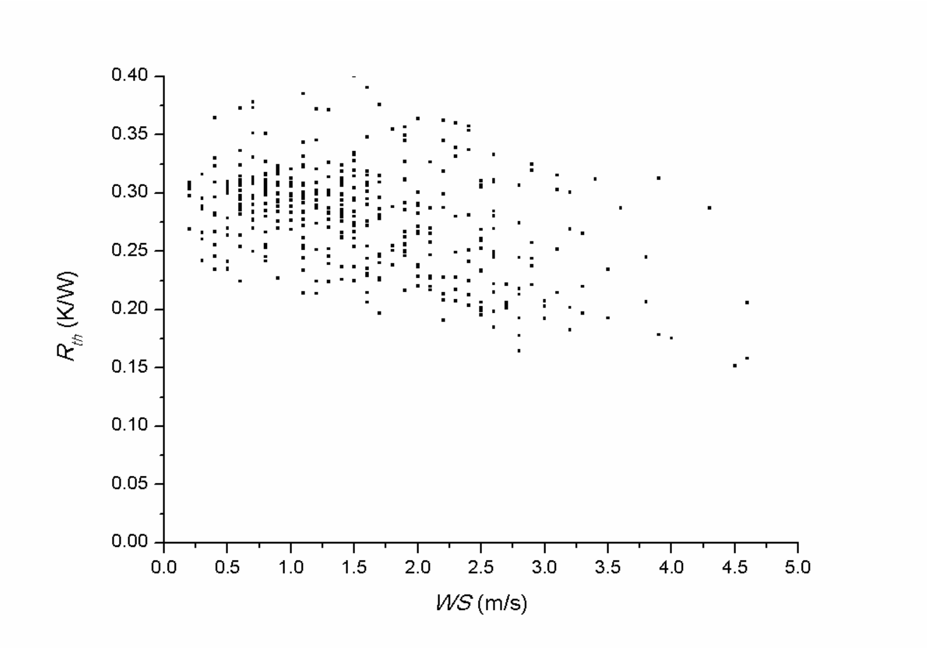

Figure 64: Effect of wind speed on monomodule's thermal resistance on the 13th of August 2015 in Albuquerque, NM.

Two examples of the temperature distribution across the monomodule are shown in Figures 65 and 66. In Figure 65, q_{heat} = 50 W, T_{amb} = 10°C and h_{HS} = 10 W/(m^2·K). The maximum cell temperature is 54.67°C in the centre of the cell while the DBC board exhibits temperatures from around 40.5°C in the edges to around 47°C near the cell. The heat sink temperature ranges from around 34.6°C at the edge to around 40.8°C in the "root". The volumetric temperatures of the solar cell and heat sink are 51.9°C and 36.7°C respectively.

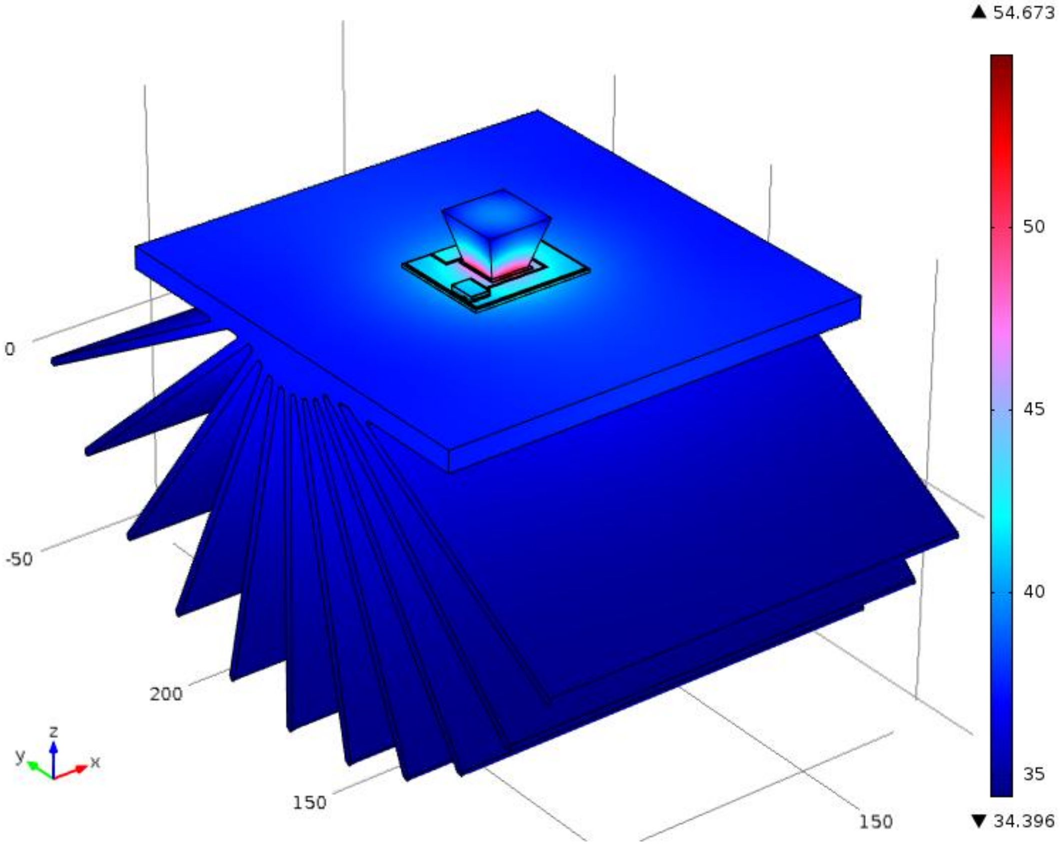

Figure 65: Temperature distribution (°C) across the monomodule for q_{heat} = 50 W, T_{amb} = 10°C and h_{HS} = 10 W/(m^2·K).

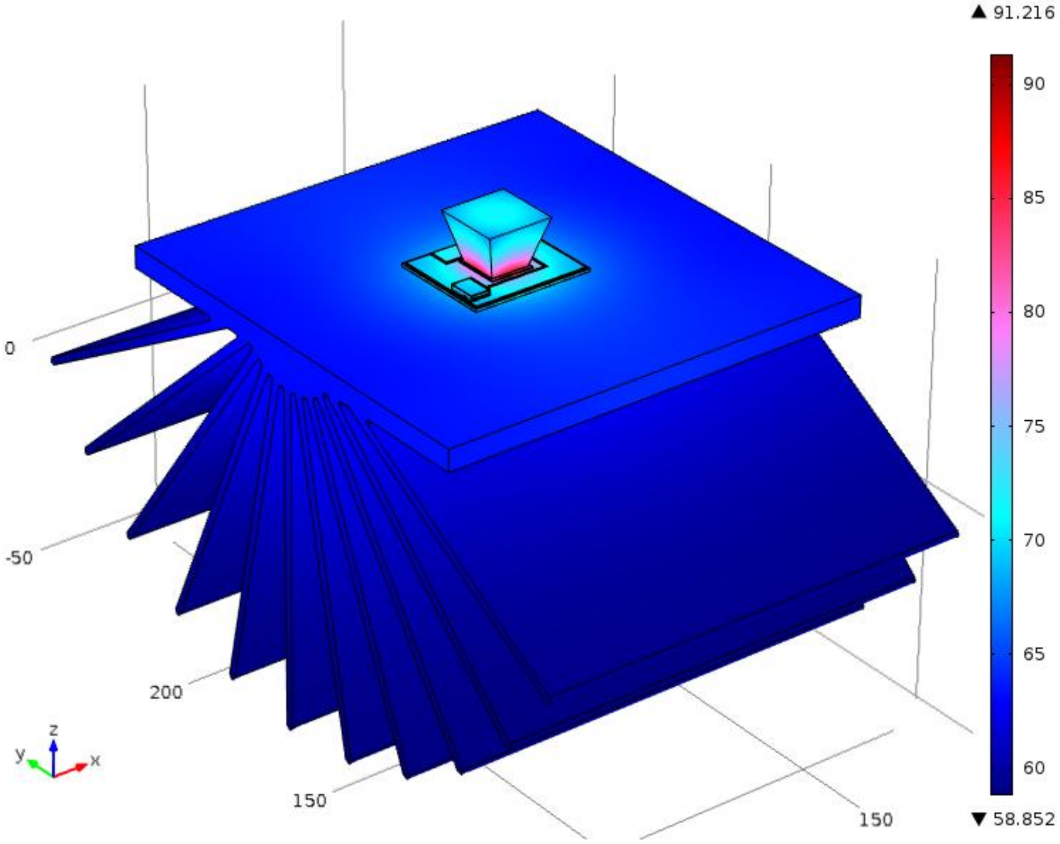

Figure 66: Temperature distribution (°C) across the monomodule for q_{heat} = 80 W, T_{amb} = 40°C and h_{HS} = 20 W/(m^2·K).

In Figure 66, the q_{heat} = 80 W, T_{amb} = 40°C and h_{HS} = 20 W/(m^2·K). In the same manner as above, the maximum cell temperature is 91.2°C in the centre of the cell while the DBC board exhibits temperatures from around 68.7°C in the edges to around 80.3°C near the cell. The heat sink temperature ranges from around 59.2°C at the edge to around 69°C in the "root". The volumetric temperatures of the solar cell and heat sink are 86.74°C and 62.4°C respectively.

5.2.3. Validation of electrical modelling

The mathematical equations used for the electrical modelling have been presented in Chapter 3. Moreover, the equipment used to measure the atmospheric, meteorological and irradiance parameters have also been presented in Chapter 3. Here, the electrical model is validated against measured data at the test site in Albuquerque, NM.

For the electrical validation, a clear-sky day has been selected in order to examine the performance of the monomodule over a course of a day. Figure 67 shows the *DNI* and *GNI* variation on the "clearest" day (13th of August 2015, 10:32 am to 17:11 pm) during the period that the experiments were conducted. From Figure 67, it can be noticed that the highest residuals between modelled and measured *DNI* are during the first 3 measurements (before noon) with a $|\Delta DNI|$ up to 48.2 W/m^2 and the lowest down to 1.9 W/m^2.

In order to calculate the I_{sc} at any temperature, a function was created that calculated the *EQE* at different temperatures using a procedure based on interpolation published by Steiner *et al.* [102]. This procedure exhibited an average difference of 1% on J_{sc} [102]. Figure 68 shows a qualitative comparison of the calculated and measured [94] *EQE* at 45°C for each subcell of the C1MJ solar cell. To quantify the difference, equation (14) was used to calculate the I_{sc} of the whole C1MJ cell using the calculated and measured *EQE* at AM1.5D; this resulted to a difference of 0.16% and 0.31% at 45°C and 75°C respectively. Higher differences (up to 5.3%) were observed for the Ge subcell but are considered insignificant because the low voltage bottom subcell never limits the total current output. The C1MJ solar cell has been used for this comparison because *EQE* data at higher temperatures were not available for the Emcore 3J solar cell. The rest of the analysis however will be using the *EQE* of the Emcore's 3J solar cell given in Figure 26.

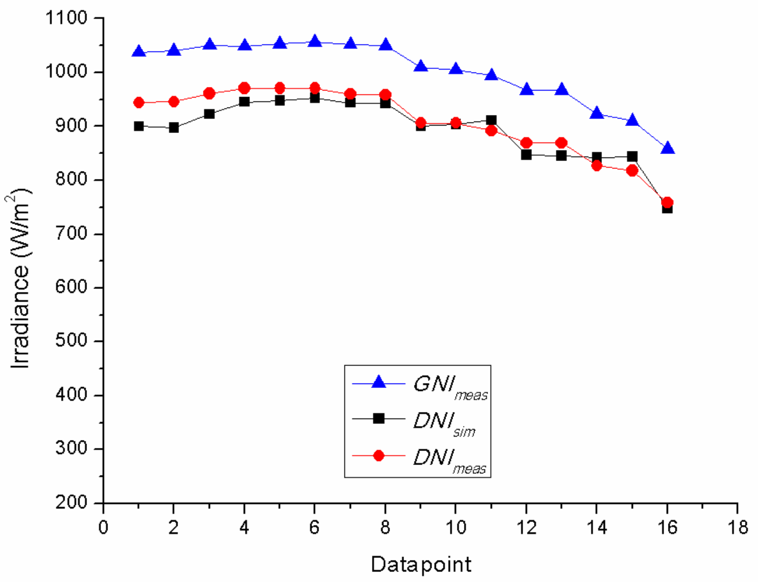

Figure 67: Measured *GNI*, *DNI* and the broadband *DNI* generated by SMARTS2 on the 13th of August 2015 in Albuquerque, NM.

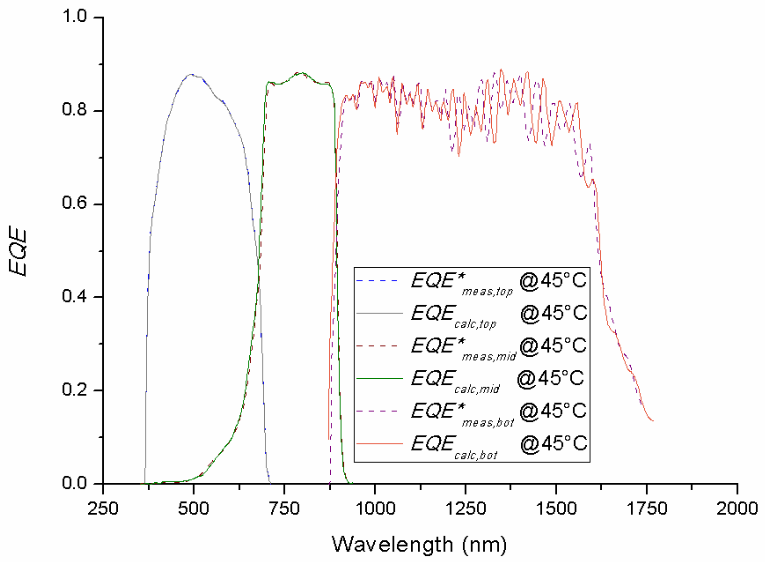

Figure 68: *EQE* comparison of simulated and measured [94] data at 45°C for each subcell of the CMJ solar cell. The measured *EQE* at 25°C is used to calculate the *EQE* at any temperature. The * indicates the *EQE* data taken from Kinsey and Edmondson [94].

The spectral transmittance of the SoG Fresnel lens (Figure 25) has been assumed to be independent of any temperature changes. Moreover, the optical efficiency of the secondary optic has been adjusted to 80% to match the I_{sc} at CSTC.

The T_{cell} was calculated based on equation (74). The inputs to the electrical model are given in Table 26 and the *I-V* curve comparison of the simulated against the measured data is presented in Figure 69. Moreover, the comparisons between each simulated and experimentally measured parameter are exhibited in Figures 70, 71, 72, 73 for I_{sc}, V_{oc}, P_{mp} and *FF* respectively.

Subcell	**1**	**2**	**3**
k **(A/(cm^2·K^4))**	5.3E-9	4.3E-8	10.5E-6
n	1.82	1.68	1.5
γ	2	2	2
R_s (Ω)	0.045		

Table 26: Input parameters to the electrical model.

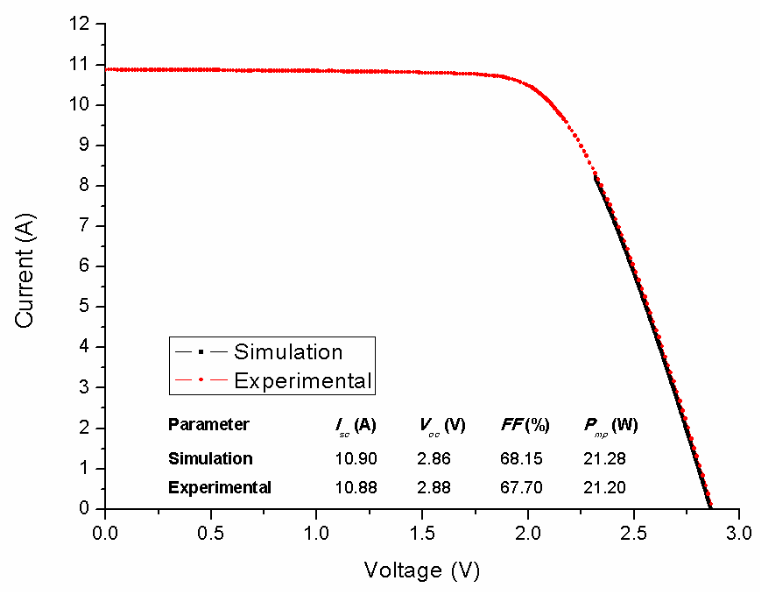

Parameter	I_{sc} (A)	V_{oc} (V)	*FF*(%)	P_{mp} (W)
Simulation	10.90	2.86	68.15	21.28
Experimental	10.88	2.88	67.70	21.20

Figure 69: Comparison of simulated *I-V* curve against the experimentally measured at 14:24 pm of the 13th of August 2015 in Albuquerque, NM.

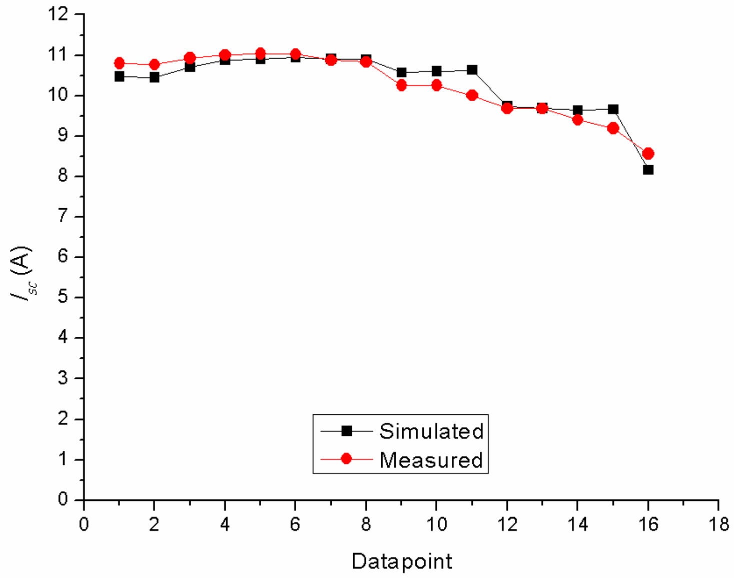

Figure 70: Comparison of simulated I_{sc} against the experimentally measured on the 13th of August 2015 in Albuquerque, NM.

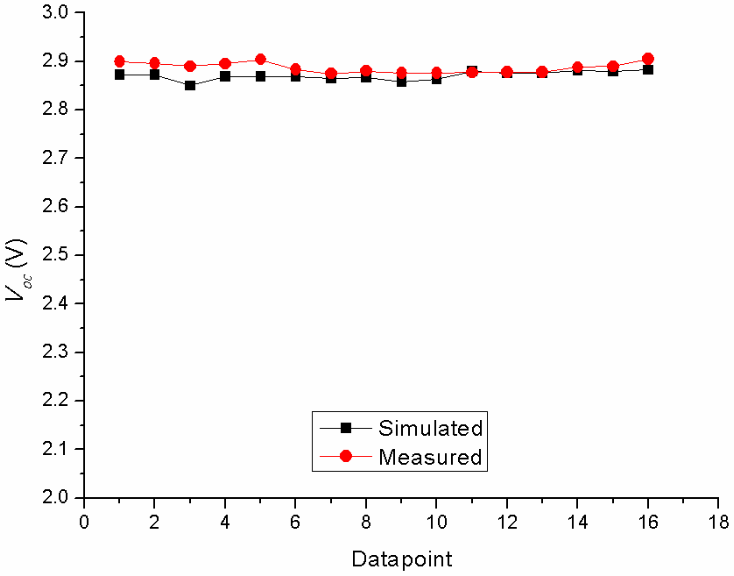

Figure 71: Comparison of simulated V_{oc} against the experimentally measured on the 13th of August 2015 in Albuquerque, NM.

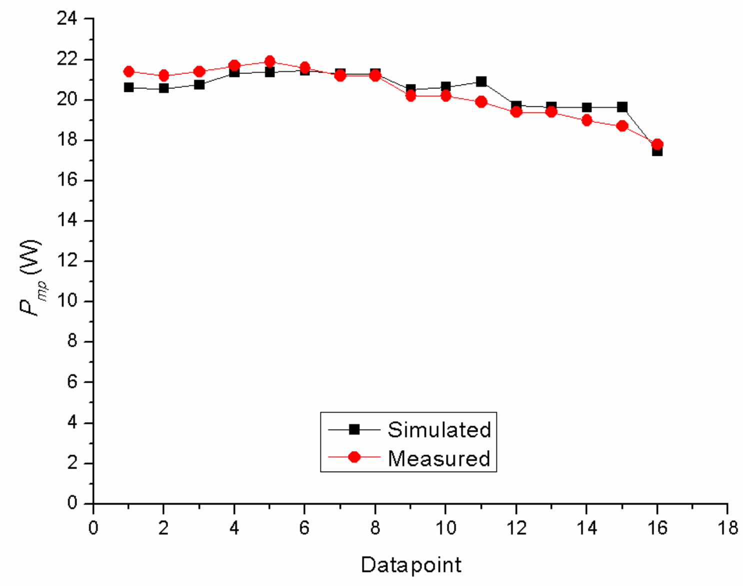

Figure 72: Comparison of simulated P_{mp} against the experimentally measured on the 13th of August 2015 in Albuquerque, NM.

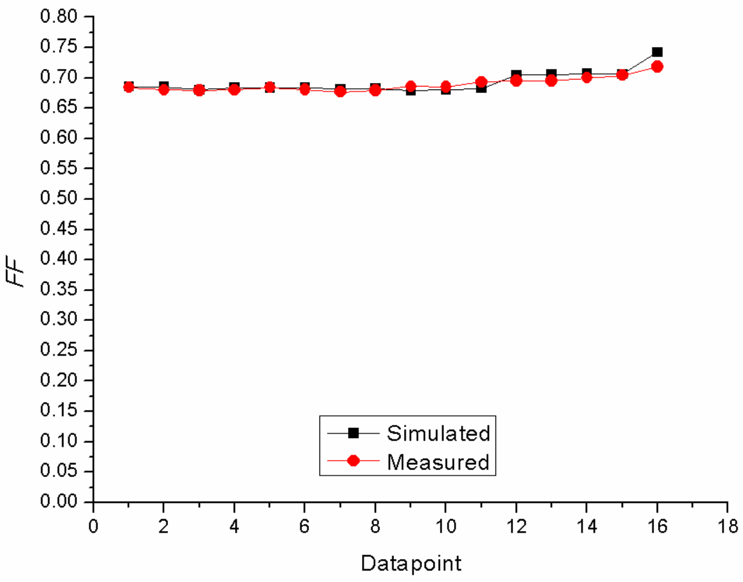

Figure 73: Comparison of simulated *FF* against the experimentally measured on the 13th of August 2015 in Albuquerque, NM.

As can be seen from Figures 69 to 73, very good agreement between measured and simulated parameters has been achieved and a summary of errors is given in Table 27. It can also be observed that the error of each prediction is highly influenced by the error of the spectral *DNI* input. Therefore, improvements on the measurement and/or calculation of spectral irradiance may reduce the errors further.

Parameter	***NRMSE***	***ARMSE***	***MAE***	***MBE***
DNI	2.78%	25.26 W/m^2	22.05 W/m^2	-1.51%
I_{sc}	2.84%	0.29 A	0.23 A	0.38%
V_{oc}	0.7%	0.02 V	0.02 V	-0.57%
P_{mp}	2.66%	0.54 W	0.47 W	0.28%
FF	1.2%	0.01	0.01	0.46%

Table 27: Summary of errors between simulated and measured I_{sc}, V_{oc}, P_{mp}, *FF* and input *DNI*.

The errors of the electrical parameters' estimation based on the T_{cell} calculated by the V_{oc}-I_{sc} method are presented in Table 28. It can be seen that V_{oc}-I_{sc} method results in lower errors on the P_{mp} and V_{oc} estimations while the method proposed in this thesis results in lower errors on the I_{sc} and *FF* estimations. Overall, the differences in errors between the two methods are very low (compare Tables 27 and 28), and therefore the proposed method can be considered acceptable for the T_{cell} calculation at both maximum power point and open-circuit conditions.

Parameter	***NRMSE***	***ARMSE***	***MAE***	***MBE***
I_{sc}	2.97%	0.3 A	0.25 A	0.39%
V_{oc}	0.55%	0.02 V	0.02 V	-0.54%
P_{mp}	2.37%	0.48 W	0.4 W	0.33%
FF	1.27%	0.01	0.01	0.48%

Table 28: Summary of errors between simulated and measured I_{sc}, V_{oc}, P_{mp}, *FF* for T_{cell} calculated using the V_{oc}-I_{sc} method.

5.3. Summary

A 3D numerical model for the DDM-1090× monomodule has been developed in order to validate the accuracy of the numerical models presented earlier. A mesh independency analysis has also been presented.

The modelling procedure has been validated independently in terms of the irradiance simulation and temperature prediction and also integrated in terms of the electrical behaviour prediction using the aforementioned as inputs. It has been shown that SMARTS2 predicts well the spectral *DNI* input, especially for $AM < 2$ (*NRMSE* = 2.8%).

Moreover, the T_{diode} and T_{HS} have been compared with measured data and the simulated T_{cell} with the V_{oc}-I_{sc} method. Good agreement has been achieved in all cases with *NRMSE* between 3.03% and 5.68%. It is important to highlight that the proposed T_{cell} estimation method can be used at both maximum power point and open-circuit conditions. It has been concluded that in order to improve the temperature prediction, the tracker position and wind speed direction should be taken into account in future studies.

The electrical model has been validated in terms of the I_{sc}, V_{oc}, P_{mp} and *FF* with *NRMSE* of 2.84%, 0.7%, 2.66% and 1.2% respectively. As expected, the error of the spectral *DNI* input propagates into the prediction of the electrical characteristics and therefore, an improvement on the measurement and/or calculation of spectral irradiance may reduce the errors further. The model was also simulated based on T_{cell} inputs calculated by the V_{oc}-I_{sc} method. It was shown that the differences between the two models were very low and therefore the proposed T_{cell} calculation is acceptable.

In summary, it was demonstrated that when adequate high-quality atmospheric data are available for a specific location, it is possible to satisfactorily predict the spectral, electrical and thermal behaviour of HCPV systems based on the proposed integrated modelling procedure. Moreover, the models can be used by HCPV designers in order to calculate the cooling requirements and avoid any possible over-sizing related to increased material usage, weight and cost, or under-sizing risking the system's reliability.

Chapter 6: The impact of atmospheric parameters on the spectral, electrical and thermal performance of a concentrating III-V triple-junction solar cell: case studies

The spectral sensitivity and cooling requirements of a concentrating 3J solar cell under variable *AM* has been investigated in Chapter 4. However, the atmospheric parameters such as the *AOD* and *PW* also change the distribution of the solar spectrum in a way that the spectral, electrical and thermal performance of a 3J solar cell is affected. In this chapter, the influence of the spectral changes on the performance of each subcell and whole cell has been analysed. It is shown that increasing the *AM* and *AOD* have a negative impact on the spectral and electrical performance of 3J solar cells while increasing the *PW* has a positive effect, although, to a lesser degree. A three-dimensional finite element analysis model is used to quantify the effect of each atmospheric parameter on the thermal performance for a range of heat transfer coefficients from the back-plate to the ambient air and also ambient temperature. It is shown that a heat transfer coefficient greater than 1300 W/(m^2·K) is required to keep the solar cell under 100°C at all times. In order to get a more realistic assessment and also to investigate the effect of heat transfer coefficient on the annual energy yield, the methodology is applied for four US locations using data from a typical meteorological year (TMY3).

This chapter contains material from Theristis *et al.* [205-207]:

M. Theristis, C. Stark, and T. S. O'Donovan, "Determination of the cooling requirements for single cell photovoltaic receivers under variable atmospheric parameters," in *Photovoltaic Specialist Conference (PVSC), 2015 IEEE 42nd*, 2015.

M. Theristis, E. F. Fernández, C. Stark and T. S. O’Donovan, "A theoretical analysis of the impact of atmospheric parameters on the spectral, electrical and thermal performance of a concentrating III–V triple-junction solar cells," *Energy Conversion and Management*, vol. 117, pp.218-227, 2016.

M. Theristis, E. F. Fernández, J. P. Ferrer-Rodríguez, C. Stark, and T. S. O'Donovan, "Energy Yield Assessment of a High Concentration Photovoltaic Receiver Based on Simulated Spectra from Typical Meteorological Year Datasets", in *12th International Conference on Concentrator Photovoltaic Systems (CPV-12)*, Freiburg, Germany, 2016.

6.1. Introduction

HCPV systems use refractive or reflective optics to concentrate sunlight onto a smaller area made of high efficiency MJ solar cells. Currently triple-junction (3J) solar cells made of GaInP/GaInAs/Ge are available in the market with an efficiency of up to 42% [208]. The in-series connection of such cells and the different energy band-gap of each subcell causes a high spectral sensitivity. It is therefore necessary to model the effect of changing spectrum on the spectral, electrical and thermal performance of such devices. The HCPV performance is predominantly affected by the incident *DNI* [209] which in turn, is mainly determined by cloud cover [210], but also by changes in spectrum by variations of *AM*, *AOD* and *PW*.

As mentioned earlier in Chapter 2, HCPV modules can be either rated indoors and outdoors [115] under CSTC, i.e. AM1.5D, DNI = 1000 W/m^2 and cell temperature T_{cell} = 25°C or outdoors under Concentrator Standard Operating Conditions (CSOC, i.e. AM1.5D, DNI = 900 W/m^2, T_{amb} = 20°C and wind speed WS = 2 m/s). The spectral conditions during the CSOC or outdoor *I-V* measurements for translation to CSTC [115] vary significantly compared to the standard ratings depending on the location and time of year because of the different atmospheric characteristics. According to Muller *et al.* [115], the spectral filtering criteria have not yet been agreed within the International Electrotechnical Commission (IEC). It is important therefore, to develop models or methods to identify the effects of each atmospheric parameter on the spectral and hence, the electrical and thermal performance of HCPV systems. Integrated modelling is necessary to enable the quantification of the spectral mismatch that will decrease the solar cell's electrical conversion efficiency resulting in an increase in heat, hence higher operating temperatures which will further reduce the electrical efficiency [178].

The passive heat exchangers can be different in terms of their area and geometry depending on the application [211]. In order to achieve a T_{cell} below safe operating limits and to avoid long-term reliability issues, the incident *DNI* needs to be quantified because it is the dominant factor which contributes to the heat power production. Due to the MJ solar cell's spectral sensitivity, analytical modelling is required to estimate the cooling requirements taking into consideration the ambient and atmospheric conditions. Moreover, although the temperature dependence of MJ solar cells is lower than silicon cells [212], it is crucial to design a robust cooling device to avoid elevated temperatures and therefore possible degradation issues or even the cause of fire [197, 213]. Oversizing the heat exchanger however will result in increasing the system's cost needlessly. Hence, a trade-off between reliability and cost must be achieved.

This chapter focuses on the accurate quantification of heat and therefore the cooling requirements using the h_{conv} (or the inverse R_{th}) from the back-plate of the CCA to the ambient air as a criterion. It extends on Chapter 4 where the impact of solar geometry (air mass) on the electrical and thermal performance of 3J solar cells was investigated. The same model is used here to assess the effect of *AM*, *AOD* and *PW* on the spectral, electrical and thermal behaviour of 3J solar cells.

6.2. Modelling procedure

Similarly to Chapter 4, three models are integrated: the spectral irradiance is generated by the NREL SMARTS2 [100], an EM uses a single-diode model to simulate the electrical characteristics and heat power of a 3J solar cell at MPP and a FETM uses the heat power as an input from the electrical model in order to predict the temperature and the cooling requirements. The equations used for the EM and FETM models are presented in Chapter 3 [148, 149]. The spectral performance is evaluated using the *SF* and *SMR1* (defined in Chapter 2) indices as criteria.

6.2.1. Impact of atmospheric parameters on spectral and electrical performance

Firstly, the impact of *AM*, *AOD* and *PW* on the spectral and electrical performance of a triple-junction solar cell has been investigated for a given cell temperature. In order to achieve this, an algorithm was developed to vary each parameter while keeping all others constant at the reference conditions of ASTM G173-03 [152]. The simulation algorithm is illustrated in Figure 74.

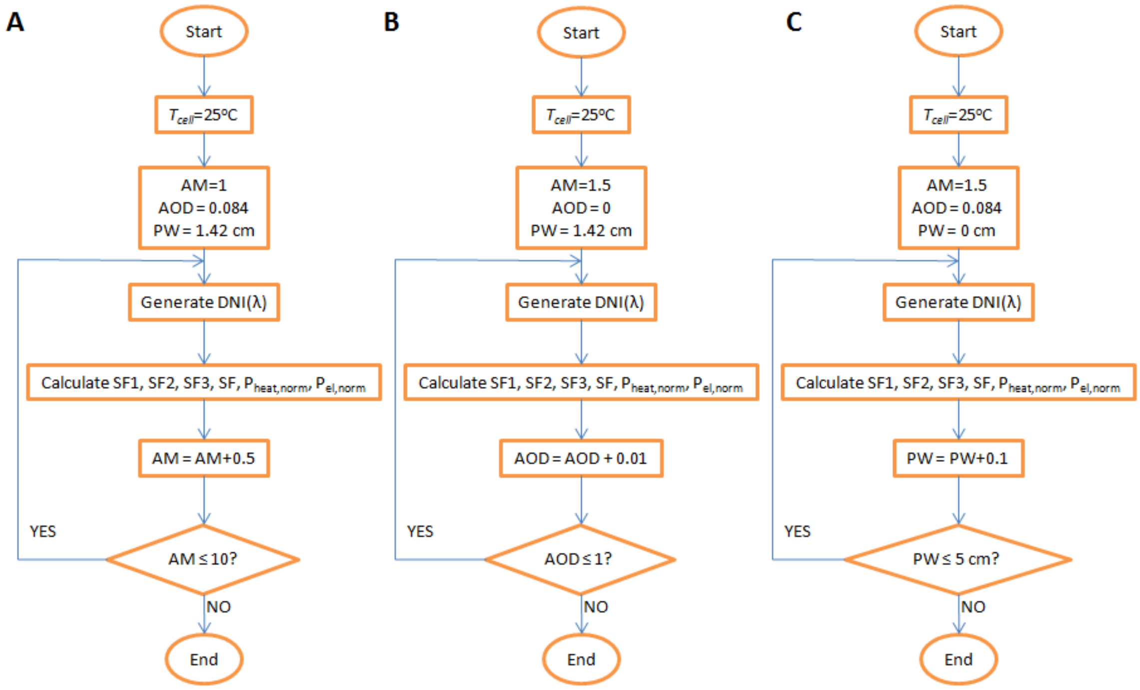

Figure 74: Simulation algorithm for the evaluation of the impact of AM (Flowchart A), *AOD* (Flowchart B) and *PW* (Flowchart C) on the spectral and electrical performance of a 3J solar cell. One atmospheric parameter is varied at a time while keeping the rest according to the reference conditions of AM1.5 ASTM G173-03.

6.2.2. Cooling requirements under worst-case conditions

In order to quantify the CCA's cooling requirements (or h_{conv}), the EM and FETM have been simulated iteratively for given solar spectra generated in SMARTS2 (Figure 75). As concluded from Chapter 4, HCPV cooling requirements should be designed for $AM < 1.5$ because of the current mismatch between the top and middle subcells, which subsequently contributes to greater heat, and also because of the higher irradiance intensity [148]. Assuming an initial temperature $T_{cell}(s) = 25°C$ the EM ran the single-diode model which calculated the electrical characteristics and hence, the heat generated within the solar cell by [123]:

$$q_{heat} = (CR \cdot DNI \cdot A_{cell} \cdot \eta_{opt}) \cdot (1 - \eta_{cell}) \tag{77}$$

The heat power was then imported to the FETM as a boundary condition on the solar cell's surface to model it as a heat source and hence, to predict the temperature distribution. The predicted volumetric solar cell temperature was then imported back to the EM and the integrated models ran iteratively until a steady state was reached between them i.e. when $|T_{cell}(s+1)-T_{cell}(s)| \leq 0.002°C$.

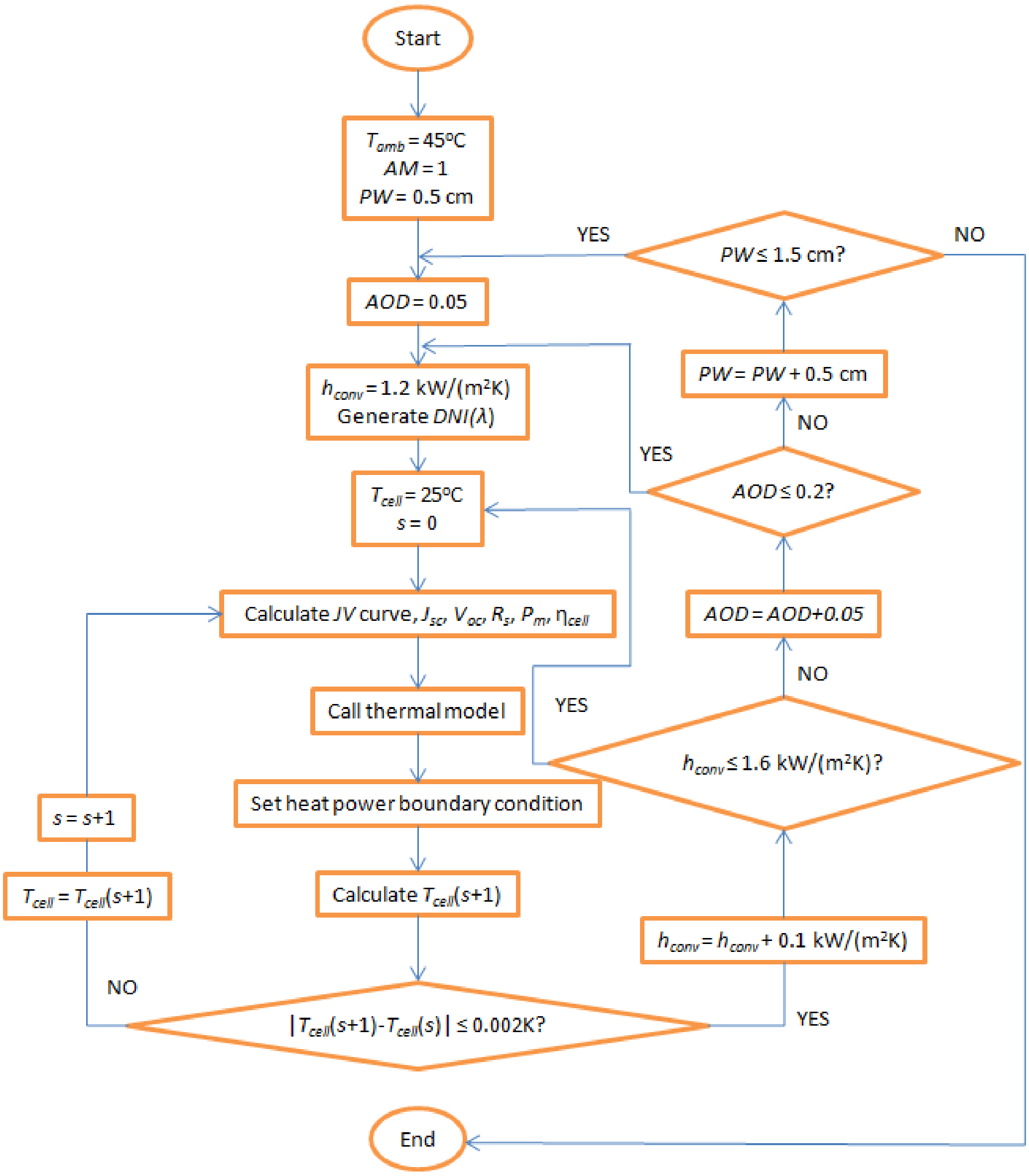

Figure 75: Simulation algorithm for the quantification of cooling requirements under worst-case conditions.

6.2.3. Case studies using TMY3 data and regression analysis

Case studies have been performed to determine the spectral and electrical performance and also to quantify the optimum h_{conv} at four USA locations with relatively high annual direct normal irradiation; Albuquerque (New Mexico), El Paso (Texas), Las Vegas (Nevada) and Tucson (Arizona). Bulk spectra that use atmospheric data from a TMY3 (generated by C. Stark, Fraunhofer USA [205, 214]) were imported to the simulation algorithm (see Figure 76). It is worth mentioning that the use of high-quality observed data of the main atmospheric parameters in conjunction with the SMARTS2 model has been widely used by the scientific community and proven to be valid for the evaluation of HCPV and PV performance [121, 215-217]. Moreover, in a study performed by

Kinsey *et al.* [218] using TMY3 data, it was shown that the predicted cumulative energy production of a CPV power plant was within 2% of the actual energy production, after 9 months of operation. To ensure clear-sky conditions, the spectral global normal irradiance $GNI(\lambda)$ generated by SMARTS2 was integrated over the whole range of wavelengths and a filter has been applied on TMY3 for $DNI/GNI > 0.8$. This filter is also included in the draft of IEC 62670-3 [115]. Furthermore, to avoid high computational time, regression analysis has been used to predict the T_{cell} as a function of q_{heat}, T_{amb} and h_{conv}.

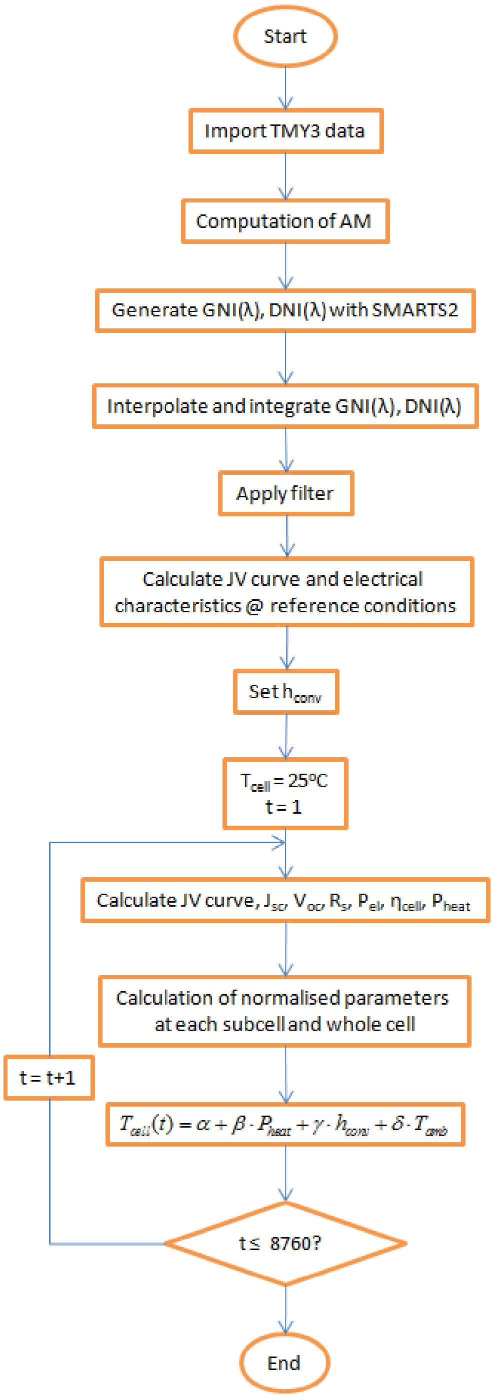

Figure 76: Simulation algorithm for the case studies using TMY3 data of four USA locations.

6.3. Results and analysis

The CCA reported in Chapter 4 [179] is also used in this chapter with the same *EQE* data at 25°C, 45°C, 65°C and 75°C which were taken from Kinsey and Edmondson [94]. As in Chapter 4, the results below correspond to a $CR = 500\times$ and an $\eta_{opt} = 80\%$. All the inputs and boundary conditions to the EM and FETM are listed in Tables 14 to 18 [148] unless otherwise stated.

6.3.1. Impact of individual atmospheric parameters on spectral and electrical performance

This section assesses the impact of individual atmospheric parameters (*AM*, *AOD*, *PW*) on the spectral and electrical performance of the Spectrolab C1MJ CCA at 25°C. Realistic ranges were selected ($1 \leq AM \leq 10$, $0 \leq AOD \leq 1$, $0\ \text{cm} \leq PW \leq 5\ \text{cm}$) for each atmospheric parameter. Although a similar approach has been reported by Fernández *et al.* [53] (using only the whole cell's *SF* as a criterion), it is also presented here in order to get a better understanding of which (and to what extent) parameters contribute to the heat generated on the CCA and therefore the cooling requirements and electrical energy performance of such devices for a range of conditions. For this reason, it is necessary to model the *SF* (whole cell and individual subcell), normalised electrical power ($P_{el,norm}$) and normalised heat power ($q_{heat,norm}$) as a function of each atmospheric parameter by varying each one (from low to high values) at a time while keeping the rest at the reference conditions of ASTM G173-03 as previously considered [53, 219, 220] (see also Figure 74).

6.3.1.1. Impact of air mass

To reiterate, Figure 34 in Chapter 4, shows the impact of *AM* on the spectral *DNI* distribution. The significant drop of the spectral intensity is obvious with increasing *AM*. It can also be noticed that there is a shift toward the longer wavelengths. The impact of changing spectrum due to variation of *AM* on the electrical performance is also shown in Figure 77; the *SF1* of the top subcell shows spectral gains up to 2.1% for $AM < 1.5$ while the middle (*SF2*) and bottom (*SF3*) subcells show the opposite behaviour (-3.7% (middle subcell), -3% (bottom subcell) losses for $AM < 1.5$ and gains for $AM > 1.5$). The whole solar cell's spectral factor (SF) follows the top subcell for $AM > 1.5$ while is close to $SF2$ for $AM < 1.5$. The reason for this is that at CSTC conditions the middle subcell limits the current by a 1.6% difference from the top's current. Furthermore, Figure 77 shows the impact of AM on the $P_{el,norm}$ and $q_{heat,norm}$; the $P_{el,norm}$ losses are $\leq 1\%$ up to AM1.9D while for $AM > 2$ the losses increase significantly (6.7% at AM3D, 20.1% at AM5D and 50.3% at AM10D). The $q_{heat,norm}$ increases with the excess current mismatch (4.1% at AM3D, 12.2% at AM5D and 30.4% at AM10D) and therefore it is always greater than 0% except when the top and middle subcells are current matched; i.e. when it operates at the reference conditions. Only the AM values up to $AM = 3$ have been illustrated in Figure 77 for clarity purposes and also due to the significantly higher solar intensity, which in turn affects the thermal performance and cooling requirements of HCPV systems. Moreover, low AM values predominantly occur during the summer months at locations with a high annual direct solar irradiation.

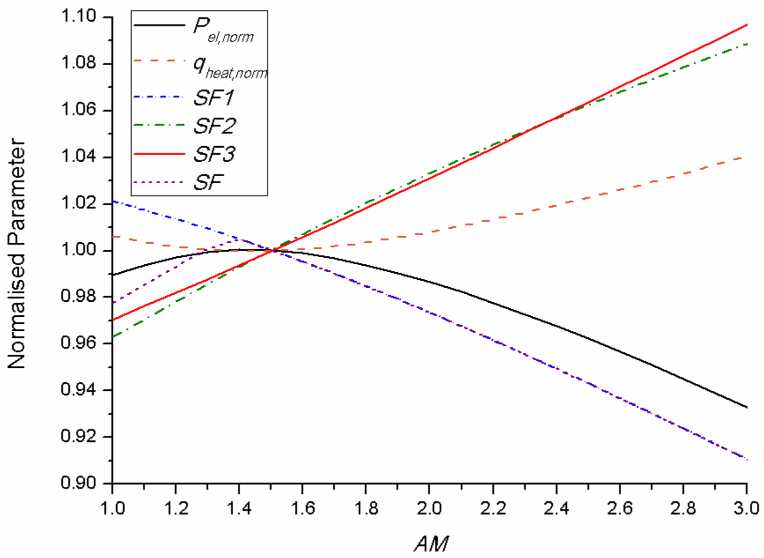

Figure 77: The impact of *AM* on the spectral and electrical performance of C1MJ CCA.

6.3.1.2. Impact of aerosol optical depth

Increasing AOD reduces the spectral irradiance in the short wavelengths region (visible light) and to a much lesser degree in the near-infrared light (Figure 78); this will have a significant influence on the current generation of the top subcell. From Figure 79 it can be seen that the middle subcell is almost unaffected by AOD (maximum losses of 1% on

SF2) while the top subcell shows losses of up to 36.3% at *AOD* = 1. However, for *AOD* lower than the reference value ($AOD_{ref} = 0.084$) the *SF1* shows spectral gains up to 3.5%. *SF3* has the opposite trend from *SF1*; spectral losses are down by 3.95% for *AOD* below reference conditions and gains up by 40.86% for $AOD > 0.084$. The SF for the whole solar cell shows the same behaviour as in the variable *AM* following the *SF1* for values higher than the reference, since the limiting subcell is the top one. The effect of the current mismatch which was just described is evident when the $q_{heat,norm}$ and $P_{el,norm}$ are assessed; when the current mismatch between the subcells increases, the $q_{heat,norm}$ increases by up to 21.1% while the $P_{el,norm}$ is reduced by 34.9% when *AOD* is equal to 1.

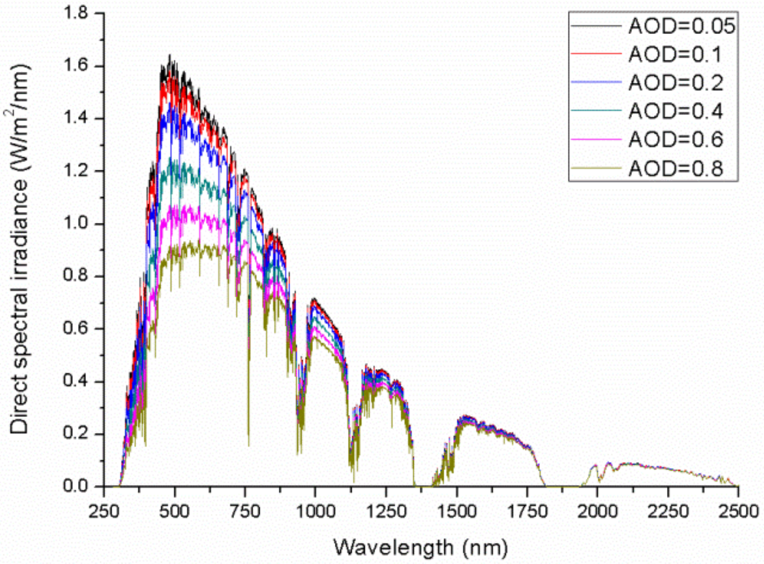

Figure 78: Effect of *AOD* on the spectral irradiance. The rest of the parameters are kept constant according to the ASTMG173-03.

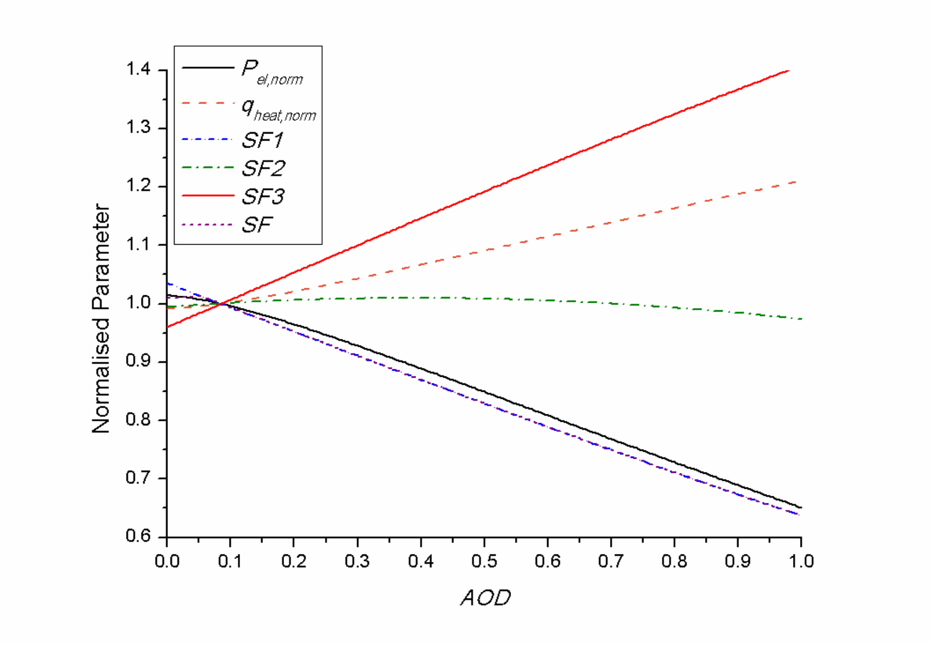

Figure 79: The impact of *AOD* variation on the spectral and electrical characteristics.

6.3.1.2. Impact of precipitable water

In a similar manner to Figure 78, Figure 80 shows the impact of *PW* on the spectral *DNI*; in contrast to *AOD*, increased *PW* has a minimal effect in the short wavelengths, however the longer wavelengths show a reduction. Hence, the bottom subcell that corresponds to the infrared region will have higher spectral losses with increasing *PW*. The middle subcell which converts the near-infrared region will also be affected but to a lesser extent. As can be seen from Figure 81, for *PW* values lower than 1.42 cm (reference conditions), *SF1*, *SF2* and hence, *SF* show losses due to the current mismatch between the top (-14.6%) and middle (-11.5%) subcells, however the *SF3* shows gains of up to 21.1% and therefore increases in $q_{heat,norm}$ occur up to 7.8% with a significant drop (12.9%) in $P_{el,norm}$. For *PW* values higher than 1.42 cm, the drop in the infrared region causes significant losses (down by 10.2%) on the bottom subcell which corresponds to the infrared proportion of the solar spectrum, hence a higher performance is noticed with $P_{el,norm}$ and *SF* gains up to 4.3%. This is due to the significant reduction of the excess current of the germanium subcell, therefore lower $q_{heat,norm}$ by 2.6% at $PW = 5$ cm and a higher electrical conversion efficiency.

Overall, as discussed also by Fernández *et al.* [53], the dominant atmospheric parameters that affect the performance of 3J solar cells are the *AM* and *AOD* with losses on the $P_{el,norm}$ down by 50.3% at AM10D and 34.9% at $AOD = 1$.

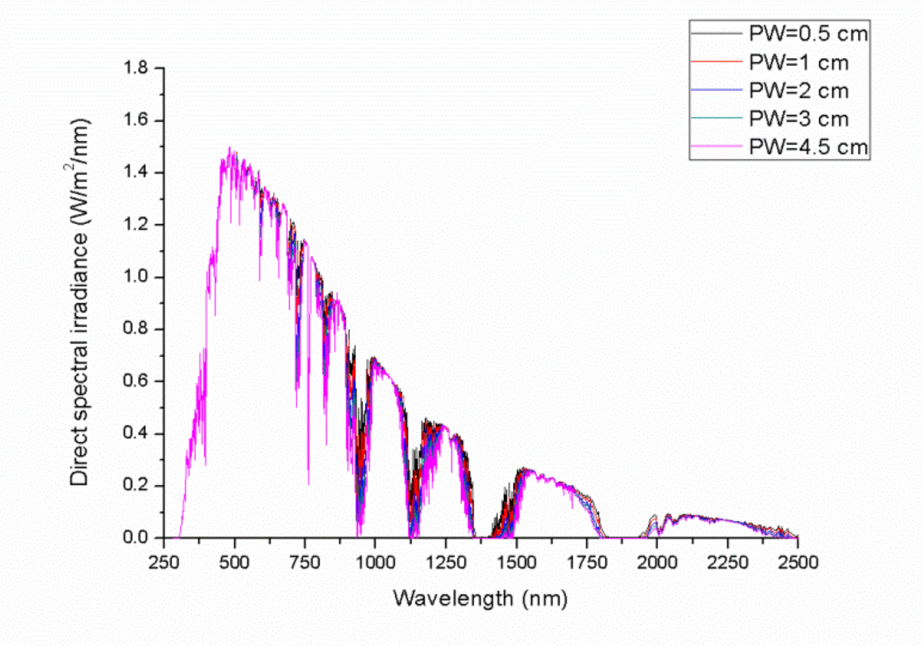

Figure 80: Effect of *PW* on the spectral irradiance. The rest of the parameters are kept constant according to the ASTMG173-03.

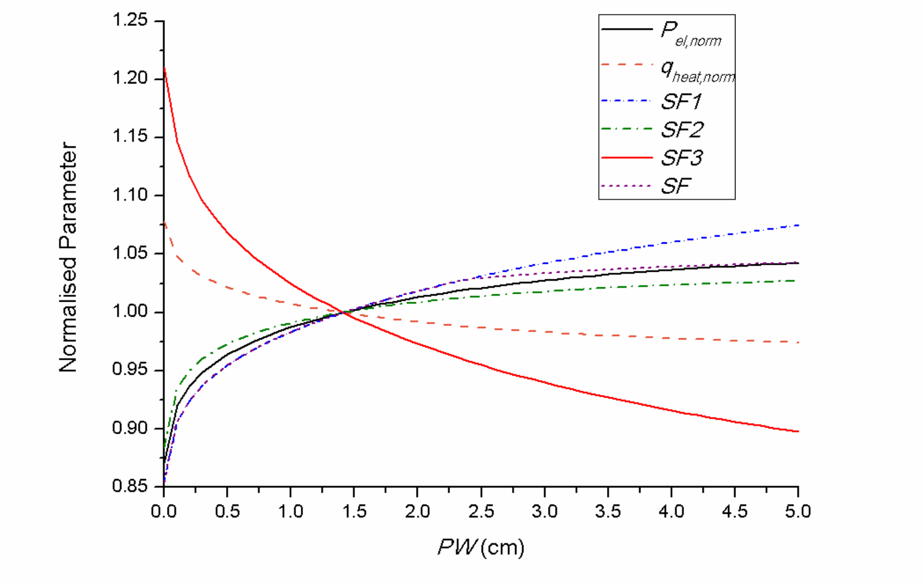

Figure 81: The impact of *PW* variation on the spectral and electrical characteristics.

6.3.2. Cooling requirements under extreme conditions

This section evaluates the cooling requirements of the C1MJ CCA. The *AM* is fixed to *AM* = 1 and the *AOD* and *PW* have been varied for specific ranges that would trigger relatively high thermal stresses on the CCA due to additional current mismatch between the subcells and also due to higher solar irradiance intensities. Moreover, in the summer months and for latitudes lower than 40°N, the AM is lower than $AM = 2$ for most of the day [56]. Therefore, AM1D is considered under variable AOD and PW, for the estimation of the required h_{conv} from the back plate to the ambient air with an ambient temperature of 45°C. Also, the ranges of AOD ($0.05 \leq AOD \leq 0.2$) and PW ($0.5\ \mathrm{cm} \leq PW \leq 1.5\ \mathrm{cm}$) were chosen to simulate the thermal behaviour of CCA at relatively hot (high T_{amb}), clear (low AOD) and dry (low PW) conditions. Any cooling device designed to dissipate heat under these conditions, will be adequate for higher AM, AOD and PW values. A range of heat transfer coefficients $1200\ \mathrm{W/(m^2{\cdot}K)} \leq \mathrm{h_{conv}} \leq 1600\ \mathrm{W/(m^2{\cdot}K)}$ are used as a boundary condition on the back surface of the CCA. Higher heat transfer coefficients were not considered in order to stay within passive cooling limits [190]. The cell's temperature is then predicted by the FETM and the integrated volumetric temperature is then imported back to the EM. The procedure is repeated until a steady state is reached between the EM and FETM; i.e. solar cell temperature difference lower than 0.002°C. The solutions converge in all cases after the 3rd iteration. The solver and mesh resolution are detailed in Chapter 4.

The temperature distribution of the C1MJ CCA is shown in Figure 82 for AM1D, $PW = 1.42$ cm, $AOD = 0.084$, $h_{conv} = 1600\ \mathrm{W/(m^2{\cdot}K)}$ (i.e. 1.22 K/W, area of $5.13 \times 10^{-4}\ \mathrm{m^2}$) and $T_{amb} = 45$°C. A maximum temperature of 89.84°C is observed at the centre of the cell while the temperature of the top layer of the DBC board, which is not illuminated, varies from 70°C at the edges to 80°C near the cell. The integrated volumetric temperature of the solar cell is 86.34°C.

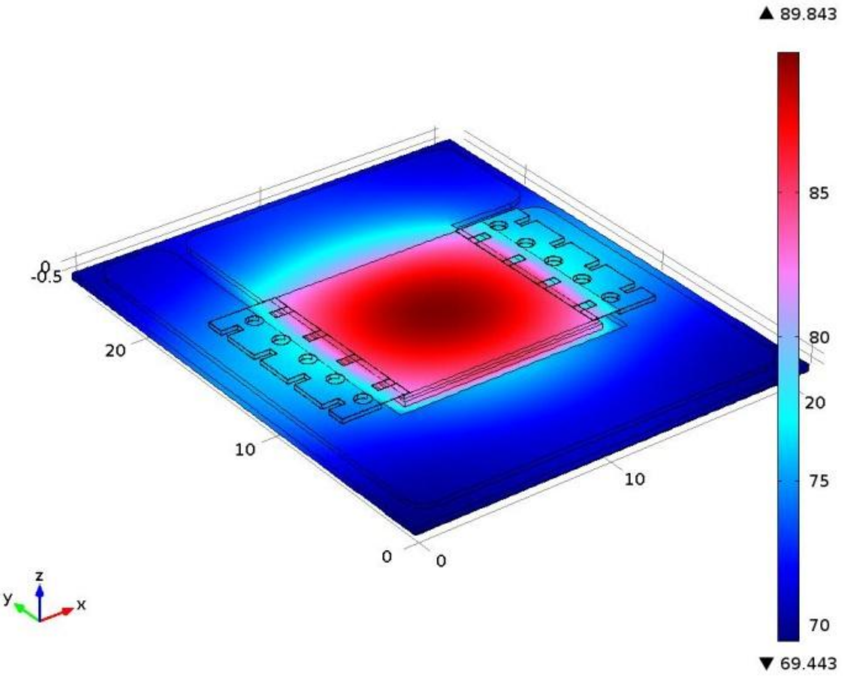

Figure 82: Temperature distribution (°C) across the C1MJ CCA for AM1D, h_{conv} = 1600 W/(m^2·K) and T_{amb} = 45°C.

The influence of the changing spectra on the calculated integrated volumetric cell temperatures are illustrated in Figure 83 for AM1D, $0.05 \leq AOD \leq 0.2$, $0.5\text{ cm} \leq PW \leq 1.5\text{ cm}$, $1200\text{ W/(m}^2\text{·K)} \leq h_{conv} \leq 1600\text{ W/(m}^2\text{·K)}$ and $T_{amb} = 45°\text{C}$. The reference spectrum AM1.5D ASTM G173-03 is also plotted (black line) for comparison. As can be seen, cooling devices designed at AM1.5D will allow higher operating temperatures (by up to 9.3°C) at relatively "hot and dry" sites. The elevated temperatures will cause long term degradation problems if kept for a prolonged time [183]. Therefore, at sites with low *AOD* and *PW*, the h_{conv} should be higher than 1300 W/(m^2·K) in order to operate at temperatures lower than 100°C.

From Figure 83, it is important to highlight the temperature difference (of up to 9.3°C) when reference conditions are assumed for the selection of an appropriate heat exchanger. Such assumptions can lead to a significant underestimation of the cooling requirements causing a suboptimal performance of the HCPV system and also, as mentioned in the previous paragraph, running the risk of a system failure.

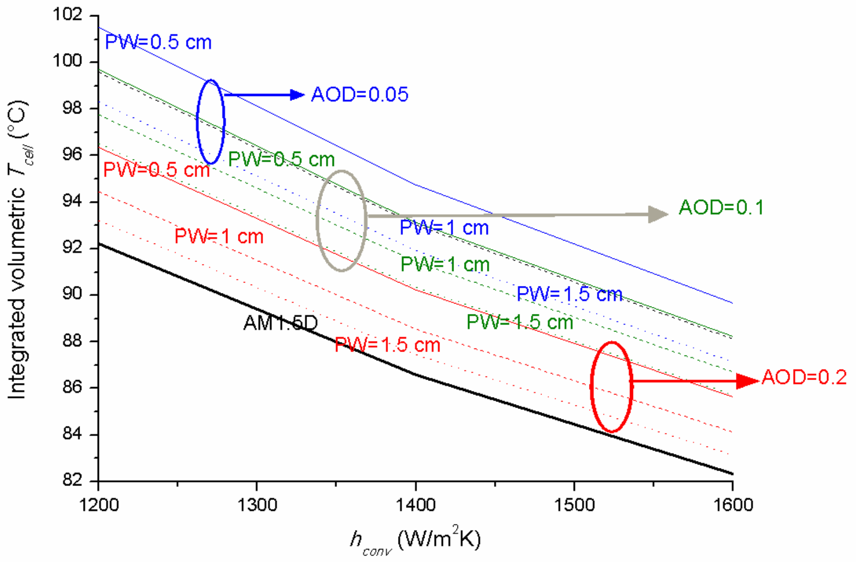

Figure 83: Integrated volumetric solar cell temperature as a function of heat transfer coefficient, aerosol optical depth (blue *AOD* = 0.05, green *AOD* = 0.1, red *AOD* = 0.2) and precipitable water (straight lines *PW* = 0.5 cm, dash lines *PW* = 1 cm, dot lines *PW* = 1.5 cm). The air mass is kept constant at AM1D. The AM1.5D ASTM G173-03 is also shown with black colour.

6.3.3. Case Studies

Locations offering relatively high annual direct solar irradiation and hence applicable for HCPV applications were selected to investigate the effect of the heat transfer coefficient on temperature and therefore, the electrical power production. Class I (lowest uncertainty data) TMY3 hourly data have been used for four locations in the USA (Albuquerque, El Paso, Las Vegas and Tucson). The location characteristics are shown in Table 29. Since these data are typical, they do not offer a real representation of the system's operation under extreme conditions (i.e. worst-case scenarios) [221]; nevertheless, they are useful for the assessment of the electrical performance of PV systems and for this work in particular, it can also offer an estimate of the operating cell temperature.

Location	Latitude	Longitude	Elevation (m)
Albuquerque	35.04°N	106.62°W	1619
El Paso	31.77°N	106.50°W	1186
Las Vegas	36.08°N	115.15°W	648
Tucson	32.13°N	110.95°W	777

Table 29: Sites used for the simulation along with the coordinates and elevation

The filtering criterion resulted in 3089 hourly spectra for Albuquerque (Figure 84), 3180 for El Paso, 3320 for Las Vegas and 3300 for Tucson. Monthly average values of the filtered data are illustrated below in Figures 85 (absolute *AM*), 86 (*DNI*), 87 (*DNI*/*GNI* ratio), 88 (*AOD*), 89 (*PW*) and 90 (T_{amb}) for all the locations.

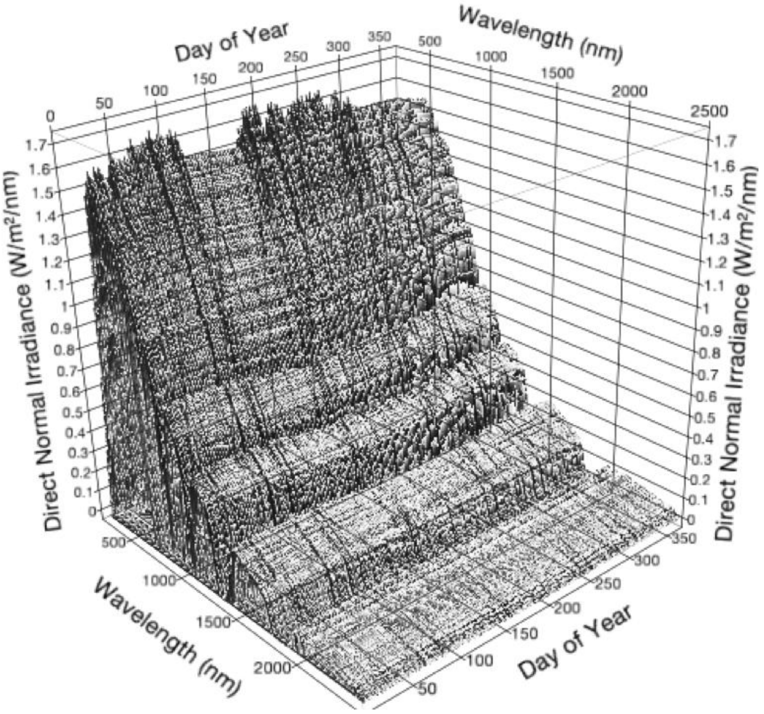

Figure 84: Hourly modelled spectra for Albuquerque, NM using SMARTS2 (Figure courtesy of C. Stark, Fraunhofer USA).

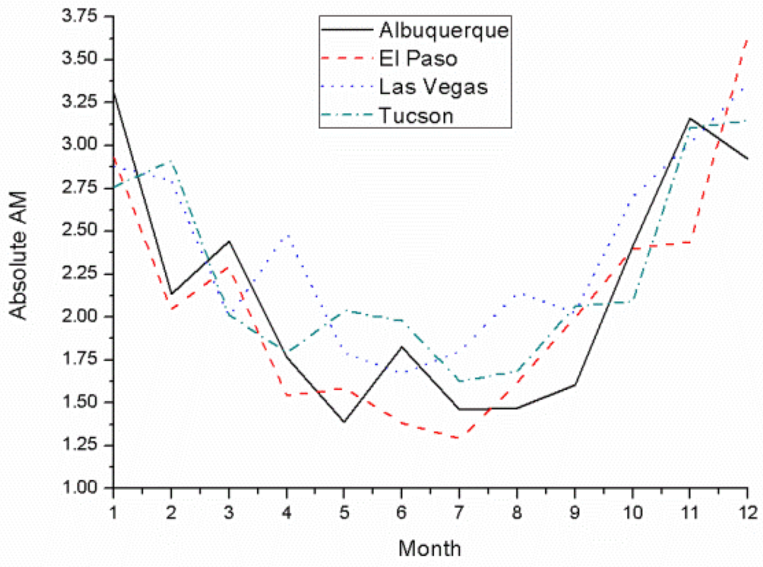

Figure 85: Monthly average values of absolute *AM* for all locations.

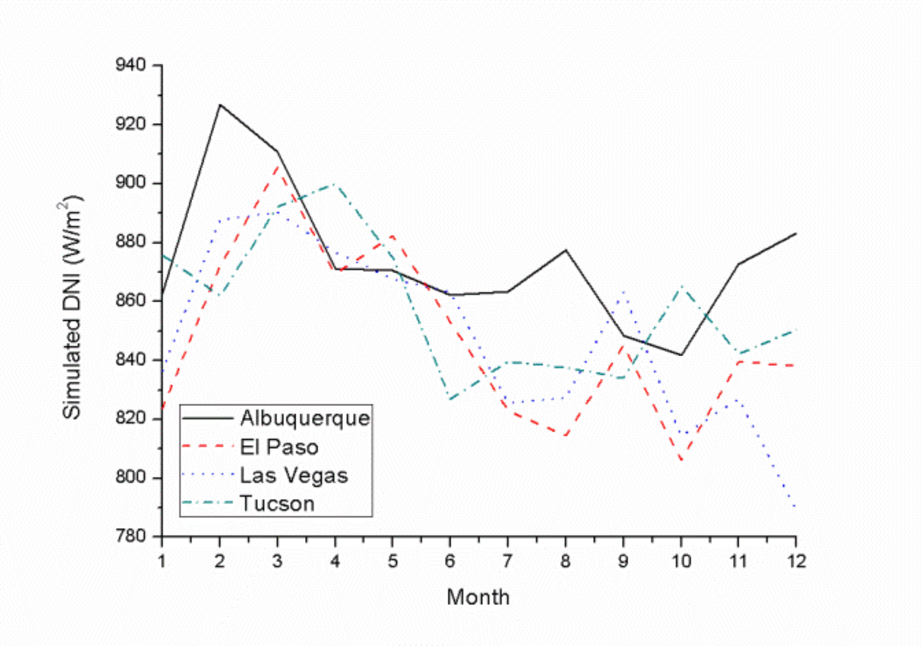

Figure 86: Monthly average values of simulated *DNI* for all locations.

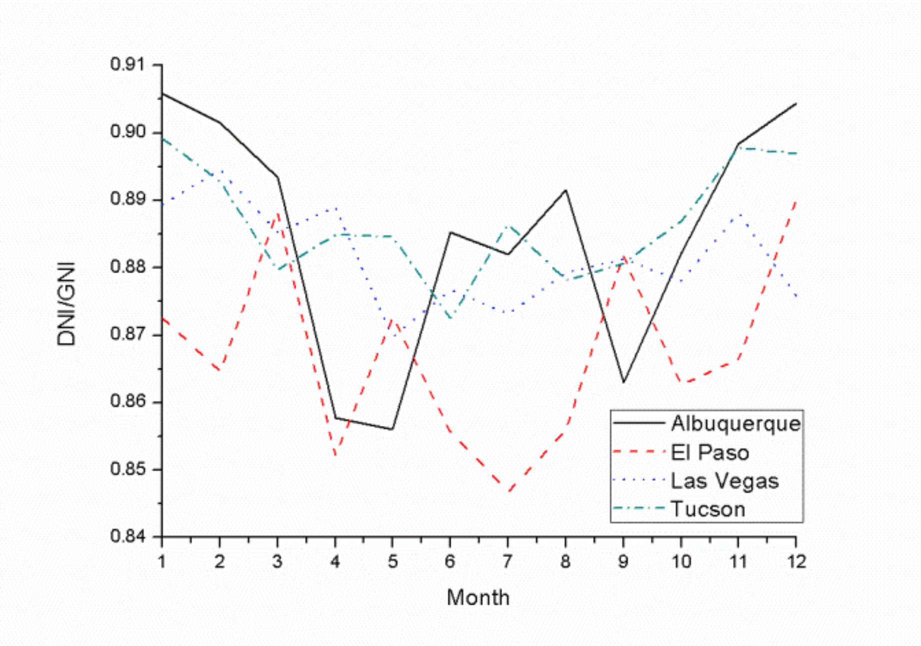

Figure 87: Monthly average values of clearness ratio (*DNI*/GNI) for all locations.

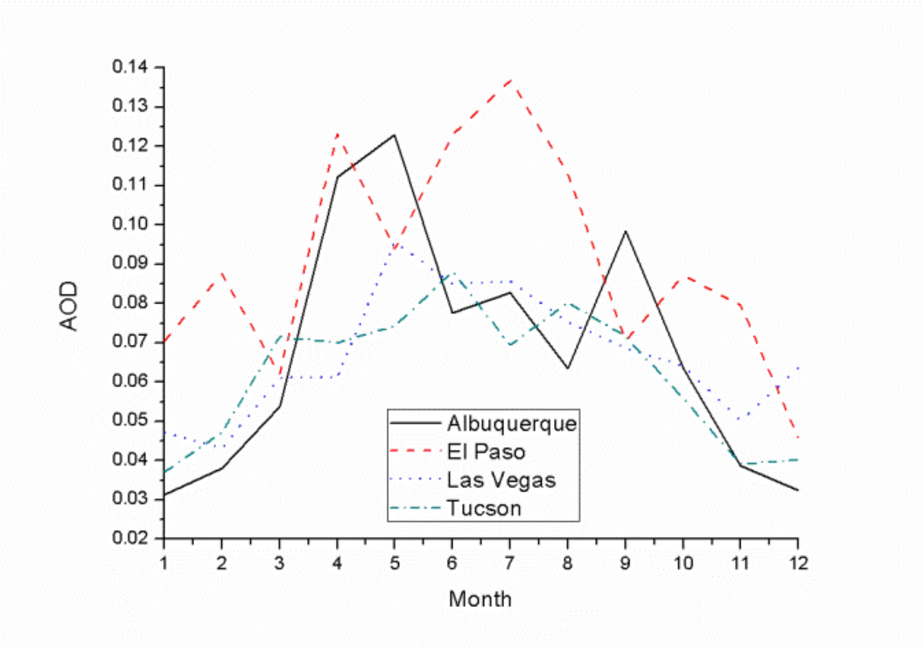

Figure 88: Monthly average values of *AOD* for all locations.

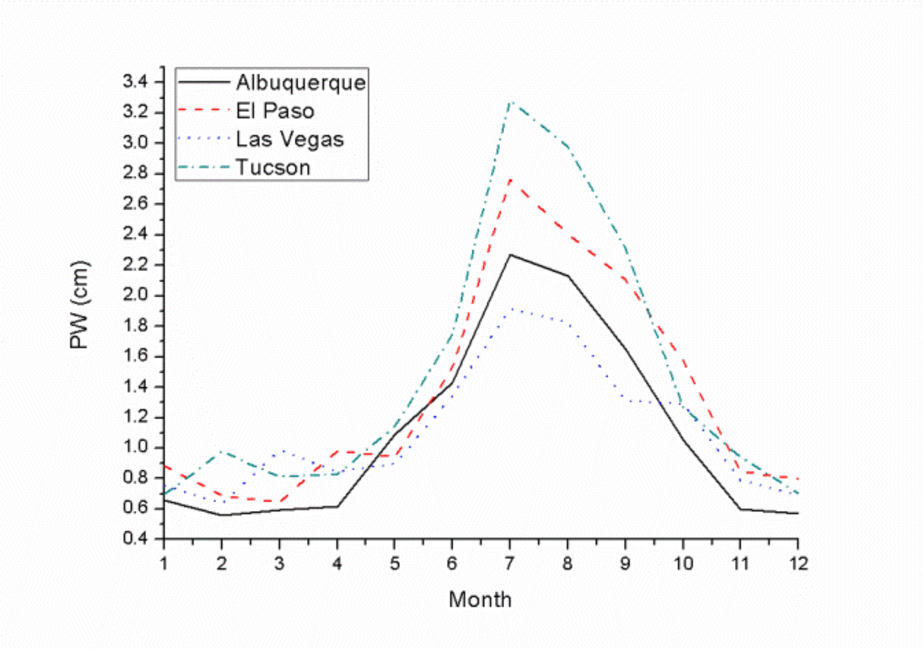

Figure 89: Monthly average values of *PW* for all locations.

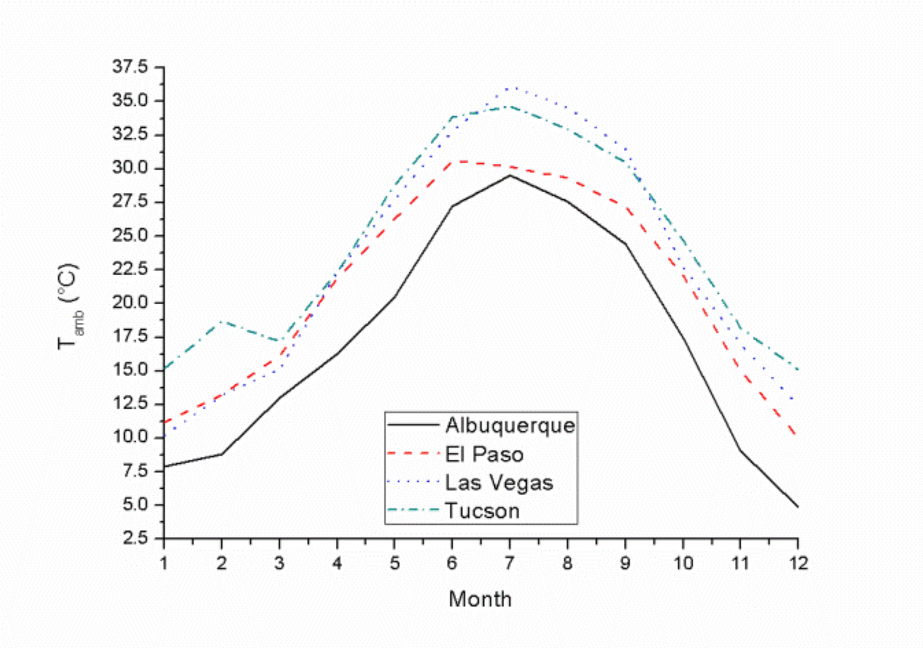

Figure 90: Monthly average values of T_{amb} for all locations.

Due to the high volume of data (>11.5x10^6 lines of generated spectra in addition to the TMY3 data), regression analysis has been performed for the calculation of cell temperature. Initially a parametric study was simulated in the FETM for 20 W ≤ q_{heat} ≤ 30 W, 1200 W/(m^2·K) ≤ h_{conv} ≤ 1600 W/(m^2·K), 15°C ≤ T_{amb} ≤ 45°C and the cell temperature could then be calculated using the following equation:

$$T_{cell} = \alpha + \beta \cdot q_{heat} + \gamma \cdot h_{conv} + \delta \cdot T_{amb} \tag{78}$$

where the intercept and linear coefficients are α = 35.12°C, β = 1.80°C/W, γ = -0.02°C/(W·$m^{-2}K^{-1}$), δ = 1.00. The R^2 between modelled (in FETM) and predicted (regression) data was 0.9975 (Figure 91). It is important to mention that the effect of wind speed, *WS*, was not taken into consideration in equation (78) however, experimental results have proven that the effect of *WS* on the estimation of T_{cell} is low, and therefore it can be neglected in a first approximation [120].

As mentioned in Chapter 2, the normalised short-circuit current or spectral factor (*SF*) is a useful index to evaluate the spectral performance of a solar cell; Figure 92 illustrates the *SF* for all locations. It can be seen that spectral gains occur in July and August for Albuquerque (0.6% and 1% respectively) and Tucson (1.7% and 1.6% respectively) while El Paso shows spectral gains only occur in July (1.9%). Las Vegas has spectral losses during all months of the year with the lowest during December (a decrease of 12.2%). The *SMR1* follows a similar trend to *SF* in Figure 93 and this is because both parameters are a function of the short-circuit current; the top subcell seems to be the current limiter for the whole year except when *SF* is above 1. This indicates that spectral gains occur when the incident spectrum is blue rich. The *SF* was plotted against the *SMR1* in Figure 94; the *SF* increases with increasing *SMR1* until a maximum is reached, at approximately *SMR1* = 1.02, where the *SF* decreases almost linearly.

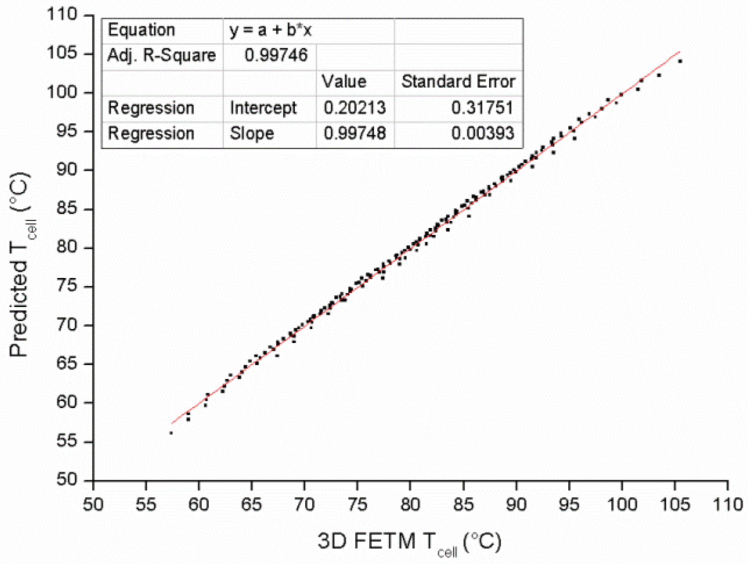

Figure 91: Linear regression analysis of T_{cell} between simulated (in 3D FETM) and predicted data for the C1MJ solar cell.

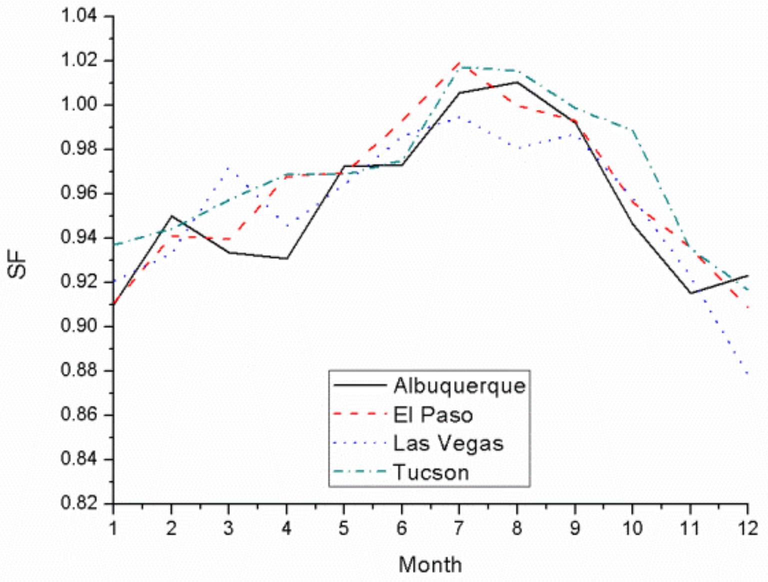

Figure 92: Monthly average spectral factor for all locations.

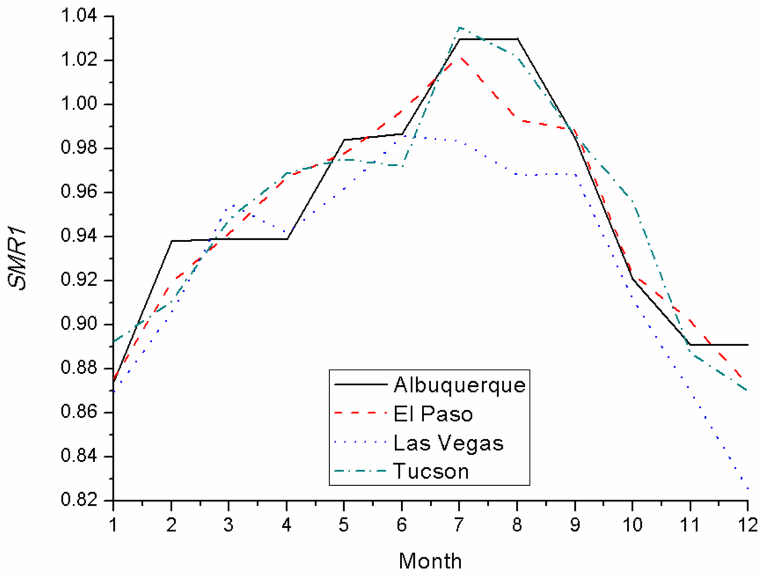

Figure 93: Monthly average spectral matching ratio of top to middle subcell for all locations.

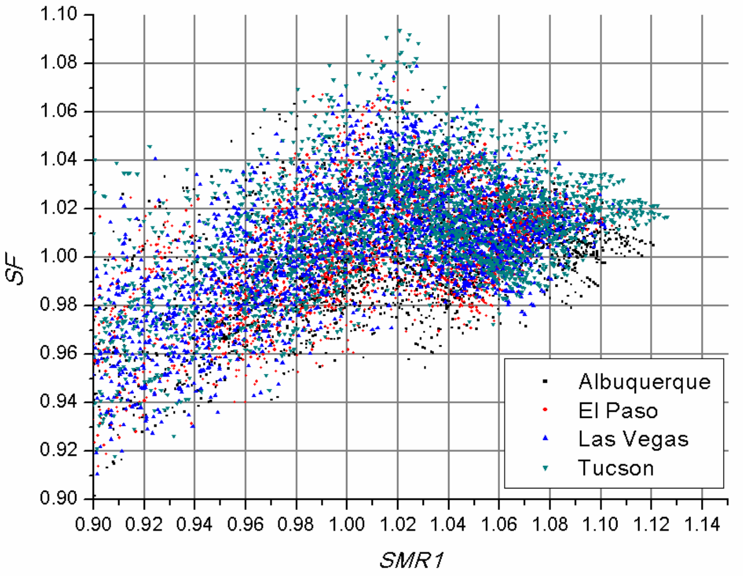

Figure 94: Spectral factor against spectral matching ratio of top to middle subcell for all locations.

In Figures 95 and 96 the normalised heat and electrical powers are shown respectively where, as expected, they exhibit the opposite behaviour. All locations show $P_{el,norm}$ losses all year round (as compared to the reference conditions) and therefore the $q_{heat,norm}$ shows gains; this is another indication that AM1.5D is not an appropriate reference for the cooling requirements estimation [148].

Finally, as expected, the calculated T_{cell} (Figure 97) peaks during the summer months for all locations; this is mainly due to the higher ambient temperatures. The monthly averages show temperatures of up to 88°C which are relatively high, if long term degradation issues are considered [183]. The heat generated on the solar cell is mainly influenced by the system's characteristics (i.e. CR, A_{cell}, η_{opt}), the electrical conversion efficiency and of course the incident DNI which in turn, is affected by the changes in the solar spectrum (i.e. AM, AOD, PW, etc.) (equation (77)). The q_{heat}, h_{conv} and T_{amb} are the parameters affecting the T_{cell} (equation (78)). Since the cooling mechanism for all locations is assumed to be the same, the cell temperature difference between locations is dependent on q_{heat} and T_{amb}. Tucson exhibits the highest T_{cell} during the year except the months from June to September where the T_{cell} is higher in Las Vegas. When Las Vegas and Tucson are compared, it can be noticed that the T_{cell} follows the trend of T_{amb} except in June where although the T_{amb} is higher in Tucson, the T_{cell} is higher in Las Vegas by 1°C. This can be attributed to the higher DNI in Las Vegas (by 4.2%) in combination with the higher PW (by 29.9%) in Tucson, which reduces the excess current on the bottom subcell and therefore contributes to the heat reduction. In July, August and September the T_{amb} is higher in Las Vegas (by 1.5°C, 1.6°C and 1°C respectively) and also the PW values are much higher in Tucson (by 71.6% in July, 63.3% in August and 76.8% in September) and therefore the T_{cell} is higher in Las Vegas by 1.3°C, 1.8°C and 3°C. Although Albuquerque exhibits higher DNI than El Paso during the year (except in May), it shows the lowest T_{cell} (except in July and August) due to the lower T_{amb}. In July, the monthly average T_{cell} in Albuquerque is 1.6°C higher than El Paso due to lower T_{amb} difference (0.64°C) between them and also due to the higher PW (by 0.5 cm or 17.8%) and AOD (by 39.6%) in El Paso. In August the $SMR1$ value for Albuquerque is 1.03 whereas for El Paso is 0.99; this indicates a clearer atmosphere (lower AOD values by 43.9%) in Albuquerque and therefore higher DNI and hence higher T_{cell} even if T_{amb} is lower by 1.78°C as compared to El Paso.

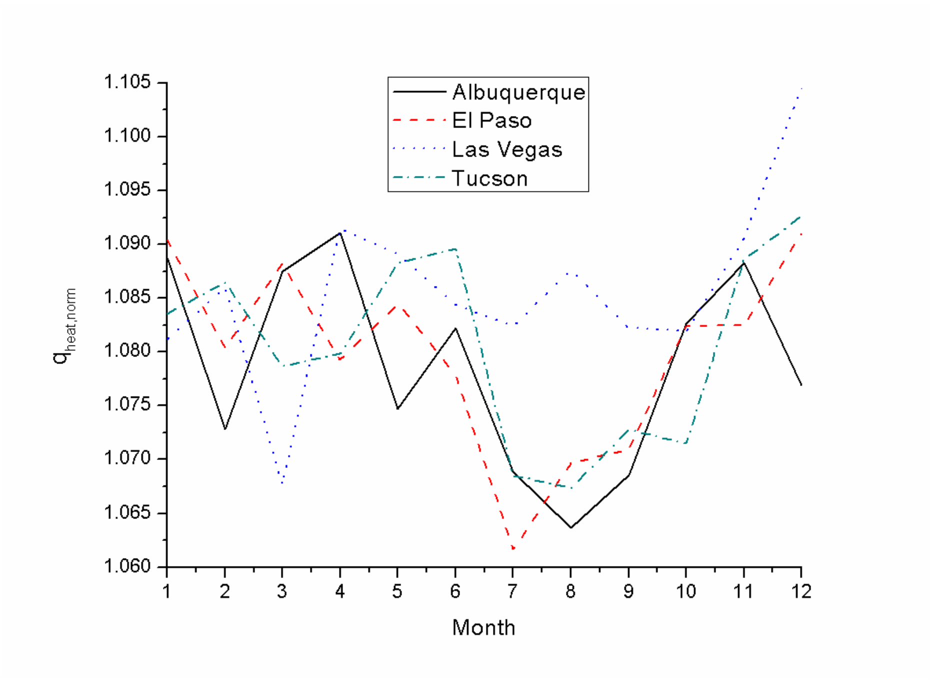

Figure 95: Monthly average normalised heat power for all locations.

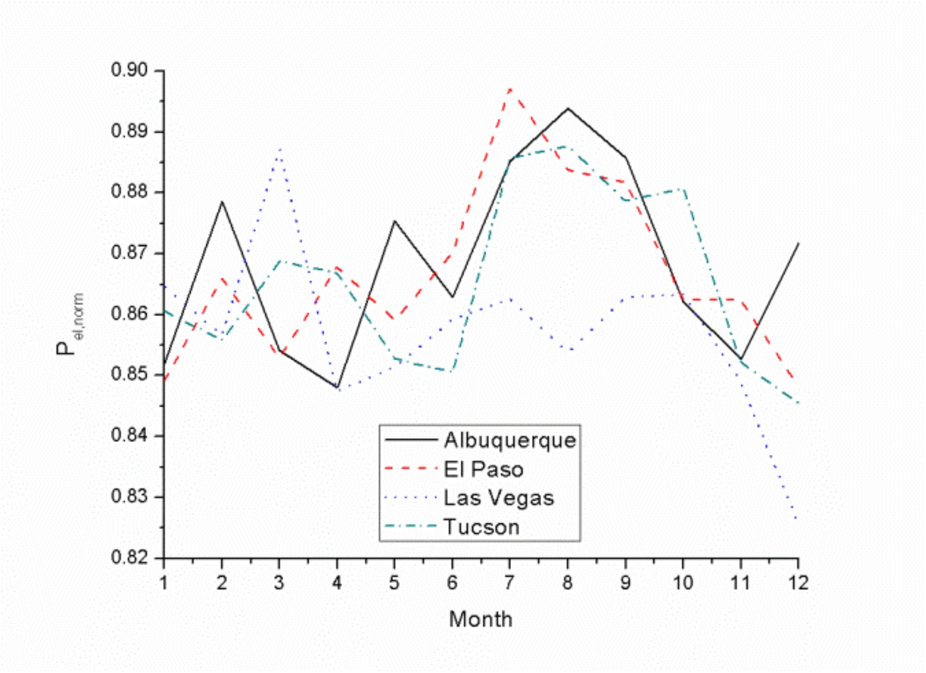

Figure 96: Monthly average normalised electrical power for all locations.

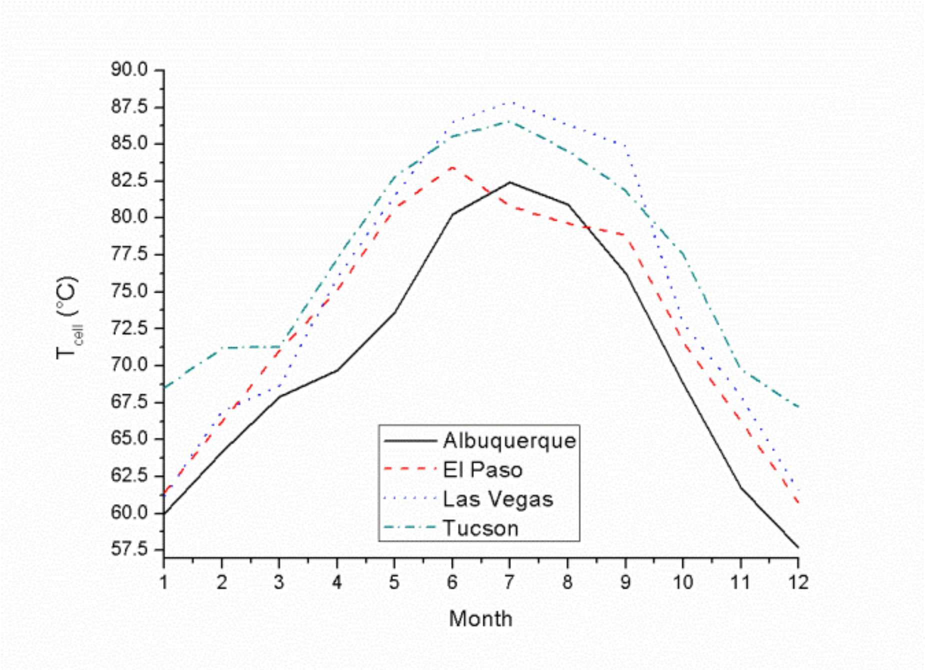

Figure 97: Monthly average solar cell temperature for all locations.

Annual average inputs and outputs for all locations can be seen in Tables 30 and 31 respectively. Due to the relatively similar atmospheric inputs, all locations exhibit similar annual average outputs; the *SF* ranges from 0.95 to 0.97, the $P_{el,norm}$ from 0.86 to 0.87 and the $q_{heat,norm}$ from 1.08 to 1.09. The T_{cell} however, ranges from 70.3°C to 77°C and follows the trend of the T_{amb} inputs. Las Vegas has the highest spectral and electrical power losses of 5% and 14% respectively and the highest gains in $q_{heat,norm}$ of 9%; it exhibits the second highest annual average T_{cell}. The highest annual average T_{cell} of Tucson can be attributed to the higher annual average T_{amb} which is 1.37°C (5.6%) higher than the one in Las Vegas. Moreover, although the higher annual average *PW* in Tucson shows a relatively better *SF* (and hence lower heat) it is shown that the dominant parameter for this temperature difference between locations with similar location characteristics is influenced by the T_{amb}. This can also be noticed when Albuquerque and El Paso are compared; although the *SF*, $P_{el,norm}$ and $q_{heat,norm}$ values are the same, the annual average T_{cell} is 2.7°C higher in El Paso because of the higher T_{amb}.

Location	***DNI*** **(W/m^2)**	**T_{amb} (°C)**	**AM_{abs}**	***AOD***	***PW*** **(cm)**
Albuquerque	874.25	17.21	2.16	0.07	1.10
El Paso	847.71	21.08	2.10	0.09	1.35
Las Vegas	847.37	22.97	2.39	0.07	1.11
Tucson	858.42	24.34	2.27	0.06	1.47

Table 30: Annual average inputs for all locations.

Location	***SF***	$P_{el,norm}$	$q_{heat,norm}$	T_{cell} **(°C)**
Albuquerque	0.96	0.87	1.08	70.3
El Paso	0.96	0.87	1.08	73.0
Las Vegas	0.95	0.86	1.09	75.2
Tucson	0.97	0.87	1.08	77.0

Table 31: Annual average outputs for all locations.

Additional simulations were conducted in order to assess the impact of h_{conv} on the energy yield at each location using a range of h_{conv} within the passive cooling limits (i.e. 1000 W/(m^2·K) $\leq h_{conv} \leq$ 1600 W/(m^2·K) with a step of 200 W/(m^2·K)). The results are shown in Figure 98 and Table 32 for the following annual direct normal irradiation values: 2696 kWh/m^2 in Albuquerque, 2698.3 kWh/m^2 in El Paso, 2812.1 kWh/m^2 in Las Vegas and 2830.2 kWh/m^2 in Tucson.

Figure 98 shows the annual energy yield (E_{yield}) in kWh/kWp as a function of h_{conv} for all the locations; as expected, the E_{yield} increases with the annual direct normal irradiation, since the *DNI* is the main driver for the energy output. The E_{yield} also increases linearly with h_{conv} with the slopes of the linear fit at 0.14 for Albuquerque and El Paso and 0.15 for Las Vegas and Tucson. Table 32 shows the annual maximum T_{cell} for four values of h_{conv} and also the annual average T_{cell} in parenthesis. It can be seen that the cell temperature exceeds 100°C in Las Vegas and Tucson for h_{conv} = 1000 W/(m^2·K). If the temperature limit is set at 90°C, the cooling requirements for Albuquerque and El Paso would be h_{conv} > 1250 W/(m^2·K); for Las Vegas h_{conv} > 1450 W/(m^2·K) and for Tucson a h_{conv} > 1350 W/(m^2·K). The annual average T_{cell} reduction per W/(m^2·K) increase is 0.027 for all four locations.

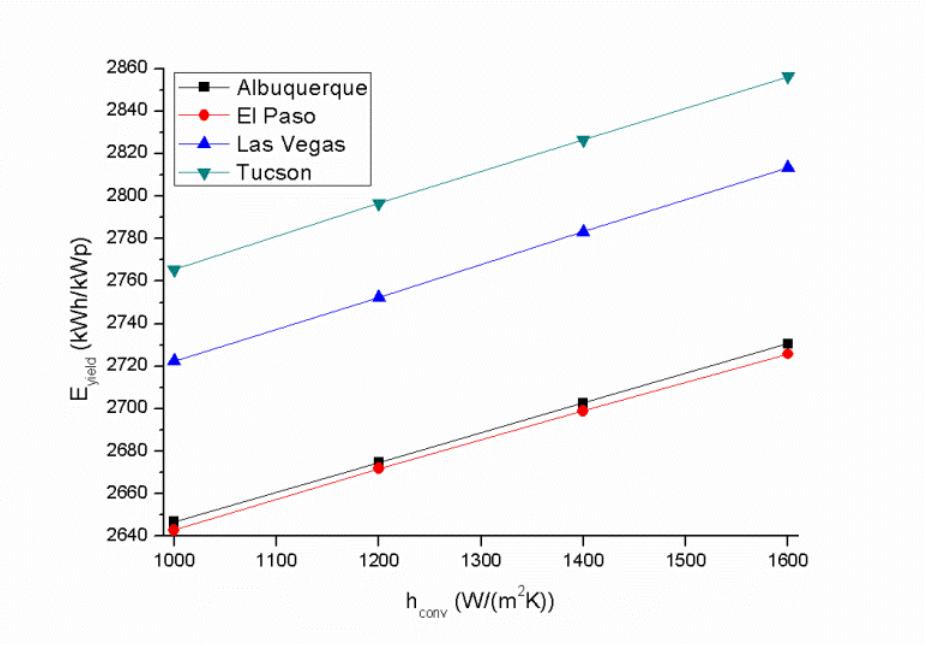

Figure 98: Annual values of energy yield as a function of the heat transfer coefficient.

Location	h_{conv} (W/(m^2·K))			
	1000	1200	1400	1600
Albuquerque	96.5°C (71.4°C)	90.9°C (65.9°C)	85.4°C (60.5°C)	79.8°C (55°C)
El Paso	97.1°C (74.1°C)	91.5°C (68.6°C)	86°C (63.2°C)	80.4°C (57.7°C)
Las Vegas	102.5°C (77°C)	96.9°C (71.5°C)	91.4°C (66.1°C)	85.8°C (60.6°C)
Tucson	100°C (78°C)	94.5°C (72.5°C)	88.9°C (67.1°C)	83.3°C (61.6°C)

Table 32: Annual maximum and average (in parenthesis) T_{cell} as a function of h_{conv}.

6.4. Discussion and conclusion

An integrated modelling procedure has been presented in order to evaluate the impact of atmospheric parameters on the spectral, electrical and thermal performance of a concentrating III-V triple-junction solar cell under a *CR* of 500×. The results show that such solar cells are mainly influenced by changes in *AM* and *AOD* with spectral losses of 51.3% at AM10D and 36.3% when $AOD = 1$. The effect of *PW* however showed spectral gains of up to 4.3% when $PW = 5$ cm; this is attributed to the reduction of the infrared portion of spectrum. Moreover, the $P_{el,norm}$ losses are < 1% up to AM1.9D while for *AM* values greater than AM2D the losses increase significantly (up to 50.3% at AM10D). The $q_{heat,norm}$ increases with the excess current mismatch between the subcells and therefore it is always greater than 0%, except when the top and middle subcells are current matched; i.e. when it operates at the reference conditions. Similarly with increasing AOD, the $P_{el,norm}$ is reduced by 34.9% when $AOD = 1$ while for $PW = 5$ cm it is increased by 4.3% and therefore the $q_{heat,norm}$ is decreased by 2.6%.

A method was also presented in order to evaluate the cooling requirements under worst-case conditions; i.e. AM1D, $T_{amb} = 45°C$ and a relatively clear (low AOD) and dry (low PW) atmosphere. It has been shown that in order to operate at a maximum T_{cell} lower than 100°C, the h_{conv} should be greater than 1300 W/(m^2·K).

Finally, the procedure was simplified in order to handle bulk spectra. Instead of using the 3D FETM model, regression analysis has been performed for the calculation of T_{cell} using equation (78). Class I TMY3 data have been used for four US locations with relatively high annual DNI (Albuquerque, El Paso, Las Vegas and Tucson) in order to evaluate the performance of a CCA. It was shown that Las Vegas and Tucson exhibited the highest annual average spectral losses and T_{cell} respectively. $P_{el,norm}$ is always underperforming in Las Vegas while for Albuquerque and El Paso gains were visible for a $h_{conv} > 1200$ W/(m^2·K); Tucson exhibited $P_{el,norm}$ gains for $h_{conv} \geq 1600$ W/(m^2·K). By varying the h_{conv} at each location, its influence on E_{yield} could then be determined. Because the TMY3 represent average values, a stricter T_{cell} limit was assumed suggesting a different h_{conv} at each location; 1250 W/(m^2·K) for Albuquerque and El Paso, 1450 W/(m^2·K) for Las Vegas and 1350 W/(m^2·K) for Tucson. Future work should incorporate costs in order to optimise the electrical and thermal performance at the lowest heat sink cost.

Chapter 7: Outdoor testing of a HCPV monomodule in Albuquerque, NM

This chapter evaluates the outdoor characterisation of the Suncore HCPV monomodule in Albuquerque, NM. The monomodule has been electrically characterised based on spectral changes. The diurnal electrical characteristics and temperature of the monomodule as a function of spectral, irradiance and ambient conditions have also been analysed. A CSOC and CSTC estimation is performed using different scenarios and are compared with indoor CSTC measurements.

7.1. Introduction

For the evolution and competitiveness of CPV, it is crucial to understand the behaviour of such systems under a variety of different atmospheric conditions. Although the indoor testing of CPV [77, 222, 223] in laboratory (controlled) conditions can provide valuable information about their behaviour or optimisation, the real conditions in the field can vary significantly, in terms of the spectral irradiance, alignment or tracker errors, soiling, etc [224].

Therefore, the outdoor testing of CPV modules is important for their performance and rating evaluation that can also lead to design improvements. Moreover, it provides information about the sensitivity of the electrical parameters to the ambient conditions, irradiance and spectral variations. As discussed earlier the spectrum varies with cloud cover and changing *AM*, *AOD*, *PW*. The understanding of the module's performance as a function of these parameters is significant in order to interpret any inconsistencies or anomalies in the measurements due to seasonal or diurnal variation. In addition, the effect of temperature on the electrical performance is also an important issue to evaluate.

7.2. Performance of HCPV monomodule

The monomodule's characteristics have been described earlier in Chapters 3 and 5. The equipment used have also been described in Chapter 3. The frequency distribution of the irradiance and ambient conditions from 25/06/2015 to 21/08/2015 in Albuquerque, NM are shown in Figures 99, 100, 101 for *DNI*, T_{amb} and *WS* respectively. The distribution of *AM* is also given in Figure 102. It has to be noted that these figures contain raw data (i.e. no filtering) and that during rainy and cloudy (i.e. $DNI \approx 0$ W/m^2) instances or days, no measurements were taken.

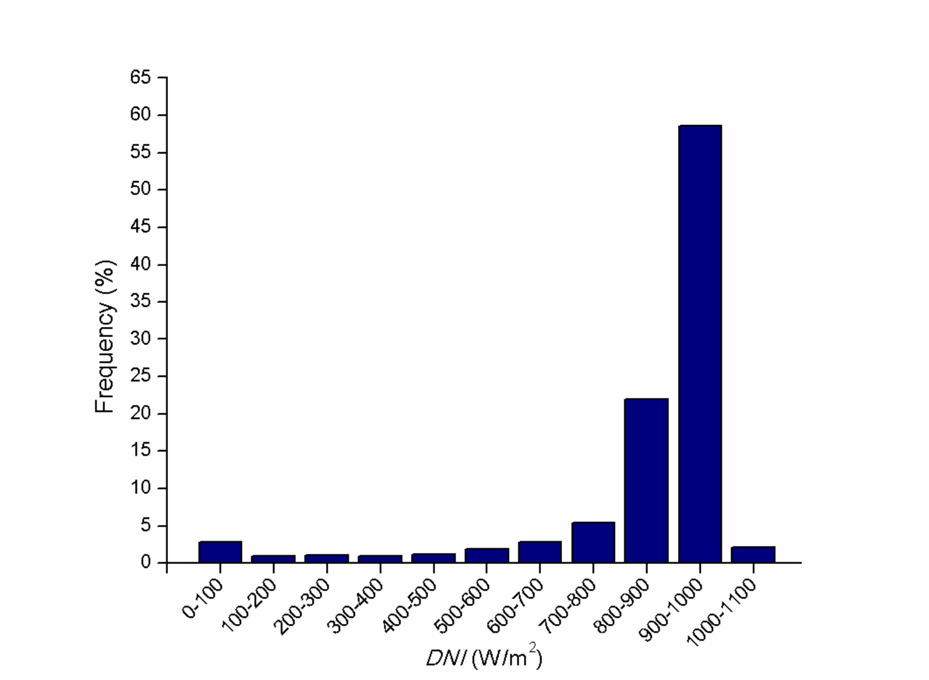

Figure 99: ***DNI*** **distribution over the period that the experiments were conducted in Albuquerque, NM.**

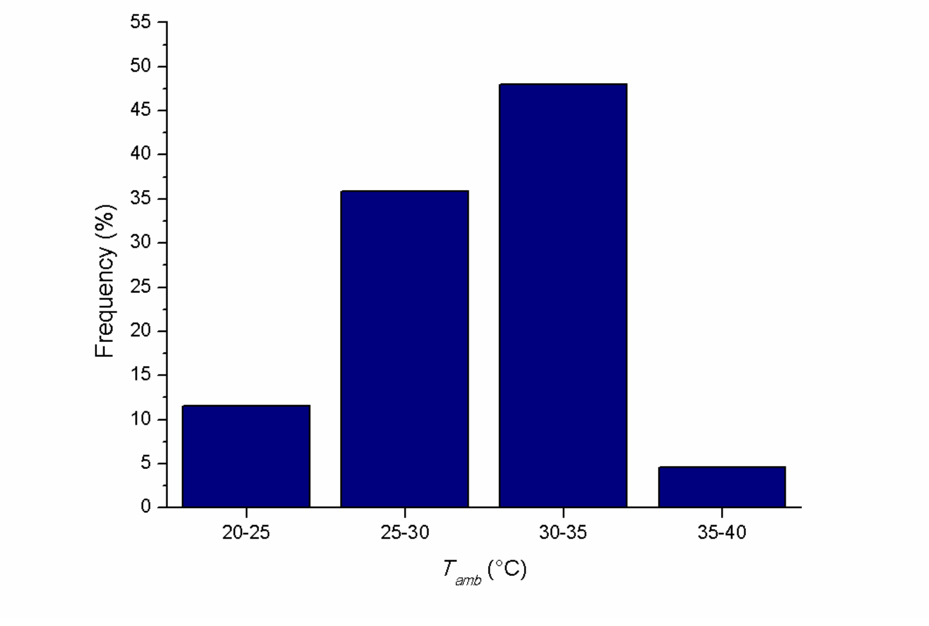

Figure 100: T_{amb} **distribution over the period that the experiments were conducted in Albuquerque, NM.**

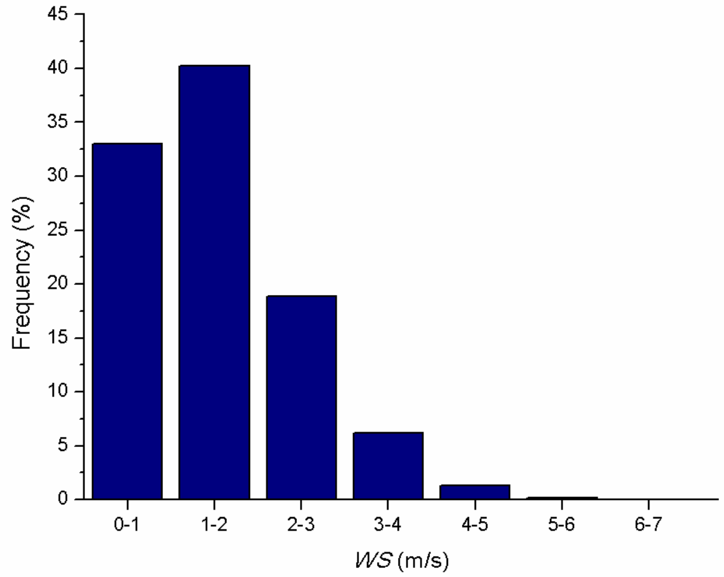

Figure 101: ***WS*** **distribution over the period that the experiments were conducted in Albuquerque, NM.**

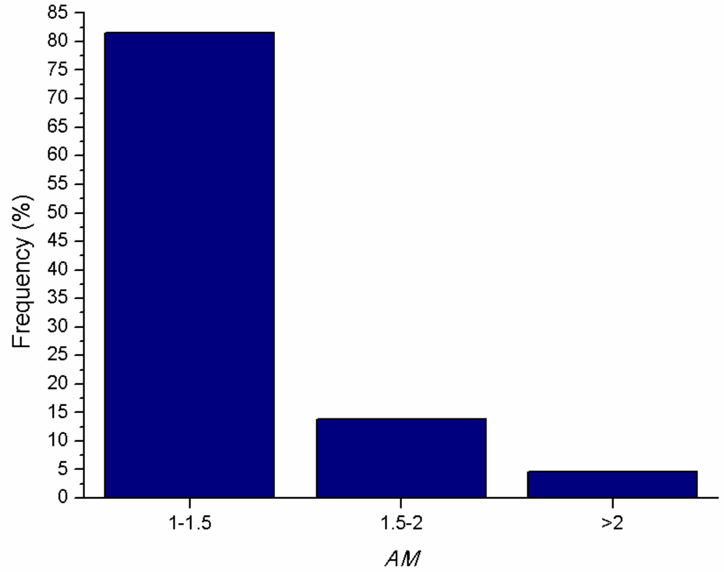

Figure 102: ***AM*** **distribution over the period that the experiments were conducted in Albuquerque, NM.**

New Mexico is affected by the North American Monsoon System every Summer [225] and therefore during the measurement periods, most mornings were characterised by a relatively clear-sky, while most of the afternoons were characterised by heavy clouds and rain or/and thunderstorms. In order to capture the effects of spectrum changes over a course of a day, only three relatively clear-sky days occurred and therefore have been selected for the evaluation of the outdoor testing; these days were: 03/08/2015, 13/08/2015 and 19/08/2015. The data were filtered for 1-minute *DNI* variation < 2%;

this resulted to 1735 datapoints out of 1781 (raw datapoints), i.e. 614, 600, 521 datapoints for 03/08/2015, 13/08/2015 and 19/08/2015 respectively.

7.2.1. Spectral performance

Figure 103 shows the *AM* diurnal variation during the three selected days; an increase in *AM* can be noticed with each passing day since the measurements were taken after the Summer solstice. The sunphotometer measurements are given in Figures 104 and 105 for *AOD* and *PW* respectively. The maximum *AOD* change during a single day was 0.02, 0.05, 0.09 on 03/08/2015, 13/08/2015, 19/08/2015 respectively. Similarly, the maximum *PW* change during a single day was 0.75 cm, 0.23 cm, 0.26 cm on 03/08/2015, 13/08/2015, 19/08/2015 respectively. The average values are given in Table 33. It can be seen that on 03/08/2015 the lowest average *AOD* and highest average *PW* occurred while on the 19/08/2015 the highest *AOD* and lowest *PW* occurred.

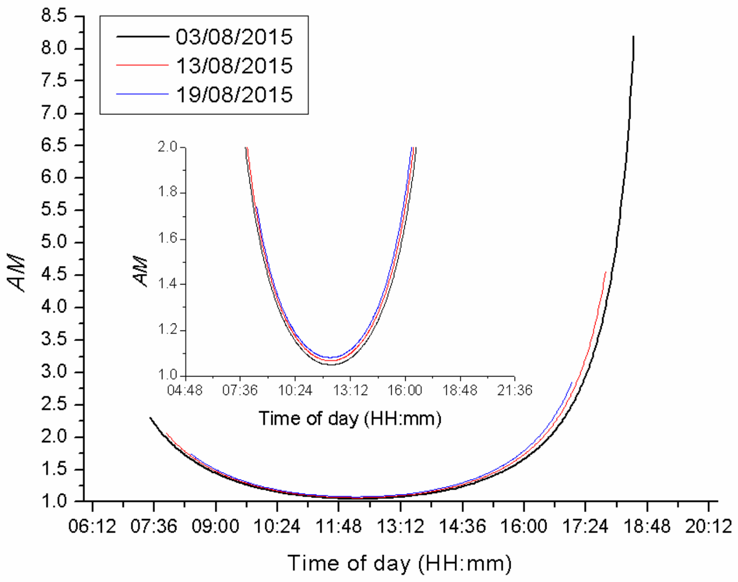

Figure 103: ***AM*** **variation over a course of the day on the 03/08/2015, 13/08/2015, 19/08/2015 in Albuquerque, NM.**

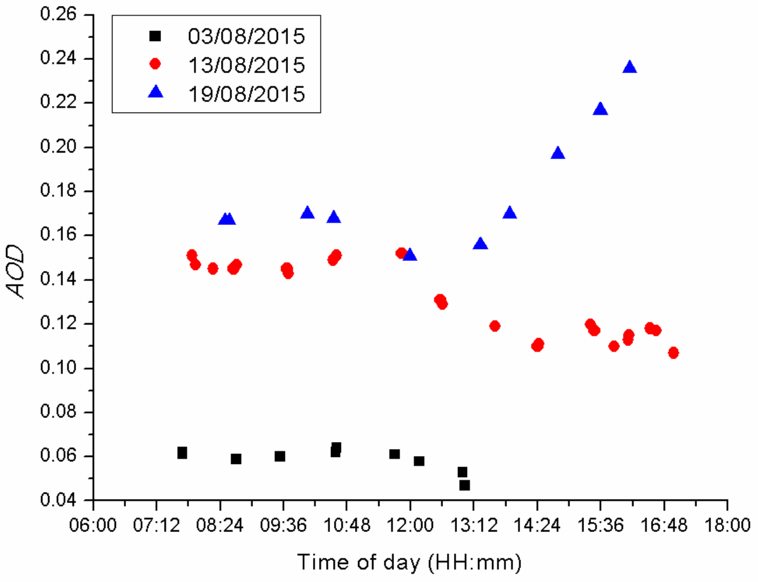

Figure 104: *AOD* variation over a course of the day on the 03/08/2015, 13/08/2015, 19/08/2015 in Albuquerque, NM.

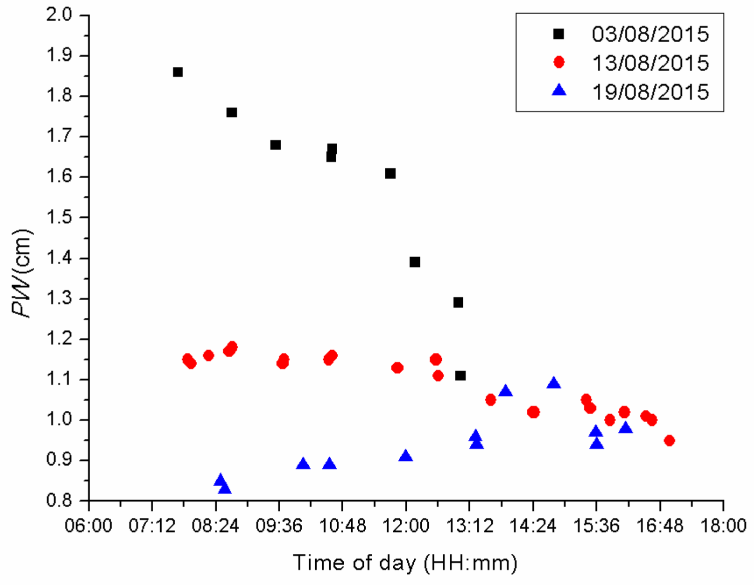

Figure 105: *PW* variation over a course of the day on the 03/08/2015, 13/08/2015, 19/08/2015 in Albuquerque, NM.

Date	*AOD*	*PW* (cm)
03/08/2015	0.06	1.59
13/08/2015	0.13	1.09
19/08/2015	0.18	0.94

Table 33: Average daily values of *AOD* and *PW* for 3rd, 13th, 19th of August 2015 in Albuquerque, NM.

The diurnal *DNI* variation is shown in Figure 106; since the *DNI* is affected by *AM* and *AOD* in a higher degree than *PW* (see Chapter 6), it can be seen that the *DNI* is higher on 03/08/2015 because of the lower *AM* and *AOD* values. In addition, it can be noticed that on the 13/08/2015 and 19/08/2015 the diurnal variation of *DNI* is similar until around noon, where *AOD* are also similar (see Figure 104), and that during the afternoon the *DNI* is lower on 19/08/2015 because of the increase in *AOD*.

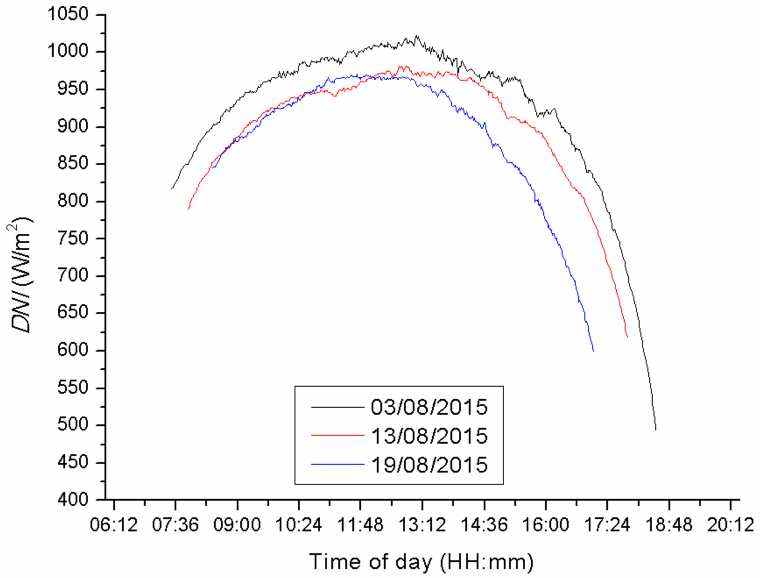

Figure 106: Diurnal variation of *DNI* on the 03/08/2015, 13/08/2015, 19/08/2015 in Albuquerque, NM.

The *DNI* decreases with increasing *AM* as expected and as illustrated in Figure 107. However, it can be noticed that the *AM* influence on *DNI* during the morning hours is different than the afternoon hours and that is mainly due to the *AOD* content in the atmosphere. While on 03/08/2015 and 13/08/2015, the *DNI* is lower during the morning hours, on 19/08/2015 the trend is different exhibiting higher *DNI* during the morning as compared to the *DNI* measured in the afternoon. This can be explained, again, by comparing Figures 104, 106 and 107 where it can be seen that on 03/08/2015 (although not enough data, the trend can be assumed to decrease around noon) and 13/08/2015 the *AOD* is reduced in the afternoon while on 19/08/2015 the *AOD* is increased.

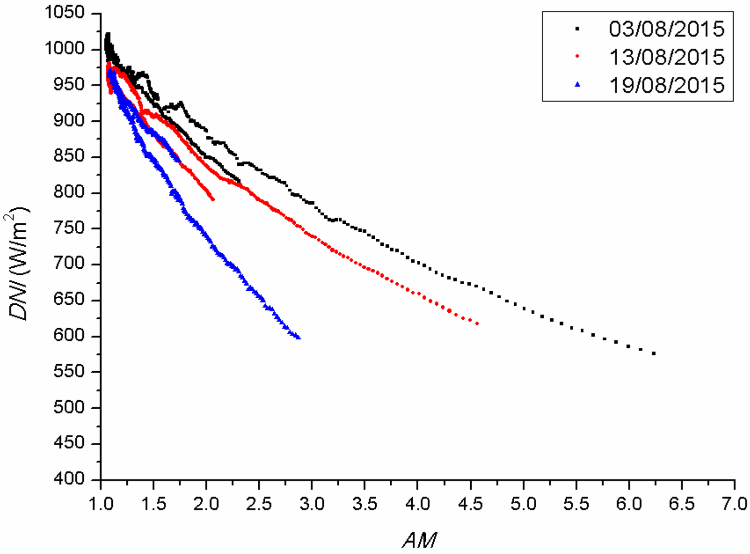

Figure 107: *DNI* as a function of *AM* on the 03/08/2015, 13/08/2015, 19/08/2015 in Albuquerque, NM.

The *SF* variation as a function of *AM* is shown in Figure 108. On the 03/08/2015, the diurnal variation of *SF* is roughly divided into three areas: morning, afternoon, sunset (see also Figure 109). In the morning hours, for $AM < 2.5$, the $SF \approx 1.05$ at 7.37 am ($AM = 2.3$, $AOD \approx 0.06$ and $PW \approx 1.9$ cm) and decreases below $SF = 1$ at around 10 am ($AM < 1.25$, $AOD \approx 0.06$ and $PW \approx 1.65$ cm) down to $SF = 0.98$ at around 12.15 pm ($AM \approx 1.05$, $AOD \approx 0.06$ and $PW \approx 1.4$ cm). During the afternoon, the *SF* slowly increases with increasing *AM* up to $SF \approx 1.03$ at around 17.30 pm ($AM \approx 3.2$, no atmospheric data available) where it decreases again almost linearly (for approximately $AM > 4$) during the rapid increase of *AM* (i.e. sunset). The lower peak in Figure 109 between morning and afternoon hours can be explained by the decrease of the *PW* during the day (see Figure 105). Similar behaviours, but to a lesser extent, are noticed on the 13/08/2015 and 19/08/2015; this is mainly due to the higher *AOD* and lower *PW* during those days (see Table 33). By comparing these two days, it can be seen that spectral gains (i.e. $SF > 1$) occurred only during the morning of 13/08/2015 (until 8.20 am approximately). On the 19/08/2015, the $SF < 1$ during the day, due to the lower *PW* and the increased *AOD* after around noon (see Figure 104); this can explain the "collapse" in Figures 108 and 109. In addition, the arrow in Figure 108 indicates the decreasing *AOD* and increasing *PW* similar to results presented by Muller *et al.* [226], where the I_{sc}/DNI change was used as a criterion. More details explaining the behaviour can be found in Chapter 6.

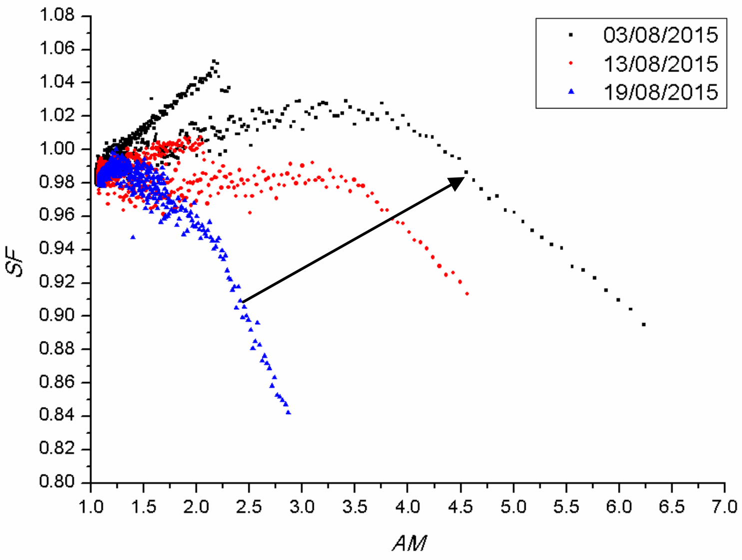

Figure 108: *SF* as a function of *AM* on the 03/08/2015, 13/08/2015, 19/08/2015 in Albuquerque, NM. The arrow indicates decreasing *AOD* and increasing *PW*.

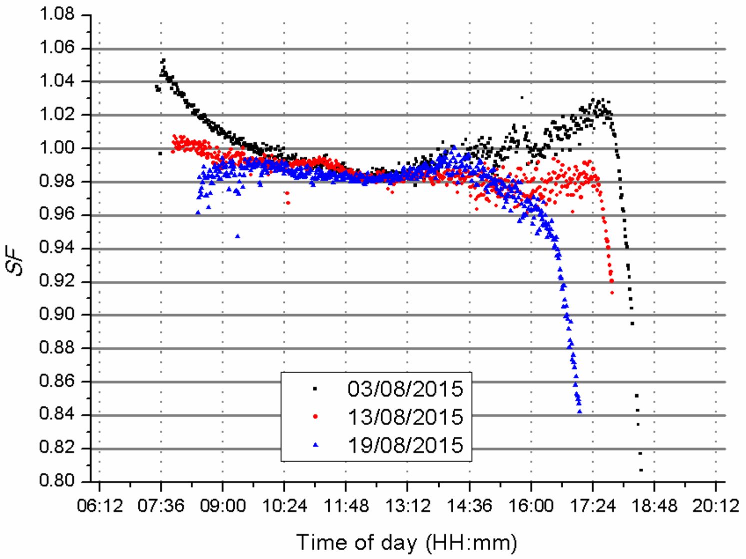

Figure 109: Diurnal variation of *SF* on the 03/08/2015, 13/08/2015, 19/08/2015 in Albuquerque, NM.

As mentioned in Chapters 2 and 3, BPI isotype (or component) cells were used to characterise the spectral solar irradiance. Such devices have the same composition as 3J III-V solar cells but with only one active p-n junction [84]. Therefore, they can provide information about the current generation at each subcell of a 3J III-V solar cell which in turn can be used to characterise the spectrum through the *SMR* index, described in Chapter 2. For reminder purposes, the *SMR1* (i.e. top to middle) indicates a blue rich spectrum when > 1, a red rich spectrum when < 1 and a similar to reference conditions spectrum when equal to 1. On the other hand, the *SMR2* (i.e. middle to bottom) is not described quantitatively in the literature, but in general terms, the higher the *SMR2*, the higher the *PW* (i.e. wetter atmosphere) [80].

SMR1 and *SMR2* were plotted against *AM* in Figures 110 and 111 respectively. Similar to the earlier discussion, the *SMR* indices on the 03/08/2015 are also higher than for the other days in both cases (*SMR1* and *SMR2*) due to the lower *AOD* and higher *PW*. The *SMR1* on the 03/08/2015 is slightly higher (by up to ~ 0.002) in the morning due to the higher compared to the afternoon *PW*; similarly *SMR2* during the morning of the same day is higher (by up to ~ 0.05). On the 13/08/2015 however, the *SMR1* starts lower (= 0.94) and increases during the afternoon for *AM* < 2, due to the reduction in *AOD*. In Figure 112, the diurnal variations of *SMR1* and *SMR2* are shown; overall, it is obvious that the highest *SMR1* and *SMR2* occur during the 03/08/2015 due to the lowest *AOD* and highest *PW*. Also, similar to the *SF*, it can be noticed that the *SMR2* during the afternoon (see also Figure 110) is lower than the beginning of the day because of the *PW* reduction. The same effects as in Figure 106 can be noticed on the 13/08/2015 and 19/08/2015; after around 12 pm the *SMR1* is higher on the 13/08/2015 compared to the 19/08/2015, because of the increase in *AOD* on the 19/08/2015. A sudden drop was observed in *SMR2* similar to *SF* (Figure 109), due to the increase in *AOD* after the noon of the 19/08/2015. In addition, the spectrum can be considered blue rich for the largest part of the day.

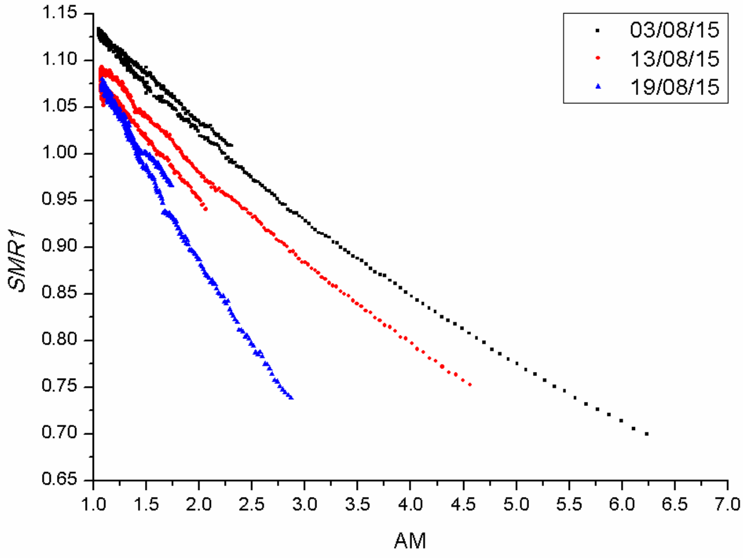

Figure 110: *SMR1* as a function of *AM* on the 03/08/2015, 13/08/2015, 19/08/2015 in Albuquerque, NM

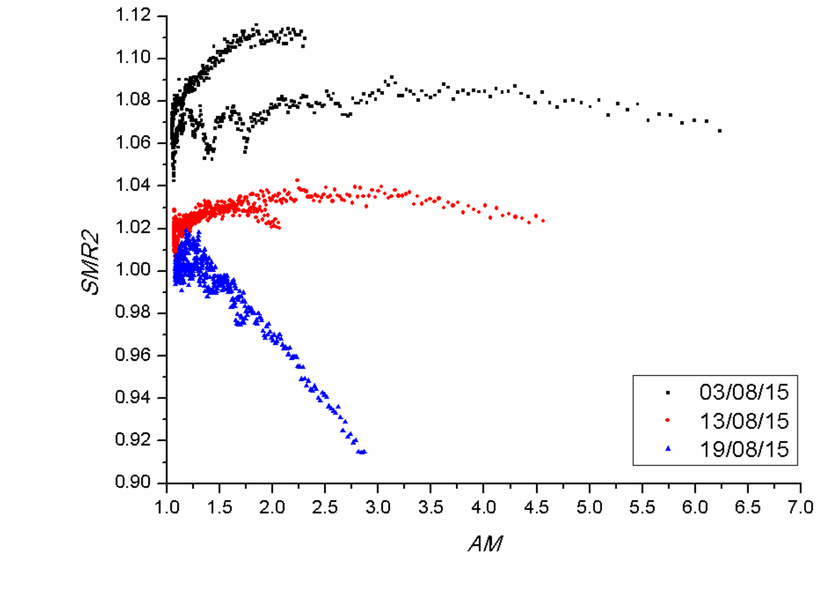

Figure 111: ***SMR2*** **as a function of** ***AM*** **on the 03/08/2015, 13/08/2015, 19/08/2015 in Albuquerque, NM**

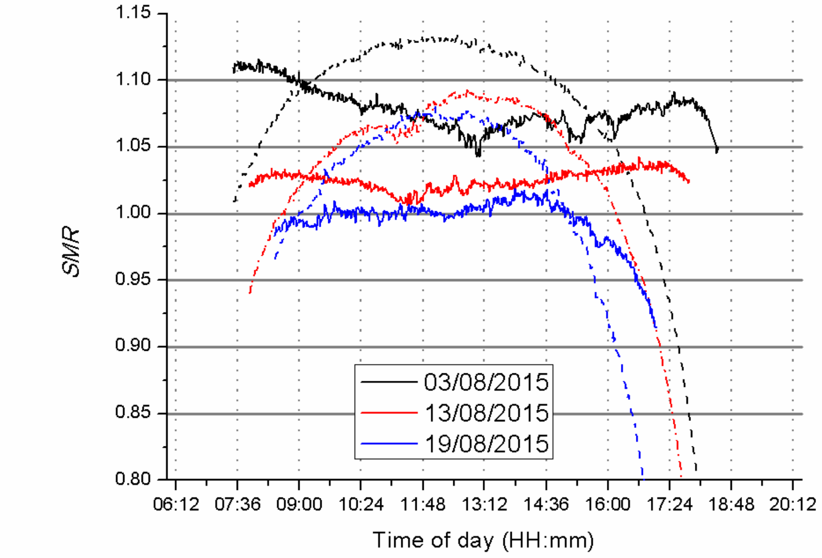

Figure 112: Diurnal variation of ***SMR1*** **(dash lines) and** ***SMR2*** **(solid lines) on the 03/08/2015 (black colour), 13/08/2015 (red colour), 19/08/2015 (blue colour) in Albuquerque, NM.**

The influence of *SMR1* on *SF* is shown in Figure 113. Overall, the trend is similar to the modelled data in Figure 94; the *SF* increases with increasing *SMR1* until it reaches the maximum and then it decreases. On the 03/08/2015, the *SF* presents gains up to 5% for the majority of the day while the spectrum is blue-rich. On the 13/08/2015 spectral gains up to 1% occur while spectrum is on the "boundary" between blue- and red-rich; on the 19/08/2015 no spectral gains occur even when the solar spectrum is blue-rich.

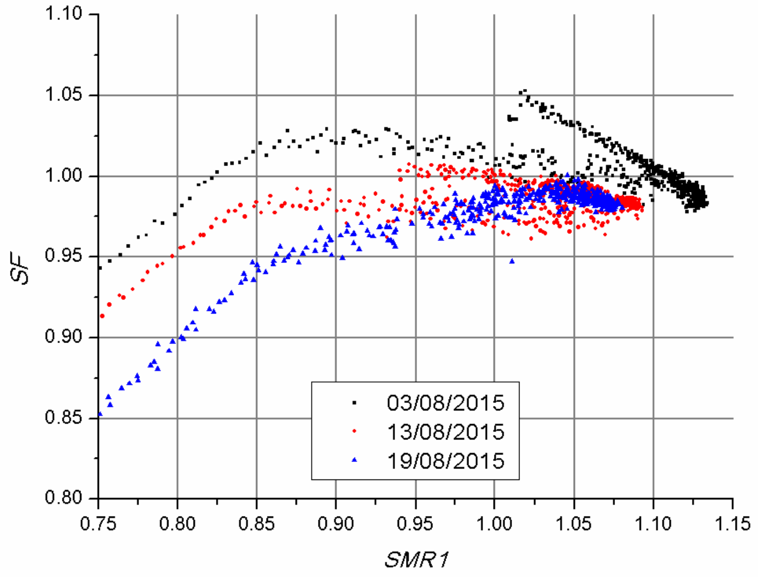

Figure 113: ***SF*** **as a function of** ***SMR1*** **on the 03/08/2015, 13/08/2015, 19/08/2015 in Albuquerque, NM.**

7.2.2. Electrical and thermal performance

The irradiance and ambient conditions during the selected days are shown in Figure 114 for *DNI*, *DNI*/*GNI* ratio, T_{amb} and *WS*. For comparison purposes the *DNI* figure is repeated; on the 03/08/2015, the highest *DNI* was measured at 1022 W/m^2 mainly due to the lowest *AOD* and *PW*, as explained earlier. The *DNI*/*GNI* ratio shows that on the 03/08/2015, some "light" clouds introduced some spikes, although the ratio was still above 0.8 (i.e. less than 20% diffused irradiance). The highest T_{amb} was 34.8°C and was recorded on the 13/08/2015 while the minimum was 21.2°C during the early morning of 03/08/2015. The *WS* on the 03/08/2015 and 13/08/2015 was similar, while on the 19/08/2015 the morning was windy with a maximum *WS* of 6.5 m/s.

Figure 115 shows the diurnal variation of measured electrical parameters P_{mp}, I_{sc}, V_{oc} and *FF*. As expected, since *DNI* is the dominant parameter that affects the electrical performance, the I_{sc} and hence the P_{mp} follows the same trend as the *DNI*. The maximum P_{mp}, I_{sc}, V_{oc} and *FF* were 23.1 W, 11.58 A, 2.98 V and 83% respectively. V_{oc} and *FF* exhibit their lowest values during midday to afternoon due to the higher temperatures. During the morning of the 19/08/2015 the V_{oc} and *FF* is higher due to the higher *WS* and lower T_{amb}.

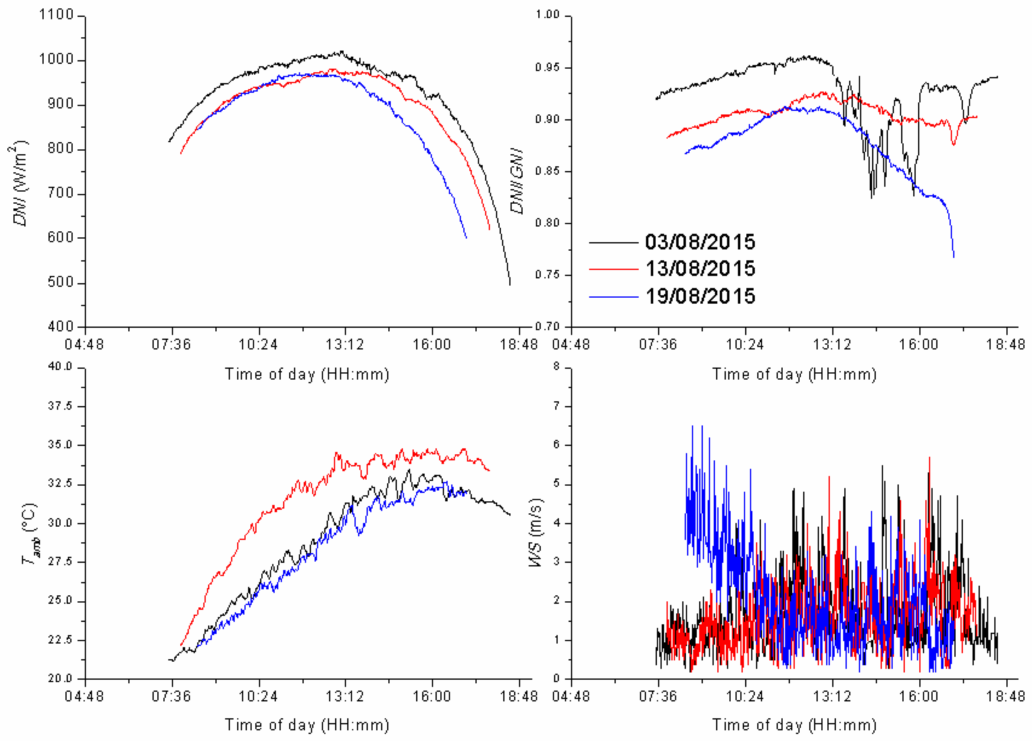

Figure 114: Diurnal variation of *DNI* (top left), *DNI*/*GNI* ratio (top right), T_{amb} (bottom left) and *WS* (bottom right) on the 03/08/2015, 13/08/2015, 19/08/2015 in Albuquerque, NM. The top left *DNI* figure is repeated for comparison purposes.

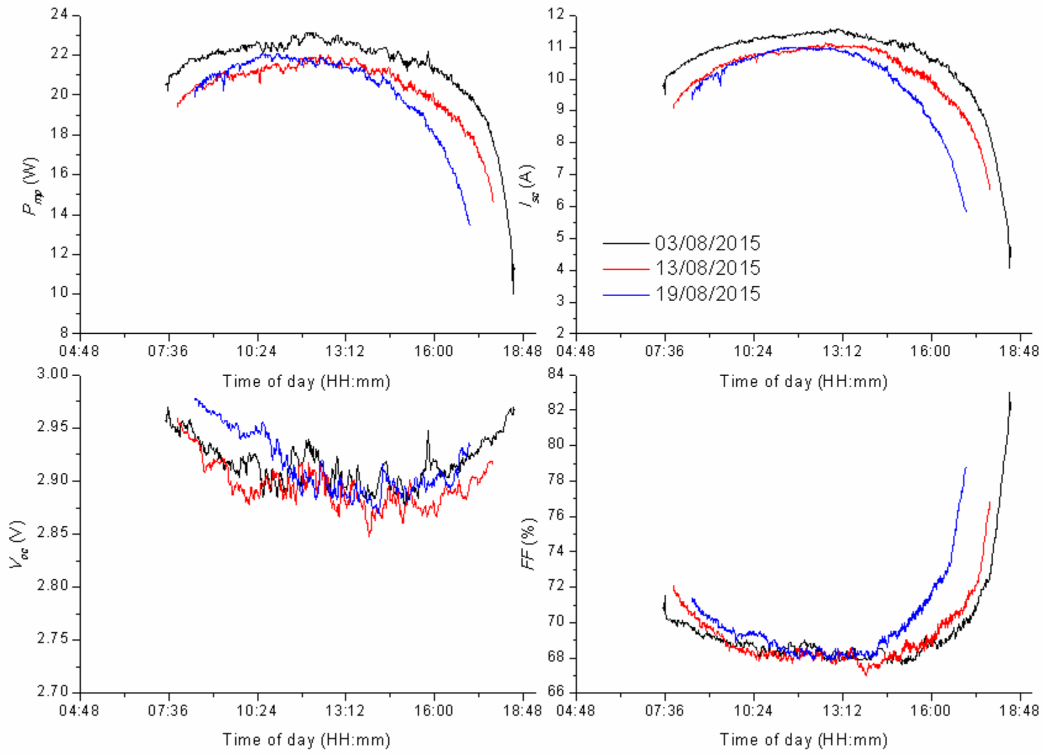

Figure 115: Diurnal variation of P_{mp} (top left), I_{sc} (top right), V_{oc} (bottom left) and *FF* (bottom right) on the 03/08/2015, 13/08/2015, 19/08/2015 in Albuquerque, NM.

In addition, the T_{diode} and T_{HS} are illustrated in Figure 116; the highest average temperatures were measured on the 13/08/2015 with T_{diode} = 61.7°C and T_{HS} = 57.36°C; this can be attributed to the T_{amb}, because although the *DNI* is lower (compared to the 03/08/2015), the T_{amb} is much higher (by an average of 3°C) and therefore contributes to the higher temperatures. On the same day the maximum T_{diode} = 70.32°C and T_{HS} = 67.56°C. Minimum, maximum and average T_{diode} and T_{HS} are given in Tables 34 and 35 respectively.

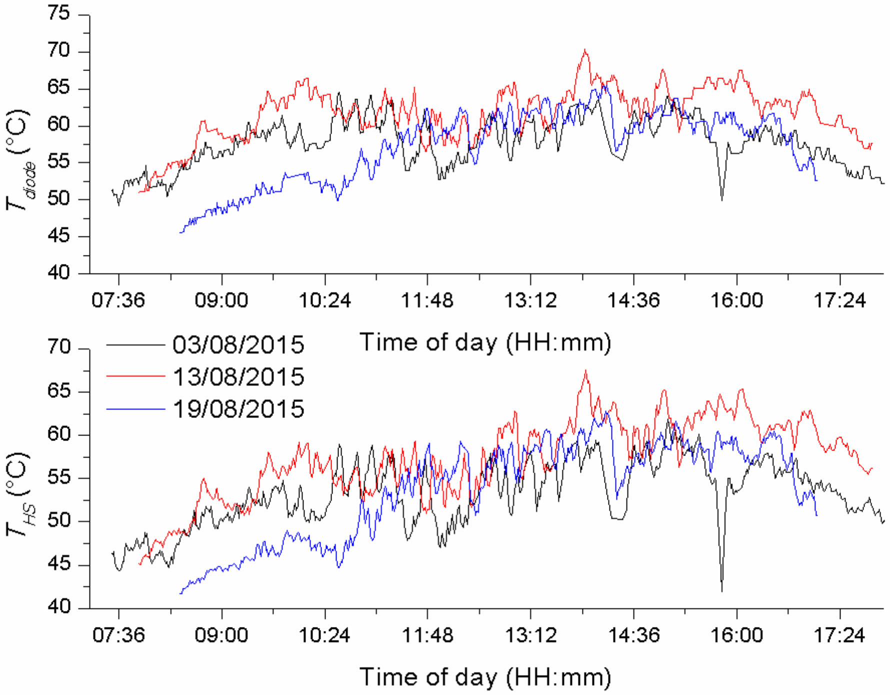

Figure 116: Diurnal variation of T_{diode} (top figure) and T_{HS} (bottom figure) on the 03/08/2015, 13/08/2015, 19/08/2015 in Albuquerque, NM.

T_{diode} (°C)	Minimum	Maximum	Average
03/08/2015	46.00	64.49	57.35
13/08/2015	51.04	70.32	61.71
19/08/2015	45.63	65.50	57.27

Table 34: Minimum, maximum and average T_{diode} measured on the 03/08/2015, 13/08/2015, 19/08/2015 in Albuquerque, NM.

T_{HS} (°C)	Minimum	Maximum	Average
03/08/2015	41.97	61.88	53.01
13/08/2015	45.05	67.56	57.36
19/08/2015	41.70	62.78	53.81

Table 35: Minimum, maximum and average T_{HS} measured on the 03/08/2015, 13/08/2015, 19/08/2015 in Albuquerque, NM.

The linear relation between I_{sc} and DNI is shown in Figure 117 for all three days for a DNI between approximately 500 W/m^2 to approximately 1050 W/m^2. The R^2 values of the linear fits for each day and all together are given in Table 36 and it ranges between 0.967 to 0.992. Although Figure 117 shows that the I_{sc} is predominantly affected linearly by the DNI as a first approximation [209], it is also important to evaluate the spectral sensitivity of MJ solar cells [226]. This was the aim of the investigation presented earlier in section 7.2.1. using the SF and SMR indices.

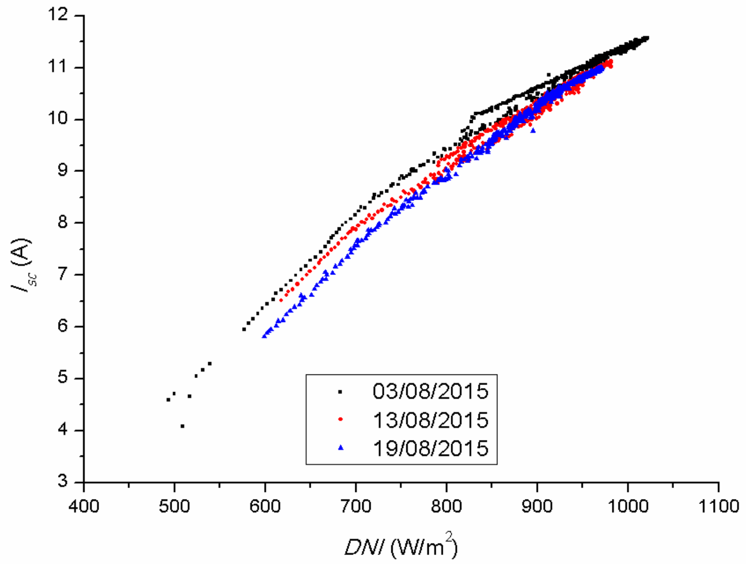

Figure 117: I_{sc} as a function of DNI on the 03/08/2015, 13/08/2015, 19/08/2015 in Albuquerque, NM.

Day	**03/08/2015**	**13/08/2015**	**19/08/2015**	**All**
R^2	0.967	0.989	0.992	0.974

Table 36: R^2 values obtained by linear fit of I_{sc} Vs DNI for each day and all three together.

Similarly, the influence of DNI on P_{mp} is shown in Figure 118. Again, the relation is described linearly and the R^2 values were 0.932, 0.9304, 0.959, 0.920 for 03/08/2015, 13/08/2015, 19/08/2015 and all days together respectively (Table 37). Although the linear fit is considered good (range from 0.92 to 0.959), it can be seen that, on the 19/08/2015 the fit is higher than the rest days, probably because the rapid changes in AM during the late afternoon were not measured during that day. This statement however, needs further investigation comparing measured data from other locations and also during different seasons.

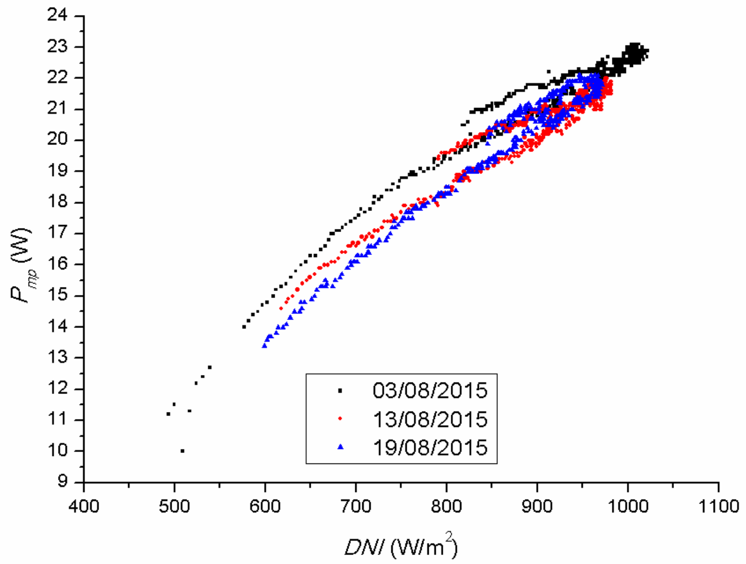

Figure 118: P_{mp} as a function of *DNI* on the 03/08/2015, 13/08/2015, 19/08/2015 in Albuquerque, NM.

Day	03/08/2015	13/08/2015	19/08/2015	All
R^2	0.932	0.9304	0.959	0.920

Table 37: R^2 values obtained by linear fit of P_{mp} Vs *DNI* for each day and all three together.

Figures 119 and 120 show the diurnal variation of electrical conversion efficiency during the selected days and the influence of AM on the efficiency respectively. Qualitatively, the trend is similar to the *SF* (Figure 109) with peak efficiencies during the early morning (23.2% at 07:37 am) and late afternoon hours (23.1% at 17:59 pm) on the 03/08/2015. The average efficiencies measured were 21.4%, 20.9%, 21% and the maximum 23.2%, 22.6%, 22.15% on the 03/08/2015, 13/08/2015, 19/08/2015 respectively. When the effect of *AM* on the electrical conversion efficiency is compared, it can be seen that the trend is similar to *SF* again (Figure 108), but to a lesser extent due to the other electrical parameters that affect the efficiency (i.e. voltage). It can be seen that on the 03/08/2015 the efficiency peaks when the $AM \approx 2$ but only during the morning hours where the $PW_{morning} > PW_{afternoon}$ (also discussed earlier). Again, the arrow in Figure 120 indicates the decreasing *AOD* and increasing *PW*; the combination of which, affects the performance in a positive manner (as described thoroughly earlier in this chapter and also in Chapter 6).

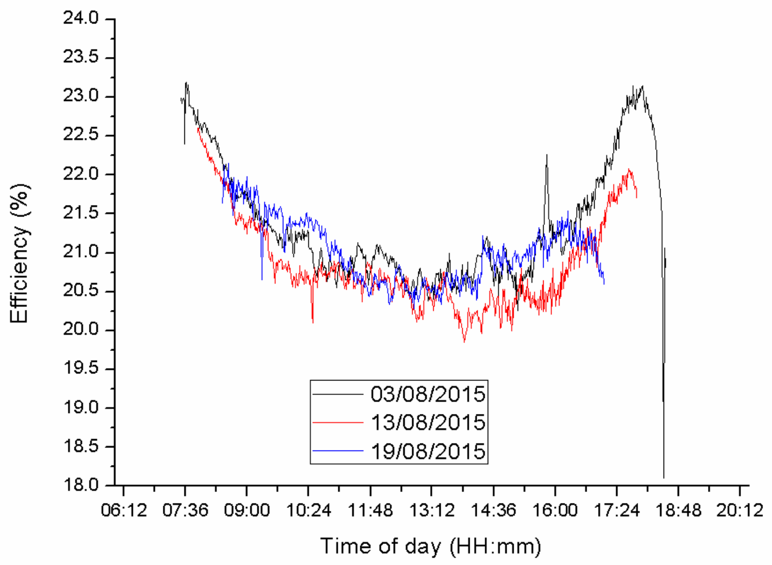

Figure 119: Diurnal variation of electrical conversion efficiency on the 03/08/2015, 13/08/2015, 19/08/2015 in Albuquerque, NM.

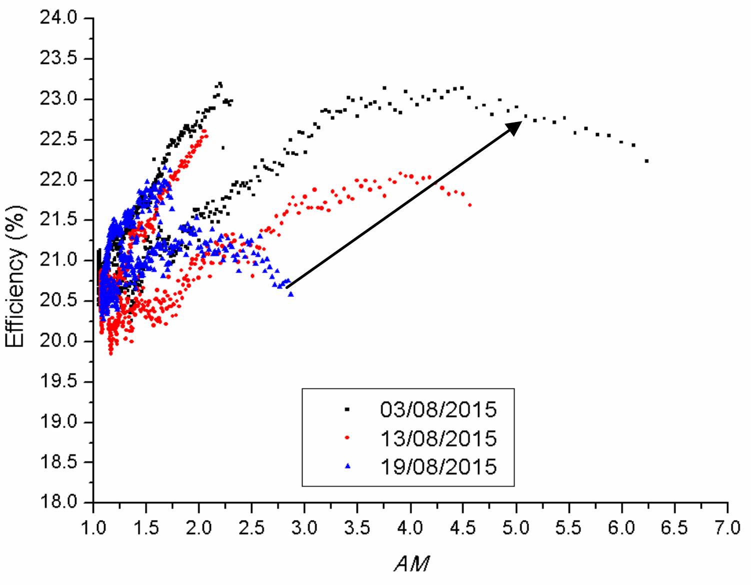

Figure 120: Influence of *AM* on electrical conversion efficiency on the 03/08/2015, 13/08/2015, 19/08/2015 in Albuquerque, NM. The arrow indicates the decreasing *AOD* and increasing *PW*.

The influence of T_{amb} on the $V_{oc}/V_{oc,ref}$ is illustrated in Figure 121; as expected the ratio is decreasing with increasing T_{amb} due to its effect on T_{cell}. The maximum value recorded was 0.945 (on the 19/08/2015 at T_{amb} = 22.1°C) while the minimum was 0.904 (on the 19/08/2015 at T_{amb} = 33.8°C), for a range of T_{amb} = 21.2°C to 34.8°C. Hence, the T_{amb} has a relatively low impact on the V_{oc} although longer datasets are required to verify the observation.

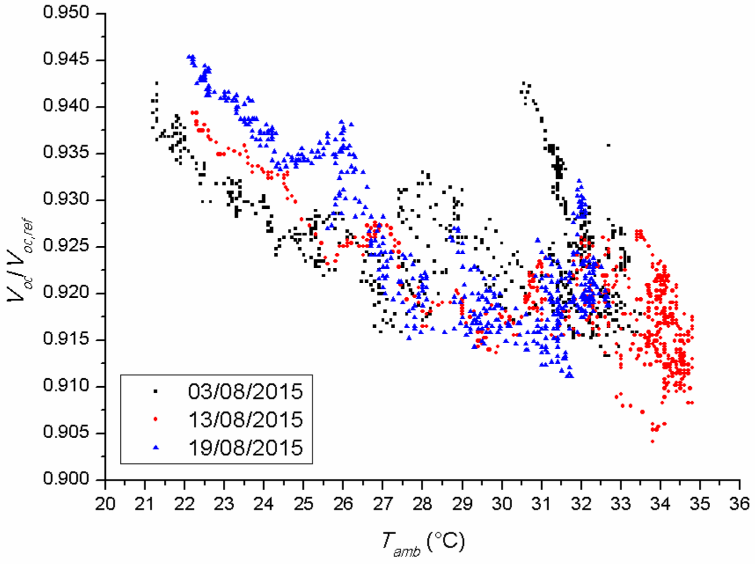

Figure 121: Ratio of $V_{oc}/V_{oc,ref}$ as a function of T_{amb} on the 03/08/2015, 13/08/2015, 19/08/2015 in Albuquerque, NM.

Similarly the I_{sc}/DNI is plotted in Figure 122; although the ratio was expected to increase with increasing T_{amb} (since the T_{diode} is increasing with T_{amb}, see Figure 123) this was not observed during the measurements. This could be caused by two effects: spectral or/and Fresnel lens thermal expansion. The spectral analysis presented earlier has shown how the performance varies during the day and the peaks observed in Figure 122 are similar to the ones of *SF*; this can be an indication that the spectral performance balances out the effect of T_{amb} on the I_{sc}/DNI. Therefore, the ratio is higher when spectral gains occur and lower when losses occur. On the other hand, research has shown that the increasing temperatures can modify the optical efficiency due to the temperature dependence of the refractive index and also due to surface deformation of the Fresnel lens [111, 121, 208, 227, 228]. The effect was also noticed by García-Domingo *et al*. [81]. Further investigations are required to quantify the effect of changing Fresnel lens temperature on the optical, spectral and electrical performance of CPV systems.

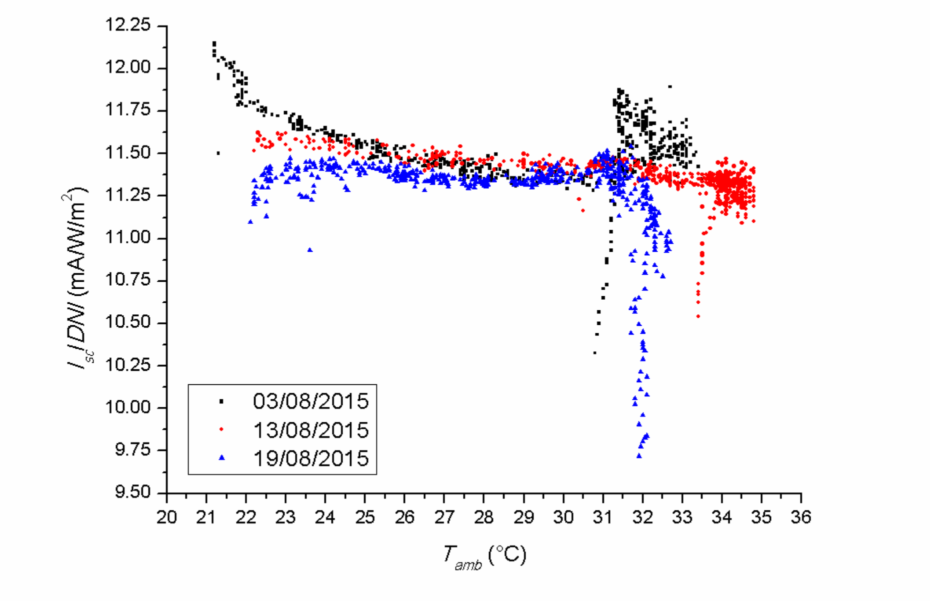

Figure 122: Ratio of I_{sc}/DNI as a function of T_{amb} on the 03/08/2015, 13/08/2015, 19/08/2015 in Albuquerque, NM.

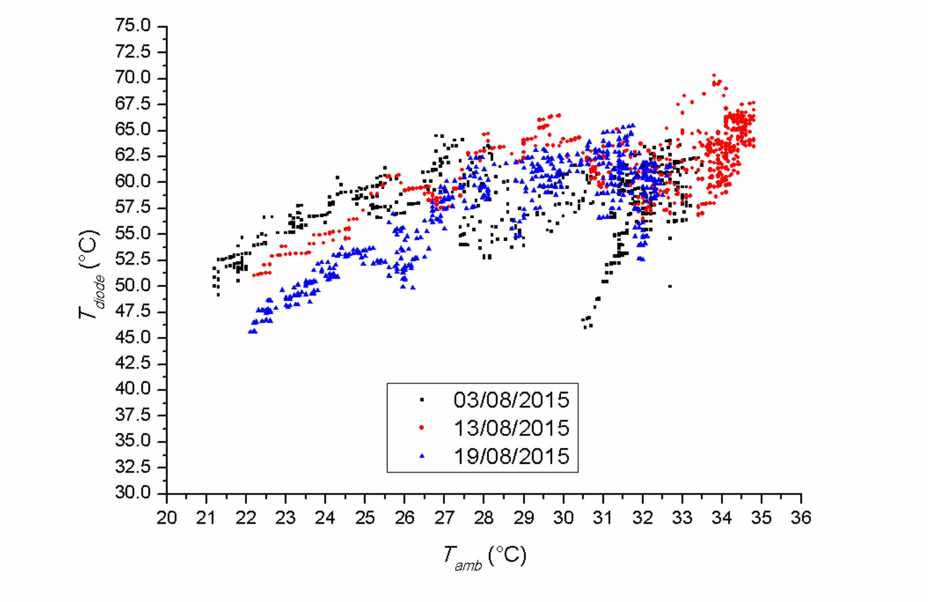

Figure 123: T_{diode} against T_{amb} on the 03/08/2015, 13/08/2015, 19/08/2015 in Albuquerque, NM.

7.3. CSOC and CSTC calculations of monomodule

Although, the DDM-1090× monomodule is only used for research purposes, it was evaluated outdoors in terms of the standarised procedures of CSOC and CSTC in order to gain a better understanding and detect possible deviations using different procedures and/or filtering criteria. The CSOC and CSTC have been described in Chapter 2.

7.3.1. CSOC

The filtering criteria were adopted from Muller *et al.* [115] and the range of *WS* from Steiner *et al.*[145]; these are given in Table 38. The criteria ensure stability on the outdoor conditions in terms of irradiance, spectral characteristics in terms of *SMR1* and *SMR2* and not extreme ambient conditions in terms of wind speed and temperature. In addition, filters regarding the tracker's accuracy are also included.

Filtering parameter	**Acceptable range**
DNI	700 - 1100 W/m^2
DNI/*GNI*	> 0.8
10 min *DNI* variation prior to *I-V* curve	< 10%
DNI variation during *I-V* sweep	< 1%
SMR1	within X% of unity*
SMR2	within X% of unity*
Instantaneous azimuth pointing error	< 0.2 times the acceptance angle
Instantaneous elevation pointing error	< 0.2 times the acceptance angle
T_{amb}	0 - 40°C
WS	0 - 6 m/s**

* The *SMR1* and *SMR2* ranges have not yet been agreed by the IEC group.
** The *WS* has not yet been agreed either but the range reported in [145] was used.

Table 38: Filtering criteria for CSOC and CSTC per the draft of IEC 62670-03, directly adopted from Muller *et al.* [115].

The methods described by the equations (40) to (42) (see Chapter 2), were considered for the CSOC estimation. The same filters were applied to all methods, for the three days described earlier and also for all measurements from 25/06/2015 to 21/08/2015 in Albuquerque, NM. The *SMR1* was considered to be *SMR1* = 1±1% and the *SMR2* was varied according to the ranges used by Fraunhofer ISE (*SMR2* = 1±5%), NREL (*SMR2* = 1±2.5%) [115] and UPM (*SMR2* = 1±1%) [80]. From the three days dataset, out of 1735 datapoints, the data were reduced to 85, 48, 45 with "tighter" *SMR2*, while with for all measurements from 25/06/2015 to 21/08/2015, out of 14082 datapoints, the data were reduced to 224, 146, 91 with "tighter" *SMR2*. The results of the CSOC estimations are given in Tables 39 and 40 for the three relatively clear-sky days and also for all measurements, respectively. In parenthesis the R^2 values of the regression are shown. In the case of the three clear-sky days, the P_{CSOC} range was found to vary from 20.74 W to 21.53 W between all methods and *SMR2* filters; this is a difference of 3.7%.

When all measurements were considered the P_{CSOC} range was found to vary from 21.08 W to 21.54 W, a maximum 2.2% difference. By comparing the R^2 values of the ASTM E2527-09 method between the two scenarios, it can be seen that the larger dataset has significantly lower R^2.

***SMR2* Filter**	**Eq. 40 (W)**	**Eq. 41 (W)**	**Eq. 42 (W)**	**No. of data**
SMR2 = 1±5%	21.51 (0.94)	20.97	20.74	85
SMR2 = 1±2.5%	21.49 (0.93)	21.02	21.11	48
SMR2 = 1±1%	21.53 (0.94)	21.01	21.09	45

Table 39: P_{CSOC} estimations during the three selected days using equations (40) to (42) along with the number of remaining datapoints after filtering of *SMR2* and Table 38. In parenthesis is the R^2 value of the regression.

***SMR2* Filter**	**Eq. 40 (W)**	**Eq. 41 (W)**	**Eq. 42 (W)**	**No. of data**
SMR2 = 1±5%	21.32 (0.81)	21.22	21.08	224
SMR2 = 1±2.5%	21.54 (0.73)	21.11	21.30	146
SMR2 = 1±1%	21.45 (0.72)	21.21	21.30	91

Table 40: P_{CSOC} estimations for all measurements from 25/06/2015 to 21/08/2015 in Albuquerque, NM using equations (40) to (42) along with the number of remaining datapoints after filtering of *SMR2* and Table 38. In parenthesis is the R^2 value of the regression.

Figure 124 shows a contour plot of *SMR1* against *SMR2* for $DNI \geq 750$ W/m^2. The bold horizontal lines filter the *SMR1* = 1±1% and the vertical ones *SMR2* = 1±5%; these correspond to a *DNI* range between 850 W/m^2 to 900 W/m^2. Higher intensities occur during blue-rich skies, i.e. when the *AM* or/and the *AOD* are low and hence, higher *SMR1*. Having in mind the seasonal variations, the *SMR* distributions will vary, and therefore the CSOC estimations will be affected. Therefore, for an accurate CSOC evaluation, the rating has to be compared with data in different locations, during different times of the year in both hemispheres. Although a lower range *SMR2* can avoid the seasonal or location dependencies, the "tighter" filtering can cause a significant reduction in the amount of data, introducing a higher uncertainty in the CSOC estimation. It also has to be noted that the differences of 3.7% and 2.2% between methods can be considered satisfactorily.

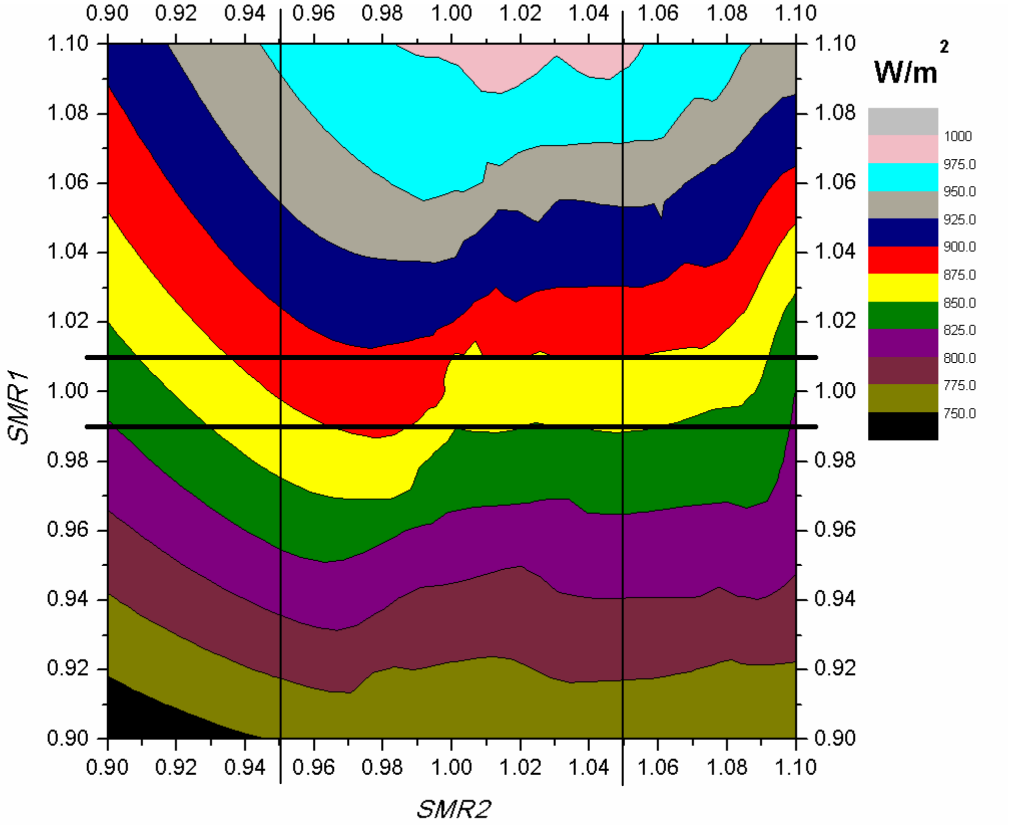

Figure 124: *SMR1* and *SMR2* contour plot for *DNI* ≥ 750 W/m^2 during the three selected days in Albuquerque, NM. The bold horizontal lines filter the *SMR1* = 1±1% and the vertical ones *SMR2* = 1±5%.

7.3.2. CSTC

As mentioned in Chapter 2, the CSTC can be evaluated using the method described by Muller *et al.* [115], i.e. by the translation of outdoor *I-V* measurements. Knowledge of the operating T_{cell} is therefore necessary in order to correct to standard test conditions. Hence, the V_{oc}-I_{sc} method given in the procedure was used (see equation (25)).

Although the procedure suggests the calculation of reference conditions through thermal transient measurements (TTM), here it is assumed that the CSTC data from the manufacturer are accurate and therefore the $I_{sc,ref}$, $V_{oc,ref}$ and temperature coefficients will be taken from the available datasheet.

The same filters as in the CSOC evaluation have been applied, and the *SMR2* was varied in a similar way. The results of the CSTC estimations are summarised in Tables 41 and 42. It can be seen that the P_{CSTC} ranges from 25.38 W to 25.73 W, depending on the *SMR2* filter and the amount of data considered (after filtering). This translates to only 1.37% difference and can be concluded that three clear days of measurements can be adequate for the CSTC estimation, independent of the *SMR2* range although this might be different for other locations. When the outdoor P_{CSTC} estimation is compared with another monomodule CSTC tested indoors (with a solar simulator), the difference jumps up to 8.9%, for an indoor P_{CSTC} of 27.74 W. This can be attributed again, to the effect of the Fresnel lens temperature since the indoors test is flash (so the impact of the temperature dependence of the Fresnel lens is negligible). In addition, since the trackers present errors (even very low; see filtering criteria), they can contribute to the difference between indoors and outdoors CSTC.

***SMR2* Filter**	**$\eta_{CSTC,avg}$ (%)**	**P_{CSTC} (W)**	**No. of data**
SMR2 = 1±5%	23.34	25.44	85
SMR2 = 1±2.5%	23.28	25.38	48
SMR2 = 1±1%	23.29	25.38	45

Table 41: P_{CSTC} and $\eta_{CSTC,avg}$ estimations during the three selected days along with the number of remaining datapoints after filtering of *SMR2* and Table 38.

***SMR2* Filter**	**$\eta_{CSTC,avg}$ (%)**	**P_{CSTC} (W)**	**No. of data**
SMR2 = 1±5%	23.60	25.73	224
SMR2 = 1±2.5%	23.43	25.53	146
SMR2 = 1±1%	23.45	25.56	91

Table 42: P_{CSTC} and $\eta_{CSTC,avg}$ estimations for all measurements from 25/06/2015 to 21/08/2015 in Albuquerque, NM along with the number of remaining datapoints after filtering of *SMR2* and Table 38.

7.4. Summary and conclusions

The outdoor spectral, electrical and thermal performance of a HCPV monomodule has been described in this chapter. Initially, the frequency distributions of the irradiance and ambient conditions have been described. In order to reduce the noise in the characterisation, three relatively clear-sky days have been selected for the evaluation.

The influence of the solar geometry and atmospheric parameters has been found to be of great importance when the spectral gains were compared between the three selected days. In particular, it was shown that on the 03/08/2015 spectral gains up to 5% were observed due to the lower *AOD* (i.e. relatively clear atmosphere) and higher *PW* (i.e. relatively wet atmosphere). This was also observed on the diurnal variation of *DNI* where on 03/08/2015 *DNI* was higher at all times, and that during the afternoon hours, the *DNI* on the 19/08/2015 was at the lowest because of the increase in *AOD*. Significant differences were found in *DNI*, *SF*, *SMR* during the morning and afternoon hours, mainly because of the variation in *AOD* and *PW*.

The electrical characterisation showed a similar behaviour as the spectral, verifying the importance of the spectrum variations on CPV performance. The I_{sc} and P_{mp} exhibited a linear relation against the *DNI,* however it was agreed that the spectral sensitivity of III-V 3J solar cells also plays a significant role. This was noticed when diurnal variation of the electrical conversion efficiency was plotted and also against the *AM*; the peaks were measured during the early morning and late afternoon due to the spectrum changes (also mentioned in the previous paragraph). In terms of the thermal behaviour, and as expected, the measured temperatures on heat sink and diode peaked during the afternoon, i.e. when *DNI* and T_{amb} were also high. Maximum temperatures of 70.32°C and 67.56°C were observed on the diode and heat sink respectively. The V_{oc} and I_{sc} did not exhibit a dependence on T_{amb}; this was attributed to the temperature dependence of the Fresnel lens and that future work should try to quantify the effect based on measured data so a correction factor can be proposed.

CSOC and CSTC ratings were evaluated, based on the procedures described in literature and are currently in the draft stage and also the ASTME2527-09. In terms of CSOC, the proposed methods were compared using a different *SMR2* range as a filter (in addition to the filters that have been agreed within the IEC subgroup). Differences of 3.7% and 2.2% have been found depending on the number of data considered (i.e. the filters applied) and the method used. The estimation of CSTC power was within 1.37% between *SMR2* ranges however, when the outdoor CSTC was compared to an indoor one, a maximum of 8.9% was found (using a different monomodule). The extent of this difference was attributed to the Fresnel lens dependence on temperature and also the tracker errors that occur when operated in the field.

Chapter 8: Conclusions & recommendations for future work

In this research, a spectral dependent electrical and thermal model has been developed for 3J HCPV receivers. While other traditional models predict the cooling requirements and thermal behaviour using constant parameters (e.g. AM1.5D, constant electrical efficiency or even T_{amb} = 25°C), the model described in this study quantified the cooling requirements based on the solar spectrum taking into account the mismatch between individual subcells and also the ambient and atmospheric characteristics. Other models are not applicable to systems operating in "hot and dry" climates (i.e. with high T_{amb}, low AM, low AOD and low PW) because the cooling requirements are usually underestimated. In addition, when the electrical performance and energy yield are evaluated, the integrated modelling approach is simulated iteratively taking into account the generated heat based on the spectral variations, resulting in a more realistic approximation. In summary, when high-quality atmospheric data are available for a given location, it is possible to predict the spectral, electrical and thermal performance of HCPV systems based on the proposed integrated modelling procedure. Moreover, these models can also be used by HCPV designers in order to calculate the cooling requirements and avoid any unnecessary increased material usage (by oversizing and increasing the weight and cost), or undersizing and risking the system's long-term reliability.

8.1. Conclusions

The mathematical formulation of the electrical and thermal models was presented in Chapter 3. A schematic explaining the integrated modelling process was also presented along with the experimental setup and equipment used to carry out the validation and outdoor characterisation. In Chapter 4, the integrated solar spectrum dependent electrical and thermal model was described for 3J solar cells under concentration followed by an application for the C1MJ CCA. Input ranges and boundary conditions were also given. The model examined the electrical and thermal behaviour of 3J solar cells under variable air mass and ambient temperature conditions. The electrical parameters were characterised as a function of the spectrum and T_{cell}. The heat power due to current mismatch was also quantified. It was found that CPV single cell configurations of 1 cm^2 area, can be adequately cooled passively with a heat sink thermal resistance below 1.63 K/W while for locations with extreme ambient conditions (i.e. low AM and high T_{amb}), a thermal resistance less than 1.4 K/W is needed to keep the CCA operating below 90°C. Solar cells with lower area can withstand higher concentrations for the same thermal resistance values or higher thermal resistance at CR of 500×. It was also concluded that since the solar spectrum is transient during the day, the AM1.5D does not offer representative results of the realistic operation of the solar cell in the field. Instead, designing the cooling or heat sinking requirements at AM < AM1.5D is more preferable because the 3J solar cell is not current matched and also because the heat is higher, due to higher solar radiation intensity.

In Chapter 5, a 3D FEA model for the DDM-1090× monomodule has been developed in order to validate the accuracy of the numerical process presented in Chapters 4 and 6. The boundary conditions and a mesh independency analysis were also presented. The models were validated independently and as an integrated model. The errors between measurements and simulations were considered to be acceptable. The SMARTS2 predicted well spectral DNI input well, especially for $AM < 2$ ($NRMSE$ = 2.8%). The T_{diode} and T_{HS} were compared with measured data and the simulated T_{cell} with the V_{oc}-I_{sc} method with a good agreement in all cases ($NRMSE$ between 3.03% and 5.68%). It is important to highlight that the proposed T_{cell} estimation method can be used at both maximum power point and open-circuit conditions. The electrical model has been validated in terms of the I_{sc}, V_{oc}, P_{mp} and FF with $NRMSE$ of 2.84%, 0.7%, 2.66% and 1.2% respectively.

The model presented and validated in Chapters 4 and 5 was extended in Chapter 6 in order to assess the influence of AM, AOD and PW on the spectral, electrical and thermal behaviour of 3J solar cells. The results showed that such solar cells exhibited spectral losses with increasing AM and AOD while with increasing PW they showed spectral gains; this was attributed to the irradiance reduction at the longer wavelengths of the solar spectrum. The normalised electrical power losses increased significantly for AM values greater than $AM = 2$ (up to 50.3% at $AM = 10$). The procedure was then simplified in order to handle bulk spectra, introducing a cell temperature estimation based on regression analysis. Class I TMY3 data have been used for four US locations with relatively high annual DNI (Albuquerque, El Paso, Las Vegas and Tucson) in order to evaluate the performance of a CCA. By varying the h_{conv} at each location, its influence on E_{yield} could then be determined. Different h_{conv} were suggested for each location; 1250 W/(m^2·K) for Albuquerque and El Paso, 1450 W/(m^2·K) for Las Vegas and 1350 W/(m^2·K) for Tucson. In order to quantify the h_{conv} under extreme conditions, a method was presented in order to evaluate the cooling requirements under worst-case scenarios; i.e. AM1D, T_{amb} = 45°C and a relatively clear (low *AOD*) and dry (low *PW*) atmosphere. It has been shown that in order to operate at maximum T_{cell} lower than 100°C, the h_{conv} should be greater than 1300 W/(m^2·K). Moreover, the results were compared with the ASTM G173-03 and a ΔT_{cell} up to 9.3°C was observed.

Finally in Chapter 7, the outdoor spectral, electrical and thermal performance of a HCPV monomodule were described. Three relatively clear-sky days have been selected for the evaluation and the influence of the *AM, AOD, PW* which have been found to be of great importance when the spectral gains were compared between the three selected days. In particular, it was shown that the day with the lowest *AOD* and highest *PW* exhibited a better spectral and electrical performance. The *DNI* was also found to vary with the changes in *AOD* and *PW*; a similar effect was observed on *SF*, *SMR* and electrical conversion efficiency. As expected, the I_{sc} and P_{mp} exhibited a linear relation against the *DNI*, however it was agreed that the spectral sensitivity of III-V 3J solar cells also plays a significant role. CSOC and CSTC ratings were evaluated for different datasets and *SMR2* filter. Differences were observed depending on the number of data considered, the method used and the *SMR2* filter. Suggestions and recommendations were drafted in order to improve the rating procedures.

8.2. Recommendations for future work

Although in this work, a spectral distribution validation was not performed due to the lack of an accurate spectroradiometer, it can be suggested for a future study. As expected, the error of the spectral *DNI* input influences the prediction of the electrical prediction and therefore, an improvement on the measurement and/or calculation of spectral irradiance may reduce the errors further. The integrated modelling procedure could also benefit if the following recommendations were included:

1) The non-uniformity of irradiance on the solar cell's surface needs to be considered. One suggestion to achieve this is by dividing the solar cell's area into regions with different corresponding spectral irradiances; this will also take

into account the chromatic aberrations that take place when refractive optical components are used to concentrate the direct sunlight.

2) The concentrator optics need to be modelled in terms of their spectral transmittance or reflectivity as a function of temperature. Increasing temperatures on refractive optics will result in a change in the refractive index of the lens due to thermal expansion; this will lead to an increase in the focal length and therefore change the overall system power generation [121]. The effect of lens temperature was also observed during the outdoor characterisation (see Chapter 7).

3) In order to improve the cell temperature prediction, the tracker position and wind speed and direction should be taken into account.

4) Future work should incorporate costs in order to optimise the electrical and thermal performance at the lowest heat sink cost.

5) The complexity of the model can be significantly reduced if analytical equations are established to quantify the *SF* at each subcell and whole cell. This will significantly reduce the simulation time and complexity since bulk spectra will not be required as input. The analytical equations of *SF* could potentially be used to calculate the effective irradiance and also other spectral indices such as the *SMR*.

6) The modelling procedure presented in this thesis was based on steady-state models that were simulated iteratively. The system's behaviour however is dynamic especially during transient irradiance or/and wind. Therefore, dynamic modelling would be beneficial for the integrated model's accuracy.

References

[1] T. Markvart, *Solar Electricity*, 2nd Edition ed.: John Wiley & Sons, 2000.

[2] REN21, "Renewables 2015 Global Status Report," 2015.

[3] V. Fthenakis, "Preface," in *Third Generation Photovoltaics*, V. Fthenakis, Ed., ed: InTech, 2012, pp. VII-X.

[4] J. Aguilera, "Introduction," in *High Concentrator Photovoltaics*, P. Pérez-Higueras and E. F. Fernández, Eds., ed: Springer International Publishing, 2015, pp. 1-8.

[5] R. McConnell and V. Fthenakis, "Concentrated Photovoltaics," in *Third Generation Photovoltaics*, V. Fthenakis, Ed., ed: InTech, 2012, pp. 167-182.

[6] A. Vossier, E. Al Alam, A. Dollet, and M. Amara, "Assessing the Efficiency of Advanced Multijunction Solar Cells in Real Working Conditions: A Theoretical Analysis," *Photovoltaics, IEEE Journal of,* vol. 5, pp. 1805-1812, 2015.

[7] W. Shockley and H. J. Queisser, "Detailed Balance Limit of Efficiency of p ‐ n Junction Solar Cells," *Journal of Applied Physics,* vol. 32, pp. 510-519, 1961.

[8] A. D. Vos, "Detailed balance limit of the efficiency of tandem solar cells," *Journal of Physics D: Applied Physics,* vol. 13, p. 839, 1980.

[9] V. Paraskeva, M. Hadjipanayi, M. Norton, M. Pravettoni, and G. E. Georghiou, "Voltage and light bias dependent quantum efficiency measurements of GaInP/GaInAs/Ge triple junction devices," *Solar Energy Materials and Solar Cells,* vol. 116, pp. 55-60, Sep 2013.

[10] H. Helmers, M. Schachtner, and A. W. Bett, "Influence of temperature and irradiance on triple-junction solar subcells," *Solar Energy Materials and Solar Cells,* vol. 116, pp. 144-152, 2013.

[11] S. P. Philipps, A. W. Bett, K. Horowitz, and S. Kurtz, "Current status of concentrator photovoltaic (CPV) technology," 2015.

[12] NREL. (2016, May 03, 2016). *National Center for Photovoltaics. Best research-cell efficiencies chart. <http://www.nrel.gov/ncpv/images/efficiency_chart.jpg>.*

[13] F. Dimroth. (2014, December 30, 2015). *New world record for solar cell efficiency at 46%*.

[14] M. Vazquez, C. Algora, I. Rey-Stolle, and J. R. Gonzalez, "III-V concentrator solar cell reliability prediction based on quantitative LED reliability data," *Progress in Photovoltaics,* vol. 15, pp. 477-491, Sep 2007.

[15] J. R. González, M. Vázquez, N. Núñez, C. Algora, and P. Espinet, "Reliability Improvement in III–V Concentrator Solar Cells by Means of Perimeter Protection," *AIP Conference Proceedings,* vol. 1277, pp. 221-224, 2010.

[16] W. M. Rohouma, I. M. Molokhia, and A. H. Esuri, "Comparative study of different PV modules configuration reliability," *Desalination,* vol. 209, pp. 122-128, 2007.

[17] E. V. Yastrebova, "High-efficiency multi-junction solar cells : Current status and future potential," *Centre for Research in Photonics, University of Ottawa, Ottawa, Canada,* 2007.

[18] D. Barlev, R. Vidu, and P. Stroeve, "Innovation in concentrated solar power," *Solar Energy Materials and Solar Cells,* vol. 95, pp. 2703-2725, Oct 2011.

[19] A. Gombert, I. Heile, J. Wüllner, T. Gerstmaier, S. van Riesen, E. Gerster, M. Röttger, and H. Lerchenmüller, "Recent progress in concentrator photovoltaics," in *SPIE 7725, Photonics for Solar Energy Systems III*, Brussels, Belgium, 2010, pp. 772508-772508-9.

[20] R. M. Swanson, "The promise of concentrators," *Progress in Photovoltaics: Research and Applications,* vol. 8, pp. 93-111, 2000.

[21] W. T. Xie, Y. J. Dai, R. Z. Wang, and K. Sumathy, "Concentrated solar energy applications using Fresnel lenses: A review," *Renewable and Sustainable Energy Reviews,* vol. 15, pp. 2588-2606, 2011.

[22] A. Chatterjee, E. Bernal, S. Seshadri, O. Mayer, and M. Greaves, "Linear Fresnel Reflector based Solar Radiation Concentrator for Combined Heating and Power," *7th*

International Conference on Concentrating Photovoltaic Systems (CPV-7), vol. 1407, 2011.

[23] S. K. Natarajan, T. K. Mallick, M. Katz, and S. Weingaertner, "Numerical investigations of solar cell temperature for photovoltaic concentrator system with and without passive cooling arrangements," *International Journal of Thermal Sciences,* vol. 50, pp. 2514-2521, Dec 2011.

[24] H. Helmers, A. Boos, F. Jetter, A. Heimsath, M. Wiesenfarth, and A. W. Bett, "Outdoor Test Setup for Concentrating Photovoltaic and Thermal (CPVT) Systems," *7th International Conference on Concentrating Photovoltaic Systems (CPV-7),* vol. 1407, 2011.

[25] A. Kribus, D. Kaftori, G. Mittelman, A. Hirshfeld, Y. Flitsanov, and A. Dayan, "A miniature concentrating photovoltaic and thermal system," *Energy Conversion and Management,* vol. 47, pp. 3582-3590, Dec 2006.

[26] G. Sala, J. C. Arboiro, A. Luque, I. Antón, M. P. Gasson, N. B. Mason, K. C. Heasman, T. Bruton, E. Mera, E. Camblor, P. Datta, M. Cendagorta, M. P. Friend, P. Valera, S. González, F. Dobón, and F. Pérez, "480 kWpeak EUCLIDES Concentrator Power Plant Using Parabolic Troughs," in *2nd World Conference on PV Solar Energy Converstion*, Vienna, Austria, 1998, pp. 1963-1968.

[27] F. Calise, A. Palombo, and L. Vanoli, "A finite-volume model of a parabolic trough photovoltaic/thermal collector: Energetic and exergetic analyses," *Energy,* vol. 46, pp. 283-294, 2012.

[28] T. K. Mallick and P. C. Eames, "Electrical performance evaluation of low-concentrating non-imaging photovoltaic concentrator," *Progress in Photovoltaics,* vol. 16, pp. 389-398, Aug 2008.

[29] T. K. Mallick, P. C. Eames, T. J. Hyde, and B. Norton, "The design and experimental characterisation of an asymmetric compound parabolic photovoltaic concentrator for building facade integration in the UK," *Solar Energy,* vol. 77, pp. 319-327, 2004.

[30] T. K. Mallick, P. C. Eames, and B. Norton, "Power losses in an asymmetric compound parabolic photovoltaic concentrator," *Solar Energy Materials and Solar Cells,* vol. 91, pp. 1137-1146, Jul 23 2007.

[31] S. V. Vasylyev, V. P. Vasylyev, and V. A. Sergeev, "Concept and Design of "Flat-Plate" Cpv Module Based on Ring-Array Concentrator," *35th IEEE Photovoltaic Specialists Conference,* pp. 3087-3091, 2010.

[32] W. G. Van Sark, K. W. Barnham, L. H. Slooff, A. J. Chatten, A. Buchtemann, A. Meyer, S. J. McCormack, R. Koole, D. J. Farrell, R. Bose, E. E. Bende, A. R. Burgers, T. Budel, J. Quilitz, M. Kennedy, T. Meyer, M. Donega Cde, A. Meijerink, and D. Vanmaekelbergh, "Luminescent Solar Concentrators--a review of recent results," *Optics Express,* vol. 16, pp. 21773-92, Dec 22 2008.

[33] M. G. Debije and P. P. C. Verbunt, "Thirty Years of Luminescent Solar Concentrator Research: Solar Energy for the Built Environment," *Advanced Energy Materials,* vol. 2, pp. 12-35, 2012.

[34] K. Shanks, S. Senthilarasu, and T. Mallick, "High-Concentration Optics for Photovoltaic Applications," in *High Concentrator Photovoltaics*, P. Pérez-Higueras and E. F. Fernández, Eds., ed: Springer International Publishing, 2015, pp. 85-113.

[35] P. Perez-Higueras, E. Munoz, G. Almonacid, and P. G. Vidal, "High Concentrator PhotoVoltaics efficiencies: Present status and forecast," *Renewable & Sustainable Energy Reviews,* vol. 15, pp. 1810-1815, May 2011.

[36] A. Y. Kuo, B. Lin, C. C. Huang, J. Chen, P. K. Chiang, S. Shao, R. Wu, and I. Lin, "A Modular Solar Engine with Solar Cell, Heat Pipe, and Heat Sink in an Integrated Package for High Concentrating Photovoltaic," in *34th IEEE Photovoltaic Specialists Conference*, Philadelphia, PA, USA, 2009, pp. 166-169.

[37] K. Araki, H. Uozumi, and M. Yamaguchi, "A simple-passive cooling structure and its heat analysis for 500 X concentrator PV module," in *29th IEEE Photovoltaic Specialists Conference*, New Orleans, LA, USA, 2002, pp. 1568-1571.

[38] C. Min, C. Nuofu, Y. Xiaoli, W. Yu, B. Yiming, and Z. Xingwang, "Thermal analysis and test for single concentrator solar cells," *Journal of Semiconductors,* vol. 30, 2009.

[39] Z. B. Ye, Q. F. Li, Q. Z. Zhu, and W. G. Pan, "The cooling technology of solar cells under concentrated system," in *6th IEEE International Power Electronics and Motion Control Conference* Wuhan, China, 2009, pp. 1252-1256.

[40] A. Royne, C. J. Dey, and D. R. Mills, "Cooling of photovoltaic cells under concentrated illumination: a critical review," *Solar Energy Materials and Solar Cells,* vol. 86, pp. 451-483, Apr 1 2005.

[41] Soitec. (2015, January 04, 2016). *Four-junction solar cell developed using Soitec's expertise in semiconductor materials sets new efficiency record of 38.9% for CPV module, http://www.soitec.com/en/news/press-releases/article-1737/.*

[42] M. Steiner, G. Siefer, T. Schmidt, M. Wiesenfarth, F. Dimroth, and A. W. Bett, "43% Sunlight to Electricity Conversion Efficiency Using CPV," *IEEE Journal of Photovoltaics,* vol. 6, pp. 1020-1024, 2016.

[43] F. J. Olmo, J. Vida, I. Foyo, Y. Castro-Diez, and L. Alados-Arboledas, "Prediction of global irradiance on inclined surfaces from horizontal global irradiance," *Energy,* vol. 24, pp. 689-704, 1999.

[44] J. Boland, J. Huang, and B. Ridley, "Decomposing global solar radiation into its direct and diffuse components," *Renewable and Sustainable Energy Reviews,* vol. 28, pp. 749-756, 2013.

[45] M. Iqbal, "Chapter 6 - SOLAR SPECTRAL RADIATION UNDER CLOUDLESS SKIES," in *An Introduction to Solar Radiation*, M. Iqbal, Ed., ed: Academic Press, 1983, pp. 107-168.

[46] J. Ruiz-Arias and C. Gueymard, "Solar Resource for High-Concentrator Photovoltaic Applications," in *High Concentrator Photovoltaics*, P. Pérez-Higueras and E. F. Fernández, Eds., ed: Springer International Publishing, 2015, pp. 261-302.

[47] P. Blanc, B. Espinar, N. Geuder, C. Gueymard, R. Meyer, R. Pitz-Paal, B. Reinhardt, D. Renné, M. Sengupta, L. Wald, and S. Wilbert, "Direct normal irradiance related definitions and applications: The circumsolar issue," *Solar Energy,* vol. 110, pp. 561-577, 2014.

[48] M. Sengupta, A. Habte, S. Kurtz, A. Dobos, S. Wilbert, E. Lorenz, T. Stoffel, D. Renne, C. Gueymard, D. Myers, S. M. Wilcox, P. Blanc, and R. Perez, *Best practices handbook for the collection and use of solar resource data for solar energy applications*: NREL/TP-5D00-63112, 2015.

[49] C. A. Gueymard, D. Myers, and K. Emery, "Proposed reference irradiance spectra for solar energy systems testing," *Solar Energy,* vol. 73, pp. 443-467, 2002.

[50] A. B. Murphy, P. R. F. Barnes, L. K. Randeniya, I. C. Plumb, I. E. Grey, M. D. Horne, and J. A. Glasscock, "Efficiency of solar water splitting using semiconductor electrodes," *International Journal of Hydrogen Energy,* vol. 31, pp. 1999-2017, 2006.

[51] F. Kasten and A. T. Young, "Revised optical air mass tables and approximation formula," *Applied Optics,* vol. 28, pp. 4735-4738, 1989/11/15 1989.

[52] M. Iqbal, "Chapter 5 - A CLOUDLESS-SKY ATMOSPHERE AND ITS OPTICS," in *An Introduction to Solar Radiation*, M. Iqbal, Ed., ed: Academic Press, 1983, pp. 85-105.

[53] E. F. Fernández, F. Almonacid, J. A. Ruiz-Arias, and A. Soria-Moya, "Analysis of the spectral variations on the performance of high concentrator photovoltaic modules operating under different real climate conditions," *Solar Energy Materials and Solar Cells,* vol. 127, pp. 179-187, 2014.

[54] N. L. A. Chan, H. E. Brindley, and N. J. Ekins-Daukes, "Impact of individual atmospheric parameters on CPV system power, energy yield and cost of energy," *Progress in Photovoltaics: Research and Applications,* vol. 22, pp. 1080-1095, 2014.

[55] N. L. A. Chan, T. B. Young, H. E. Brindley, N. J. Ekins-Daukes, K. Araki, Y. Kemmoku, and M. Yamaguchi, "Validation of energy prediction method for a concentrator photovoltaic module in Toyohashi Japan," *Progress in Photovoltaics: Research and Applications,* vol. 21, pp. 1598-1610, 2013.

[56] P. Faine, S. R. Kurtz, C. Riordan, and J. M. Olson, "The Influence of Spectral Solar Irradiance Variations on the Performance of Selected Single-Junction and Multijunction Solar-Cells," *Solar Cells,* vol. 31, pp. 259-278, Jun 1991.

[57] C. P. Jacovides, N. A. Kaltsounides, D. N. Asimakopoulos, and D. G. Kaskaoutis, "Spectral aerosol optical depth and Angstrom parameters in the polluted Athens atmosphere," *Theoretical and Applied Climatology,* vol. 81, pp. 161-167, 2005/07/01 2005.

[58] A. Ångström, "On the Atmospheric Transmission of Sun Radiation and on Dust in the Air," *Geografiska Annaler,* vol. 11, pp. 156-166, 1929.

[59] A. Ångström, "On the Atmospheric Transmission of Sun Radiation. II," *Geografiska Annaler,* vol. 12, pp. 130-159, 1930.

[60] G. L. Schuster, O. Dubovik, and B. N. Holben, "Angstrom exponent and bimodal aerosol size distributions," *Journal of Geophysical Research: Atmospheres,* vol. 111, pp. n/a-n/a, 2006.

[61] E. F. Fernández and F. Almonacid, "Spectrally corrected direct normal irradiance based on artificial neural networks for high concentrator photovoltaic applications," *Energy,* vol. 74, pp. 941-949, 2014.

[62] F. Almonacid, E. F. Fernández, T. K. Mallick, and P. J. Pérez-Higueras, "High concentrator photovoltaic module simulation by neuronal networks using spectrally corrected direct normal irradiance and cell temperature," *Energy,* vol. 84, pp. 336-343, 2015.

[63] C. Jardine, T. R. Betts, R. Gottschalg, D. G. Infield, and K. Lane, "Influence of spectral effects on the performance of multijunction amorphous silicon cells," in *17th European Photovoltaic and Solar Energy Conference (PVSEC)*, 2002.

[64] S. R. Williams, T. R. Betts, T. Helf, R. Gottschalg, H. G. Beyer, and D. G. Infield, "Modelling long-term module performance based on realistic reporting conditions with consideration to spectral effects," in *Photovoltaic Energy Conversion, 2003. Proceedings of 3rd World Conference on*, 2003, pp. 1908-1911 Vol.2.

[65] C. A. Gueymard, "Daily spectral effects on concentrating PV solar cells as affected by realistic aerosol optical depth and other atmospheric conditions," in *SPIE Conference #7410, Optical Modeling and Measurements for Solar Energy Systems III*, Sand Diego, CA, 2009, pp. 741007-741007-14.

[66] K. Nomura, Y. Ota, T. Minemoto, and K. Nishioka, "Seasonal variation of performance in concentrator photovoltaic system," *physica status solidi (c),* vol. 11, pp. 1427-1430, 2014.

[67] B. García-Domingo, C. J. Carmona, A. J. Rivera-Rivas, M. J. del Jesus, and J. Aguilera, "A differential evolution proposal for estimating the maximum power delivered by CPV modules under real outdoor conditions," *Expert Systems with Applications,* vol. 42, pp. 5452-5462, 2015.

[68] J. Chantana, S. Ueno, Y. Ota, K. Nishioka, and T. Minemoto, "Uniqueness verification of direct solar spectral index for estimating outdoor performance of concentrator photovoltaic systems," *Renewable Energy,* vol. 75, pp. 762-766, 2015.

[69] N. Kei, I. Kenta, O. Yasuyuki, M. Takashi, and N. Kensuke, "Effect of aerosols on performance of concentrator photovoltaics," *Japanese Journal of Applied Physics,* vol. 54, p. 08KE07, 2015.

[70] I. R. Cole and R. Gottschalg, "Improved Model for Circumsolar Irradiance Calculation as an Extended Light Source and Spectral Implications for High-Concentration Photovoltaic Devices," *Photovoltaics, IEEE Journal of,* vol. 6, pp. 258-265, 2016.

[71] M. Norton, V. Paraskeva, R. P. Kenny, and G. E. Georghiou, "Field Investigation of the Effect of Spectral Response Upon Photovoltaic Energy Yields," *IEEE Journal of Photovoltaics,* vol. 6, pp. 739-745, 2016.

[72] M. Norton, A. M. G. Amillo, and R. Galleano, "Comparison of solar spectral irradiance measurements using the average photon energy parameter," *Solar Energy,* vol. 120, pp. 337-344, 2015.

[73] R. Gottschalg, T. R. Betts, D. G. Infield, and M. J. Kearney, "The effect of spectral variations on the performance parameters of single and double junction amorphous silicon solar cells," *Solar Energy Materials and Solar Cells,* vol. 85, pp. 415-428, 2005.

[74] T. Ishii, K. Otani, T. Takashima, and Y. Xue, "Solar spectral influence on the performance of photovoltaic (PV) modules under fine weather and cloudy weather conditions," *Progress in Photovoltaics: Research and Applications,* vol. 21, pp. 481-489, 2013.

[75] K. M. Armijo, R. K. Harrison, B. H. King, and J. B. Martin, "Spectral derates phenomena of atmospheric components on multi-junction CPV technologies," *AIP Conference Proceedings,* vol. 1616, pp. 264-271, 2014.

[76] C. Dominguez, I. Anton, and G. Sala, "Multijunction solar cell model for translating I-V characteristics as a function of irradiance, spectrum, and cell temperature," *Progress in Photovoltaics: Research and Applications,* vol. 18, pp. 272-284, Jun 2010.

[77] C. Dominguez, S. Askins, I. Anton, and G. Sala, "Characterization of five CPV module technologies with the Helios 3198 solar simulator," in *Photovoltaic Specialists Conference (PVSC), 2009 34th IEEE*, 2009, pp. 001004-001008.

[78] C. Domínguez, I. Antón, G. Sala, and S. Askins, "Current-matching estimation for multijunction cells within a CPV module by means of component cells," *Progress in Photovoltaics: Research and Applications,* vol. 21, pp. 1478-1488, 2013.

[79] J. Hashimoto, S. Kurtz, K. Sakurai, M. Muller, and K. Otani, "Performance of CPV system using three types of III-V multi-junction solar cells," in *AIP Conference Proceedings*, 2012, pp. 372-375.

[80] R. Núñez, C. Domínguez, S. Askins, M. Victoria, R. Herrero, I. Antón, and G. Sala, "Determination of spectral variations by means of component cells useful for CPV rating and design," *Progress in Photovoltaics: Research and Applications,* vol. 24, pp. 663-679, 2016.

[81] B. García-Domingo, J. Aguilera, J. de la Casa, and M. Fuentes, "Modelling the influence of atmospheric conditions on the outdoor real performance of a CPV (Concentrated Photovoltaic) module," *Energy,* vol. 70, pp. 239-250, 2014.

[82] G. Nofuentes, B. García-Domingo, J. V. Muñoz, and F. Chenlo, "Analysis of the dependence of the spectral factor of some PV technologies on the solar spectrum distribution," *Applied Energy,* vol. 113, pp. 302-309, 2014.

[83] E. F. Fernández, F. Almonacid, A. Soria-Moya, and J. Terrados, "Experimental analysis of the spectral factor for quantifying the spectral influence on concentrator photovoltaic systems under real operating conditions," *Energy,* vol. 90, pp. 1878-1886, 2015.

[84] J. Jaus, T. Mißbach, S. Philipps, G. Siefer, and A. Bett, "Spectral measurements using component cells: Examinations on measurement precision," in *26th European Photovoltaic Solar Energy Conference and Exhibition (EU PVSEC)*, Hamburg, Germany, 2011, pp. 1-6.

[85] M. Meusel, R. Adelhelm, F. Dimroth, A. W. Bett, and W. Warta, "Spectral mismatch correction and spectrometric characterization of monolithic III-V multi-junction solar cells," *Progress in Photovoltaics: Research and Applications,* vol. 10, pp. 243-255, Jun 2002.

[86] G. Peharz, G. Siefer, and A. W. Bett, "A simple method for quantifying spectral impacts on multi-junction solar cells," *Solar Energy,* vol. 83, pp. 1588-1598, 2009.

[87] P. Rodrigo, E. Fernández, F. Almonacid, and P. Pérez-Higueras, "Models for the electrical characterization of high concentration photovoltaic cells and modules: A review," *Renewable and Sustainable Energy Reviews,* vol. 26, pp. 752-760, 2013.

[88] B. Galiana, C. Algora, I. Rey-Stolle, and I. G. Vara, "A 3-D model for concentrator solar cells based on distributed circuit units," *IEEE Transactions on Electron Devices,* vol. 52, pp. 2552-2558, 2005.

[89] G. Segev, G. Mittelman, and A. Kribus, "Equivalent circuit models for triple-junction concentrator solar cells," *Solar Energy Materials and Solar Cells,* vol. 98, pp. 57-65, 2012.

[90] A. Ben Or and J. Appelbaum, "Estimation of multi-junction solar cell parameters," *Progress in Photovoltaics: Research and Applications,* vol. 21, pp. 713-723, Jun 2013.

[91] K. Nishioka, T. Takamoto, T. Agui, M. Kaneiwa, Y. Uraoka, and T. Fuyuki, "Evaluation of InGaP/InGaAs/Ge triple-junction solar cell and optimization of solar cell's structure focusing on series resistance for high-efficiency concentrator photovoltaic systems," *Solar Energy Materials and Solar Cells,* vol. 90, pp. 1308-1321, May 23 2006.

[92] K. Nishioka, T. Sueto, M. Uchida, and Y. Ota, "Detailed Analysis of Temperature Characteristics of an InGaP/InGaAs/Ge Triple-Junction Solar Cell," *Journal of Electronic Materials,* vol. 39, pp. 704-708, 2010/06/01 2010.

[93] G. S. Kinsey, P. Hebert, K. E. Barbour, D. D. Krut, H. L. Cotal, and R. A. Sherif, "Concentrator multijunction solar cell characteristics under variable intensity and temperature," *Progress in Photovoltaics: Research and Applications,* vol. 16, pp. 503-508, Sep 2008.

[94] G. S. Kinsey and K. M. Edmondson, "Spectral Response and Energy Output of Concentrator Multijunction Solar Cells," *Progress in Photovoltaics: Research and Applications,* vol. 17, pp. 279-288, Aug 2009.

[95] E. F. Fernandez, G. Siefer, F. Almonacid, A. J. G. Loureiro, and P. Perez-Higueras, "A two subcell equivalent solar cell model for III-V triple junction solar cells under spectrum and temperature variations," *Solar Energy,* vol. 92, pp. 221-229, Jun 2013.

[96] E. F. Fernández, "Modelizacion y caracterizacion de celulas solares III-V multiunion y de modulos de concentracion," PhD, Universidade de Santiago de Compostela, Santiago de Compostela, 2012.

[97] D. L. King, W. E. Boyson, and J. A. Kratochvil, "Photovoltaic array performance model," SAND2004-3535; TRN: US200825%%193 United States10.2172/919131TRN: US200825%%193Mon Dec 22 09:36:17 EST 2008SNLEnglish, 2004.

[98] N. J. Ekins-Daukes, T. R. Betts, Y. Kemmoku, K. Araki, H. S. Lee, R. Gottschalg, M. B. Boreland, D. G. Infield, and M. Yamaguchi, "Syracuse - a multi-junction concentrator system computer model," in *Photovoltaic Specialists Conference, 2005. Conference Record of the Thirty-first IEEE*, 2005, pp. 651-654.

[99] N. L. A. Chan, "Solar electricity from concentrator photovoltaic systems," Ph.D., Department of Grantham Institute of Climate Change, Imperial College London, London, 2013.

[100] C. A. Gueymard, "Simple Model of the Atmospheric Radiative Transfer of Sunshine, version 2 (SMARTS2): Algorithms description and performance assessment," Florida Solar Energy Center, 1995.

[101] M. Steiner, G. Siefer, A. Bosch, T. Hornung, and A. W. Bett, "Realistic Power Output Modeling Of CPV Modules," in *AIP Conference Proceedings*, 2012, pp. 309-312.

[102] M. Steiner, G. Siefer, T. Hornung, G. Peharz, and A. W. Bett, "YieldOpt, a model to predict the power output and energy yield for concentrating photovoltaic modules," *Progress in Photovoltaics: Research and Applications,* vol. 23, pp. 385-397, 2015.

[103] T. Hornung, A. Bachmaier, P. Nitz, and A. Gombert, "Temperature and wavelength dependent measurement and simulation of Fresnel lenses for concentrating photovoltaics," in *SPIE 7725, Photonics for Solar Energy Systems III*, Brussels, Belgium, 2010, pp. 77250A-77250A-6.

[104] T. Hornung, A. Bachmaier, P. Nitz, and A. Gombert, "Temperature dependent measurement and simulation of Fresnel lenses for concentrating photovoltaics," in *6th International Conference on Concentrating Photovoltaic Systems (CPV-6)*, Freiburg, Germany, 2010.

[105] M. Steiner, W. Guter, G. Peharz, S. P. Philipps, F. Dimroth, and A. W. Bett, "A validated SPICE network simulation study on improving tunnel diodes by introducing lateral conduction layers," *Progress in Photovoltaics: Research and Applications,* vol. 20, pp. 274-283, 2012.

[106] A. J. Rivera, B. García-Domingo, M. J. del Jesus, and J. Aguilera, "Characterization of Concentrating Photovoltaic modules by cooperative competitive Radial Basis Function Networks," *Expert Systems with Applications,* vol. 40, pp. 1599-1608, 2013.

[107] F. Almonacid, E. F. Fernandez, P. Rodrigo, P. J. Perez-Higueras, and C. Rus-Casas, "Estimating the maximum power of a High Concentrator Photovoltaic (HCPV) module using an Artificial Neural Network," *Energy,* vol. 53, pp. 165-172, May 1 2013.

[108] E. F. Fernández, F. Almonacid, T. K. Mallick, and P. Perez Higueras, "Analytical Modelling of High Concentrator Photovoltaic Modules Based on Atmospheric Parameters," *International Journal of Photoenergy,* 2015.

[109] E. F. Fernández, F. Almonacid, P. Rodrigo, and P. Pérez-Higueras, "Model for the prediction of the maximum power of a high concentrator photovoltaic module," *Solar Energy,* vol. 97, pp. 12-18, 2013.

[110] P. Rodrigo, L. Micheli, and F. Almonacid, "The High-Concentrator Photovoltaic Module," in *High Concentrator Photovoltaics*, P. Pérez-Higueras and E. F. Fernández, Eds., ed: Springer International Publishing, 2015, pp. 115-151.

[111] G. Peharz, J. P. Ferrer Rodríguez, G. Siefer, and A. W. Bett, "Investigations on the temperature dependence of CPV modules equipped with triple-junction solar cells," *Progress in Photovoltaics: Research and Applications,* vol. 19, pp. 54-60, 2011.

[112] E. F. Fernandez, A. J. G. Loureiro, P. Rodrigo, F. Almonacid, J. I. Fernandez, P. J. P. Higueras, G. Almonacid, and A. J. G. Loureiro, "Calculation of Cell Temperature in a HCPV Module using V-oc," in *Spanish Conference on Electron Devices*, 2013, pp. 317-320.

[113] P. Rodrigo, E. F. Fernández, F. Almonacid, and P. J. Pérez-Higueras, "Review of methods for the calculation of cell temperature in high concentration photovoltaic modules for electrical characterization," *Renewable and Sustainable Energy Reviews,* vol. 38, pp. 478-488, 2014.

[114] Standard IEC 60904-5, "Photovoltaic devices - Part 5: Determination of the equivalent cell temperature (ECT) of photovoltaic (PV) devices by the open-circuit voltage method," 2011.

[115] M. Muller, S. Kurtz, M. Steiner, and G. Siefer, "Translating outdoor CPV I–V measurements to a CSTC power rating and the associated uncertainty," *Progress in Photovoltaics: Research and Applications,* vol. 23, pp. 1557-1571, 2015.

[116] X. Ju, A. Vossier, Z. F. Wang, A. Dollet, and G. Flamant, "An improved temperature estimation method for solar cells operating at high concentrations," *Solar Energy,* vol. 93, pp. 80-89, Jul 2013.

[117] G. Peharz, J. P. Ferrer Rodríguez, G. Siefer, and A. W. Bett, "A method for using CPV modules as temperature sensors and its application to rating procedures," *Solar Energy Materials and Solar Cells,* vol. 95, pp. 2734-2744, 2011.

[118] F. Rubio, M. Martinez, R. Coronado, J. L. Pachon, and P. Banda, "Deploying CPV power plants - ISFOC experiences," in *Photovoltaic Specialists Conference, 2008. PVSC '08. 33rd IEEE*, 2008, pp. 1-4.

[119] M. Muller, C. Deline, B. Marion, S. Kurtz, N. Bosco, F. Dimroth, G. Sala, and A. W. Bett, "Determining outdoor CPV cell temperature," in *AIP Conference Proceedings-American Institute of Physics*, 2011, p. 331.

[120] F. Almonacid, P. J. Pérez-Higueras, E. F. Fernández, and P. Rodrigo, "Relation between the cell temperature of a HCPV module and atmospheric parameters," *Solar Energy Materials and Solar Cells,* vol. 105, pp. 322-327, 2012.

[121] T. Hornung, M. Steiner, and P. Nitz, "Estimation of the influence of Fresnel lens temperature on energy generation of a concentrator photovoltaic system," *Solar Energy Materials and Solar Cells,* vol. 99, pp. 333-338, 2012.

[122] E. F. Fernández, F. Almonacid, P. Rodrigo, and P. Pérez-Higueras, "Calculation of the cell temperature of a high concentrator photovoltaic (HCPV) module: A study and comparison of different methods," *Solar Energy Materials and Solar Cells,* vol. 121, pp. 144-151, 2014.

[123] E. F. Fernández, P. Rodrigo, F. Almonacid, and P. Pérez-Higueras, "A method for estimating cell temperature at the maximum power point of a HCPV module under actual operating conditions," *Solar Energy Materials and Solar Cells,* vol. 124, pp. 159-165, 2014.

[124] L. Micheli, N. Sarmah, X. Luo, K. S. Reddy, and T. K. Mallick, "Opportunities and challenges in micro- and nano-technologies for concentrating photovoltaic cooling: A review," *Renewable and Sustainable Energy Reviews,* vol. 20, pp. 595-610, 2013.

[125] D. Du, J. Darkwa, and G. Kokogiannakis, "Thermal management systems for Photovoltaics (PV) installations: A critical review," *Solar Energy,* vol. 97, pp. 238-254, 2013.

[126] S. Jakhar, M. S. Soni, and N. Gakkhar, "Historical and recent development of concentrating photovoltaic cooling technologies," *Renewable and Sustainable Energy Reviews,* vol. 60, pp. 41-59, 2016.

[127] *Suncore Website, http://suncoreus.com/, [Accessed July 27, 2015]*.

[128] *Semprius Website, http://semprius.com/, [Accessed July 27, 2015].*

[129] L. Zhu, R. F. Boehm, Y. P. Wang, C. Halford, and Y. Sun, "Water immersion cooling of PV cells in a high concentration system," *Solar Energy Materials and Solar Cells,* vol. 95, pp. 538-545, Feb 2011.

[130] L. Zhu, Y. P. Wang, Z. L. Fang, Y. Sun, and Q. W. Huang, "An effective heat dissipation method for densely packed solar cells under high concentrations," *Solar Energy Materials and Solar Cells,* vol. 94, pp. 133-140, Feb 2010.

[131] H. Helmers, A. W. Bett, J. Parisi, and C. Agert, "Modeling of concentrating photovoltaic and thermal systems," *Progress in Photovoltaics: Research and Applications,* vol. 22, pp. 427-439, 2014.

[132] H. Helmers and K. Kramer, "Multi-linear performance model for hybrid (C)PVT solar collectors," *Solar Energy,* vol. 92, pp. 313-322, Jun 2013.

[133] A. Royne and C. J. Dey, "Design of a jet impingement cooling device for densely packed PV cells under high concentration," *Solar Energy,* vol. 81, pp. 1014-1024, 2007.

[134] J. Barrau, D. Chemisana, J. Rosell, L. Tadrist, and M. Ibanez, "An experimental study of a new hybrid jet impingement/micro-channel cooling scheme," *Applied Thermal Engineering,* vol. 30, pp. 2058-2066, Oct 2010.

[135] J. Barrau, J. Rose, and M. Ibanez, "Design Of A Hybrid Jet Impingement/Microchannel Cooling Device For Densely Packed PV Cells Under High Concentration," *6th International Conference on Concentrating Photovoltaic Systems (CPV-6),* vol. 1277, pp. 74-77, 2010.

[136] N. Xu, J. Ji, W. Sun, L. Han, H. Chen, and Z. Jin, "Outdoor performance analysis of a 1090× point-focus Fresnel high concentrator photovoltaic/thermal system with triple-junction solar cells," *Energy Conversion and Management,* vol. 100, pp. 191-200, 2015.

[137] A. J. García, A. J. Órpez, and F. Cruz-Peragón, "A simplified finite element model for uncoupled thermal analysis in CPV heat sink design to reduce time-to-market," in *AIP Conference Proceedings*, 2013, p. 274.

[138] J. C. Minano, J. C. Gonzalez, and I. Zanesco, "Flat high concentration devices," presented at the 24th IEEE Photovoltaic Specialists Conference, Hawaii, 1994.

[139] T. L. Chou, Z. H. Shih, H. F. Hong, C. N. Han, and K. N. Chiang, "Thermal Performance Assessment and Validation of High-Concentration Photovoltaic Solar Cell Module," *IEEE Transactions on Components Packaging and Manufacturing Technology,* vol. 2, pp. 578-586, Apr 2012.

[140] J. Jaus, R. Hue, M. Wiesenfarth, G. Peharz, and A. W. Bett, "Thermal management in a passively cooled concentrator photovoltaic module," presented at the 23rd European Photovoltaic Solar Energy Conference, Valencia, Spain, 2008.

[141] L. Micheli, S. Senthilarasu, K. S. Reddy, and T. K. Mallick, "Applicability of silicon micro-finned heat sinks for 500× concentrating photovoltaics systems," *Journal of Materials Science,* vol. 50, pp. 5378-5388, 2015.

[142] K. Emery, A. Anderberg, M. Campanelli, P. Ciszek, C. Mack, T. Moriarty, C. Osterwald, L. Ottoson, S. Rummel, and R. Williams, "Rating photovoltaics," in *Photovoltaic Specialists Conference (PVSC), 2013 IEEE 39th*, 2013, pp. 0001-0006.

[143] Standard IEC 62670-1, "Concentrator Photovoltaic (CPV) - Performance Testing Part 1: Standard Conditions," 2013, Geneva, Switzerland.

[144] Standard IEC 62670-3, "Concentrator Photovoltaic (CPV) - Performance Testing Part 3: Performance Measurements and Power Rating," 2013, Geneva, Switzerland.

[145] M. Steiner, M. Baudrit, C. Dominguez, I. Antón, F. Roca, R. Fucci, P. Pugliatti, A. Di Stefano, R. Kenny, and P. Morabito, "SOPHIA CPV Module Round Robin: Power Rating at CSOC," in *European Photovoltaic Solar Energy Conference and Exhibition (EU PVSEC)*, Amsterdam, 2014.

[146] Standard IEC 60904-3, "Measurement Principles for Terrestrial PV Solar Devices with Reference Spectral Irradiance Data," ed.2, 2008, Geneva, Switzerland.

[147] ASTM E2527-09, "Standard test method for electrical performance of concentrator terrestrial photovoltaic modules and systems under natural sunlight," 2009, West Conshohocken, PA, USA.

[148] M. Theristis and T. S. O'Donovan, "Electrical-thermal analysis of III–V triple-junction solar cells under variable spectra and ambient temperatures," *Solar Energy,* vol. 118, pp. 533-546, 2015.

[149] M. Theristis and T. S. O'Donovan, "An integrated thermal electrical model for single cell photovoltaic receivers under concentration," in *15th International Heat Transfer Conference (IHTC-15)*, Kyoto, Japan, 2014, pp. n/a-n/a.

[150] M. Theristis, N. Sarmah, T. K. Mallick, and T. S. O'Donovan, "Design and Numerical Analysis of Enhanced Cooling Techniques for a High Concentration Photovoltaic (HCPV) System," in *27th European Photovoltaic Solar Energy Conference and Exhibition (EU PVSEC)*, Frankfurt, Germany, 2012, pp. 260 - 265.

[151] J. Leloux, D. Pachón, and G. Sala, "Spectral Solar Radiation Measurements and Models for CPV Module Production Estimation," *AIP Conference Proceedings,* vol. 1277, pp. 329-332, 2010.

[152] ASTM G173-03(2012), Standard Tables for Reference Solar Spectral Irradiances: Direct Normal and Hemispherical on 37° Tilted Surface, ASTM International, West Conshohocken, PA, 2012, www.astm.org

[153] C. A. Gueymard, "Parameterized transmittance model for direct beam and circumsolar spectral irradiance," *Solar Energy,* vol. 71, pp. 325-346, 2001.

[154] *Matlab® - The Language of Technical Computing [Details at: http://www.mathworks.com/]*.

[155] Y. Varshni, "Temperature dependence of the energy gap in semiconductors," *Physica,* vol. 34, pp. 149-154, 1967.

[156] *COMSOL Multiphysics® FEA Software [Details at: http://www.comsol.com/]*.

[157] F. P. Incropera and D. P. DeWitt, *Fundamentals of Heat and Mass Transfer*, Fourth Edition ed. New York: John Wiley & Sons, 1996.

[158] *Fraunhofer CSE Website, http://cse.fraunhofer.org/, [Accessed November 27, 2015]*.

[159] *CFV Solar Test Laboratory Website, http://cfvsolar.com/, [Accessed November 27, 2015].*

[160] Emcore. (2012). *CTJ Photovoltaic Cell - 10 mm x 10 mm - Datasheet. <http://www.emcore.com/wp-content/uploads/CTJ-Cell_10mm.pdf>.*

[161] *Vaisala Weather Transmitter WXT520 User's Guide [Details at: http://www.vaisala.com/en/vaisalalists/Documents/WXT520%20User's%20Guide%20in%20English%20M210906EN-C.pdf].*

[162] *Vaisala Weather Transmitter WXT520 Datasheet [Details at: http://www.vaisala.com/Vaisala%20Documents/Brochures%20and%20Datasheets/WEA-MET-WXT520-Weather-datasheet-B210417EN-K-LOW.pdf].*

[163] *The Eppley Laboratory, Inc., Normal Incidence Pyrheliometer Specifications [Details at: http://www.eppleylab.com/instrumentation/snip_spec_2015.pdf].*

[164] *Kipp & Zonen, CHP1 Pyrheliometer Specifications [Details at: http://www.kippzonen.com/Product/18/CHP1-Pyrheliometer#.Vm8wE79I5SE].*

[165] *Black Photon Instruments, BPI-TA1 Tracking Accuracy Sensor Specifications [Details at: http://www.black-photon.de/products/tracking-accuracy.html].*

[166] *Black Photon Instruments, BPI-IT1 Isotype Spectral Sensor Specifications [Details at: http://www.black-photon.de/products/isotype-sensors.html].*

[167] *Kipp & Zonen, CMP6 Pyranometer Specifications [Details at: http://www.kippzonen.com/Product/12/CMP6-Pyranometer#.Vng8G1JI5SE].*

[168] *Daystar Inc., DS-1000 I-V curve tracer manual and specifications [Details at: http://www.daystarpv.com/DS1000.pdf].*

[169] *Daystar Inc., IVPC Software [Details at: http://www.daystarpv.com/curvetracer4.html].*

[170] D. A. Bachour, "Measuring and Estimating Solar Direct Normal Irradiance using LIDAR, Solar Station and Satellite Data in Qatar," Departament de Fisica, Universitat Autonoma de Barcelona, Barcelona, 2015.

[171] *Solar Light Co., Inc., MICROTOPS II Sunphotometer User's Guide [Details at: http://solarlight.com/wp-content/uploads/2014/11/Meters_Model-540-.pdf].*

[172] *Campbell Scientific, CR1000 Specifications [Details at: https://www.campbellsci.com/cr1000].*

[173] E. F. Fernández, A. J. G. Loureiro, and G. P. Smestad, "Multijunction Concentrator Solar Cells: Analysis and Fundamentals," in *High Concentrator Photovoltaics*, P. Pérez-Higueras and E. F. Fernández, Eds., 1 ed: Springer International Publishing, 2015, pp. 9-37.

[174] W. Guter, J. Schone, S. P. Philipps, M. Steiner, G. Siefer, A. Wekkeli, E. Welser, E. Oliva, A. W. Bett, and F. Dimroth, "Current-matched triple-junction solar cell reaching 41.1% conversion efficiency under concentrated sunlight," *Applied Physics Letters,* vol. 94, Jun 1 2009.

[175] P. J. Verlinden, A. Lewandowski, C. Bingham, G. S. Kinsey, R. A. Sherif, and J. B. Lasich, "Performance and reliability of multijunction III-V modules for concentrator dish and central receiver applications," in *4th World Conference on Photovoltaic Energy Conversion*, Hawaii, 2006, pp. 592-597.

[176] H. Cotal and J. Frost, "Heat Transfer Modeling of Concentrator Multijunction Solar Cell Assemblies Using Finite Difference Techniques," in *35th IEEE Photovoltaic Specialists Conference (PVSC)*, Honolulu, HI, USA, 2010.

[177] H. Cotal and R. Sherif, "Temperature dependence of the IV parameters from triple junction GaInP/InGaAs/Ge concentrator solar cells," in *4th World Conference on Photovoltaic Energy Conversion*, 2006, pp. 845-848.

[178] K. Nishioka, T. Takamoto, T. Agui, M. Kaneiwa, Y. Uraoka, and T. Fuyuki, "Annual output estimation of concentrator photovoltaic systems using high-efficiency InGaP/InGaAs/Ge triple-junction solar cells based on experimental solar cell's characteristics and field-test meteorological data," *Solar Energy Materials and Solar Cells,* vol. 90, pp. 57-67, Jan 6 2006.

[179] Spectrolab. (2009, June 10, 2014). *C1MJ concentrator solar cell assembly data sheet (prototype product). <http://www.spectrolab.com/DataSheets/PV/CPV/C1MJ%2009%2018%2009.pdf>.*

[180] Azurspace. (2014, August 08, 2014). *CPV triple junction solar cell assembly - Type 3C42A data sheet. <http://azurspace.com/images/products/DB_3987-00-00_3C42_AzurDesign_EFA_10x10_2014-03-27.pdf>.*

[181] Azurspace. (2015). *CPV triple junction solar cell assembly - Type 3C44A data sheet. <http://www.azurspace.com/images/products/DB_4359-00-00_3C44_AzurDesign_EFA_10x10_2015-04-02.pdf>.*

[182] Azurspace. (2010, August 08, 2014). *CPV triple junction solar cell assembly - Type 3C40A data sheet. <http://azurspace.de/images/pdfs/CPV%20TJ%20Solar%20Cell%203C40A%2032x37mm.pdf>.*

[183] P. Espinet-González, C. Algora, N. Núñez, V. Orlando, M. Vázquez, J. Bautista, and K. Araki, "Temperature accelerated life test on commercial concentrator III–V triple-junction solar cells and reliability analysis as a function of the operating temperature," *Progress in Photovoltaics: Research and Applications,* vol. 23, pp. 559-569, 2015.

[184] K. Nishioka, T. Takamoto, T. Agui, M. Kaneiwa, Y. Uraoka, and T. Fuyuki, "Evaluation of temperature characteristics of high-efficiency InGaP/InGaAs/Ge triple-junction solar cells under concentration," *Solar Energy Materials and Solar Cells,* vol. 85, pp. 429-436, Jan 31 2005.

[185] G. Kinsey, "High-Concentration, III–V Multijunction Solar Cells," in *Solar Cells and their Applications*, ed: John Wiley & Sons, Inc., 2010, pp. 293-312.

[186] Y. N. Wang, T. T. Lin, J. C. Leong, Y. T. Hsu, C. P. Yeh, P. H. Lee, and C. H. Tsai, "Numerical investigation of high-concentration photovoltaic module heat dissipation," *Renewable Energy,* vol. 50, pp. 20-26, Feb 2013.

[187] F. Al-Amri and T. K. Mallick, "Alleviating operating temperature of concentration solar cell by air active cooling and surface radiation," *Applied Thermal Engineering,* vol. 59, pp. 348-354, 2013.

[188] M. D. Yandt, J. F. Wheeldon, J. Cook, R. Beal, A. W. Walker, O. Theriault, H. Schriemer, T. J. Hall, and K. Hinzer, "Estimating Cell Temperature In A Concentrating Photovoltaic System," in *AIP Conference Proceedings*, 2012, pp. 172-175.

[189] G. Siefer and A. W. Bett, "Analysis of temperature coefficients for III–V multi-junction concentrator cells," *Progress in Photovoltaics: Research and Applications,* vol. 22, pp. 515-524, 2014.

[190] I. Mudawar, "Assessment of high-heat-flux thermal management schemes," *Components and Packaging Technologies, IEEE Transactions on,* vol. 24, pp. 122-141, 2001.

[191] C. A. Gueymard and D. Myers, "Solar Resource for Space and Terrestrial Applications," in *Solar Cells and their Applications*, ed: John Wiley & Sons, Inc., 2010, pp. 425-461.

[192] Spectrolab, "Application Note 0902 - Analytical model for C1MJ and C3MJ CDO-100 Solar Cells and CCAs," Spectrolab, Sylmar, CA, 2009.

[193] R. I. Rabady, "Optimized multi-junction photovoltaic solar cells for terrestrial applications," *Solar Energy,* vol. 106, pp. 72-81, 2014.

[194] I. R. Cole, T. R. Betts, and R. Gottschalg, "Solar Profiles and Spectral Modeling for CPV Simulations," *Photovoltaics, IEEE Journal of,* vol. 2, pp. 62-67, 2012.

[195] L. Micheli, "Enhancing Electrical and Heat Transfer Performance of High-Concentrating Photovoltaic Receivers," Ph.D., University of Exeter, 2015.

[196] C. Domínguez and P. García-Linares, "Characterization of Multijunction Concentrator Solar Cells," in *High Concentrator Photovoltaics*, P. Pérez-Higueras and E. F. Fernández, Eds., ed: Springer International Publishing, 2015, pp. 39-84.

[197] E. F. Fernández and F. Almonacid, "A new procedure for estimating the cell temperature of a high concentrator photovoltaic grid connected system based on

atmospheric parameters," *Energy Conversion and Management,* vol. 103, pp. 1031-1039, 2015.

[198] C. Renno, F. Petito, and A. Gatto, "Artificial neural network models for predicting the solar radiation as input of a concentrating photovoltaic system," *Energy Conversion and Management,* vol. 106, pp. 999-1012, 2015.

[199] C. J. Willmott, "Some Comments on the Evaluation of Model Performance," *Bulletin of the American Meteorological Society,* vol. 63, pp. 1309-1313, 1982/11/01 1982.

[200] C. A. Gueymard, "Direct solar transmittance and irradiance predictions with broadband models. Part II: validation with high-quality measurements," *Solar Energy,* vol. 74, pp. 381-395, 2003.

[201] S. Z. Aljoaba, A. M. Cramer, and B. L. Walcott, "Thermoelectrical Modeling of Wavelength Effects on Photovoltaic Module Performance-Part I: Model," *IEEE Journal of Photovoltaics,* vol. 3, pp. 1027-1033, Jul 2013.

[202] Y. Kemmoku, T. Egami, M. Hiramatsu, Y. Miyazaki, K. Araki, N. J. Ekins-Daukes, and T. Sakakibara, "Modelling of module temperature of a concentrator PV system," in *19th European Photovoltaic Solar Energy Conference and Exhibition (EU PVSEC)*, Paris, France, 2004.

[203] E. F. Fernández, F. Almonacid, L. Micheli, and T. Mallick, "Comparison of methods for estimating the solar cell temperature and their influence in the calculation of the electrical parameters in a HCPV module," *AIP Conference Proceedings,* vol. 1616, pp. 183-186, 2014.

[204] M. Castro, C. Domínguez, R. Núñez, I. Antón, G. Sala, and K. Araki, "Detailed effects of wind on the field performance of a 50 KW CPV demonstration plant," in *AIP Conference Proceedings*, 2013, p. 256.

[205] M. Theristis, C. Stark, and T. S. O'Donovan, "Determination of the cooling requirements for single cell photovoltaic receivers under variable atmospheric parameters," in *Photovoltaic Specialist Conference (PVSC), 2015 IEEE 42nd*, 2015, pp. 1-5.

[206] M. Theristis, E. F. Fernández, C. Stark, and T. S. O'Donovan, "A theoretical analysis of the impact of atmospheric parameters on the spectral, electrical and thermal performance of a concentrating III–V triple-junction solar cell," *Energy Conversion and Management,* vol. 117, pp. 218-227, 2016.

[207] M. Theristis, E. F. Fernández, J. P. Ferrer-Rodríguez, C. Stark, and T. S. O'Donovan, "Energy Yield Assessment of a High Concentration Photovoltaic Receiver Based on Simulated Spectra from Typical Meteorological Year Datasets," in *12th International Conference on Concentrator Photovoltaic Systems (CPV-12)*, Freiburg, Germany, 2016.

[208] M. Steiner, A. Bösch, A. Dilger, F. Dimroth, T. Dörsam, M. Muller, T. Hornung, G. Siefer, M. Wiesenfarth, and A. W. Bett, "FLATCON® CPV module with 36.7% efficiency equipped with four-junction solar cells," *Progress in Photovoltaics: Research and Applications,* vol. 23, pp. 1323-1329, 2015.

[209] E. F. Fernández, P. Pérez-Higueras, A. J. Garcia Loureiro, and P. G. Vidal, "Outdoor evaluation of concentrator photovoltaic systems modules from different manufacturers: first results and steps," *Progress in Photovoltaics: Research and Applications,* vol. 21, pp. 693-701, 2013.

[210] B. Marion, "Influence of atmospheric variations on photovoltaic performance and modeling their effects for days with clear skies," in *Photovoltaic Specialists Conference (PVSC), 2012 38th IEEE*, 2012, pp. 003402-003407.

[211] M. D. Perez and N. E. Gorji, "Modeling of temperature profile, thermal runaway and hot spot in thin film solar cells," *Materials Science in Semiconductor Processing,* vol. 41, pp. 529-534, 2016.

[212] S. Kurtz, M. Muller, D. Jordan, K. Ghosal, B. Fisher, P. Verlinden, J. Hashimoto, and D. Riley, "Key parameters in determining energy generated by CPV modules," *Progress in Photovoltaics: Research and Applications,* vol. 23, pp. 1250-1259, 2015.

[213] P. Blumenfeld, J. Foresi, Y. Lang, and J. Nagyvary, "Thermal management and engineering economics in CPV design," in *MEPTEC Symposium Proceedings No. 41*, San Jose, CA, USA, 2011, pp. 206-234.

[214] C. Stark and M. Theristis, "The impact of atmospheric parameters on the spectral performance of multiple photovoltaic technologies," in *Photovoltaic Specialist Conference (PVSC), 2015 IEEE 42nd*, 2015, pp. 1-5.

[215] S. P. Philipps, G. Peharz, R. Hoheisel, T. Hornung, N. M. Al-Abbadi, F. Dimroth, and A. W. Bett, "Energy harvesting efficiency of III-V triple-junction concentrator solar cells under realistic spectral conditions," *Solar Energy Materials and Solar Cells,* vol. 94, pp. 869-877, May 2010.

[216] G. S. Kinsey, "Spectrum Sensitivity, Energy Yield, and Revenue Prediction of PV Modules," *Photovoltaics, IEEE Journal of,* vol. 5, pp. 258-262, 2015.

[217] E. F. Fernández, A. Soria-Moya, F. Almonacid, and J. Aguilera, "Comparative assessment of the spectral impact on the energy yield of high concentrator and conventional photovoltaic technology," *Solar Energy Materials and Solar Cells,* vol. 147, pp. 185-197, 2016.

[218] G. S. Kinsey, K. Stone, J. Brown, and V. Garboushian, "Energy prediction of Amonix CPV solar power plants," *Progress in Photovoltaics: Research and Applications,* vol. 19, pp. 794-796, 2011.

[219] S. Senthilarasu, E. F. Fernández, F. Almonacid, and T. K. Mallick, "Effects of spectral coupling on perovskite solar cells under diverse climatic conditions," *Solar Energy Materials and Solar Cells,* vol. 133, pp. 92-98, 2015.

[220] E. F. Fernández, F. Almonacid, T. K. Mallick, and S. Sundaram, "Effect of Spectral Irradiance Variations on the Performance of Highly Efficient Environment-Friendly Solar Cells," *Photovoltaics, IEEE Journal of,* vol. 5, pp. 1150-1157, 2015.

[221] NREL. (2015). *National solar radiation database; Typical meteorological year 3 (TMY3)*. Available: http://rredc.nrel.gov/solar/old_data/nsrdb/1991-2005/tmy3/

[222] M. G. Liu, G. S. Kinsey, W. Bagienski, A. Nayak, and V. Garboushian, "Indoor and Outdoor Comparison of CPV III-V Multijunction Solar Cells," *IEEE Journal of Photovoltaics,* vol. 3, pp. 888-892, Apr 2013.

[223] I. Garcia, W. E. McMahon, M. A. Steiner, J. F. Geisz, A. Habte, and D. J. Friedman, "Optimization of Multijunction Solar Cells Through Indoor Energy Yield Measurements," *Photovoltaics, IEEE Journal of,* vol. 5, pp. 438-445, 2015.

[224] J. Hashimoto, S. Kurtz, K. Sakurai, M. Muller, and K. Otani, "Field experience and performance of CPV system in different climates," in *AIP Conference Proceedings*, 2013, p. 261.

[225] R. W. Higgins, Y. Yao, and X. L. Wang, "Influence of the North American Monsoon System on the U.S. Summer Precipitation Regime," *Journal of Climate,* vol. 10, pp. 2600-2622, 1997/10/01 1997.

[226] M. Muller, B. Marion, S. Kurtz, J. Rodriguez, A. W. Bett, R. D. McConnell, G. Sala, and F. Dimroth, "An investigation into spectral parameters as they impact CPV module performance," in *AIP Conference Proceedings*, 2010, p. 307.

[227] A. Gombert, J. C. Miñano, P. Benitez, and T. Hornung, "Concentrator Optics for Photovoltaic Systems," in *Photon Management in Solar Cells*, ed: Wiley-VCH Verlag GmbH & Co. KGaA, 2015, pp. 153-182.

[228] V. Rumyantsev, N. Y. Davidyuk, E. Ionova, P. Pokrovskiy, N. Sadchikov, and V. Andreev, "Thermal Regimes of Fresnel Lenses and Cells in "All-Glass'' HCPV Modules," in *American Institute of Physics Conference Series*, 2010, pp. 89-92.